NOAA Technical Memorandum ERL PMEL-86

# OBSERVATIONS OF LONG ROSSBY WAVES IN THE NORTHERN TROPICAL PACIFIC

William S. Kessler

Pacific Marine Environmental Laboratory
Seattle, Washington
March 1989

**UNITED STATES**
**DEPARTMENT OF COMMERCE**

**Robert A. Mosbacher**
**Secretary**

NATIONAL OCEANIC AND
ATMOSPHERIC ADMINISTRATION

William E. Evans
Under Secretary for Oceans
and Atmosphere/Administrator

Environmental Research
Laboratories

Joseph O. Fletcher
Director

Contribution No. 1113 from NOAA/Pacific Marine Environmental Laboratory

For sale by the National Technical Information Service, 5285 Port Royal Road
Springfield, VA 22161

# CONTENTS

PAGE

## LIST OF FIGURES

## LIST OF TABLES

# Observations of Long Rossby Waves in the Northern Tropical Pacific

William S. Kessler*

ABSTRACT. Long baroclinic Rossby waves are potentially important in the adjustment of the tropical Pacific pycnocline to both annual and interannual wind stress curl fluctuations. Evidence for such waves is found in variations of the depth of the 20°C isotherm in the northern tropical Pacific during 1970 through 1987. 190,000 bathythermograph profiles have been compiled from the archives of several countries; the data coverage is dense enough that westward-propagating events may be observed with a minimum of zonal interpolation. After extensive quality control, 20°C depths were gridded with a resolution of 2° latitude, 5° longitude and bimonths; statistical parameters of the data were estimated. A simple model of low-frequency pycnocline variability allows the physical processes of Ekman pumping, the radiation of long (non-dispersive) Rossby waves due to such pumping in mid-basin, and the radiation of long Rossby waves from the observed eastern boundary pycnocline depth fluctuations. Although the wind stress curl has very little zonal variability at the annual period in the northern tropical Pacific, an annual fluctuation of 20°C depth propagates westward as a long Rossby wave near 4°-6°N and 14°-18°N in agreement with the model hindcast. Near the thermocline ridge at 10°N, however, the annual cycle is dominated by Ekman pumping. The wave-dominated variability at 4°-6°N weakens the annual cycle of Countercurrent transport in the western Pacific. El Niño events are associated with westerly wind anomalies concentrated in the central equatorial Pacific; an upwelling wind stress curl pattern is generated in the extra-equatorial tropics by these westerlies. Long upwelling Rossby waves were observed to raise the western Pacific thermocline well outside the equatorial waveguide in the later stages of El Niños, consistent with the simple long-wave model. It has been suggested that El Niño events are initiated by downwelling long Rossby waves in the extra-equatorial region reflecting off the western boundary as equatorial Kelvin waves. The bathythermograph observations show that although such downwelling waves commonly arrive at the western boundary (the Philippines coast), there is a low correlation between these occurrences and the subsequent initiation of El Niño events.

## INTRODUCTION

Long baroclinic Rossby waves are potentially important in the adjustment of the tropical (extra-equatorial) Pacific pycnocline to both annual and interannual wind stress curl fluctuations. The purpose of this report is to document the occurrence of these waves from historical data and to show that much of the observed low-frequency pycnocline variability in the northern tropical Pacific may be represented by a simple model expressing the physical processes of Ekman pumping, the radiation of long (non-dispersive) Rossby waves due to such pumping in mid-basin, and the radiation of long Rossby waves from observed eastern boundary thermocline depth fluctuations. Evidence of long Rossby waves is found in bathythermograph (BT) observations of the depth of the 20°C isotherm, which is used as a proxy for pycnocline variability. The progenitor of the present study is Meyers' (1979a) investigation of the annual cycle of 14°C depth, which used a similar simple model of a reduced-gravity ocean on a $\beta$-plane. Much of

---

* Joint Institute for the Study of Atmosphere and Ocean (JISAO, University of Washington, AK-40, Seattle, WA, 98195.

Meyers' (1979a) work is updated (and largely confirmed) in Section 3 of this report, with the addition of ten more years of both BT and wind observations.

In a series of papers, White and collaborators (White, 1977, 1983; White *et al.*, 1982, 1985; Inoue *et al.*, 1987; Pazan *et al.*, 1986; Pazan and White, 1987; Graham and White, 1988) have sought to interpret BT observations in the extra-equatorial north Pacific in terms of similar simple physics, often using the linear reduced-gravity model developed by Busalacchi and O'Brien (1980). Some of their results are consistent with conclusions reported here, however the expendable BT (XBT) data available to these investigators are distributed primarily along a few shipping lines, with large gaps in important areas, requiring relatively elaborate interpolation schemes between the ship tracks or the use of model output to fill data gaps. Because of this, their interpretation of observed interannual variability as evidence of zonal propagation has been controversial. An essential element of the present study is in the addition of a large set of mechanical BT (MBT) data taken by Japanese fishing vessels, which is concentrated in a previously data-poor region in the western tropical Pacific and makes possible the construction of long time series of thermocline depths in the western Pacific with a minimum of zonal interpolation.

Section 1 of this report discusses the BT data sets, their processing and gridding. The simple model of low-frequency pycnocline variability is developed in Section 2, and the approximations used are discussed. The mean thermal structure and the average annual cycle of thermocline depth anomalies are described in Section 3, and annual variability is discussed in terms of the simple physics outlined above, comparing the observations with hindcasts derived assuming either local Ekman pumping alone or β-plane vorticity dynamics. Section 4 focuses on the role of long extra-equatorial Rossby waves in the evolution of El Niño. Waves due to two principal forcings are identified: upwelling long Rossby waves generated in mid-basin by the large scale wind stress curl pattern associated with strong equatorial westerly wind anomalies; and downwelling long Rossby waves which radiate from the eastern boundary following the reflection of the deep equatorial thermocline anomaly which occurs during El Niños. The suggestion that long Rossby waves in the extra-equatorial tropics can be a trigger for subsequent El Niños, which has been debated in the recent literature, is evaluated from several time series which extend back to the 1950's, spanning seven major El Niño events.

Much of the discussion in Sections 2, 3 and 4 makes use of a long wave (non-dispersive) assumption; Appendix 1 seeks to justify that simplification by considering in detail the dispersion of a pulse originating at the eastern boundary with a Gaussian time history (thus a summation over many frequencies). Ray theory is used to study the dispersion in the manner of Schopf *et al.* (1981); however Appendix 1 goes further to show that time-stepping along a ray, as in classical ray theory, is not necessary since Rossby wave characteristics have a simple sinusoidal form, and ray variables can be found directly at any point. This new approach has the advantage that the wave amplitude can be found straightforwardly.

A few notes on terminology are necessary: the word "tropical" is used in the sense of "extra-equatorial", to refer to the regions between about 5° and about 25° latitude. As discussed in Section 1, the observations are inadequate to study the rapid zonal propagation which occurs in the equatorial waveguide, so dynamical interpretation is confined to the extra-equatorial, "tropical" regions. Appendix 1 examines the difference between the use of an equatorial versus a mid-latitude β-plane approximation to analyze the tropical long waves.

The parsing of the words "El Niño" has been a subject of discussion in the community. In this report, "El Niño" is treated as if it were a single English noun, including such usage as "the El Niño", "several El Niños", "during El Niño", much as one might use a noun such as "summer". This usage is consistent with other foreign words adopted into English: for example, because few of us know Japanese, we don't know whether "tsunami" is one word or two, and we don't question whether its plural is really "tsunamis". The alternative, which is to recognize the Spanish meaning, leads to locutions like "Los Niños" = "The Christ Children", or on the other hand to repeating the early oceanographic confusion about the role of a small, *annually-occurring*, warm current. It seems clearer to adopt "El Niño" as a new English word meaning "the oceanic component of the El Niño/Southern Oscillation phenomenon first described by Bjerknes (1966)".

# 1. DATA COLLECTION AND PROCESSING

## A. Introduction

Several organizations hold large archives of historical BT observations, each of which densely samples particular regions; however none of these data sets individually has sufficient coverage to document zonally propagating events over the width of the tropical north Pacific. In particular, the XBT data sets which have formed the basis for many studies of tropical Pacific variability (e.g. Meyers and Donguy, 1980, 1984; Kessler *et al.*, 1985; Rebert *et al.*, 1985; White *et al.*, 1985; Pazan and White, 1987; Kessler and Taft, 1987; Graham and White, 1988; McPhaden *et al.*, 1988a,b) are derived principally from merchant and navy vessels, which densely sample a few specific shipping lanes, but poorly observe a large region of the western north Pacific southwest of Hawaii (Fig. 1.1). It has proven difficult to draw convincing evidence of zonal propagation from these data. On the other hand, many MBT profiles were made (mostly by Japanese fishing vessels) in the western tropical Pacific during the 1970's, which nicely complement the XBT data distribution (Fig. 1.2). Even the combined data are adequate to construct long time series only in the region between 5°N and 30°N, where the observations are densest and zonal propagation of long waves is relatively slow. Although it would be desirable to develop a historical time series of thermocline fluctuations in the equatorial waveguide, the data are insufficient to do so, particularly since time scales near the equator are so short. In most of the southern hemisphere east of 150°W the observations are so sparse that even the mean cannot be found with confidence. In this section the various data sets are described and the methodology and criteria for combining and gridding them are set forth. Table 1 summarizes the numbers of profiles acquired from the various sources and number removed during the quality control process. Although the BT sampling is highly irregular and the data are aliased by high-frequency phenomena, so gridding, interpolation and smoothing are necessary, every effort has been made to keep the processing of data to a minimum, in order to let the data "speak for itself", with as few intermediary steps as possible. In particular, care was taken that interpolation in longitude was minimized to avoid the possibility that such interpolation would lead to a misleading interpretation as zonal propagation. Secondly, since the tropical Pacific is characterized by sharp zonally oriented ridge and trough features, interpolation in latitude might tend to smooth these structures; thus no interpolation in latitude was used.

## B. Description of bathythermograph data sets

The largest single temperature profile data collection is in the archives of the National Ocean Data Center (NODC), consisting of 108632 XBT observations in the Pacific Ocean part of the region 30°S-30°N, 110°E-70°W, during 1967 through 1985. This data set provides much of the basis for the Levitus (1982) climatology. The NODC data comprise most of the XBT observations shown in Fig. 1.1, with the exception of the sharply defined route from New Caledonia (21°S, 166°E) to Japan and the routes emanating from Tahiti (17°S, 150°W), which are due to the French-U.S. ship of opportunity (SOP) program discussed below. About half the observations shown on the routes from the southwest Pacific to Hawaii and North America were also made by SOP ships. The NODC data are densest on ship tracks traveled by United States Navy and merchant vessels, particularly between the U.S. mainland and Hawaii, Guam (13°N, 145°E), the Philippines, Japan and Australia (Fig. 1.1). The very dense sampling in the South China Sea was associated with the Vietnam War. However, south of the Hawaii-Guam-Philippines ship track and west of the Dateline the NODC data set has only sparse and sporadic sampling (Fig. 1.1). It is clearly an insufficient basis for study of the western tropical and equatorial Pacific.

The French-American SOP program began collecting surface observations (temperature, salinity and biological variables) in 1972 (Donguy and Dessier, 1983) and XBT profiles in 1979 (Meyers and Donguy, 1980) from volunteer merchant ships operating out of Noumea, New Caledonia. The ships traverse primarily three routes as mentioned in the previous paragraph (Fig. 1.1). A total of 26,373 XBT profiles were collected and made available during 1979 through 1987, only about one-quarter as many as in the NODC set, however the SOP data is much more concentrated in the tropics, with relatively dense sampling along the three tracks. Since much of the present work is concerned with events occurring in the 1970's, the SOP data set is of somewhat limited utility here.

The combined XBT data shown in Fig. 1.1 amounts to 135,005 total observations during 1967 through 1987. (Possibly a few thousand more might be available from sources such as the French Navy (J. Picaut, personal communication), or other foreign military organizations, particularly in recent years.) Almost all of the XBT profiles extend to 450 m depth (Table 1), which is well below the thermocline in most of the tropical Pacific. Instrumental errors of 0.1 to 0.2°C and 10 m depth are typical (Heinmiller *et al.*, 1983). Although this combined data set has been used to study zonal propagation of thermocline depth anomalies (e.g. White *et al.*, 1985), it is clear from Fig. 1.1 that a very large region southwest of Hawaii was sampled principally on a single meridional section, which did not begin until 1979, so the XBT data alone is a poor antenna for zonally propagating variability in that important region, requiring relatively elaborate statistical interpolation schemes between the tracks (Pazan and White, 1987). Because of this interpolation, interpretation of observed variability as evidence of zonal propagation has been controversial. The present work avoids this problem by merging the XBT data with MBT data collected by Japanese fishing vessels, which fortuitously fills the large gap southwest of Hawaii (Fig. 1.2) and makes possible the construction of time series of thermocline depth across most of the northern tropical Pacific with a minimum of zonal interpolation.

Although the MBT was once very widely used in oceanographic surveys (e.g. Iselin and Fuglister, 1948; Stommel, 1965; Snodgrass, 1968; Seckel, 1975), since about 1970 it has been generally superseded by the XBT. However, since the instrument does not require any on-board electronics (the profile is scratched on a smoked-glass slide or metal foil), and is considered rugged and reliable (Baker, 1981), it has continued in use on Japanese fishing vessels. The instrumental accuracy of the MBT is about ±0.2°C, somewhat larger than the estimated XBT errors (Snodgrass, 1968). The MBT data set studied here was compiled by the Japanese Far Seas Fisheries Research Laboratory (FSFRL), Shimizu, Japan, and was generously made available through a cooperative agreement with PMEL (K. Mizuno, personal communication). There is also a large collection of MBT observations taken before 1970 in the NODC archives, which were included in the Levitus (1982) climatology. These data are for the most part not used in the present study, since the data coverage in the tropical Pacific is not dense enough to grid on the relatively fine scales possible with the combined data after 1970. However, in a few regions (for example along the ship route from the U.S. West Coast to the Panama Canal) the NODC MBT data has been used to construct several long time series which are presented in Section 3.

A total of 64,062 FSFRL MBT profiles were received, covering the period 1970 through 1980. The MBT observations extend only to 250 m depth, which is below the thermocline near the equator, but within the lower thermocline in the subtropical gyres. The 20°C isotherm is practically the deepest isotherm sampled over the entire tropical Pacific by MBTs. The MBT profiles studied here are taken principally in the course of fishing operations, in which many ships work for several months in a small region, and so have a different type of spatial distribution than the XBT data, which were generally sampled along underway ship routes (Fig. 1.2). Additionally, there is seasonal variability in the data distribution, in which the central Pacific east of the dateline and north of the equator was sampled more densely in May-June, while the region near 150°E north of the equator was poorly sampled in January through April, but well-sampled during July through December (Fig. 1.3). This skewed sampling is a problem, since if there is a large annual signal the simple average of a quantity sampled only at particular seasons will not be a good estimate of the true longterm mean. A better estimate, which was used for both the XBT and MBT data, is the average of 12 monthly means, so each month has equal weight no matter how many observations it contains. The difference between the average of monthly means (henceforth referred to as the "mean") and the simple longterm average of MBT isotherm depths was typically less than 2 m, with a maximum about 5 m. Differences were smaller for the XBT data, which is more evenly distributed seasonally.

The interannual time distribution of the sampling is roughly constant during 1970 through 1980, when data from both the NODC and the FSFRL are available, with the highest sampling density during 1970 through 1975. The SOP data begins in 1979 while the FSFRL ends in 1980, so the distribution in the large region between Hawaii and the Indonesian Archipelago changes from the fishery MBT pattern (Fig. 1.2) to mostly meridional XBT tracks (Fig. 1.1). During the El Niño years of 1982-83 the observations available in this region were essentially just from the SOP program and have large gaps between the tracks. In 1985, for unknown reasons, there is a large number of NODC profiles in this region, but then relatively few observations are available during 1986-87. The total data set is thus most useful for studying zonally propagating events during the 1970's.

There are apparently no studies comparing the accuracy of the MBT and XBT. To ascertain whether systematic differences exist between the two instruments, the mean depth of various isotherms was computed (after quality control described below) from each of the instrument sets separately in regions where each data set had had at least ten observations in any 5° longitude by 2° latitude box (Fig. 1.4). This comparison indicates that the depth of the 20°C isotherm measured by the MBT appears to be typically 2 to 5 m deeper than that measured by the XBT at the same location. (The maximum of 15 m near the Philippines occurs because of very different spatial sampling patterns near and within the Philippines (Figs. 1.1 and 1.2).) It is possible that the mid-ocean discrepancy between the instruments results from different temporal sampling, but since the difference pattern is relatively constant over the northern tropical Pacific there appears to be a systematic deep bias of the MBT compared to the XBT. In the remainder of this work, it is principally anomalies of isotherm depth which are of interest, so any small instrument bias can be avoided by finding anomalies from the mean of the corresponding data set, rather than from the mean of the total. With this caveat, it is permissible to merge the MBT and XBT data sets, giving a total of 199,067 profiles of both types.

## C. Quality control

Raw bathythermograph observations contain erroneous data due to instrument malfunction, errors in reading the data, and errors occurring in the transcription of the data or position. In addition, some profiles are duplicated, either within a data set (for example if both a near-real-time radio message and a later taped record are given) or in separate sets. The three data sets studied here have all been subjected to some unknown level of quality control by the originating organizations, however further checking found and eliminated a few percent of the data in each (Table 1). Quality control performed as part of this work first eliminated duplicates (which occurred only within the MBT data and are not counted in the totals given above) and removed 112 profiles with positions on land (all of which were in the NODC collection). Many errors in the remaining observations consisted of spikes in a vertical profile, which often occurred at the bottom of a profile, or strong inversions. Software was written to find the occurrence of large gradients, spikes and inversions and unrealistic values of temperature, and plot each such profile on the computer screen. Provision was made to interactively drop a profile entirely, or correct it by cutting it above the bottom or eliminating a spike in the profile, while viewing the plot. Inversions were not automatically dropped (for example small inversions within the mixed layer or at the top of the thermocline are common, particularly in the western Pacific), unless they were clearly unrealistic. It does not appear possible to develop a fully automatic computer program which could find all cases of erroneous data without losing a large amount of good data, so the interactive procedure, though extremely tedious, was the only choice. A standard deviation test, which is used later, might be suitable to eliminate erroneous observations of a particular variable, say the depth of 20°C or the temperature at a given level, but would have to be carried out for many isotherms or levels to be sure of eliminating spikes over the entire profile, and in regions where the standard deviation was high such a test might not find all errors. Approximately 9,000 profiles were flagged as suspicious and visually scrutinized; 519 were dropped entirely and another 826 were corrected interactively. Including the 112 profiles with locations on land, this represents slightly less than 1% of the total profiles, which indicates that the quality control by the originating agencies was fairly effective.

The partially cleaned data set was then used to find the mean and standard deviation of temperature at 10 levels from zero meters to 450 m by 50 m intervals, in grid boxes 2° longitude by 1° latitude. Any gridbox with a standard deviation greater than 50 m was dropped from this calculation and the mean and standard deviation replaced by the average of surrounding boxes. Then the calculation of the mean and standard deviation at the ten levels was repeated with the additional criteria that any profile which differed by more than three standard deviations from the mean (both found from the first calculation) at any level was excluded from the second mean and standard deviation. This eliminated about 5% of the profiles. The resulting means and standard deviations were considered to be final estimates. (In fact the second estimates differed only slightly from the first.) Finally, all profiles were again compared with the second mean and standard deviation and dropped if the temperature at any level differed by more than three standard deviations from the mean. This procedure resulted in eliminating 6943 of the XBT profiles (5.1%) and 4992 of the MBT profiles (7.8%), for a total cleaned data set of 186,501 profiles in the Pacific between 30°S and 30°N, 110°E and 70°W, during 1967 through 1987. The data actually input to the gridding process described below was restricted to east of 120°E (i.e. observations in the South China Sea were excluded (see Fig. 1.1)), which removed 24,813 profiles. In addition, the gridding was restricted to the years 1970 through 1987 (since XBT observations during the 1960's were very scattered and not suitable for gridding), which removed a further 17,391 profiles (although some of these were used to construct extended time series in specific regions). The final total number of data input to the gridding described in Section 1.d was 144,297. Table 1 summarizes the disposition of data.

### D. Gridding of data

The cleaned data were gridded with a gridsize of 2° latitude, 5° longitude and 2 months, for the period 1970 through 1987. The gridsize was chosen as the smallest possible with an average of at least one observation per gridbox over most of the tropical north Pacific. The timescale of two months is sufficient to clearly resolve the annual cycle; Barnett and Patzert (1980) suggested that 23 months was an appropriate scale for thermal variability in the central Pacific. Two degrees of latitude is about the largest meridional scale which could be employed while still resolving the major zonal currents and zonally-oriented ridge/trough features, which have typical meridional scales of 5° latitude (Kessler and Taft, 1987). The 5° longitude scale is essentially dictated by practical considerations of data density, as noted above; it is at least twice the size of the internal (first baroclinic mode) Rossby radius everywhere in the study region. In some areas north of the equator it was possible to grid the data in 2° longitude boxes; these will be mentioned below. A variety of grid sizes were studied (ranging by at least factors of 2 or 1/2 from those shown) in both the zonal and meridional directions and time; the conclusions drawn below are robust in the sense that very similar results were obtained regardless of the gridding and smoothing employed. Figure 1.5 shows the number of observations of 20°C depth in each 2° by 5° box during this period. Since there are 108 bimonths during 1970-87, the period under study, 100 observations per box is approximately one observation per bimonth, and is indicated by solid contours in Fig. 1.5. By this standard, most of the tropical north Pacific is adequately sampled; sparse regions occur at 120°-140°W and near 10°N, 165°E. The eastern boundary is well sampled north of the equator, while the western boundary is densely sampled along the Philippines coast (north of 6°N) but less so near the equator. The southern hemisphere is very poorly sampled except along the SOP tracklines in the western South Pacific. Laplacian interpolation was used to fill small holes in the gridded data. Interpolation was allowed to expand the data region by one gridbox from existing data in the zonal and time directions only.

Even in the relatively well-sampled regions, however, aliasing by high-frequency internal waves and tides is the bane of those who would construct time series from observations taken at intervals of two weeks to two months, as is typical for these data. Chereskin *et al.*, (1986) made vertical profiles of temperature and salinity at 10 minute intervals for 12 days at 140°W on the equator. Their time series shows that the 20°C isotherm (which was in the core of the Equatorial Undercurrent) had semi-diurnal depth fluctuations with peak-to-peak amplitudes on the order of 10-15 m, which indicates an RMS variability of about 45 m. Since standard deviations of 20°C depth measured in the BT data set are typically 5-15 m (discussed in the following section), the unresolvable high-frequency variability is a major problem. Smoothing is necessary to reduce this small-scale noise; a 1-2-1 filter was run across the gridded data three times in time and longitude. The 1-2-1 filter (on data gridded by bimonths and 5° longitude) repeated three times, reduces the power of frequencies higher than one cycle per six months and 15° longitude by a factor of ten (Bracewell, 1978). (The corresponding values for a single pass of the filter are one cycle per 3.7 months and 9.3° longitude). Comparison of the resulting time series with the unsmoothed ones showed that the standard deviation of 20°C depth was reduced about 25% by the smoothing. Other statistical parameters such as the phase of the annual harmonic (discussed in the following section) were nearly unchanged. An alternative method, which accomplishes both interpolation and smoothing in one operation, would be to use the formalism developed by Chelton and Davis (1982) for implementing a double running mean filter (which is exactly equivalent to the triangular filter used here for suitable choices of filter length) on gappy time series. Chelton and Davis' (1982) method has the advantage that an estimate can be made of the expected error of the interpolated data. In a developmental test, the Chelton and Davis (1982) filter was used to smooth and fill the BT time series. However, since the technique requires that a running mean calculation be performed twice in succession, each time over at least three gridpoints, it was necessary to grid the data twice as densely in both longitude and time to get the same smoothing as the 1-2-1 filter used here (a double running mean is equivalent to a triangular filter of twice the length (Bracewell, 1978); with the same gridding the smoothing is much heavier for the double running mean). The results of this operation were very similar, in both visual character of the plots and statistical properties of the smoothed data set, to the results of the Laplacian interpolation and 1-2-1 smoother; since the computation and computer memory requirements were much greater, Chelton and Davis' (1982) method was abandoned.

## E. Wind data

In Section 2, a simple wind-forced model is developed to help explain observed pycnocline depth fluctuations. The winds which are used to force this model are produced by the Mesoscale

Air-Sea Interaction Group at Florida State University under the direction of J.J. O'Brien and D. Legler, from ship winds subjectively analyzed onto a 2° latitude by 2° longitude grid (Legler, personal communication), and generously made available by them. This ship wind processing effort was begun at the University of Hawaii by G. Meyers and K. Wyrtki (Wyrtki and Meyers, 1975a, 1975b, 1976) and continued at Florida State University (Goldenberg and O'Brien, 1981). This wind data set has been used to force a variety of models of the tropical Pacific (e.g. Busalacchi and O'Brien, 1980; Busalacchi *et al.*, 1983; McPhaden *et al.*, 1988; Harrison *et al.*, 1989). The pseudo-stress values provided were converted to stress using a value of $1.5 \times 10^{-3}$ for the drag coefficient. Since the meridional scale of the wind stress is typically much smaller than the zonal scale, the winds stress curl was found by differencing $\tau^x$ over 2° latitude and $\tau^y$ over 4° longitude.

Two recent studies discuss the sensitivity of model solutions to wind forcing. McPhaden *et al.* (1988) forced a linear multiple-vertical-mode model with three wind products (including the FSU winds used here) in a simulation of the average annual cycle of dynamic height anomalies during 1979-81. They found that coherences between the model simulation and dynamic heights (from XBT data) were in general higher in the equatorial waveguide than in the tropics. They attributed the poleward dropoff to the fact that extra-equatorial variability is forced by the wind stress curl, which is a spatial derivative of the wind stress and hence tends to amplify the small-scale noise. Harrison *et al.* (1989) forced an ocean general circulation model (GCM) with five wind products (also including the FSU winds) in a hindcast of the 1982-83 El Niño. Similarly to McPhaden *et al.* (1988), they also found that hindcast skill dropped off considerably in the tropical regions. In addition, substantial differences (above those which could be attributed to noise) were found in the wind stress curl fields (and hence the model hindcasts in the tropics) among the five wind products. The hindcasts made using the FSU winds produced one of the better simulations of the tropical variability during the 1982-83 event (Harrison *et al.*, 1989).

TABLE 1. Summary of the numbers of bathythermograph profiles received from the various sources and their disposition during quality control. Negative numbers are given for profiles dropped from the analysis.

| Category | Number |
|---|---|
| ***Observations received:*** | |
| NODC XBT | 108,632 |
| SOP XBT | 26,373 |
| Total XBT | 135,005 |
| FSFRL MBT | 64,062 |
| **Total raw profiles** | 199,067 |
| ***Initial screening:*** | |
| Position on land | −112 |
| Visual screening rejection | −519 |
| Total initial screening rejection | −631 |
| ***Three standard deviation test rejection:*** | |
| XBT | −6943 |
| MBT | −4992 |
| Total rejected | −12,566 |
| **Total cleaned data** | 186,501 |
| Data west of 120°E | −24,813 |
| Data before 1970 | −17,391 |
| Total omitted from gridding | −42,204 |
| **Total input to gridding** | 144,297 |
| ***Percent of gridded profiles extending to each depth range:*** | |
| 0/99 m | 1.2% |
| 100/199 m | 1.9% |
| 200/299 m | 33.2% |
| 300/399 m | 5.3% |
| 400/499 m | 57.3% |
| 500 m or deeper | 1.1% |
| Number to the depth of 20°C or deeper | 135,151 |

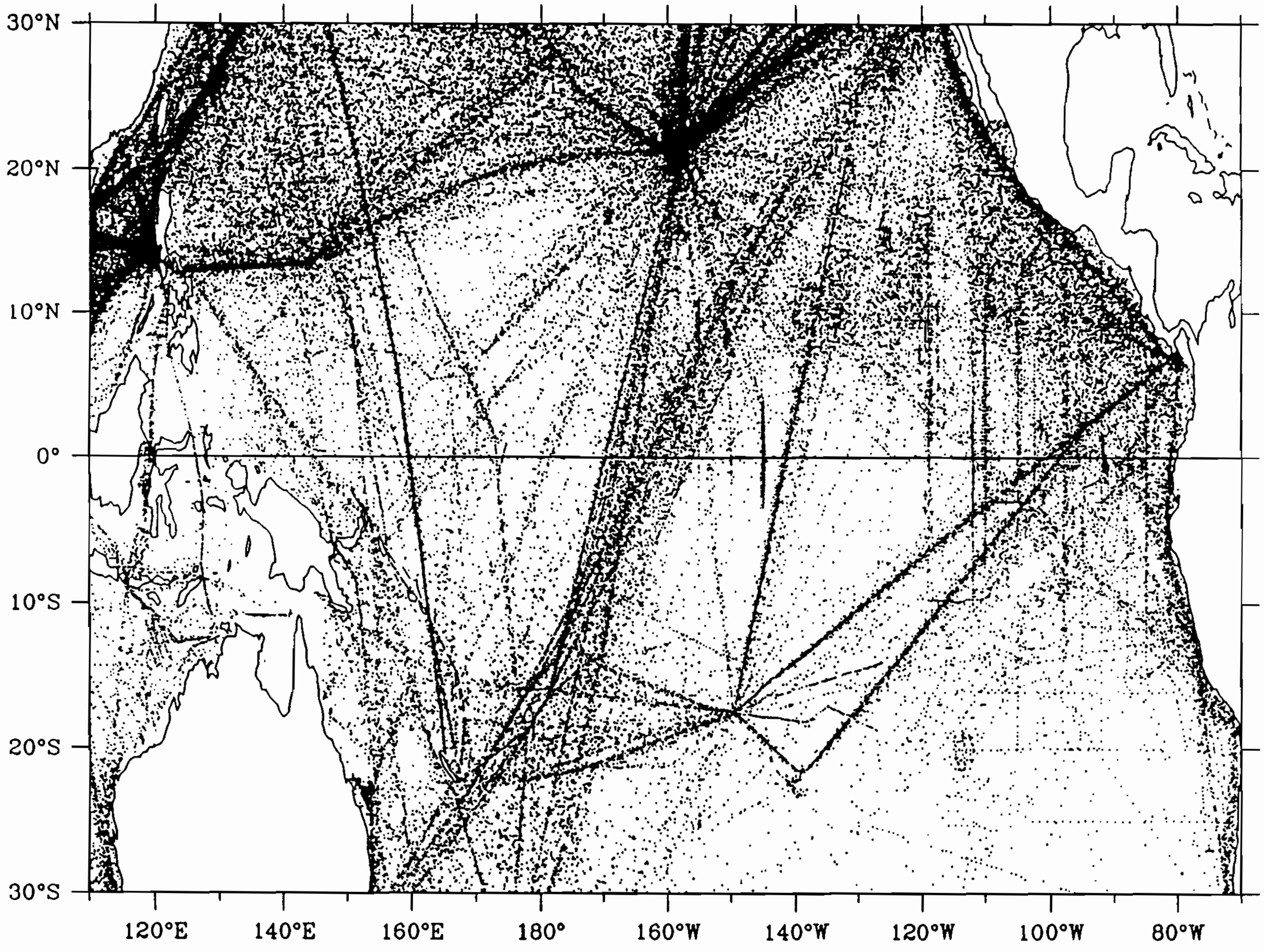

Figure 1.1. Distribution of XBT observations during 1970 through 1987.

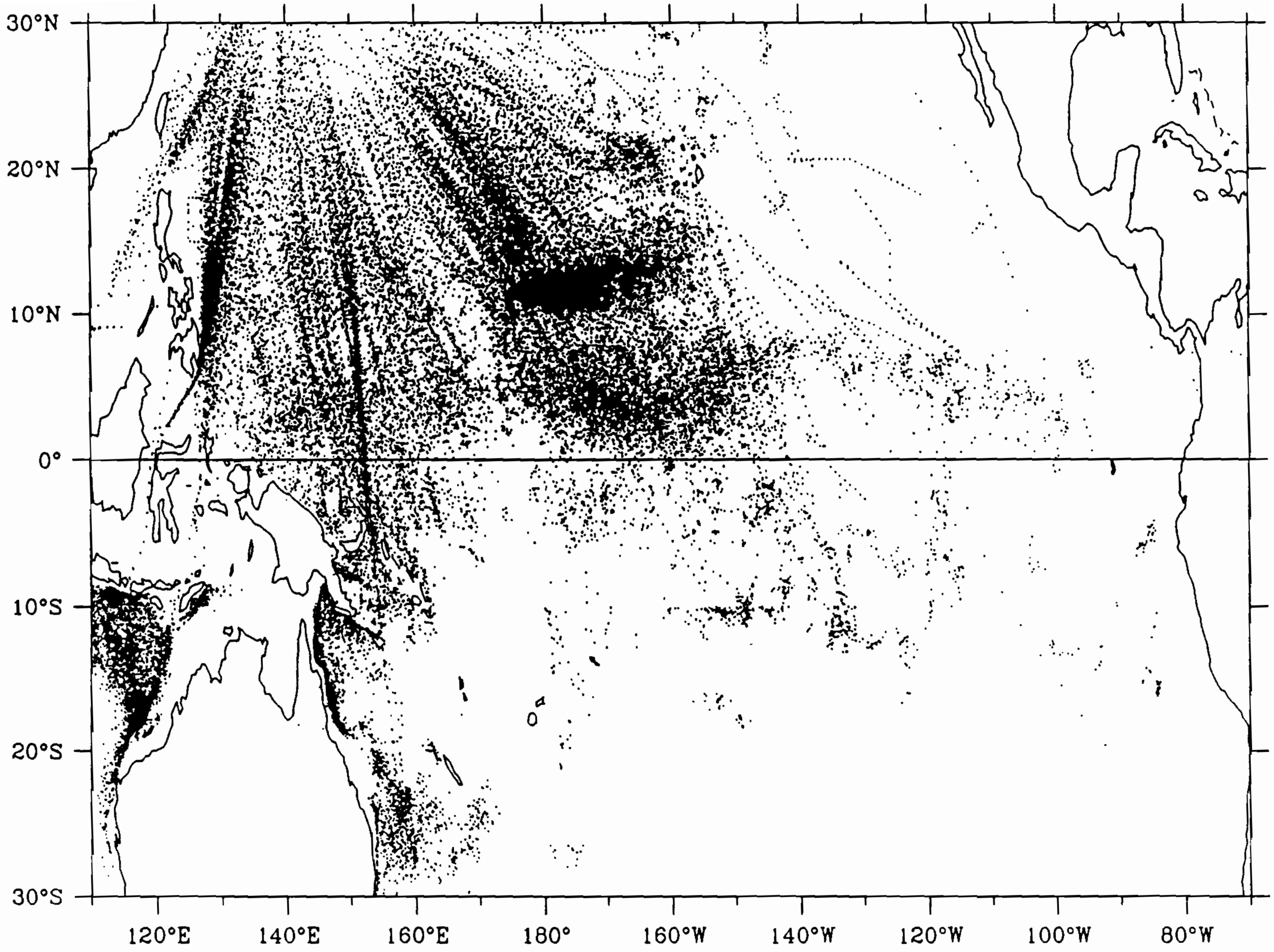

Figure 1.2. Distribution of MBT observations during 1970 through 1980.

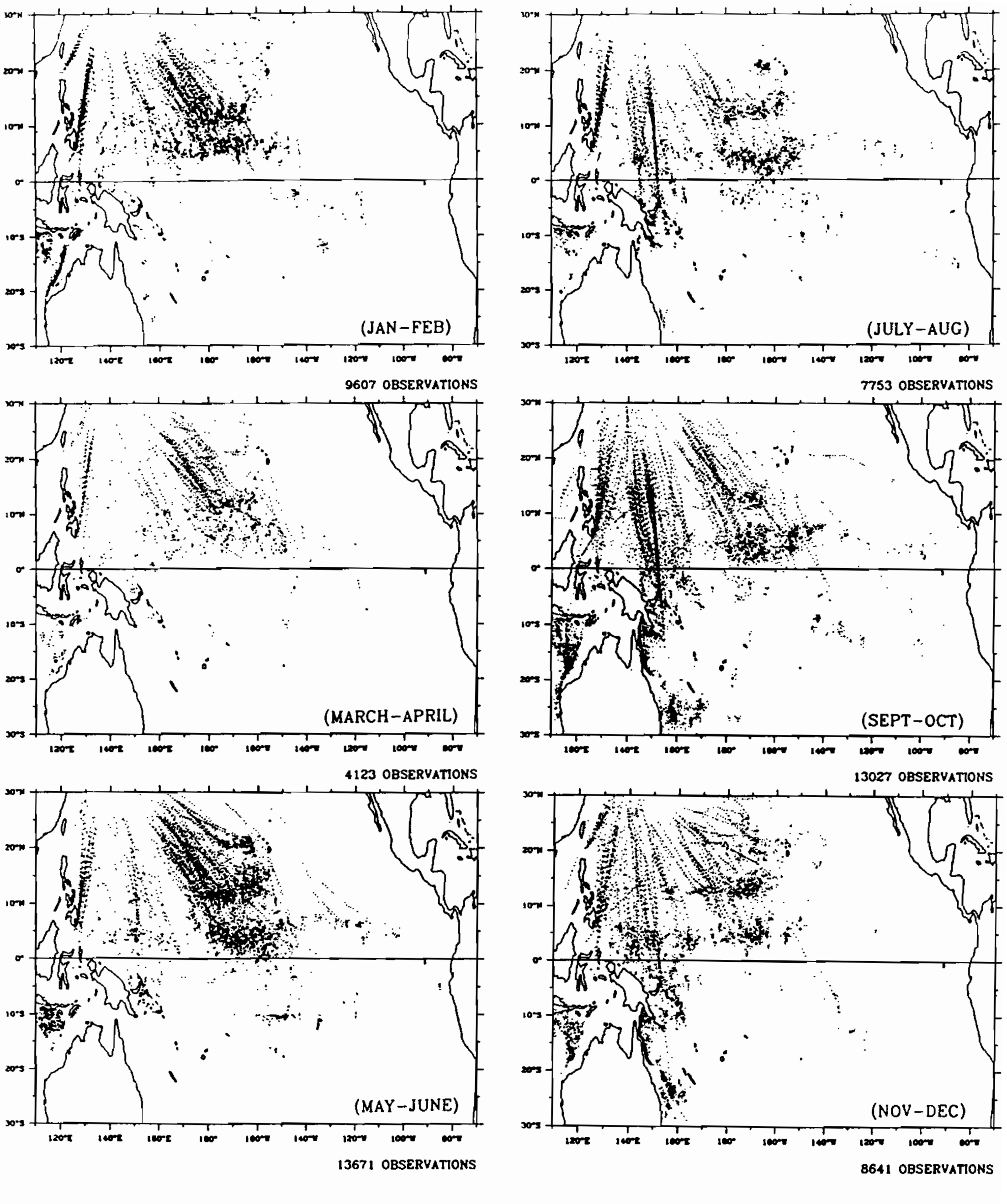

Figure 1.3. Distributions of MBT observations by bimonths.

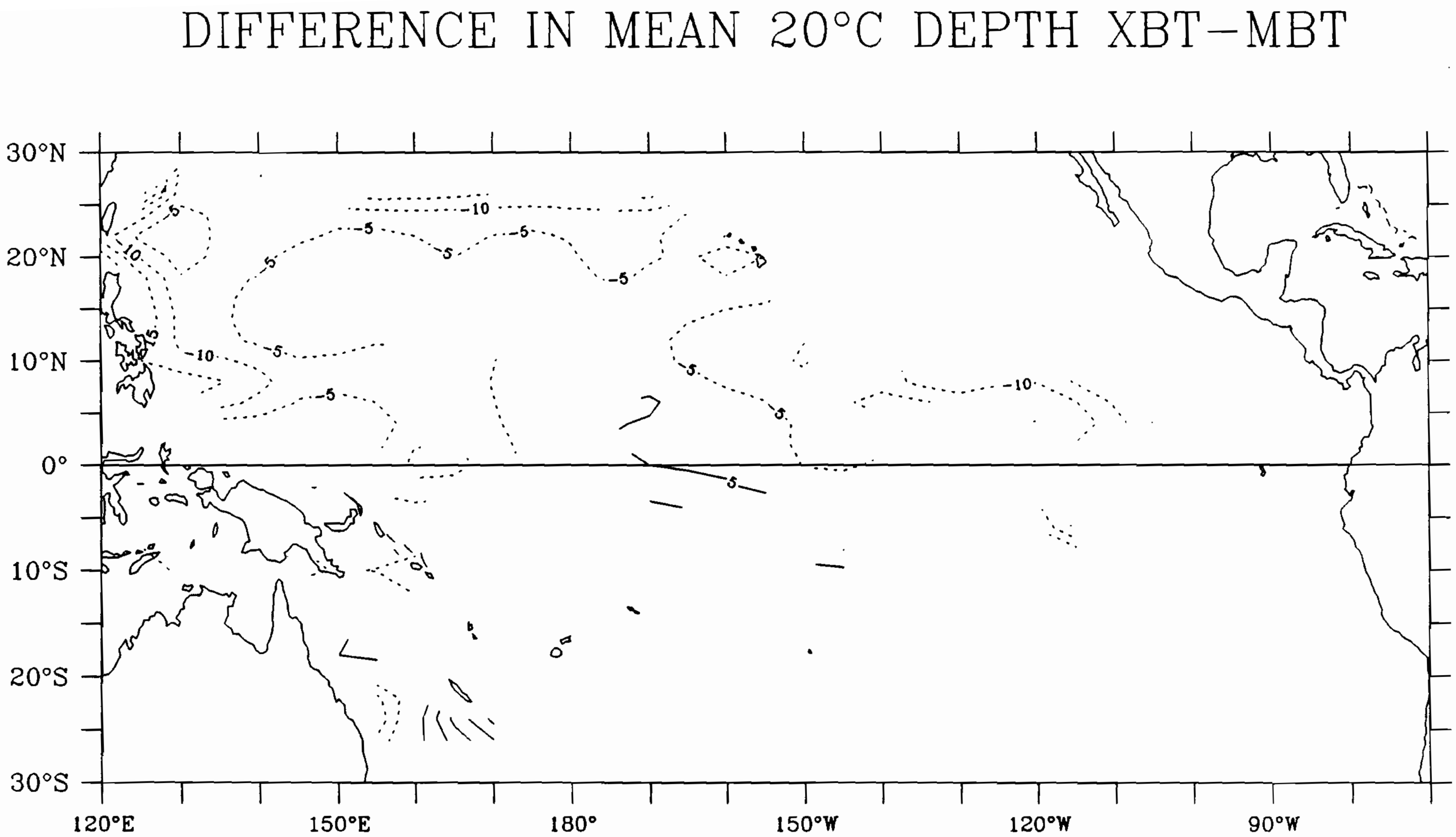
DIFFERENCE IN MEAN 20°C DEPTH XBT−MBT

Figure 1.4. Difference (m) in the mean depth of the 20°C isotherm observed from XBTs versus MBTs. Negative values (dashed contours) indicate that the MBT observation is deeper.

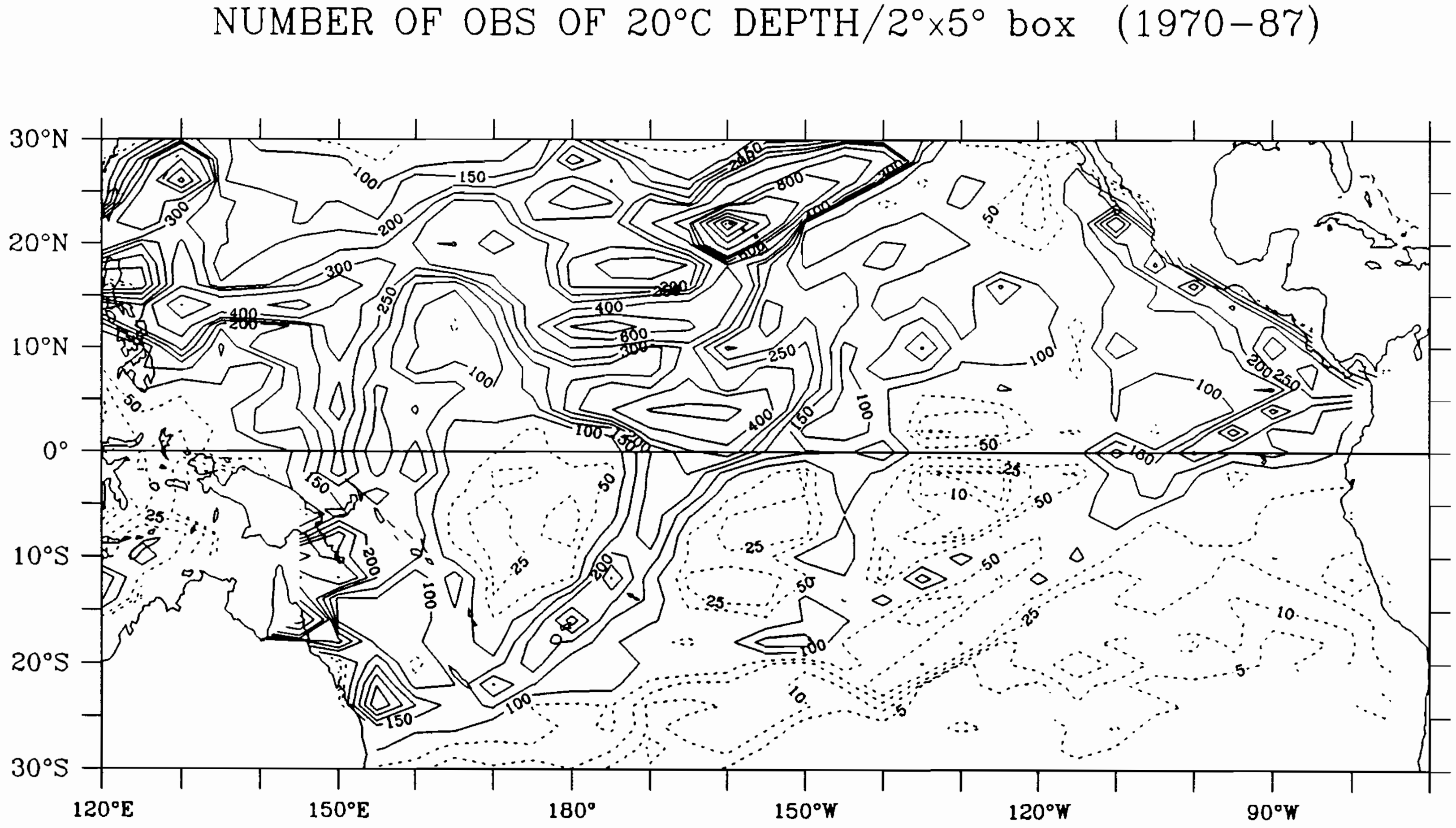

Figure 1.5. Number of observations of 20°C depth in each 2° latitude by 5° longitude gridbox. Solid contours indicate more than 100 observations per gridbox.

# 2. A SIMPLE MODEL OF LOW-FREQUENCY PYCNOCLINE DEPTH VARIATIONS

## A. Introduction

The field of 20°C isotherm depth was chosen as the clearest, simplest representation of the observed variability. Implicit in this choice is the idea that the tropical Pacific may be approximated as a two-layer system divided by a sharp pycnocline, for which the 20°C isotherm is a proxy. Meyers (1979a,b) used the depth of the 14°C isotherm in this way to study the annual cycle. Kessler and Taft (1987) showed that volume transports of the North Equatorial Current and Countercurrent derived from the two-layer assumption, using the vertical motion of the 20°C isotherm to represent interfacial movement, give a reasonably good estimate of zonal geostrophic volume transport variability. In the same spirit, many modeling studies have used a reduced gravity, single-active-layer approximation (e.g. Busalacchi and O'Brien, 1980, and successors; see also McCreary, 1985). The principal advantage of this choice is that it simplifies the three-dimensional variability into a two-dimensional field which can be mapped and viewed conveniently. For practical reasons, since the BT profiles extend to a variety of depths a calculation needing a common reference level (such as dynamic height) poses problems and requires further assumptions necessary to extrapolate all profiles to the same depth (but see Kessler *et al.*, (1985) for a discussion of a scheme for dealing with this). As discussed in Section 1.b, the Japanese MBT data extends only to 250 m, so 20°C is effectively the deepest isotherm fully sampled over the entire tropical Pacific. The observations cannot be reasonably gridded with a time resolution of less than two months (and must be smoothed in time (see Section 1.d)), so the BT data set is suitable only for the study of low-frequency variability. Although some theoretical discussion of the role of short (dispersive) waves is offered (see Section 2.c below and Appendix 1), all comparisons with observations were made assuming that the variability can be described by low-frequency, large-scale (long wave limit) fluctuations of a sharp pycnocline.

## B. The simple model

A simple quasi-geostrophic model of low-frequency pycnocline variability was employed by Meyers (1979a) to study annual fluctuations of the 14°C isotherm in the tropical (not equatorial) Pacific. The physical processes allowed by the model are Ekman pumping, the radiation of long (non-dispersive) Rossby waves due to such pumping in mid-basin, and the radiation of long Rossby waves from observed eastern boundary depth fluctuations. The ocean is assumed to consist of a rigid lid over a single active layer, separated by a sharp pycnocline from a deep motionless lower layer; both layers are homogeneous (the reduced gravity, $g' = g\Delta\rho/\rho$ describes the potential difference between them). The wind stress $\tau$ (see Section 1.e) is assumed to act as a body force in the upper layer. Since monthly average wind data is used, the forcing frequency is much slower than inertial ($\partial/\partial t << f$). The long wave approximation is made (for the time being). The mean depth of the upper layer is given by the positive number H, and the momentum equations are linearized by assuming that H is spatially uniform (this requirement will subsequently be relaxed to allow a discussion of the effect of mean geostrophic currents (see Section 2.c below)). Defining eastward and northward velocity components (u,v) and vertical excursions of the thermocline h (positive down), the equations of motion are:

$$-fv = -g'h_x + \tau^x/\rho H \tag{2.1a}$$

$$fu = -g'h_y + \tau^y/\rho H \tag{2.1b}$$

and the continuity equation is:

$$h_t + H(u_x + v_y) = 0. \tag{2.2}$$

The possible motions include nearly steady Ekman and geostrophic flow, with a time derivative appearing explicitly only in the continuity equation. Curling (2.1), then using (2.2) to eliminate the horizontal divergence and (2.1a) for v, gives the low-frequency forced quasi-geostrophic vorticity equation as was used by Meyers (1979a):

$$h_t - (\beta c^2/f^2)h_x = -\mathrm{Curl}(\tau/\rho f), \tag{2.3}$$

where $c^2 = g'H$ is the long baroclinic gravity wave speed. Balance (2.3) is the simplest relation obtainable describing time-dependent β-plane dynamics. The long wave, low frequency limit has been assumed in (2.1) by neglecting the local accelerations; this approximation makes wave solutions to (2.3) non-dispersive, so Rossby waves in the simple model propagate exactly westward. Thus, in this limit, solutions at each latitude are independent. Furthermore, there is no need to assume that the forcing or solution has a sinusoidal form. Neglecting $v_t$ in (2.1b) removes the short Rossby waves, and is only valid where the zonal length scale of solutions is much greater than the local gravest internal Rossby radius (Fig. 2.1), since $v_t$ would produce a term $h_{xxt}$ in (2.3). Neglecting $u_t$ in (2.1a) excludes the equatorial Kelvin wave and is not valid within about 5° of the equator, so (2.3) is a mid-latitude approximation (see Appendix 1, section d for a discussion of the difference between the use of mid-latitude and equatorial β-plane approximations in the extra-equatorial tropics). Garzoli and Katz (1983) estimated the magnitude of the contribution of the acceleration terms which have been neglected in (2.1) to the balance (2.3), using BT data in the tropical Atlantic. They concluded that these terms did not contribute significantly to the thermocline displacement anywhere in the region which they studied (3° to 10°N). Appendix 1 considers in detail the role of dispersion and short waves: a consequence of dispersion shown there is that a pulse-like signal loses amplitude to a trailing wake as frequency components with slightly different group speeds disperse (see Appendix 1, section d). To take this amplitude loss roughly into account (as well as the unknown losses from frictional dissipation, scattering and non-linear interactions), a simple damping rate R equaling (3 years)$^{-1}$ has been added to the vorticity equation (2.3), so that the equation which will be referred to henceforth as "the simple model" becomes:

$$h_t - (\beta c^2/f^2)h_x + Rh = -\mathrm{Curl}(\tau/\rho f). \tag{2.4}$$

The three year damping time has little effect equatorward of about 10° latitude where the propagation is rapid; in subtropical latitudes where speeds are of the order of 20 cm/s a pulse loses about half its amplitude between the Central American coast and the Philippines due to this damping. Sensitivity studies with various damping rates showed that as long as the decay time is at least a few years, little difference in the solutions was found. This is principally because poleward of 10°N most of the large-amplitude wind stress curl forcing is in the central or western Pacific) on both annual and interannual timescales), so these signals reach the western boundary before much damping has occurred. The damping does prevent minor anomaly peaks from appearing unchanged, many years later, in the west.

Solutions h(x,t) to (2.4) are referred to as the "upper layer thickness anomalies" (ULT) (positive down, or thicker), continuing terminology used by Busalacchi and O'Brien (1980). These solutions were found according to the procedure given by Gill and Clarke (1974, section 7), integrating along characteristics (which are just latitude circles in the long wave limit) from the eastern boundary, where h(x = 0,t) is taken to be the observed annual cycle of 20°C depth. Meyers (1979a) gives an equivalent procedure. The time step used in the integration was 6 days, which is adequate in the extra-equatorial region. If the wind stress $\tau$ is taken as given, then (2.4) can be straightforwardly solved if a value for the long Rossby wave speed $c_r = \beta c^2/f^2$ is known. As did Meyers (1979a), $c_r$ was treated as an unknown and studied by integrating (2.4) at each latitude, trying all values of $c_r$ from 1 cm/s to 1 m/s at 1 cm/s intervals, then correlating each solution h(x,t) with the observed 20°C depth variations, either at the annual period (Section 3) or for interannual variability (Section 4), to find a best-fit value for $c_r$ at each latitude. Since only the long gravity wave speed c is truly unknown, effectively the fitting process finds an estimate of c which maximizes the correlation between model and data over the width of the basin at each latitude. Estimates of $c_r$ derived from other choices of c are discussed and compared with the best-fit estimates in Section 3.e (see Fig. 3.12).

Several limitations of the simple model (2.4) are evident: the assumption that all waves can be described by the long wave limit, the linearizing assumption in the derivation of the model that the mean pycnocline is flat and the strong zonal geostrophic currents of the tropical Pacific are absent, and the neglect of the more complicated observed vertical structure in favor of simple single-active-layer dynamics.

The first of these limitations is studied extensively in Appendix 1, which discusses the dispersion of a pulse-like signal (which contains waves of all frequencies) originating at the eastern boundary in an idealized ocean. Dispersion of medium-to-long waves changes principally the direction of wave propagation as ray paths of these waves are sinusoidal about the equator; dispersion can lead to shadow zones, focusing and order one changes in the region of wave influence. However, very low frequency waves (with periods greater than about one year) experience turning of ray paths quite slowly, and do not converge significantly towards the equator until more than 10,000 km west of their turning latitudes (see Appendix 1, section c; also Cane and Sarachik, 1981). It is concluded in Appendix 1 that waves with periods greater than about one year can be treated approximately non-dispersively, especially in the region of the North Equatorial Current (Appendix 1, section d).

The second limitation, that of neglecting the strong zonal geostrophic currents of the tropical Pacific, is discussed in Section 2.c below. Again the results are essentially negative in that it is concluded that for the low-frequency pycnocline variability studied here the effect of the mean zonal currents is small and that a more complex model which included wave-mean current interactions would produce very similar results in the extra-equatorial region.

It is much more difficult to study (even in the highly idealized formalism used for the zonal currents in Section 2.c below) the effects of zonal variation of the mean state and consequent meridional geostrophic currents (Appendix 1, section d). There is a substantial zonal slope of the thermocline in the eastern tropical Pacific (see Section 3.b) which leads to a westward increase (by a factor of about 1.5) in the gravest baroclinic long gravity wave speed c (Fig. 2.2). The fitting process described above finds the value of $c_r$ which most closely models the observed variability at a given latitude over the width of the basin, and thus represents a kind of zonal average. Although it seems likely that the effect of the zonal thermocline slope would be to increase the long wave speed as a wave propagates west into the deeper thermocline region, it has not been possible to demonstrate this analytically, and the subtlety of the non-Doppler effect discussed in the following section implies that caution is necessary before jumping to that apparently simple conclusion. In addition, non-linear effects of the mean zonal slope could be important. In a two-layer model, for example, wave-induced geostrophic transport anomalies are directly proportional to the mean pycnocline depth. If this depth increases westward along a ray path, then either the magnitude of a pycnocline anomaly must decrease, or the transport anomaly will increase. Since this would require a net input of energy (with no apparent source), it is clear that a model which did not correctly formulate the wave-zonal slope dynamics could be in error. Lacking a satisfactory approach to this problem, it has simply been ignored. Appendix 1, section d shows how dependent the ray tracing mathematics is on a zonally-invariant assumption.

The third limitation, that of approximating the complex observed vertical structure in favor of a simple two-homogeneous-layer system, makes the assumption that all motion (wave and mean flow) occurs in the upper layer, hence the vertical scale of the waves and mean currents are equal. However, the zero-crossing of the observed first baroclinic mode for wave-induced currents is near 1200 m depth (although the amplitude drops by a factor of at least 2 at about 200 m) (Eriksen, 1982), while the mean zonal currents are generally found only in the upper 200 m, so the vertical scales might actually be quite different. The following discussion of the non-Doppler effect is thus an idealized simplification of the true dynamics. In addition, second baroclinic mode variability has been found to be important in the eastern equatorial Pacific both in observational studies (Lukas *et al.*, 1984) and in linear wind-driven models (Busalacchi and Cane, 1985).

## C. The effect of mean zonal geostrophic currents: the non-Doppler effect

Meyers (1979a) best-fit an equation like (2.3) to data at the annual cycle to estimate $c_r$. His results, which are in many regions consistent with work described in Section 3, showed that in the NEC region $c_r$ did not follow a $1/f^2$ latitudinal dependence (in fact he estimated $c_r$ increasing with latitude north of 14°N), which indicated that the mean meridional pycnocline depth variations must be having a significant effect on the wave propagation speed. Meyers (1979a) ignored the fact that meridional variations of H imply the existence of mean zonal geostrophic currents, which in the NEC have typical speeds (5-20 cm/s) of the same order as long Rossby wave zonal speeds in that region. Although it might appear that the zonal currents would strongly affect the zonal propagation through Doppler shifting, this is not the case, as was first pointed out by Held (1983) and discussed in relation to the northern tropical Pacific by Chang and Philander (1988). The fundamental reason for this is that stretching a water column is equivalent (in the measure of potential vorticity) to moving equatorward, and vice versa. If a water column is constrained to remain within an assumed fixed thickness (but spatially varying) mean upper layer, then any motion parallel to a mean pycnocline gradient vector will induce a potential vorticity change due to the change in height of the column, as well as due to the change in the local value of the Coriolis parameter. In a resting ocean, the meridional gradient of potential vorticity is just $\beta$, but in the presence of a zonal geostrophic current this gradient gains terms associated with the pycnocline slope and thus the wave speed may be different than in the resting case. This modifies the ordinary Doppler-shifting by the mean flow. As will be shown below, for westward-propagating extra-equatorial Rossby waves, the sense of the zonal wave speed change by the pycnocline slope is always such as to oppose the Doppler-shifting by a zonal geostrophic current. For long waves the change in wave speed nearly cancels the Doppler shifting by the mean current (in the long wave limit the cancellation is exact), so the zonal propagation at any latitude is nearly the same as if no mean currents were present. This surprising fact has been called the "non-Doppler effect" by Held (1983). There are three ways in which zonal currents do significantly modify wave propagation: first, the change in the potential vorticity gradient alters the meridional component of the group velocity in the same proportion as the zonal component (equations (2.8) below), but in the meridional case there is no cancellation by the mean current (Chang and Philander, 1988). Ray paths can be very different due to the altered meridional component even though the zonal propagation speed is unaffected. Second, the variation in pycnocline depth changes the local wave speed directly. Third, critical layers may occur where the group velocity relative to the mean flow is zero.

The essential mechanism of the "non-Doppler effect" can be developed by assuming a mean meridional pycnocline slope $\partial H/\partial y$ and writing the equations of motion in a reference frame moving with the mean current $U = -g'H_y/f$, which for simplicity is here taken to be spatially uniform. This uniformity means that the analysis is valid only in a region of small latitudinal extent, but is adopted because it reduces the dynamics to it's essential element. (See Held (1983) or Chang and Philander (1988) for alternative derivations.) In addition, the assumption is made that the waves and the mean currents have the same vertical scale, which would be identically true in an idealized perfect two-layer system but is not strictly valid in the real ocean where the first baroclinic mode has its zero-crossing at about 1200 m. The mean state is indicated by uppercase symbols and varies only in latitude, while lowercase symbols indicate small (O(Ro)) fluctuations; thus $h_{total} = H(y)+h(x,y,t)$. The (unforced) order Rossby number equations of motion in the moving reference frame are:

$$u_t - fv = -g'h_x \tag{2.5b}$$

$$v_t + fu = -g'h_y, \tag{2.5b}$$

and the continuity equation is:

$$h_t + H(u_x + v_y) + vH_y = 0. \tag{2.5c}$$

A water column moving with the mean current plus a wave-induced fluctuation feels the mean current through the continuity equation, which gains a term describing vertical stretching or shrinking of the column according to whether the wave-induced velocity (u,v) moves the column into a deeper or shallower mean pycnocline region, which in this case can only happen through meridional motion. The mid-latitude quasi-geostrophic vorticity equation found from (2.5) is (in the moving reference frame):

$$[a^2 - \nabla^2]h_t - [\beta + Ua^2]h_x = 0, \tag{2.6}$$

where $a = f/c$ is the inverse of the local internal Rossby radius. In addition to the short-wave $\nabla^2 h_t$ term coming from the inclusion of $(u_t, v_t)$ in (2.5a,b), in the presence of a mean zonal current the vorticity equation (2.3) gains one extra term $(Ua^2 h_x)$ paralleling the $\beta$ term; this is due to the change in the potential vorticity gradient by the mean pycnocline slope. The total meridional potential vorticity gradient, or the "effective $\beta$", is $Q_y = (\beta + Ua^2)$. The long wave limit is not assumed (it may be reapplied at any time by taking $\nabla^2 \approx 0$; $k^2 \approx 0$; $l^2 \approx 0$). Assuming sinusoidal solutions $h = A \exp\{i(kx + ly - \omega t)\}$, the dispersion relation relative to the moving current (subscripted "m") is:

$$\omega_m = -[\beta + Ua^2]k / [k^2 + l^2 + a^2], \tag{2.7a}$$

which can now be written in a fixed frame of reference (subscripted "f"):

$$\omega_f = \omega_m + Uk = [-\beta + U(k^2 + l^2)]k / [k^2 + l^2 + a^2], \tag{2.7b}$$

showing that the modification to the dispersion relation is strongest at short wavelengths and disappears in the long wave limit. The interplay of the parameters $\beta$ and $Ua^2$ in this simplified set of equations can be conveniently visualized using the dispersion diagram, Fig. 2.3, which describes five situations: a) $U = 0$; b) $-\beta/a^2 < U < 0$; c) $U = -\beta/a^2$; d) $U < -\beta/a^2$; and e) $U > 0$. Figure 2.3 shows graphically that for wavelengths longer than about 15 Rossby radii (i.e., ranging from about 2500 km at 6°N to about 1000 km at 15°N, equivalent to $kc/f \approx 0.4$ in Fig. 2.3) there is less than 10% modification of the zonal group velocity by any zonal geostrophic flow. Wavelengths shorter than this experience altered dispersion by mean currents, however. Quantitatively, the group velocity components are found by differentiating (2.7b) to get:

$$dx/dt = \partial\omega_f/\partial k = [\beta + Ua^2]\,[k^2 - l^2 - a^2] / [k^2 + l^2 + a^2]^2 + U, \tag{2.8a}$$

$$dy/dt = \partial\omega_f/\partial l = [\beta + Ua^2]\,[2kl] / [k^2 + l^2 + a^2]^2. \tag{2.8b}$$

In the long wave limit ($k^2 \approx 0$; $l^2 \approx 0$) the group velocity is exactly the same as that found with no mean current (e.g. (2.3)), and (2.8a and b) reduce to:

$$dx/dt \approx -\beta/a^2 = -\beta c^2/f^2, \quad dy/dt \approx 0, \tag{2.9}$$

keeping in mind that $c^2 = g'H(y)$ is now a function of latitude. In the long wave limit, the Doppler shift (represented by the final term U in (2.8a)) due to the mean current exactly cancels the change in zonal group velocity associated with the change in $Q_y$. Thus, for example in the case of a spatially uniform westward geostrophic current, the pycnocline sloping up towards the equator reduces the potential vorticity gradient, thus reducing the westward group speed relative to the current. However, the speed of the current Doppler shifts the wave westward, and the two tend to cancel. At a given latitude, the zonal group speed of fairly long (wavelength at least a few Rossby radii) waves observed from a fixed location will be nearly the same as in the absence of a mean current, with c chosen to reflect the mean pycnocline depth at that latitude. However, the pycnocline slope and meridional variation of c implies that the zonal propagation speed in a westward current will be smaller near the equator and larger nearer the poles than would be guessed from the overall mean pycnocline depth. In a resting ocean, the long zonal group speed varies as $1/f^2$, so an initially meridionally oriented crest line tilts to face poleward, which is a crucial aspect of the dispersion of Rossby waves (see Appendix 1). In a westward mean current, on the other hand, the meridional dependence of zonal group speed is weaker than $1/f^2$, so an initially meridionally oriented wave crest will change its orientation more slowly. An eastward current has the opposite effect. Thus although the Doppler shift cancels the change in the effective $\beta$ for long waves at any given latitude, over a range of latitudes the evolution of a wave front may be very different than in a resting ocean.

If a westward current is strong enough (if $U = -\beta/a^2$) then the effective $\beta$, $Q_y$, can equal zero or even become negative. This may indeed be the case in the NEC, where, for example if $U = -14$ cm/s and $c = 3$ m/s at 15°N then $Q_y = 0$. With $Q_y = 0$, equations (2.6) through (2.8) reduce to:

$$\partial h/\partial t = 0, \qquad \text{(in the moving reference frame)} \tag{2.6$'$}$$

$$\omega = Uk \qquad \text{(in the fixed frame)} \tag{2.7b$'$}$$

$$dx/dt = U, \qquad dy/dt = 0, \tag{2.8$'$}$$

which state that a disturbance forced at some location is carried along exactly at the speed of the current. All wavelengths travel at the same speed, and there is no gradient of zonal group speed with latitude. This is in fact a critical latitude, in which the energy of a disturbance does not propagate relative to the fluid but changes the mean pycnocline depth and hence the mean current itself. Clearly the simplified set of equations studied here (in particular the assumption of a fixed, spatially uniform mean current) is inadequate to address this situation.

In a very strong westward current, if $U < -\beta/a^2$, then $Q_y$ is negative and the group velocity relative to the mean flow becomes eastward for long waves but westward for short waves according to equation (2.8) (Fig. 2.3d). In this case the group speed (in a fixed reference frame) for long waves remains exactly the same as before (i.e. less westward than the current speed) due to the Doppler shift cancellation, but the short waves move west faster than the current. A long-wavelength wave front which is initially meridionally oriented will in a strong westward current tilt to face equatorward. Although this case is included for completeness, as in the case $Q_y = 0$ discussed in the previous paragraph, the simple dispersion relations (2.7) are probably not adequate to fully describe the dynamics in a very strong westward current. Ripa (1983) found that a necessary (though not sufficient) condition for instability of a westward zonal flow in a single active layer system is that $Q_y < 0$; therefore perturbations may gain amplitude from the mean flow. Nevertheless, the zonal propagation speed remains unchanged in the long wave limit from that predicted in the absence of a mean current.

In summary, the non-Doppler effect implies that for waves longer than $2\pi c/f$ (i.e. those waves which are westward-propagating in a resting ocean), the pycnocline slope associated with a zonal geostrophic current (of either sign) always modifies the zonal component of the group velocity in such a way as to tend to cancel the Doppler shifting due to the current. Thus the zonal propagation speed at any latitude is nearly the same as in the absence of a current. However, a principal mechanism by which zonal currents modify long Rossby wave propagation is through the variation with latitude of the long gravity wave speed $c^2 = g'H(y)$, so the meridional gradient of zonal group speed does not vary as $1/f^2$, as it does in the absence of mean currents.

A second principal mechanism by which zonal current modify wave propagation was pointed out by Chang and Philander (1989). For wavelengths shorter than the long wave limit (in which meridional propagation is zero), the non-Doppler cancellation which occurs in the *zonal* equation (2.8a) does not apply in the equation for the *meridional* component (equation 2.8b), which remains proportional to the modified $Q_y$. In a westward current, where $Q_y$ is less than $\beta$, meridional propagation is reduced, while in an eastward current it is enhanced. Chang and Philander (1988) use this idea to trace Rossby wave rays in a realistic northern tropical Pacific (mid-basin) zonal current structure and show that in the North Equatorial Current rays propagate nearly due west (in other words low frequency ray paths are hardly affected at all (see Appendix 1, section d)), while rays which enter the North Equatorial Countercurrent gain a large meridional group speed and pass rapidly across it. It is important to recognize that the meridional component is proportional to the product of the wavenumbers kl (equation 2.8b), and the shortest waves are affected most strongly as in the case of the zonal component. Chang and Philander (1988) discuss examples only of zonal wavelengths shorter than 5000 km, referring to longer waves as "ultra-long waves", where modification of the group velocity is small. In Section 3, zonal wavelengths at the annual frequency found from the observations of 20°C depth range from about 6000 km near 18°N to more than 25,000 km at 4°N, so these waves are well within the ultra-long wave region.

It is concluded that Meyers (1979a) was probably correct to use a model which took account of the variation of mean pycnocline depth only through the change in $c^2 = g'H(y)$ in the estimate of the long Rossby wave speed $c_r = \beta^2/f^2$, while ignoring the zonal geostrophic currents associated with the pycnocline slopes, since he restricted attention to a long wave, two-layer system only. In this idealized regime, there is no Doppler-shifting by mean zonal geostrophic currents. Results from the simple model hindcasts discussed below in Sections 3 and 4 confirm Meyers' findings that the observed zonal propagation had a weaker than $1/f^2$ latitudinal dependence in the NEC region, although the uncertainty of the calculation does not allow for a precise quantification of the effect (see Fig. 3.12). Limitations of the idealized formalism are noted, however. Chang and Philander (1988) have shown that ray paths of even slightly dispersive waves can be strongly modified, particularly by eastward currents. In addition, since the true vertical density and mean current structure is more complicated than the model's two homogeneous layers, the exact cancellation of the Doppler shift is an approximation even in the long wave limit. Finally, the observed mean currents (particularly the NEC) have speeds uncomfortably close to those which would produce critical latitudes for long Rossby waves.

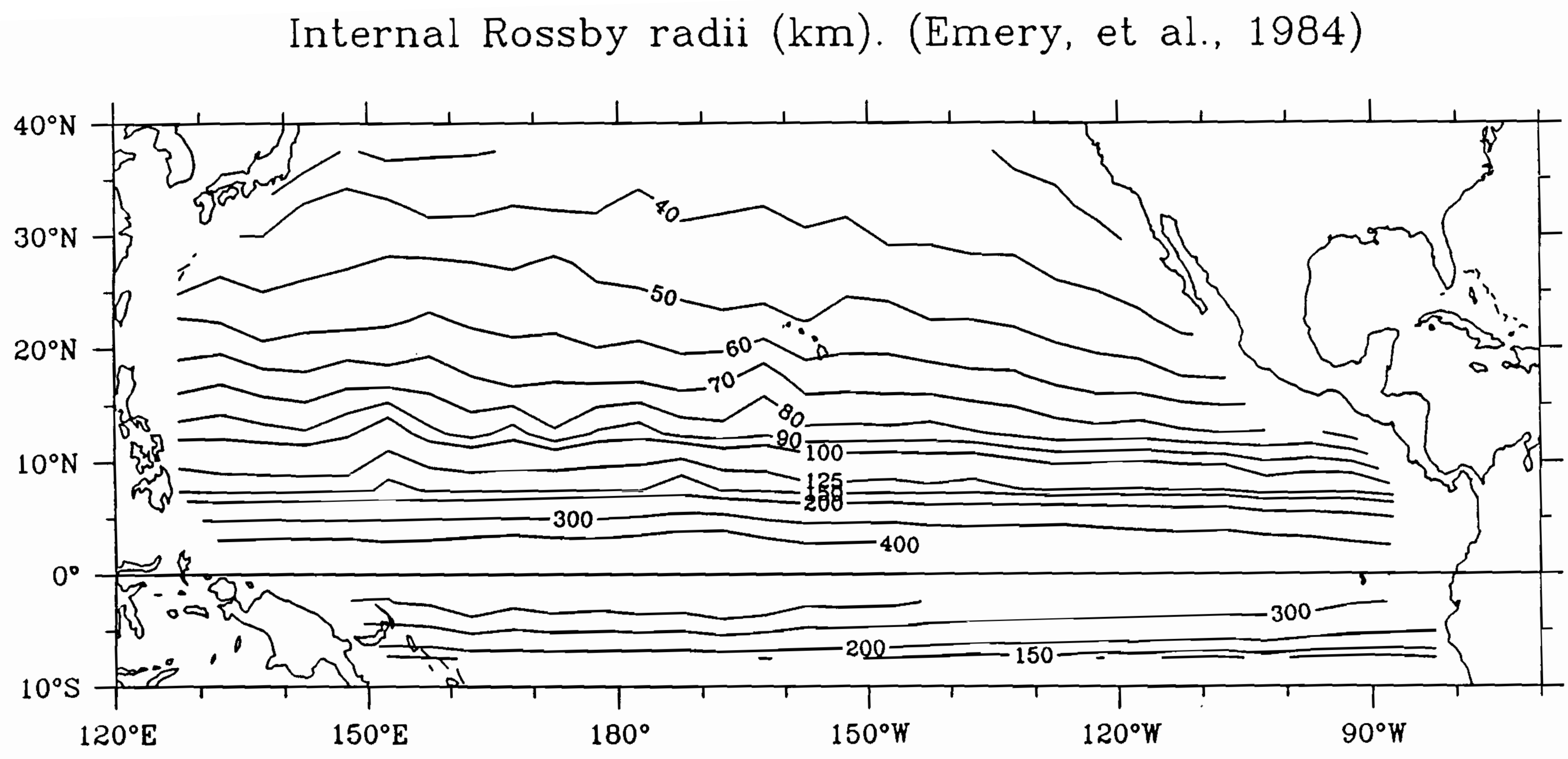

Figure 2.1. Internal (first baroclinic mode) Rossby radii (km). Plotted from tabular data given in Emery *et al.* (1984). Values are given at ±2.5°, ±7.5°, etc. by 5° latitude.

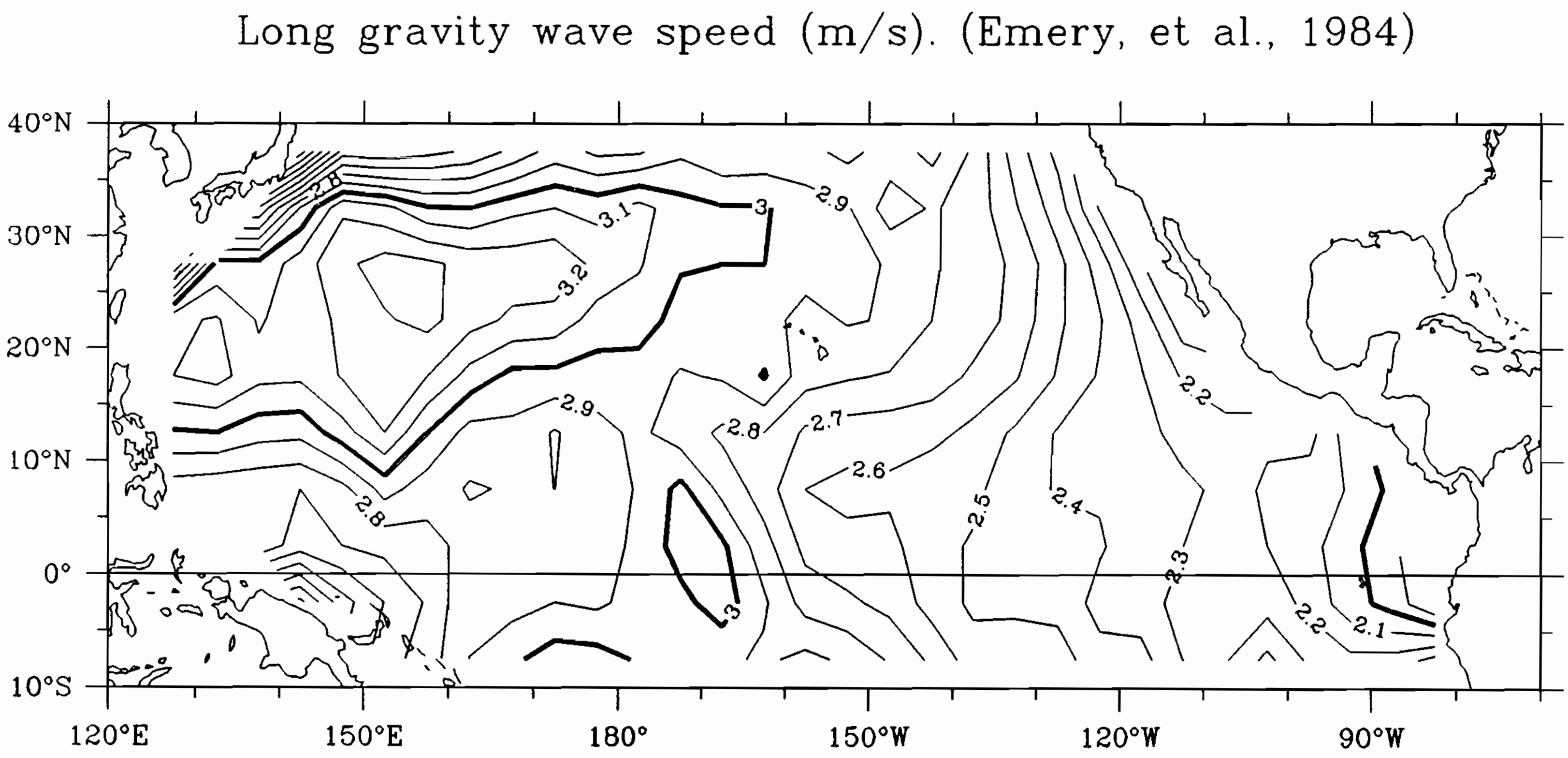

Figure 2.2. Internal (first baroclinic mode) long gravity wave speed (m/s) found by multiplying the internal Rossby radii (Figure 2.1) by *f*.

This page intentionally blank

Figure 2.3 (opposite). Rossby dispersion curves in various mean currents according to the quasi-geostrophic vorticity equation (2.4). The overall point of these diagrams is to show graphically that, although the change in the meridional gradient of potential vorticity due to pycnocline slopes alters the dispersion relative to the mean current, the Doppler-shifting by the current speed tends to cancel this change for long waves. Short waves experience strong modification by mean currents, however. The change in dispersion seen in the diagrams may be simply described by noting that westward mean flow tends to cancel $\beta$, so the dispersion curve relative to the current ($\omega_M$) is flattened and finally becomes negative; while eastward flow enhances $\beta$ and steepens the curve. The dispersion curves are non-dimensionalized with a distance scale $c/f$ (the internal Rossby radius) and a time scale $\beta c/f$. Thus, using stars to indicate non-dimensional variables:

$$k^* = kc/f, \quad l^* = lc/f, \quad \omega^* = \omega f/\beta c, \quad U^* = U^2 f/\beta c^2,$$

and the dispersion relation (2.7b) can be written:

$$\omega^* = -(1 + U^*)k^*/[k^{*2} + l^{*2} + 1] + U^*k^*.$$

a) $U = 0$. The familiar dispersion curve for mid-latitude Rossby waves in zero mean currents. The highest frequency is 1/2 in the non-dimensional units, and occurs at $kc/f = -1$; this is the boundary between eastward and westward propagating waves. The slope of the curve at the origin is one in the non-dimensional units. This curve is repeated as the dashed line in the other four diagrams. The line $U^*k^*$ falls on the k axis.

b) $U = -(1/2)\beta c^2/f^2$. The mean current is westward at half the resting long wave speed. $\omega_M$ is flatter than $\omega_0$, indicating that there is a smaller gradient of group speed with wavenumber; the highest (non-dimensional) frequency is 1/4. $\omega_F$ is identical to $\omega_0$ for $|kc/f| < .4$; unlike $\omega_0$ short waves have westward group speed relative to the fixed frame.

c) $U = -\beta c^2/f^2$. The mean current speed is exactly the same as the resting long wave speed. The pycnocline slope cancels $\beta$, and $Q_y = 0$. There is no dispersion, so $\omega_M$ falls on the k axis. Assuming that this situation is adequately described by equation (2.7b) (a poor assumption as discussed in the text), $\omega_F$ is the same as the straight line $U^*k^*$, and a disturbance is simply carried along by the mean flow. For long waves this is again the same speed as in the absence of a current.

d) $U = -(3/2)\beta c^2/f^2$. The mean current speed is faster (westward) than the resting long Rossby speed. The curve $\omega_M$ is the mirror image of case (b), and is entirely below the k axis. Long waves propagate eastward relative to the current, and short waves westward. $\omega_F$ is again identical to $\omega_0$ for long waves ($|kc/f| < .4$), and there is only a small difference of zonal group speed between large and small wavenumbers.

e) $U = +(1/2)\beta c^2/f^2$. The mean current is eastward at half the resting long Rossby speed. $\omega_M$ is steeper everywhere than $\omega_0$, with the highest (non-dimensional) frequency 3/4, as in the other cases occurring at $kc/f = -1$. Thus long waves propagate faster westward relative to the current and short waves faster eastward. Again, for wavenumbers $|kc/f| < .4$ the dispersion is the same as $\omega_0$, but short waves move rapidly eastward.

## DISPERSION DIAGRAMS

### ($\omega - k$ plane)

Thin curves are $\omega_M$ relative to the mean flow U

Straight lines are Uk

Thick curves are $\omega_F$ relative to a fixed frame,

$(\omega_F = \omega_M + Uk)$

Dashed curves are $\omega_0$ for U=0

See previous page for full description

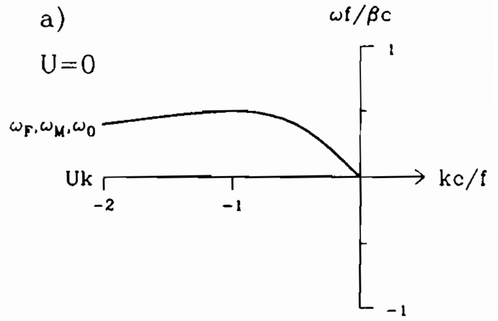

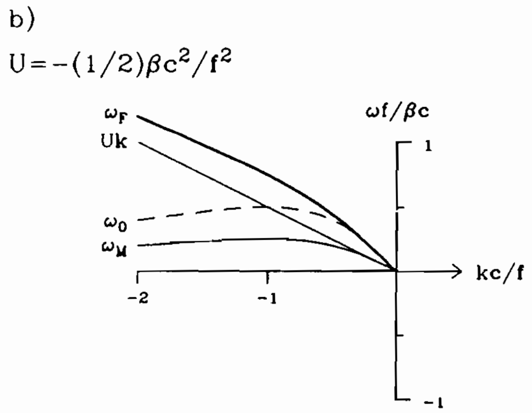

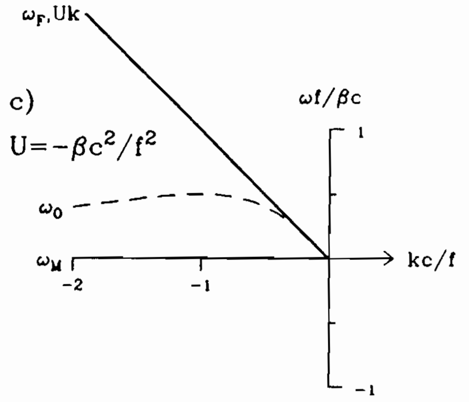

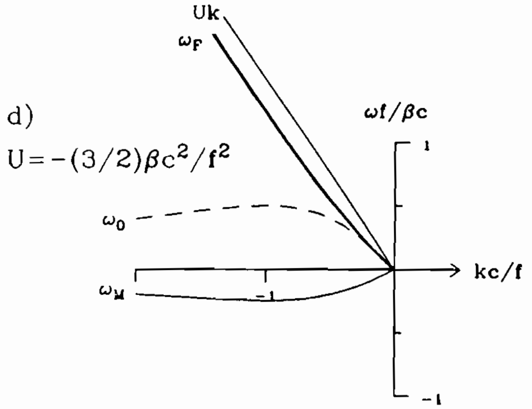

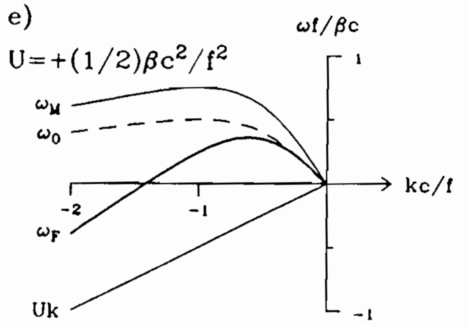

# 3. THE MEAN AND THE ANNUAL CYCLE OF THE DEPTH OF THE 20°C ISOTHERM IN THE TROPICAL PACIFIC

## A. Introduction

The combined BT data set provides the most complete historical data base for describing the annual thermocline variability in the tropical Pacific. Several earlier studies of the annual cycle used smaller sets of BT data (Meyers, 1979a,b; Kessler and Taft, 1987; McPhaden *et al.*, 1988a,b), or hydrographic station data (Seckel, 1975), or island sea level records (Wyrtki, 1974a, 1974b, 1975) to estimate thermocline depth or dynamic height fluctuations and the annual variation of the transports of the tropical zonal geostrophic currents. These studies established the fact that an annual oscillation is a major component of the variability of the tropical Pacific thermal structure and that this translates into significant annual variations of the zonal currents. Much of the observed annual variability has been ascribed to annual fluctuations of the wind stress curl through Ekman pumping, which has a relatively simple large-scale annual signal (Section 3.d, below). The present work makes no attempt to estimate geostrophic transports because of the difficulty in establishing a common reference level among the irregularly sampled BT data (see Section 1.b); however, qualitative conclusions can be drawn. The relatively complete zonal coverage of the BT compilation makes these data particularly suitable for examining the question of whether westward-propagating long Rossby waves modify the simple pattern expected from Ekman pumping alone.

As mentioned in Section 2.a, the field of 20°C depth was chosen as the main representation of thermal variability, both for practical reasons due to the nature of the BT sampling and because a two-layer model has been found to be a good approximation of tropical Pacific dynamics. Although in the remainder of this work the variability will be discussed purely in terms of the depth of the 20°C isotherm, the data set is rich in information about the vertical structure and it is appropriate to briefly discuss the mean state of the full profile. This is particularly useful in describing the complex vertical profiles near the western boundary associated with the narrow western boundary currents. As a reference, Appendix 2 gives mean vertical/meridional sections at 20° longitude intervals (Figs. A2.1a-h) and mean vertical/zonal sections at 5° latitude intervals (Figs. A2.2a-j).

## B. The mean thermal structure of the tropical Pacific in the BT data

The mean depth of 20°C computed from 135,151 observations (see Table 1) is shown in Fig. 3.1, with the locations of the major ridges and troughs (which define the boundaries of the zonal geostrophic currents) overlaid. (The names of the ridges and troughs in Fig. 3.1 are the traditional ones appropriate to sea level or dynamic topography (Wyrtki, 1974a; Wyrtki and Kilonsky, 1984). Thus, for example, the word "ridge" in the name of a feature refers to a thermocline depression. These names are always abbreviated, e.g. Equatorial Trough becomes

ET. In all cases below, the words "ridge" and "trough" in the text will be used to refer to isotherm topography, since that gives the clearest description of the two-layer dynamics, but the abbreviated names remain the traditional ones as given in Fig. 3.1.) As noted in Section 1.e (Fig. 1.5) the sampling density is quite small in the southern hemisphere east of the Dateline. Computation of the mean and standard deviation was undertaken only if six or more observations existed in a given 2° latitude by 5° longitude gridbox; regions not satisfying this criteria are blanked in Fig. 3.1.

The ridge-trough pattern shown in Fig. 3.1 is similar to that found in 0/500 db dynamic height by Wyrtki (1975), which tends to confirm the two-layer character of tropical Pacific density structure. The gross features have been known for over a hundred years (Buchanan, 1886). Thermocline troughs mark the centers of the subtropical gyres in each hemisphere (SER, NER); isotherms slope upwards to a peak on the equator (ET), but in the northern hemisphere the upward slope is kinked by a ridge near 8°-10°N (CCT) which is usually the shallowest level of the thermocline in any meridional section, and a trough near 3°-4°N (CCR) (Fig. 3.1). The CCT-CCR ridge-trough pair bounds eastward geostrophic flow (the North Equatorial Countercurrent (NECC)); both the ridge and trough are closer to the equator in the west, however the difference in 20°C depth between them is smaller in the west. The thermocline trough marking the center of the southern subtropical gyre (SER) splits into two branches west of the Dateline, separated by a ridge (SCCT) extending eastward from New Guinea at 10°S. The 200 m contour in Fig. 3.1 shows this structure. Kessler and Taft (1987) suggested that this topography was associated with the cyclonic wind stress curl of the South Pacific Convergence Zone. Taft and Kessler (1989) show meridional dynamic height sections in this region. The South Equatorial Countercurrent (SECC) flows eastward between the SCCT and the equatorial branch of the trough (SCCR) at 6°-10°S west of the Dateline (Fig. 3.1). The meridional section at 170°E (Fig. A2.1f) shows that although the SCCT ridging only occurs above about the 18°C isotherm, indicating that the SECC is a shallow current underlain by westward flow, a slope break can be seen in isotherms to at least 400 m near 12°S.

Several western boundary currents are implied by the thermal structure. North of 10°N on the western boundary, the tight packing of 20°C depth contours indicates the beginning of the western boundary current which becomes the Kuroshio (Fig. 3.1). The very dense sampling near the Philippines (Figs. 1.1 and 1.2), allows the construction of a much finer grid (55 km gridsize) of mean 20°C depth (Fig. 3.2), showing the western boundary in detail. At the level of the 20°C isotherm, the Kuroshio begins at about 12°N and is already quite strong where it passes Luzon Strait between the Philippines and Taiwan. (Note that although Luzon Strait (which is 370 km wide) has deep-water passages, it is broken up by many islands and banks so no deep-water channel is more than about 50 km wide, and it thus effectively constitutes the western boundary.) The width of the region of tightly packed 20°C depth contours is about 250 km. The zonal sections at 20°N and 25°N (Figs. A2.2a and b) show that the upward slope of the thermocline to the west associated with the boundary current is steeper for isotherms below 20°C, and northward geostrophic flow extends below the 450 m limit of BT observation, so it is not possible to use these data to measure the geostrophic transport. At 15°N along the Philippines coast where the current is just forming, this slope only occurs above about 350 m (Fig. A2.2c) however, which suggests that the current begins as a shallow flow. Northeast of Taiwan a recirculation region is observed in the overshooting curves of the 160-190 m depth contours (Fig. 3.2). At about 10°N at the Philippines coast the North Equatorial Current (NEC) splits, part flowing south around the Mindanao Eddy, centered at 7°-8°N, 130°-135°E, and emerging in the NECC (Lukas, 1988). This equatorward flow is also stronger below 20°C than above it (Fig. A2.2e) (note that this zonal section at 5°N extends into the Celebes Sea, and the "western boundary" is indistinct). Kessler and Taft (1987, Fig. 36) showed that the Sverdrup (1947) balance requires the existence of an equatorward western boundary current in this region of roughly 35 Sv (1 Sv = $10^6$ $m^3 s^{-1}$).

In the southern hemisphere near New Guinea the topography of 20°C depth implies an apparent southeastward geostrophic flow along the New Guinea coast through the Vitiaz Strait from the Bismarck Sea into the Solomon Sea (Fig. 3.1). The zonal sections at 5°S and 10°S (Figs. A2.2g and h) show that the shoaling to the west associated with this flow only occurs at 20°C and above; at lower levels the thermocline deepens near the boundary which indicates a subsurface equatorward geostrophic flow along the New Guinea coast. This deeper slope is consistent with the flow described by Lindstrom *et al.* (1987), referred to by them as the New Guinea Coastal Undercurrent. Equatorward western boundary flow in this region is required by the Sverdrup balance (Landsteiner *et al.*, 1989).

A roughly similar representation of the mean ridge-trough pattern would be seen in the mean depth of isotherms from about 15°C to 25°C. The principal difference in the pattern for isotherms below 20°C is that the isotherm troughs at the centers of the two subtropical gyres are found poleward of those seen in 20°C depth (Reid, 1965; Reid and Arthur, 1975). The meridional sections (e.g. Fig. A2.1e at 170°W) show that the trough of each isotherm occurs further poleward with decreasing temperature in both hemispheres. At 170°W, for example, the troughs of 25°C are at 8°S and 16°N, while 20°C is deepest at 16°S and 18°N, 15°C at 22°S and 24°N, and 12°C at 24°S and 26°N (Fig. A2.1e). At 400 m depth, the pattern of mean temperature shows that the warmest water (indicating the centers of the thermocline troughs defining the gyres) is found at 25°-30°N and near 22°S (Fig. 3.3). Along the equator a deep isotherm trough occurs which is much wider in the east (Fig. 3.3); this is associated with the deep subsurface countercurrents flowing east on both sides of the equator (Tsuchiya, 1972, 1975; McPhaden, 1984), and is also clearly seen in any of the meridional sections (Figs. A2.2). Despite these obvious discrepancies from a simple two-layer system, in the remainder of this work they will be ignored, and the depth of 20°C will be taken as representative of tropical Pacific thermocline variability. The mean 20°C topography is assumed to be given and constant.

### C. The annual cycle of 20°C depth

As discussed in Section 1.b, a simple longterm average may be a poor estimate of the true mean if the sampling is biased towards particular seasons of the year. A better estimate is the average of the twelve monthly averages, which removes any seasonal bias. Similarly, it is appropriate to find the variance of the average annual cycle separately from the variance of the data with the average annual cycle removed (henceforth referred to as "interannual"). The total variance is exactly the sum of these two, since they are uncorrelated. The standard deviations in the two frequency bands are shown in Figs. 3.4a and b, with the positions of the ridge and trough system overlaid; the spatial patterns of variability are quite different. The standard deviation of the average annual cycle is generally smaller by about a factor of two (which means the total standard deviation is approximately equal to the interannual standard deviation since the total variance is the sum of squares of the standard deviations); Fig. 3.5 shows the percentage of the total variance associated with the annual cycle. The regions of largest amplitude of the average annual cycle of 20°C depth in the tropics are along the axes of the ridge-trough system bounding the NECC, where the amplitude is 5-6 m east of the Dateline, accounting for up to 50% of the total variance, and in the Philippine Sea (Fig. 3.4a). In the center of the NECC, a minimum in variability is observed, which is consistent with an annual pivoting of the thermocline about a line near 7°-8°N and consequent high annual NECC transport variability (Kessler and Taft, 1987). Relatively small annual variance is found between about 15°-20°N everywhere east of 150°E; near Hawaii the annual standard deviation is less than 2 m, and the annual cycle accounts for less than 5% of the total variance (Fig. 3.5). Along the American coast, except in the northern region near Baja California, the annual variance of 20°C depth is small, typically about 2 m, which is generally 10% or less of the total variance. In the southern hemisphere to 10°S, the annual variance is also found to be small, however there is less data there so that confidence in this conclusion is relatively low.

The interannual standard deviation, on the other hand, has a minimum near the thermocline ridge at 8°-10°N in the central part of the basin where the annual standard deviation is maximum (Fig. 3.4b) (but note that this minimum is still about as large as the maximum of the annual cycle). The interannual standard deviation is largest (more than 10 m) in the equatorial waveguide over most of the basin, north of the equator in the west, and everywhere north of 20°N. Along the eastern boundary the interannual standard deviation is about 8 m (less between the equator and the Gulf of Panama), so the eastern boundary variance is dominated by the interannual signal. The interannual variability will be discussed in connection with El Niño in the next section, while the rest of this section focuses on the annual variation.

About 80-95% of the annual variance is accounted for by the first annual harmonic (this percentage has only been increased from 70-90% by the 1-2-1 smoothing in time discussed in Section 1.d), which reduced the amplitude of the high harmonic constituents. The amplitude of the annual harmonic (Fig. 3.6, top) thus has a spatial pattern very similar to the annual standard deviation (Fig. 3.4a), with maxima of 6-8 m at the axes of the CCT and CCR boundaries of the NECC, and minima of about 2-3 m in a broad region between 15°-22°N east of 160°E, in the center of the NECC, and south of the equator. Large amplitude of the annual harmonic also occurs at both poleward edges of the study region (Fig. 3.6, top).

The phase of the annual harmonic (Fig. 3.6, bottom) shows that to a first approximation the entire northern tropical region (between 10°N and about 22°N) fluctuates approximately in phase at the annual period, with the shallowest thermocline observed between November and January (there is a break in this phase pattern southwest of Hawaii, but the amplitude of the annual variability is very small there (Fig. 3.6, top)). At 10°N and 22°N there are sharp phase change boundaries spanning most of the width of the basin, with the regions north of 25°N and equatorward of 8°N (east of the Dateline) shallowest in June.

Clearly the most prominent annual signal in the tropics is the out-of-phase, large-amplitude oscillation across the NECC, in which the thermocline gradient across the current is strongest in December and weakest in June, as was also shown at 165°W by Kessler and Taft (1987). However, this out-of-phase relationship is confined east of the Dateline; in the west the isotherm trough near 4°N (CCR) has shifted phase from its value east of the Dateline and now is more nearly in phase with the CCT at 8-9°N. Figure 3.7 (top) shows the difference in the meridional profiles at 150°E and 150°W at the extremes of the average year. The annual oscillation in the thermocline gradient driving the NECC is much weaker in the west. In section 3.e below, the zonal phase shift of the CCR is attributed to the propagation of long Rossby waves.

In the NEC region between 10° and 20°N, at 150°W there is little annual variability at the poleward edge of the NEC near 20°N, but a large fluctuation at 10°N (Fig. 3.7, top). This might suggest that the NEC geostrophic transport has a large-amplitude annual signal; however Kessler and Taft (1987) showed that in the central Pacific the annual variation in the thermocline gradient driving the NEC (and hence the surface zonal geostrophic speed) tends to be opposed by the change in vertical extent of the flow. The current is confined within a thinner layer when the gradient is large (Fig. 3.7, top), so the vertically integrated transport fluctuation is minimized. At 150°E, there is little annual change in the thermocline gradient associated with the NEC as 10°N and 20°N vary in phase (Fig. 3.7, top).

In the southwest Pacific the phase pattern is nearly the mirror image of that in the northeast; the tropical region between about 10°S and 25°S is out of phase with both equatorial and higher southern latitudes (Fig. 3.6, bottom). The phase relation between the region near 5°S and that near 15°S west of 150°W shows that a downward isotherm slope towards the equator is enhanced roughly in April-May, which agrees with the suggestion made by Kessler and Taft (1987) that the SECC is strongest in the early months of the year (they associated this fluctuation with the annual cycle of wind stress curl in the South Pacific Convergence Zone which is strongest and extends furthest east during the southern summer). As in the northern hemisphere, there is a sharp phase jump between the tropics and subtropics near 25°S.

On the equator, the phase of the annual harmonic shows that the 20°C isotherm is shallowest during June and July in a large central region between 170°W and 100°W, but shallow in November-December at the eastern boundary and near 160°E (Fig. 3.8). Meyers (1979b) observed a similar phenomenon in the annual cycle of the depth of 14°C, and suggested that the eastern phase lag might be a free Kelvin response while the western lag might be a forced equatorial Rossby wave. He also found a large amplitude of the second annual harmonic in the east, and noted that the second harmonic of the zonal wind stress was large in the central but small in the eastern Pacific, suggesting that this was further evidence of free Kelvin wave propagation. In the linear equatorial model of Busalacchi and O'Brien (1980), semi-annual variability in the eastern equatorial Pacific similar to that observed by Meyers (1979b) was due to Kelvin wave propagation from the central basin. Since the present data set is so poorly sampled on the equator, no attempt was made to calculate semi-annual harmonics.

## D. The annual cycle of wind stress curl

Before comparing solutions to (2.4) with observed 20°C depths, it is useful to briefly examine the annual cycle of wind stress curl represented by the FSU wind product (Section 1.e). The annual harmonic of wind stress curl (Fig. 3.9) represents typically 30-70% of the total variance except in the region near 8°-10°N, 180° where the amplitude is small and the annual variance is less than 10% of the total. The amplitude pattern (Fig. 3.9, top) is somewhat similar to that for 20°C depth (Fig. 3.6, top) in having maxima near 5°-6°N and 12°-14°N east of the Dateline, but differs in showing more variability in the west near the equator than does 20°C depth. The phase pattern (Fig. 3.9, bottom) is remarkable in that there is almost no zonal phase variation at any latitude north of the equator. At 8°-10°N there is a sharp phase change spanning the width of the basin, with maximum positive curl (Ekman upwelling) occurring in February to the south and August to the north. Comparing this with the phase of 20°C depth (Fig. 3.6, bottom) suggests that annual thermocline variability is roughly in phase with Ekman pumping (i.e. lagging the curl by three months) over most of the northern tropical Pacific east of the Dateline and south of 20°N. North of 20°N, the wind stress curl has little phase change, unlike 20°C depth which has a second line of sharp phase jump at 22°N.

The phase pattern of wind stress curl in the southern hemisphere is similar in many respects to that in the north, with a large region poleward of about 10°-15°S exhibiting nearly uniform phase of the annual cycle (note that the irregular phases seen in the southeastern Pacific occur in a region of very low amplitude (Fig. 3.9, top) (and also very sparse ship-wind data). In the southwest tropical Pacific, comparison of the annual phase of 20°C depth and wind stress curl shows that, as in the north eastern tropical Pacific, to zero$^{th}$ order 20°C depth variations roughly lag the phase of the curl by about three months (note that Ekman pumping switches sign in the southern hemisphere so the month of maximum positive curl contoured in Fig. 3.9, bottom represents downward pumping there). Again, as in the north, the curl shows no counterpart to the abrupt phase jump seen near 25°S in 20°C depth (Fig. 3.6, bottom).

In summary, qualitative comparison of the annual harmonics of 20°C depth and wind stress curl suggest that over large regions of the tropical Pacific, particularly east of the Dateline in the north and west of about 150°W in the south, observed annual variability of 20°C depth is roughly in phase with the Ekman pumping velocity. Obvious discrepancies from this simple conclusion occur in the west north of the equator and poleward of about 20° latitude in both hemispheres.

The relative absence of zonal variability in the annual cycle of wind forcing in the northern hemisphere means that solutions of the vorticity equation (2.4) (with the eastern boundary condition $h = 0$, and annual forcing), will be approximately the sum of a traveling free wave plus a spatially uniform forced response, as discussed by White (1977). (Since the physics are linear, free waves emanating from other sources on the eastern boundary are simply added later.) Solutions like this are of the form:

$$h = \sin(kx - \omega t) + \sin(\omega t) = 2\cos(kx/2 - \omega t)\sin(kx/2); \tag{3.1}$$

a typical example is shown in Fig. 3.10, with a maximum amplitude of twice that of either the wave part or the local part. White (1977) suggested that the combination would have twice the phase speed of a free Rossby wave, as it might appear from (3.1); Fig. 3.10 shows that this is the apparent speed of the zero contours, while the true phase speed (i.e. a modulated crest line such as runs exactly from corner to corner in Fig. 3.10) is the same as for a free wave. The zonal distance between these crests is also equal to the zonal wavelength of a free wave. Due to the relatively uncomplicated nature of the wind stress curl forcing, solutions to the vorticity equation (2.4) to be discussed below typically have the diamond-shaped pattern exemplified by Fig. 3.10.

## E. Comparison of the simple model with observations of the annual cycle

The simple long-wave model of pycnocline variability is discussed in Section 2.b, which gives the assumptions and limitations of the dynamics. If the wind stress $\tau$ is taken as given, the vorticity equation (2.4) can be straightforwardly solved if a value for $c_r = \beta c^2/f^2$ is known. Following Meyers (1979a), in this section $c_r$ is treated as an unknown and studied by solving (2.4) at each latitude, trying all values of $c_r$ from 1 cm/s to 1 m/s at 1 cm/s intervals, then correlating each solution $h(x,t)$ with the observed annual cycle of 20°C depth. The results of this correlating (Fig. 3.11) show that a clear peak of correlation emerged at 4° and 6°N, and at 14° through 18°N, with correlations greater than 0.8, while 8°, 10° and 12°N had several peaks which were not clearly distinguishable. (An estimate of the confidence in the peaks is given in connection with the best-fitting for interannual frequencies, Section 4.d.) A summary of these results is given in Fig. 3.12, where it is seen that the best-fit values of $c_r$ have a meridional dependence which is weaker than $1/f^2$, as would have been expected if the long gravity wave speed c was uniform. According to the theory of the "non-Doppler effect" discussed in Section 2.c, the principal effect of the meridional variation of mean pycnocline depth is to alter the long Rossby wave zonal speed in direct proportion to $c^2 = g'H(y)$. Thus it is thought that in the NEC region the mean pycnocline slope downward towards the pole would tend to weaken the meridional gradient of $c_r$. Values of c for the first baroclinic mode can be found from data presented by Emery *et al.* (1984); these vary from about 2 m/s near the American coast to about 3.4 m/s in the deepest part of the northern subtropical gyre (Fig. 2.2). If the analysis of the non-Doppler effect in Section 2.c is correct, then the best-fit $c_r$ should equal $\beta c^2/f^2$ with c chosen as the zonal average at each latitude of the Emery *et al.* (1984) values; this comparison is given in Fig. 3.12. Two other methods are available for estimating c and are shown in Fig. 3.12b: c may be simply chosen to be constant, or c may be chosen such that $c^2 = g'H(y)$, where H(y) was found from the mean 20°C depths at 160°W ($\Delta\rho/\rho$ was taken to be $5 \times 10^{-3}$). The meridional profile of long Rossby speed using c equals constant (in this case c was chosen to be 2.6 m/s, based on the average 20°C depth between 4° and 25°N at 160°W) is very similar to the profile found from the Emery *et al.* (1984) first baroclinic mode data, except the constant c profile predicts speeds about 20% smaller (absolute differences about 1 cm/s) north of about 15°N. The profile using $c^2 = g'H(160°\text{W},y)$ has smaller speeds by about 25% (about 5 cm/s) near the isotherm ridge at 10°N (Fig. 3.12b). The absolute differences between the three profiles are so small that it is probably impossible to distinguish between them based on the fitting to data conducted here. At the annual period, the best-fit values of $c_r$ have a meridional gradient weaker than predicted by any of the three choices of c, with speeds larger than estimated from hydrography in the NEC region and smaller in the NECC; this remains unexplained. A possibility is that the idealized formalism used in evaluating the non-Doppler effect in Section 2.c has oversimplified the vertical structure by assuming a perfect two-layer fluid and some Doppler shifting has been overlooked; this tendency would increase the westward speed of waves in the NEC and decrease it in the NECC in qualitative agreement with the profile of annual variations in Fig. 3.12.

The hindcasts by the vorticity equation (2.4) using the best-fit Rossby wave speeds at each latitude are compared with observations and with pycnocline anomaly hindcasts due to Ekman pumping alone in Figs. 3.13a-h in time-longitude plots (the famous Hovmoller (1949) diagram) at each latitude, and in Figs. 3.14a-l in latitude-longitude maps of the northern tropical Pacific for each of the twelve average months. In all of these plots (and throughout the report), solid contours (positive values) indicate deep (thick upper layer) anomalies, and dashed contours shallow anomalies. As mentioned in Section 2.b, solutions h(x,t) of (2.4) will be referred to as the upper layer thickness anomalies (ULT). "Ekman pumping" refers to solutions $h_E(t)$ due to Ekman pumping only, that is, solutions to:

$$\partial h_E/\partial t = -\mathrm{Curl}(\tau/\rho f), \qquad (3.2)$$

with the boundary condition that the mean $h_E$ should be zero. This condition is required even though $\mathrm{Curl}(\tau/\rho f)$ has been demeaned, because the FSU wind product begins in 1961, and the state of the pycnocline in 1961 (which would be needed as an initial condition) is unknown. The assumption that over the 28 years of integration the mean Ekman pumping solution to (3.2) is zero (for mean $\mathrm{Curl}(\tau/\rho f) = 0$) substitutes for an initial condition. (This problem does not arise for the ULT solution since (2.4) is integrated to the eastern boundary where the exact condition is assumed to be known.)

At 4° and 6°N (Figs. 3.13a,b), the observations (top frame) clearly suggest westward propagation, although the annual cycle of Ekman pumping (bottom) has very little phase change across the basin. An estimate of the zonal wavelength of the observed annual pycnocline fluctuations can be made simply by best-fitting a straight line to the phase of the annual harmonic of the observations (for example, at 6°N this best-fit line went from 90°W at January 1 to 120°E at December 31 (Fig. 3.13b)). Since the annual harmonic wraps from December 31 to January 1 each year, the zonal wavelength can be estimated directly from the data by the recycle distance; at 6°N it is 150° longitude or 16,600 km. At 4°N it is 26,600 km. (Corresponding estimates can be made from the model-fitting process since the zonal wavelength $\lambda$ of a wave satisfying (2.4) is $\lambda = c_r T$, where T is the period. This method gives 25,900 km at 4°N and 18,300 km at 6°N). These are extremely long waves (about 50 to 100 internal Rossby radii), which should be unaffected by Doppler-shifting in the NECC to the extent that the two-layer analysis is valid (the non-Doppler effect, see Section 2.c). Although the wavelengths at 4° and 6°N are longer than the width of the Pacific, there is no conceptual difficulty in postulating such a wave in mid-basin (the western boundary currents are trickier). The ULT (middle) correlates very well with the observations and clearly has the correct character of variability; the correlation is 0.91 at 4°N ($c_r = 82$ cm/s), and 0.81 at 6°N ($c_r = 58$ cm/s). Meyers (1979a) found exactly the same long Rossby speed for the annual cycle at 6°N.

The thermocline trough at about 4°N marks the southern boundary of the NECC (the CCR, see Fig. 3.1). In the eastern Pacific, where the annual cycle of 20°C depth is approximately as hindcast by Ekman pumping (Fig. 3.13a), the CCR fluctuates out-of-phase with the CCT near 10°N; thus there is a strong annual oscillation of thermocline slope across the NECC in the east which is contributed to by both ridge and trough (Fig. 3.7, top). Both the ULT solution to (2.4) and the Ekman pumping solution to (3.2) give a similar meridional profile at 150°W, with the same phase change across roughly 8°N as observed (Fig. 3.7). However in the west, where the annual cycle at 4°-6°N is controlled not by the local pumping but by the arrival of long Rossby waves from the east, the CCR is nearly out-of-phase with the CCR in the eastern Pacific (Fig. 3.13a) and hence nearly in phase with the western CCT (Fig. 3.7). There is thus only a small annual cycle across the NECC in the western Pacific, although the local pumping has very similar zonal phase as in the east (Fig. 3.13a, bottom, Fig. 3.7, bottom).

At 8°N the dynamics are less clear, although the observations have a suggestion of westward propagation (Fig. 3.13c, top). However, the Ekman pumping pattern is not stationary as it is at 4° and 6°N, but occurs successively later to the west (Fig. 3.13c, bottom). This pattern in the Ekman pumping is not due to actual propagation of any property of the wind field, but to the fact that Curl($\tau/\rho f$) is composed of a Curl$\tau$ term and a term proportional to $\tau^x$, and these are very closely 180° out of phase across the width of the Pacific. The (appropriately scaled) Curl$\tau$ term is roughly twice as large as the $\tau^x$ term for average values at 8°N, so it tends to dominate. However, the amplitude of the annual cycle of Curl$\tau$ is high in the east but very low near the Dateline at 8°N (Fig. 3.9, top), where $\tau^x$ is large, so the Ekman pumping pattern seen in Fig. 3.13c (bottom) is like the pattern due to Curl$\tau$ alone near 120°W and in the far west but like the $\tau^x$ term alone near the Dateline, and the apparent propagation is spurious. Although the Ekman pumping solution appears superficially like the observations, closer examination shows that it actually lags the observations by 60-90 days, thus the correlation between these two fields is irregular and generally smaller than 0.5, except in the far west. The ULT including Rossby waves (Fig. 3.13c, middle) also is not a particularly good representation of the observed variability, with an overall correlation of 0.48 (Fig. 3.11), although in some locations it is distinctly better; in addition, the ULT does not have quite the same visual character as the observations. Since 8°N is approximately at the pivot line of the thermocline as the gradient across the NECC waxes and wanes during the year (Fig. 3.7), it may be that annual fluctuations at 8°N are governed by a more regional dynamics (i.e. 8°N is located at a latitude of weak variability between two latitudes of strong out-of-phase variability (Fig. 3.4b)), not just local forcing and long-wave radiation from such forcing directly to the east. Comparing the observed variability at 6°, 8° and 10°N (Figs. 3.13ac, top) shows that observed 20°C depth fluctuations at 8°N are roughly similar in phase to those at 6°N in the east but similar to 10°N in the west. (In other words 8°N is phased like the equatorward side of the NECC in the east but like the poleward side in the west.) A relatively small change in latitude of observation near the pivot point can mean a 180° phase shift. In summary, the attempt to explain the annual variability at 8°N in terms of either long non-dispersive Rossby waves or Ekman pumping has been mostly unsuccessful.

At 10° and 12°N, the results of the best-fitting did not produce peaks of correlation at reasonable values of $c_r$ (Fig. 3.11). The fitting showed peaks at very low speeds and a wide maximum with equal correlation at all speeds from about 30 cm/s to 1 m/s. Meyers (1979a) also was unable to find a satisfactory fit to a Rossby wave model at 12°N. Instead, it appears that simple Ekman pumping is the primary dynamics affecting annual thermocline depth fluctuations in this region. Figures 3.13d,e show that observed annual 20°C depth variability (top) is nearly in phase with that hindcast by Ekman pumping (bottom), with correlations mostly above 0.9, in agreement with results in the central Pacific (Kessler and Taft, 1987). Hindcasts including Rossby waves at 10° and 12°N are shown in Figs. 3.13d,e (middle), with $c_r$ estimated simply by linearly interpolating between the values found at 8°N and 14°N. These ULT hindcasts are not an improvement over the Ekman pumping hindcast and it is concluded that annual variability at 10° and 12°N is governed primarily by local forcing. However, in Section 4 it will be shown that interannual variability does propagate westward in this region.

At 14°, 16° and 18°, in the heart of the NEC, there is a clear suggestion of annual westward propagation (Figs. 3.13f-h, top), and the best-fitting process produced peaks of correlation (above 0.8) (Fig. 3.11) which closely correspond to the observed variability. Ekman pumping at the three latitudes predicts a simple annual oscillation in phase across the width of the Pacific (Figs. 3.13f-h, bottom), as expected from the annual cycle of Curl$\tau$ (Fig. 3.9), which is unlike the observed variability. The ULT hindcasts (Figs. 3.13f-h, middle), at speeds of 20 to 28 cm/s, have the same overall character as the observations. The zonal wavelengths of the observed annual depth variations, found as described above for 4° and 6°N, are about 8500 km at 14° and 16°N, and about 6300 km at 18°N, which are very long waves and will not be affected by Doppler-shifting in the NEC (see Section 2.c).

An alternative way to look at the annual variability shows how the fluctuations at the various latitudes combine over the northern tropical Pacific in latitude-longitude maps for each of the twelve average months (Figs. 3.14a-l). (As mentioned above, at 10° and 12°N, $c_r$ was estimated by linearly interpolating between the best-fit speeds at 8° and 14°N.) This representation shows that the hindcast due to Ekman pumping alone has the same or exactly opposite phase over very large regions, so the magnitude of hindcast anomalies grows and shrinks during the year, becoming very small over most of the Pacific during intermediate seasons when the near-sinusoids go through zero nearly simultaneously over a very large area. Neither the observations nor the ULT hindcast has this quality.

In January (Fig. 3.14a) the ULT (middle frame) is similar to Ekman pumping (bottom) and both resemble the observations (top) fairly well, although the ULT hindcast more correctly suggests a deep anomaly along the Mexican coast which will be seen to be important to the subsequent evolution. By March (Fig. 3.14c), the difference between the ULT including long Rossby waves and the Ekman pumping solution has become large. As mentioned above, the Ekman pumping solution to (3.2) (bottom) predicts near-zero anomalies over most of the tropical Pacific during this season, which is not the case in the observations (top). The deep anomaly in the ULT which was at the Mexican coast in January has propagated offshore, and a band of deep pycnocline depths stretches from Baja California southwestward to near Indonesia (middle), quite like the observed anomalies (top), but unlike the Ekman pumping solution (bottom). Remnants of earlier such fluctuations in the ULT are visible as the shallow anomalies near Hawaii and deep anomalies near 10°-20°N, 160°E; these bear strong similarities to the observed conditions. In June (Fig. 3.14f), anomalies predicted by Ekman pumping have become large again, and the three maps (observed anomalies, ULT and Ekman pumping) are again quite similar and of opposite sign from the January maps. Since the annual variability of all three fields is dominated by the annual harmonic, the second half of the year is nearly the mirror image of the first half.

In summary, an annual long Rossby wave corresponding to the simple model (2.4) was clearly observed at 4° and 6°N and at 14° to 18°N, but not at 8° to 12°N. The most important effect at the annual period of westward propagation is that thermocline depths at the southern boundary of the NECC in the western Pacific are controlled by waves radiating from forcing in the east. These waves reduce the amplitude of the annual cycle of thermocline gradient across the NECC in the west compared to the eastern and central Pacific. The speeds best-fit to the observations at each latitude have a less than $1/f^2$ meridional dependence, which is qualitatively understandable due to the mean pycnocline slope between 10° and 20°N, but not south of 10°N.

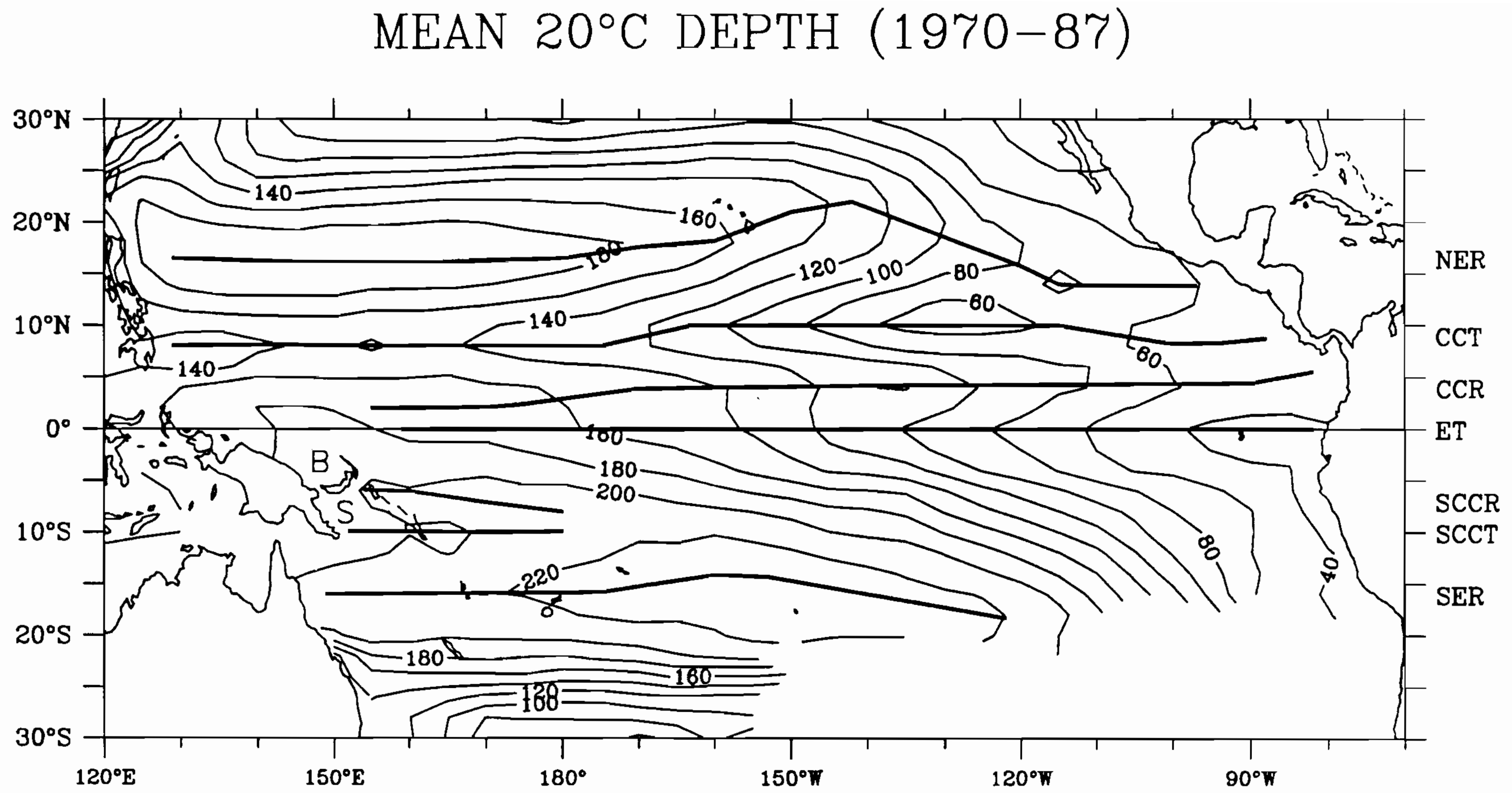

Figure 3.1. Mean depth (m) of the 20°C isotherm during 1970 through 1987. Heavy overlaid lines indicate the major ridges and troughs. Abbreviations of the names of these features are given on the right margin at the approximate mean latitude of the feature. These names are: NER = North Equatorial Ridge; CCT = Countercurrent Trough; CCR = Countercurrent Ridge; ET = Equatorial Trough; SCCR = South Countercurrent Ridge; SCCT = South Countercurrent Trough; SER = South Equatorial Ridge. The names are the traditional ones appropriate to sea level, so for example a trough refers to a shallow peak of the thermocline. The Bismarck and Solomon Seas (referred to in text) are marked with a "B" and "S", respectively; the Vitiaz Strait connects them along the New Guinea coast.

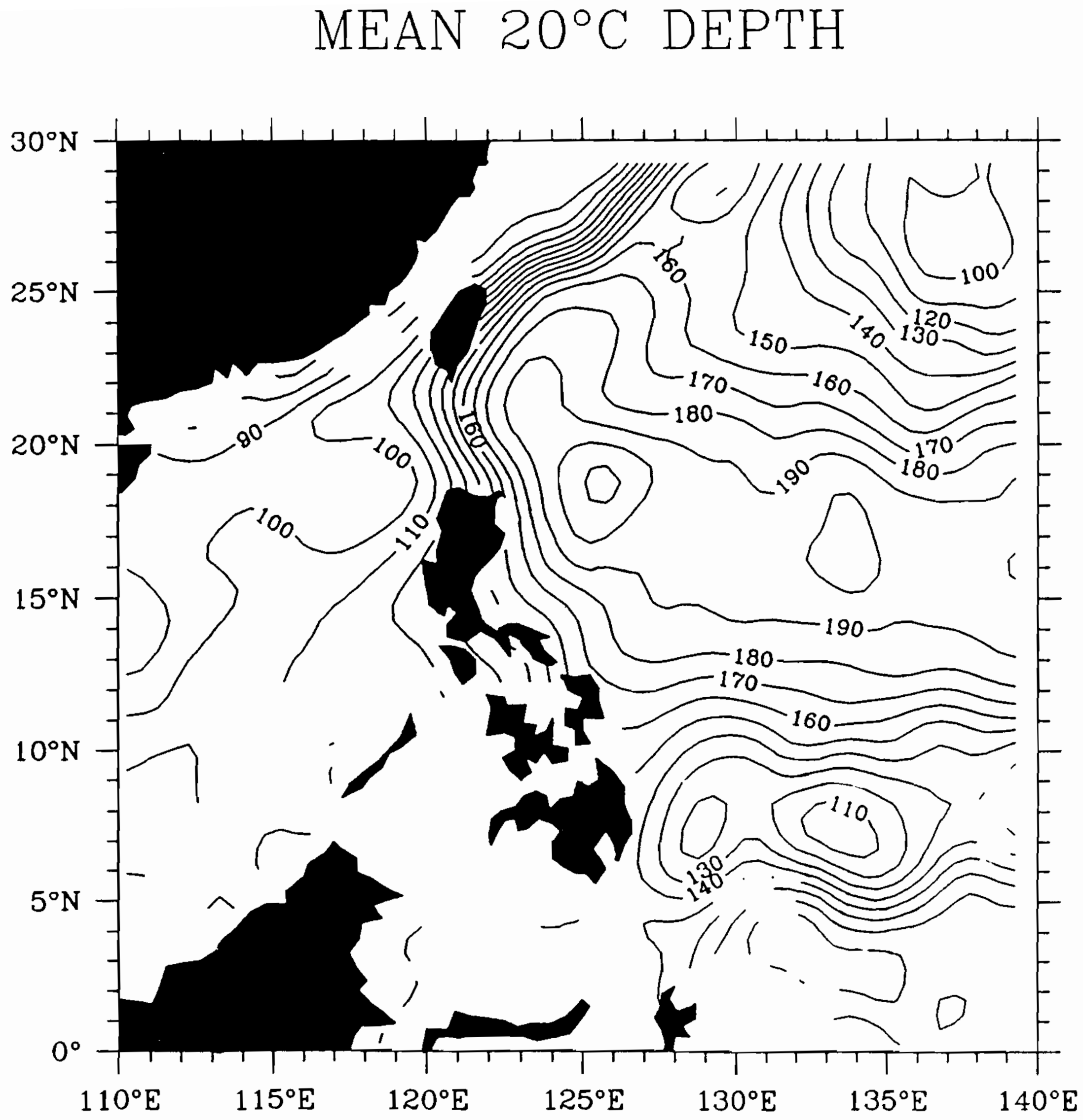

Figure 3.2. Mean depth (m) of the 20°C isotherm during 1970 through 1987 in the far western tropical Pacific. This differs from Figure 3.1 in being gridded by 1/2° latitude/longitude gridboxes. The tight packing of depth contours near Taiwan is associated with the Kuroshio.

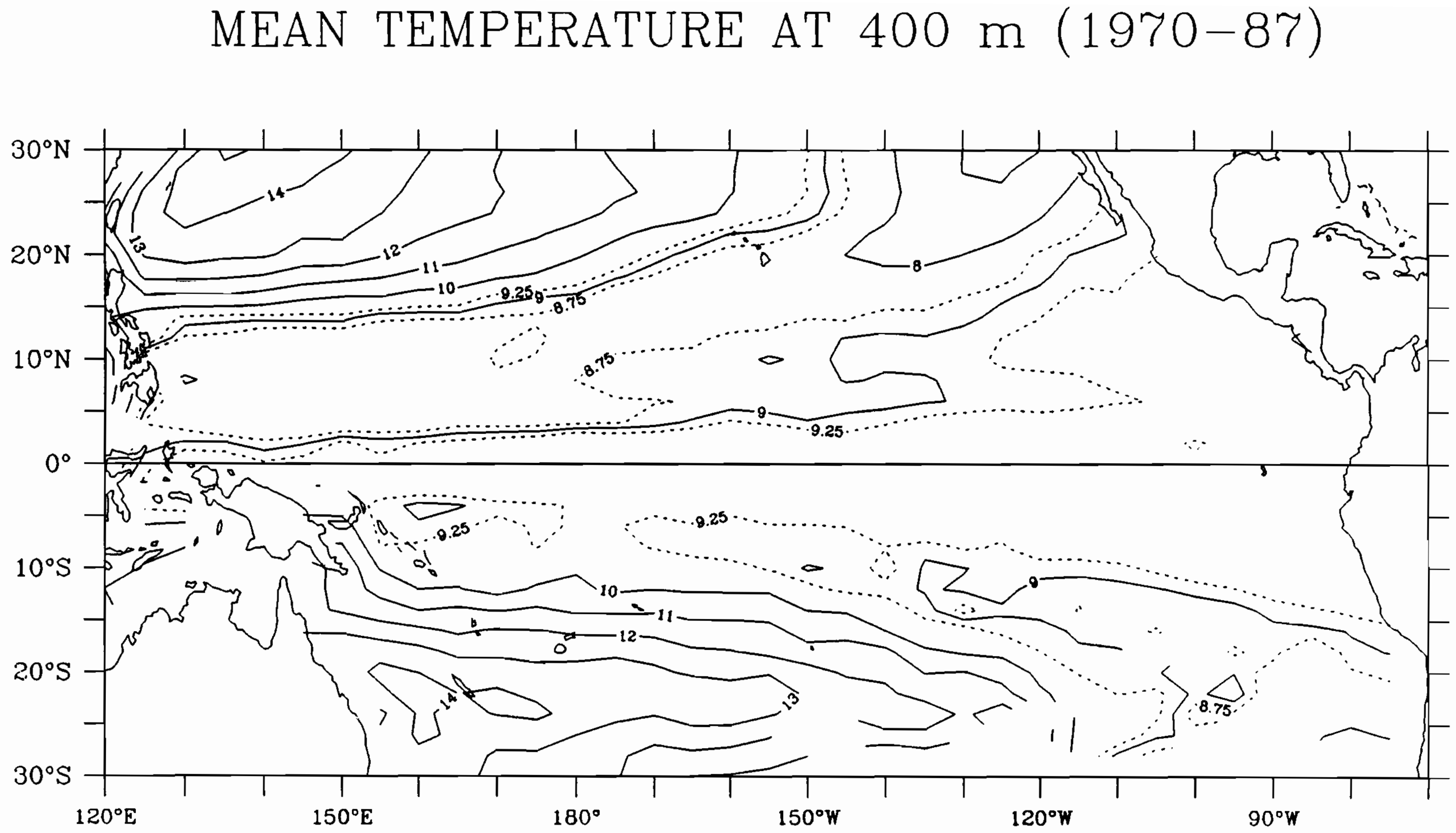

Figure 3.3. Mean temperature (°C) at 400 m depth during 1970 through 1987. Solid contours are given every °C, with supplementary (dashed) contours at 8.75°C and 9.25°C.

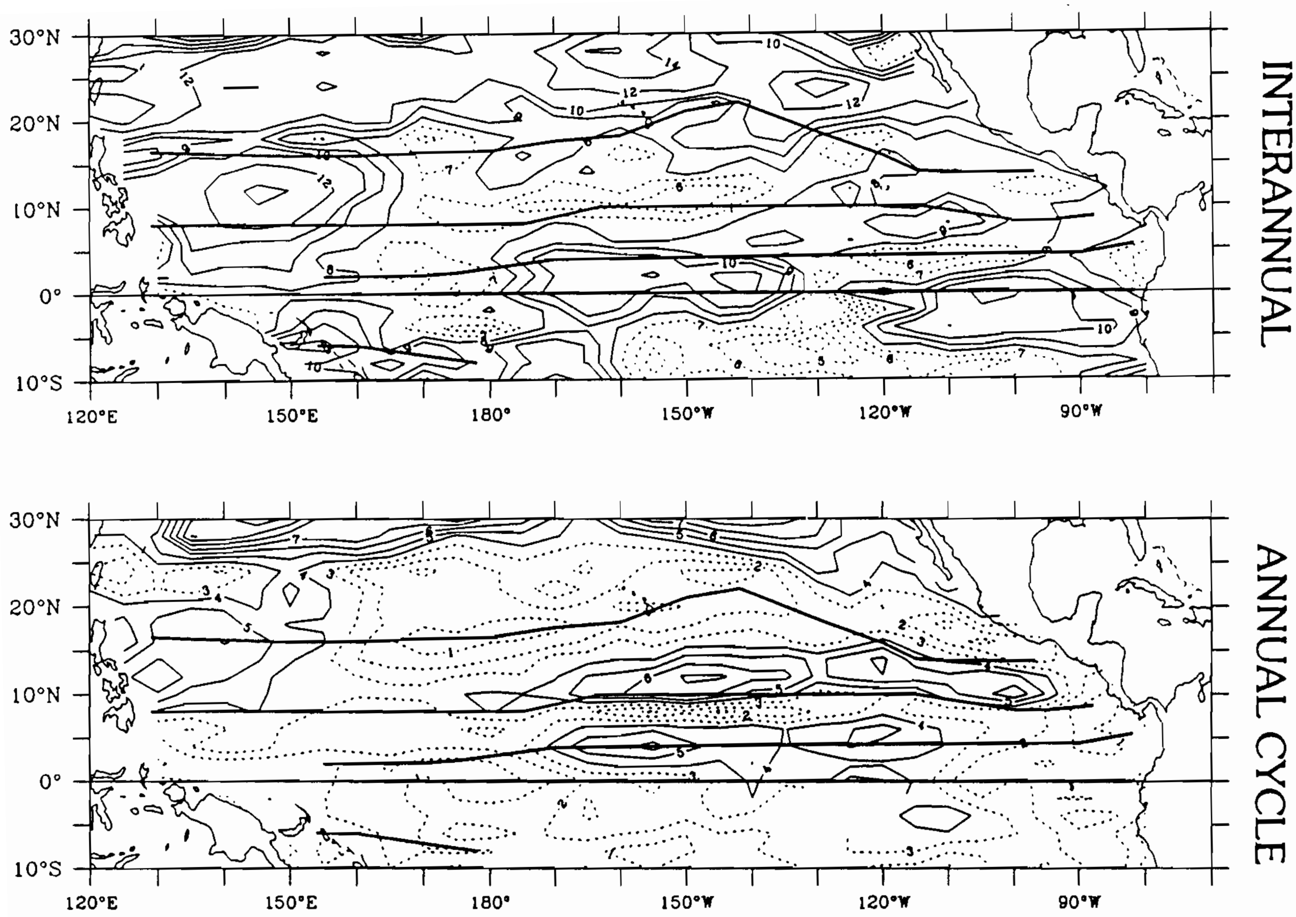

Figure 3.4a and b. Standard deviation (m) of 20°C depth. Mean positions of ridges and troughs are overlaid as in Figure 3.1. Top panel (3.4a) is the interannual standard deviation. Contours are given every meter to 10 m, with 7 m or less dashed, then every 2 m above 10 m. Bottom panel (3.4b) is the standard deviation of the average annual cycle. Contours are given every meter to 10 m, with 3 m or less dashed, then every 2 m above 10 m.

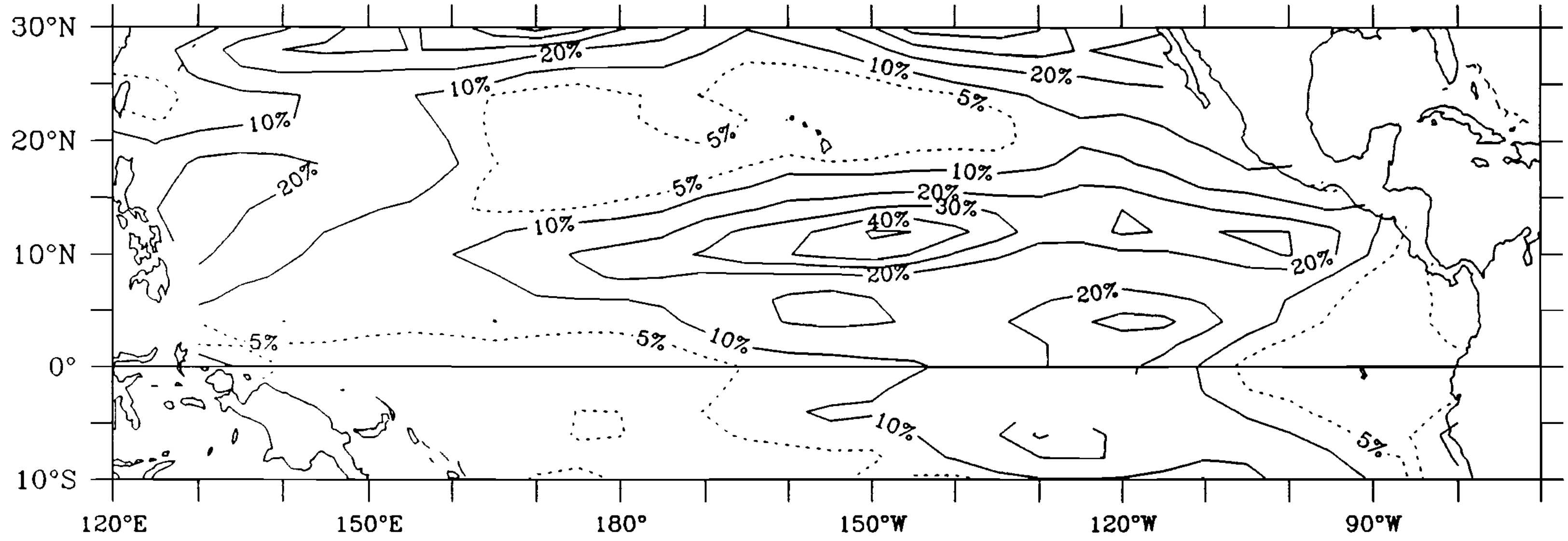
PERCENT OF TOTAL VARIANCE IN ANNUAL CYCLE

Figure 3.5. Percentage of total variance of 20°C depth expressed by the average annual cycle.

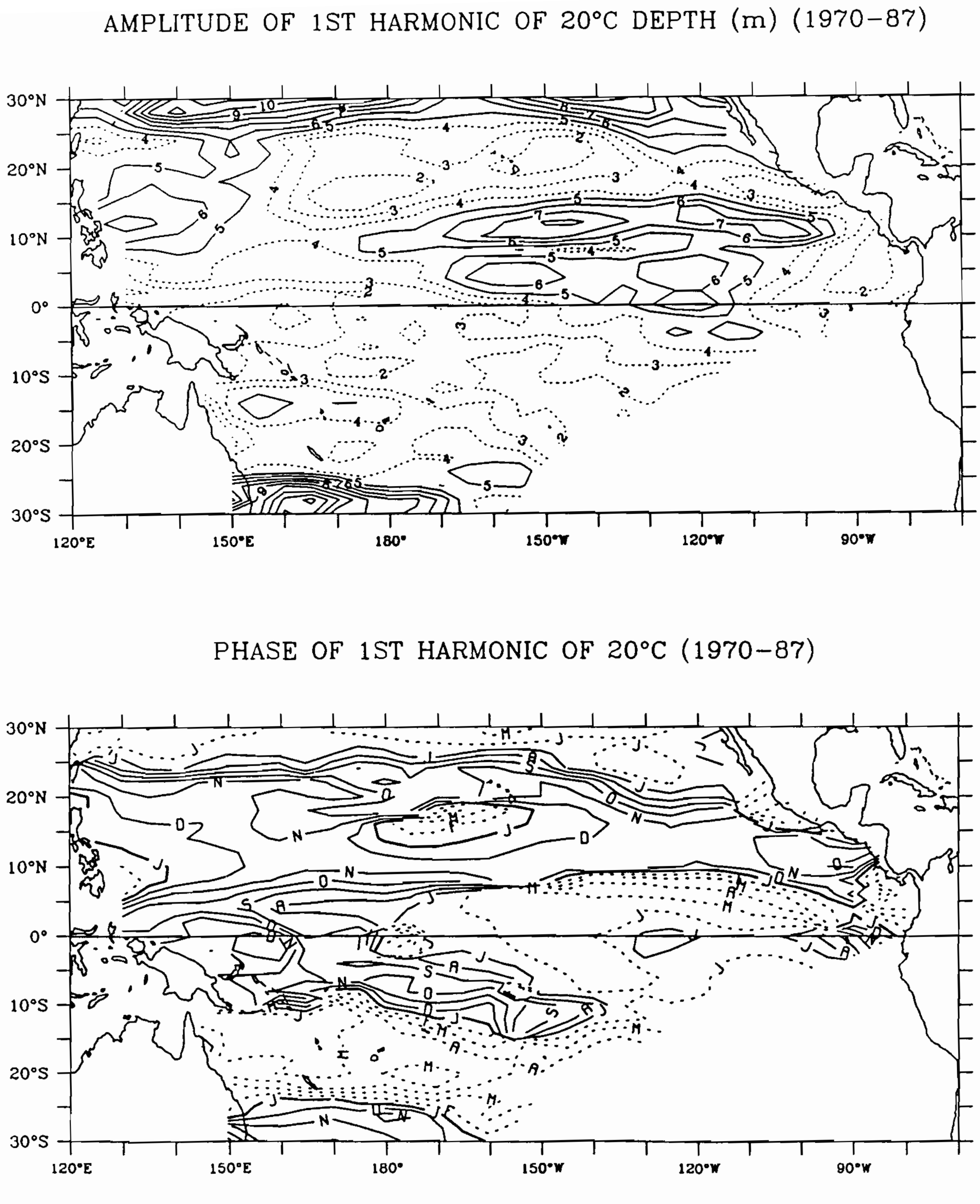

Figure 3.6. Amplitude (top, m) and phase (bottom) of the first annual harmonic of 20°C depth during 1970 through 1987. Contours of amplitude are given every meter, with values of 4 m or less in dashed contours and higher values in solid contours. Phase is shown as the date of shallowest isotherm depth. Contours of phase are given in months, contoured at the first day of each month. Labels are abbreviated months, with the heavy contour being January, dashed contours February through June, and solid contours July through December.

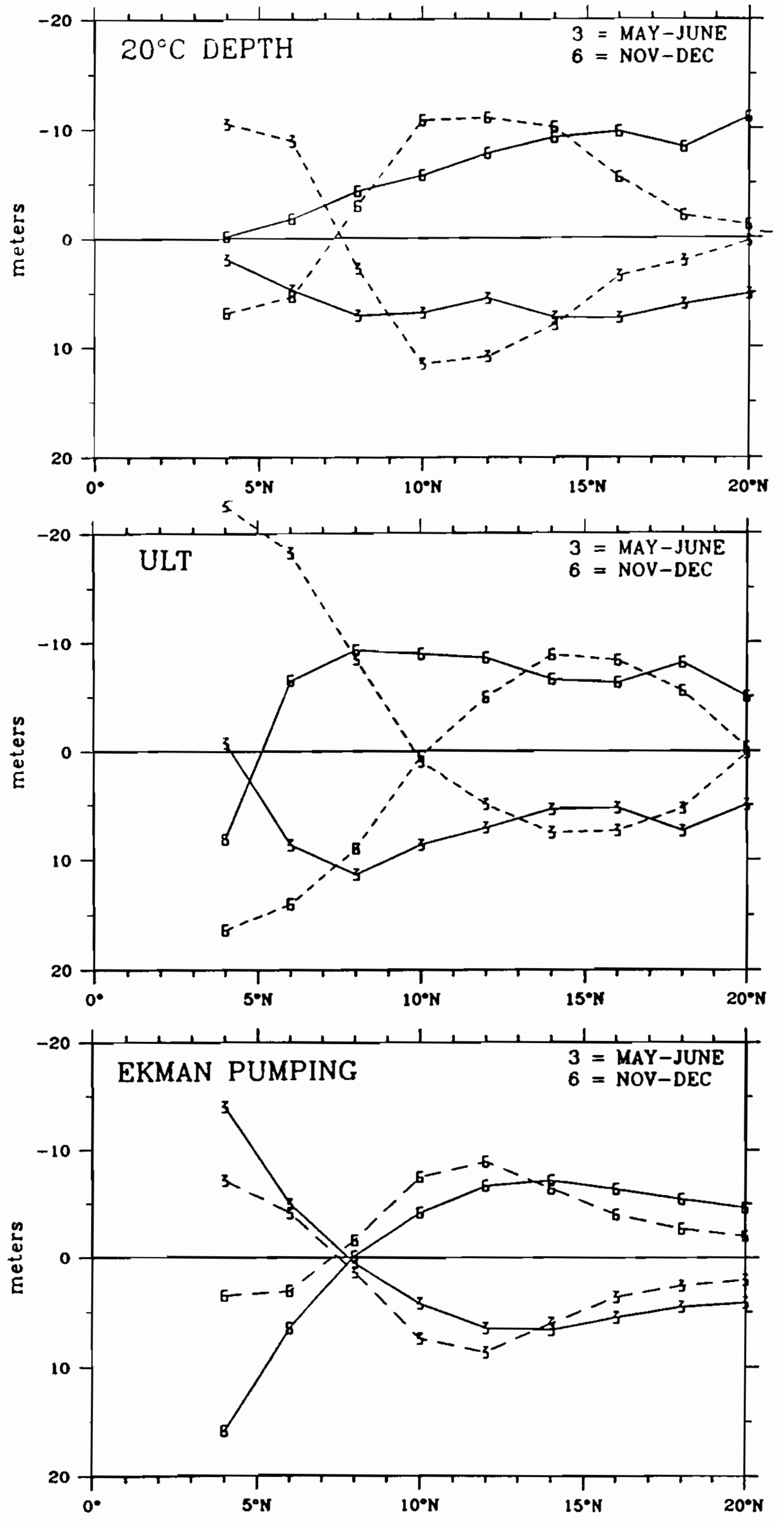

Figure 3.7. Meridional profiles of the annual cycles of 20°C depth (top), upper layer thickness anomalies (ULT, middle) and pycnocline anomalies due to Ekman pumping (bottom) at 150°W (dashed line) and 150°E (solid line). Each variable is shown during the average May-June (line labeled 3) and the average November-December (labelled 6), which are approximately the extremes of annual variability.

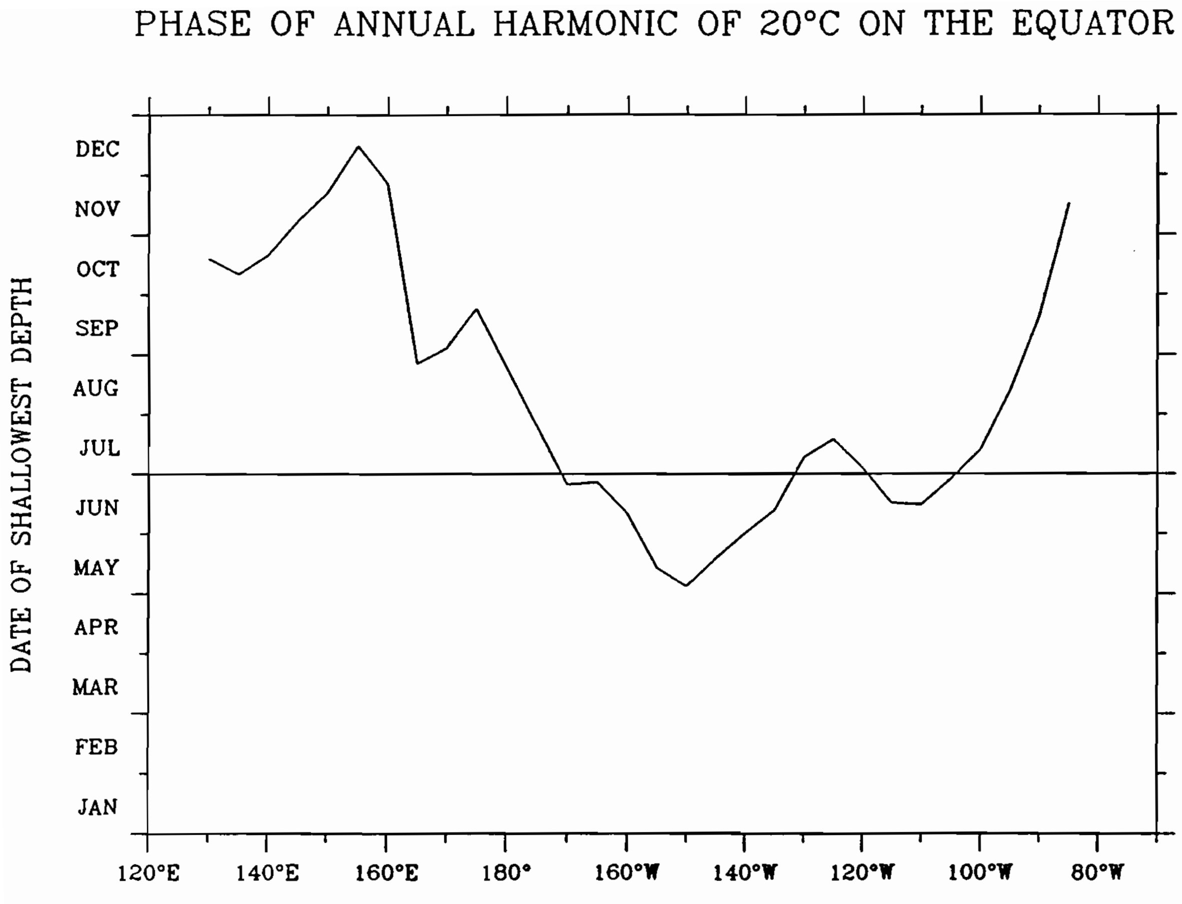

Figure 3.8. Phase of the first annual harmonic of 20°C depth along the equator. The phase is shown as the date of shallowest isotherm depth.

AMPLITUDE OF 1ST HARMONIC OF $\mathrm{Curl}_z\tau$ ($10^{-8}$ N m$^{-3}$)

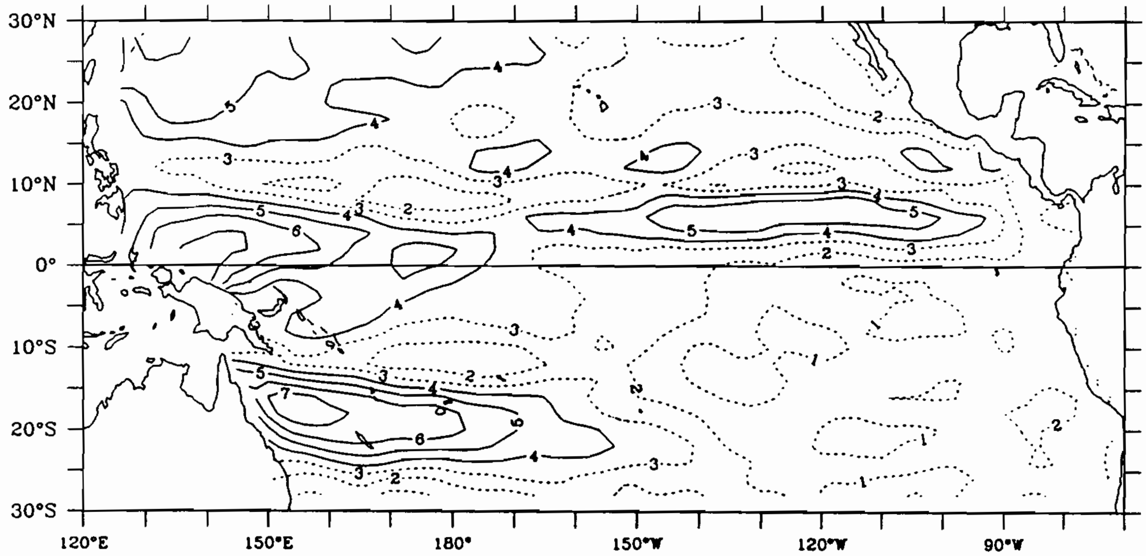

PHASE OF 1ST HARMONIC OF $\mathrm{Curl}_z\tau$

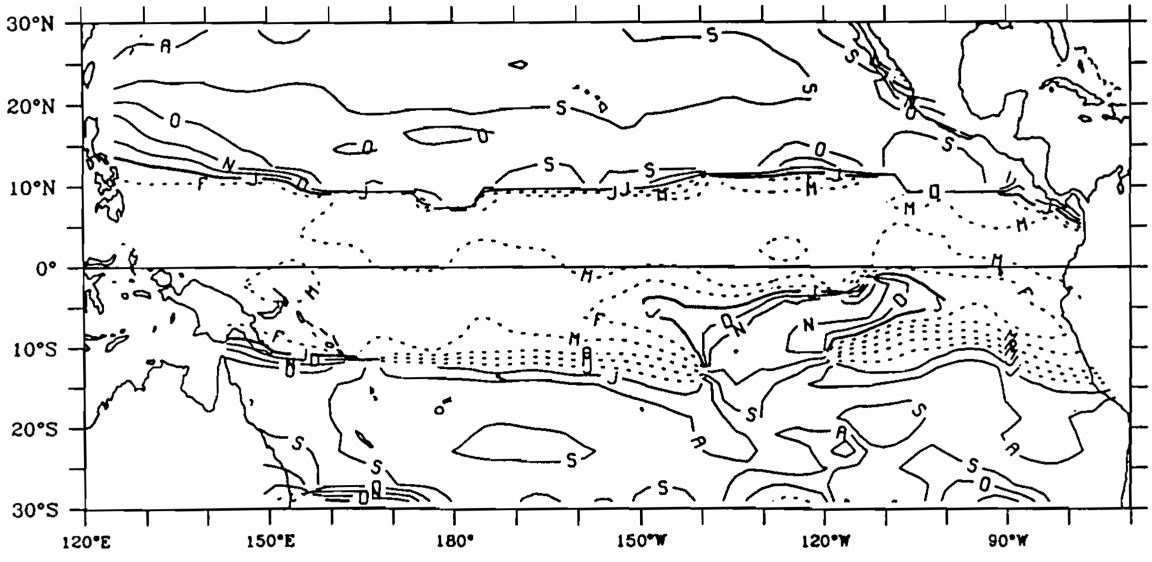

Figure 3.9. Amplitude (top, $10^{-8}$ N m$^{-3}$) and phase (bottom) of the first annual harmonic of wind stress curl during 1970 through 1987. Contours of amplitude are given every $10^{-8}$ N m$^{-3}$, with values of $3 \times 10^{-8}$ N m$^{-3}$ or less in dashed contours and higher values in solid contours. Phase shown is the date of maximum positive curl. Contours of phase are given in months, contoured at the first day of each month. Labels are abbreviated months, with the heavy contour being January, dashed contours February through June, and solid contours July through December.

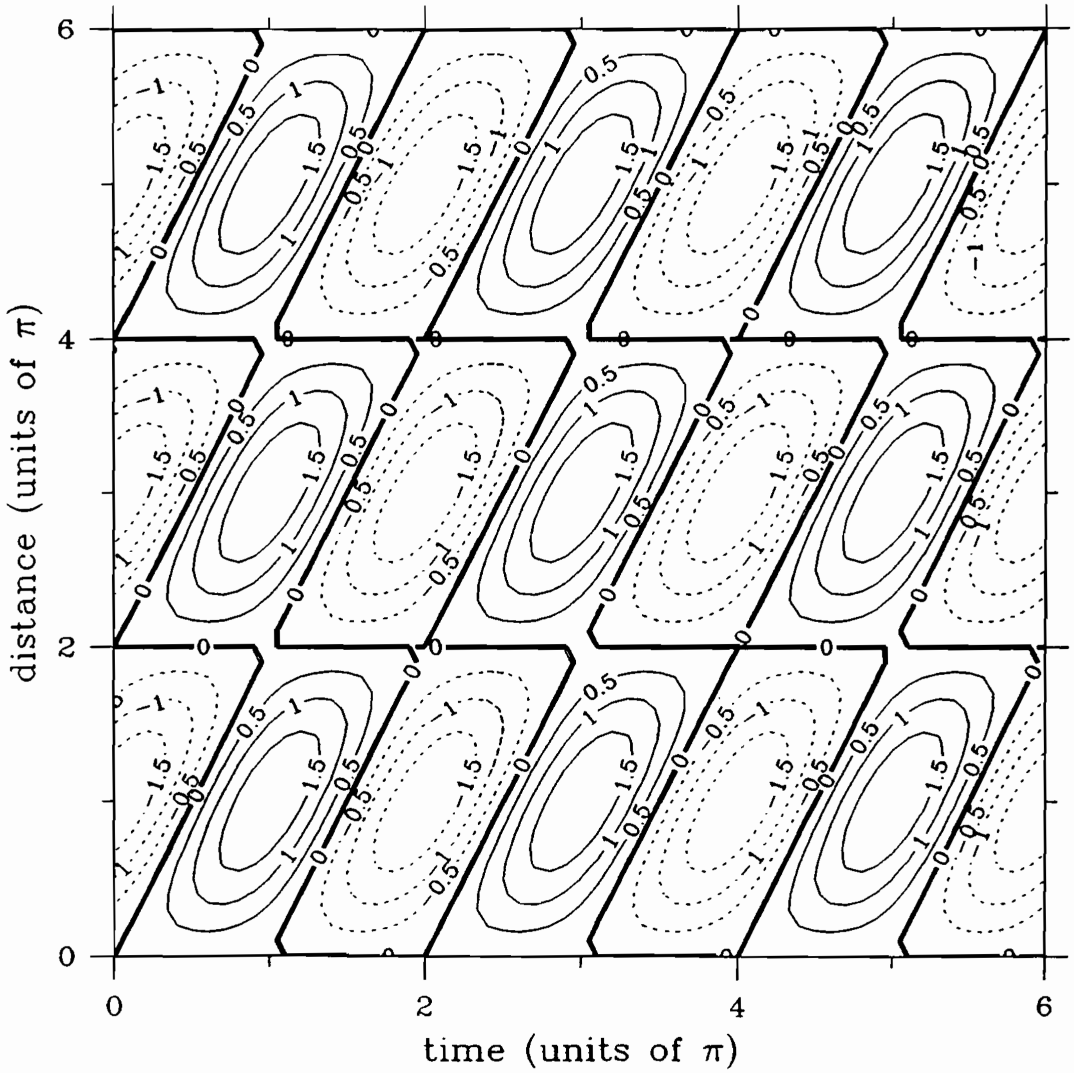

Figure 3.10. Contours of anomalies due to a spatially uniform, sinusoidally time-varying forcing with the boundary condition that anomalies are fixed to zero at the "eastern" boundary (bottom edge of plot).

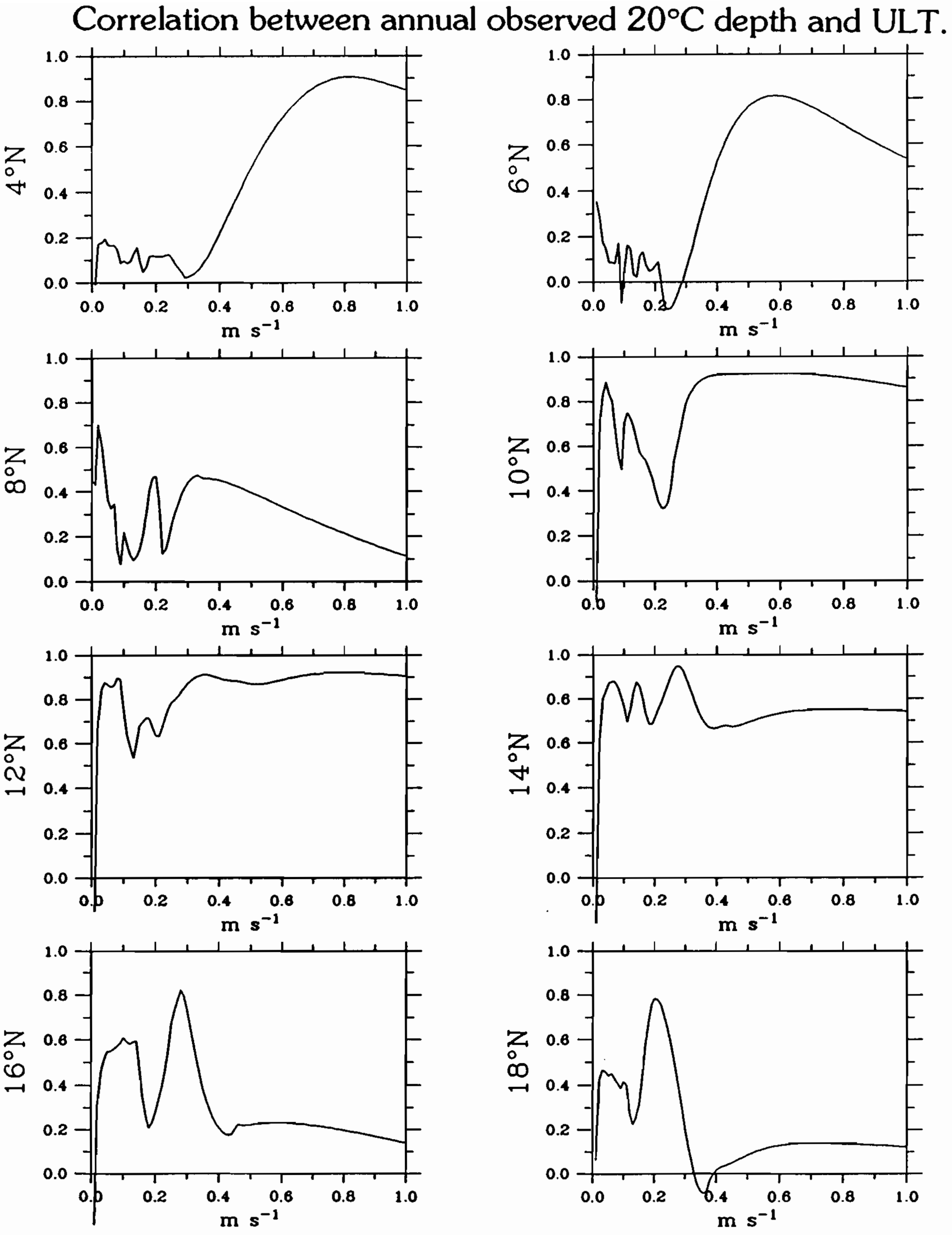

Figure 3.11. Correlation between the observed annual cycle of 20°C depths and upper layer thickness (ULT) hindcasts made using the vorticity equation (2.4), as a function of phase speed $c_r$ (shown on the bottom axes in m/s). The best-fit phase speed was chosen as the highest correlation at each latitude (see text).

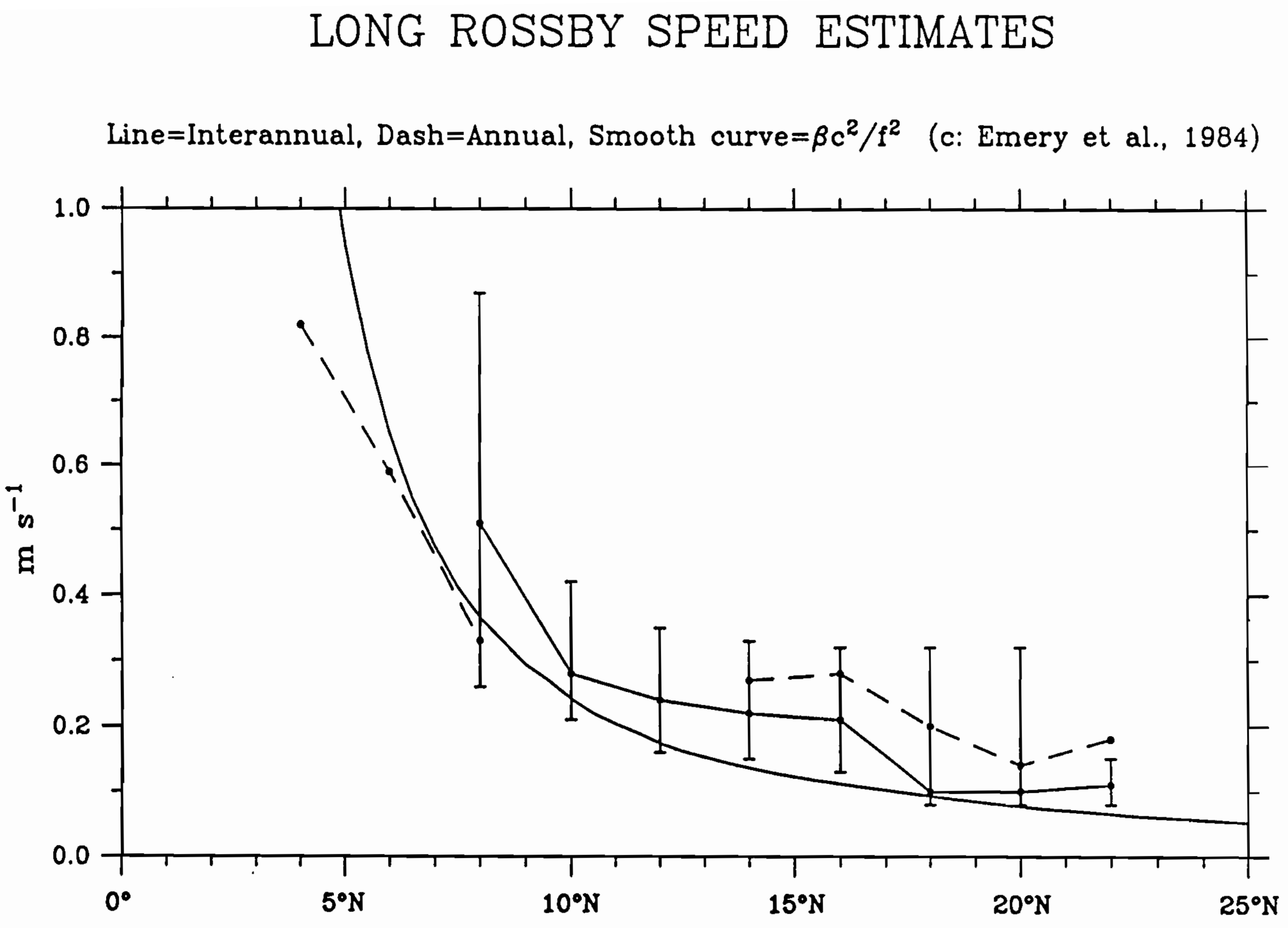

Figure 3.12. Best-fit estimates of the propagation speed of long Rossby waves. The smooth curve represents the theoretical speed $c_r = \beta c^2/f^2$, with the long gravity wave speed c found as the zonal average of data given in Emery *et al.* (1984), shown in Figure 2.2. The dashed line represents bestfit estimates for the annual cycle (discussed in Section 3.e). No estimates were made at 10° or 12°N for annual cycle. The solid line represents bestfit estimates for interannual variability (discussed in Section 4.d). The "error bars" refer to these interannual estimates; the method used to calculate these is discussed in the text (see also Figure 4.8).

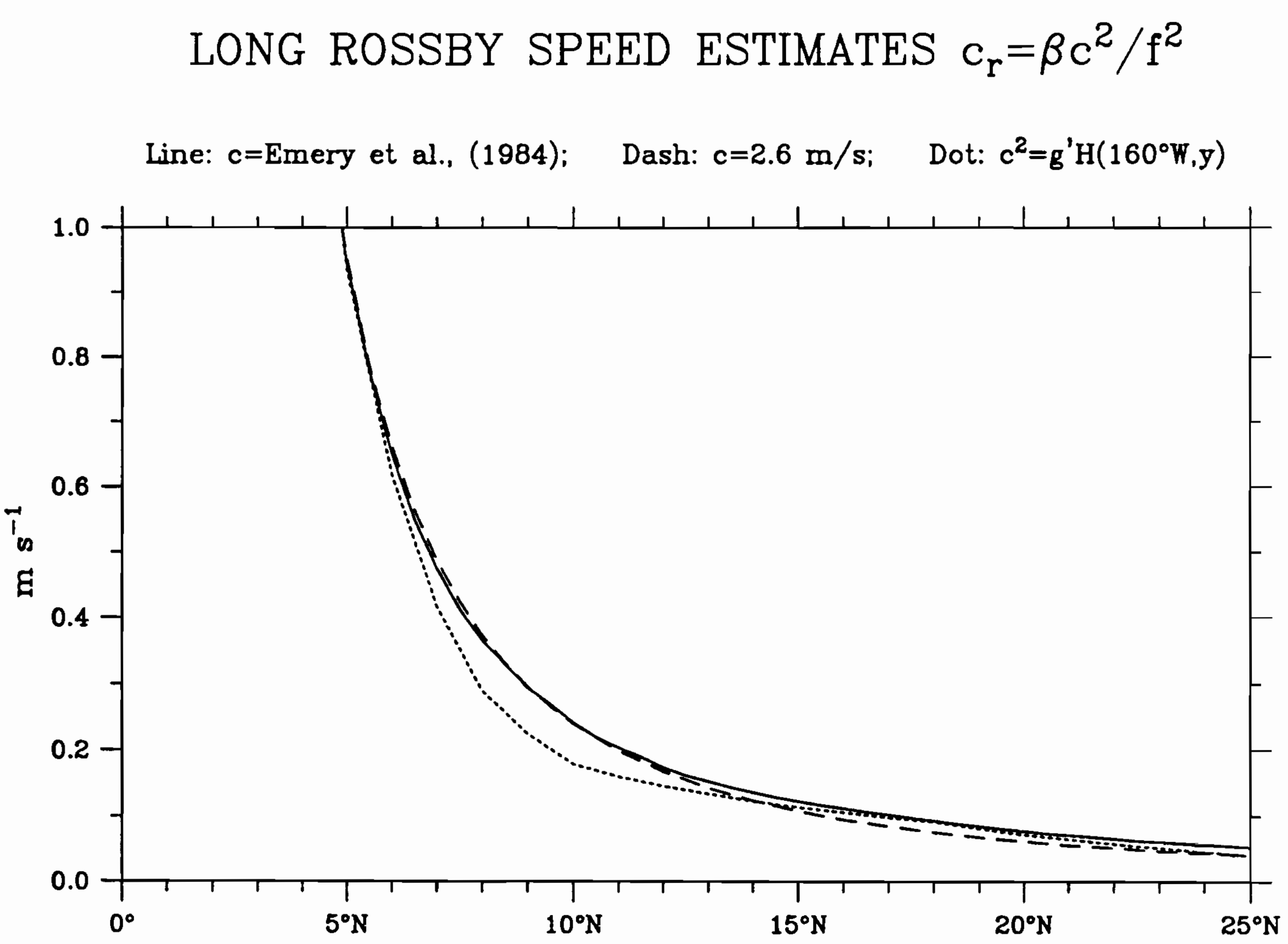

Figure 3.12b. Comparison of estimates of the long Rossby wave speed $c_r = \beta c^2/f^2$ with several choices of the long gravity wave speed c. The solid line is the meridional profile of $c_r$ if c is chosen to be the zonal average of internal gravity wave speeds found from data presented by Emery *et al.* (1984) (same curve as in Figure 3.12). The long dashes give the profile if the meridional average (between 5° and 25°N) of the zonal average Emery speeds is used (c=2.6 m/s). The dotted line gives the profile if $c^2 = g'H$, where H(y) is the mean 20°C depth at 160°W (Figure 3.1) and $\Delta\rho/\rho = 5 \times 10^{-3}$.

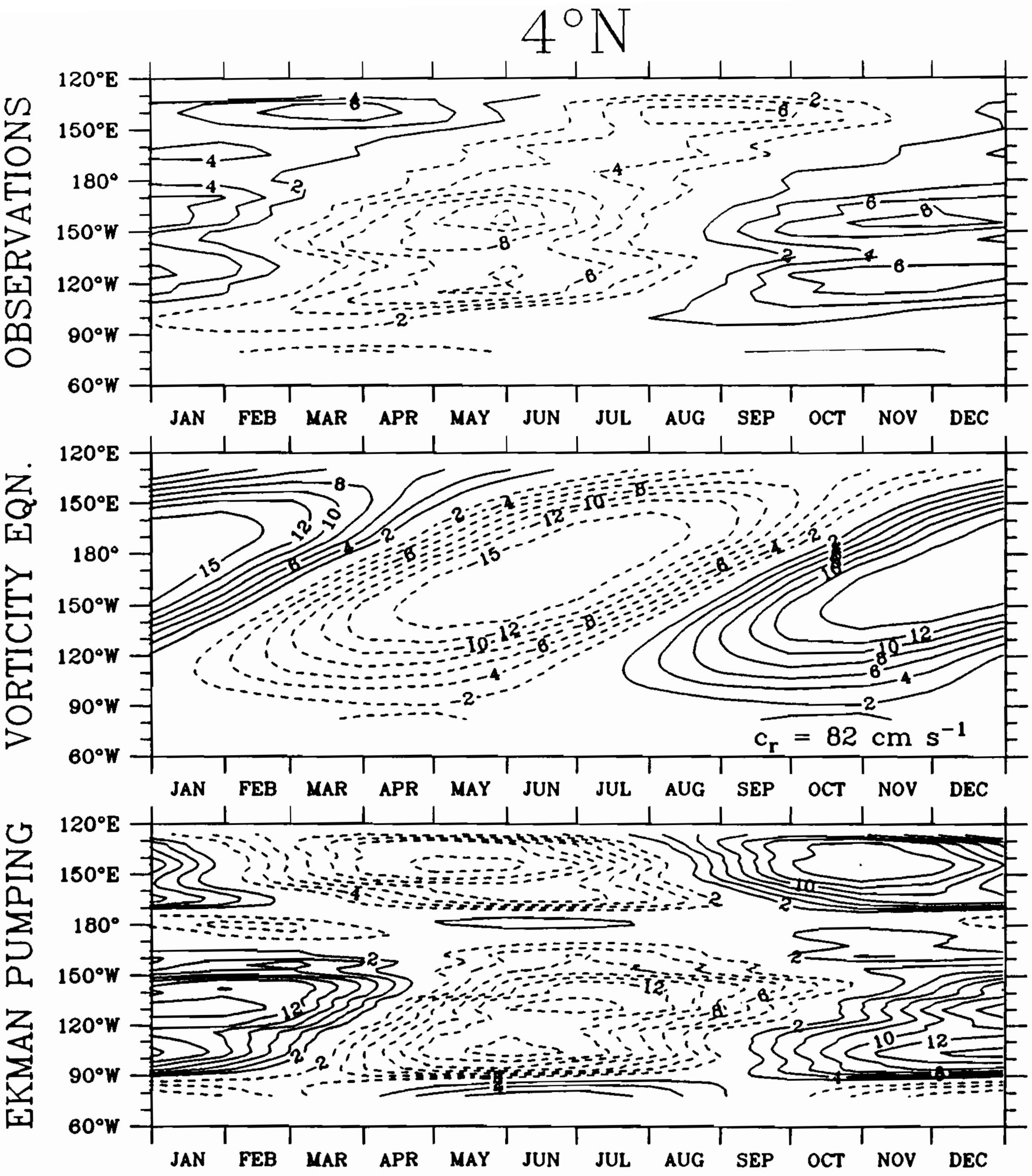

Figure 3.13a. Top: the annual cycle of 20°C depth (m) at 4°N (longterm mean removed). Solid contours indicate deep anomalies, dashed contours shallow anomalies. Middle: hindcast of annual upper layer thickness (ULT) anomalies (m) made using the vorticity equation (2.4) with best-fit speeds $c_r$ shown in lower right. Bottom: Hindcast of annual pycnocline depth anomalies (m) made assuming Ekman pumping alone.

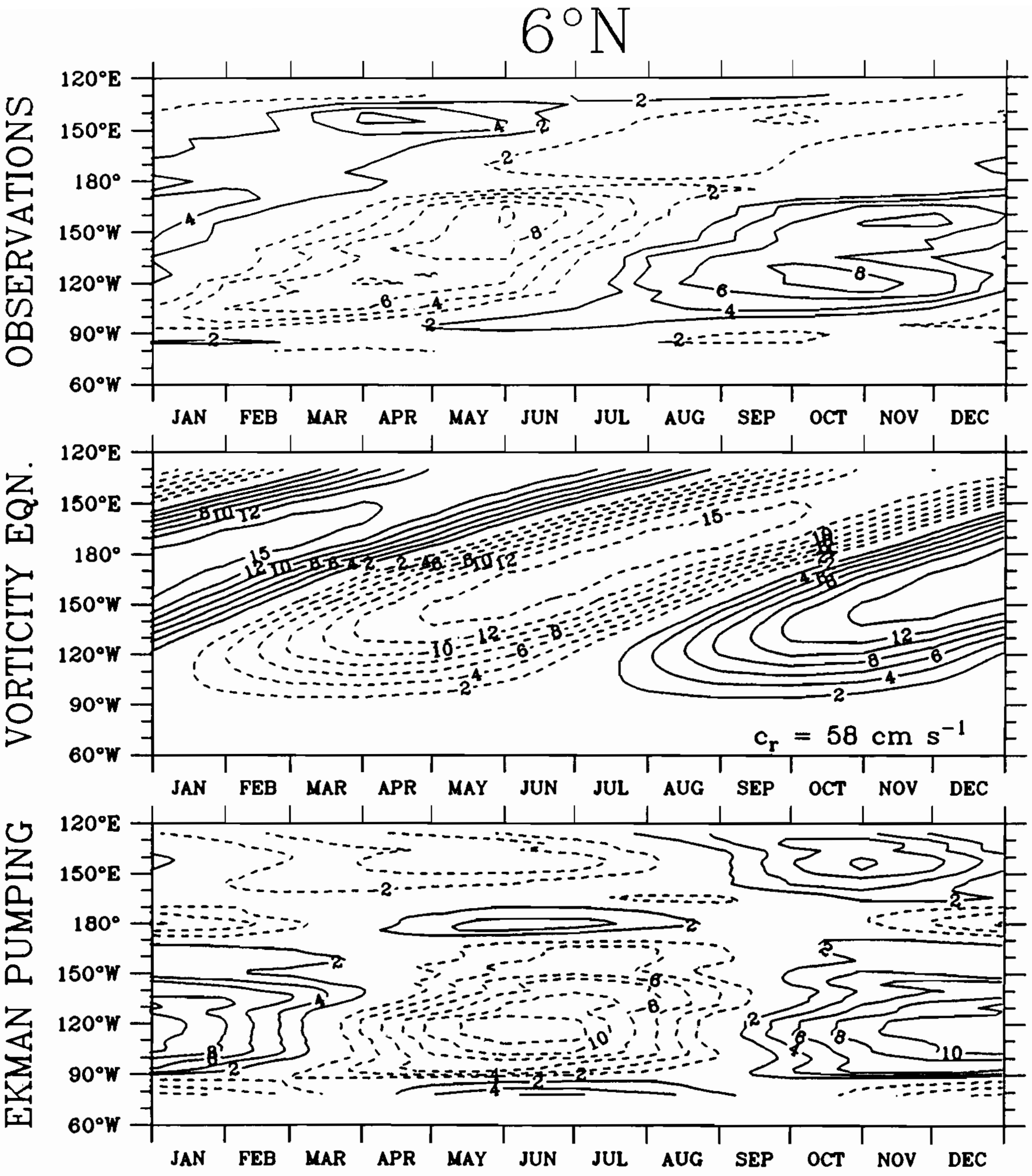

Figure 3.13b. As Figure 3.13a but at 6°N.

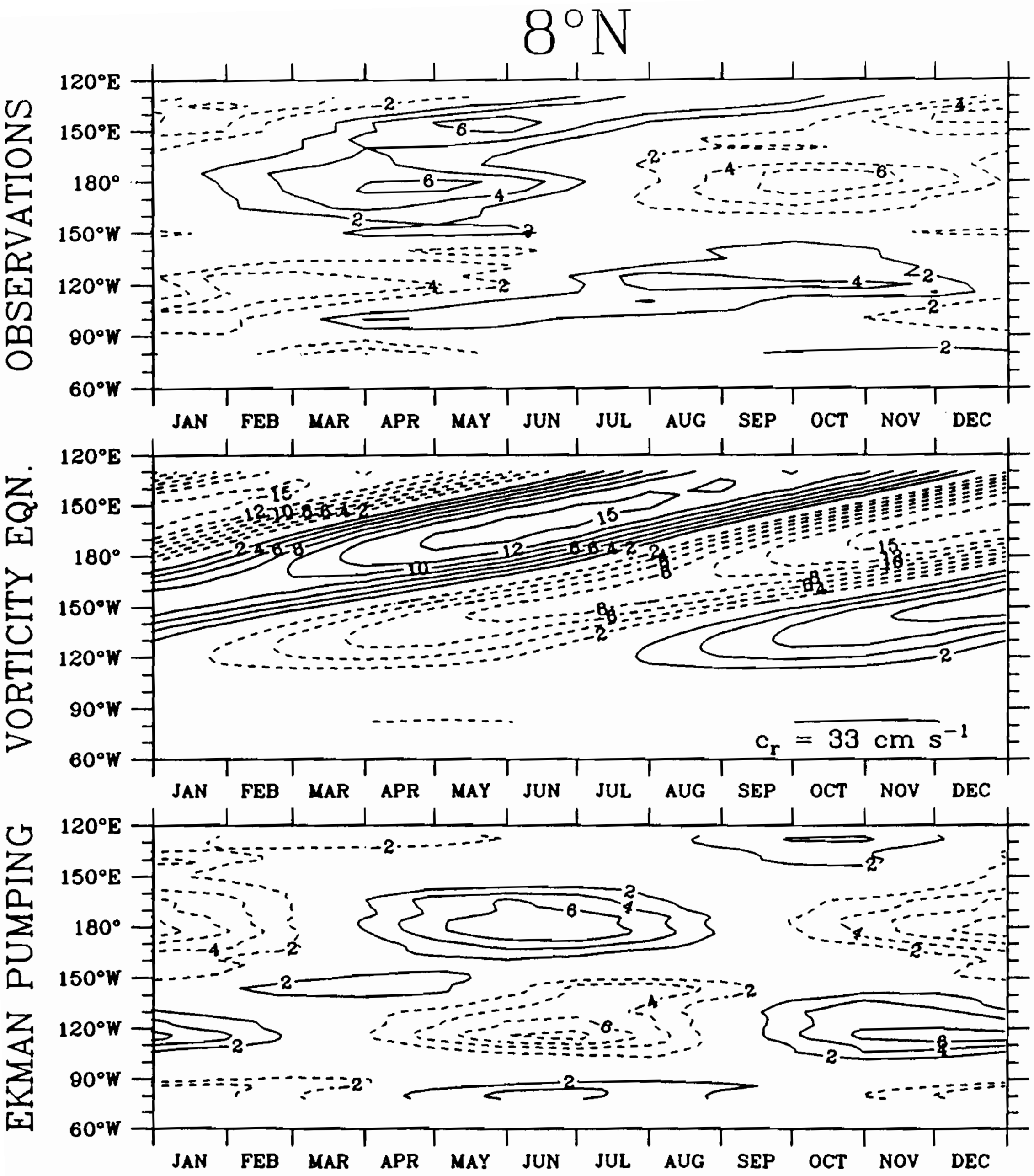

Figure 3.13c. As Figure 3.13a but at 8°N.

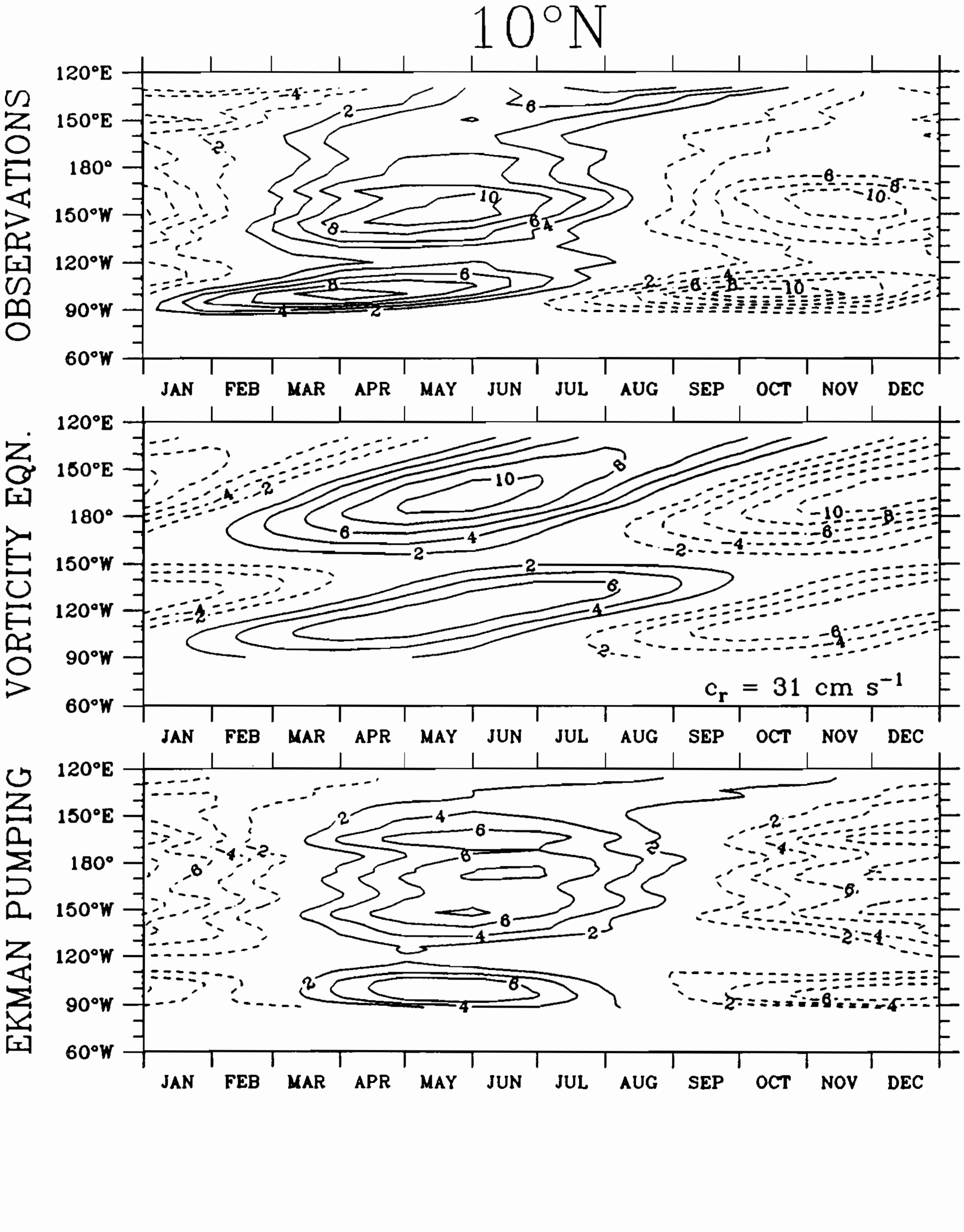

Figure 3.13d. As Figure 3.13a but at 10°N.

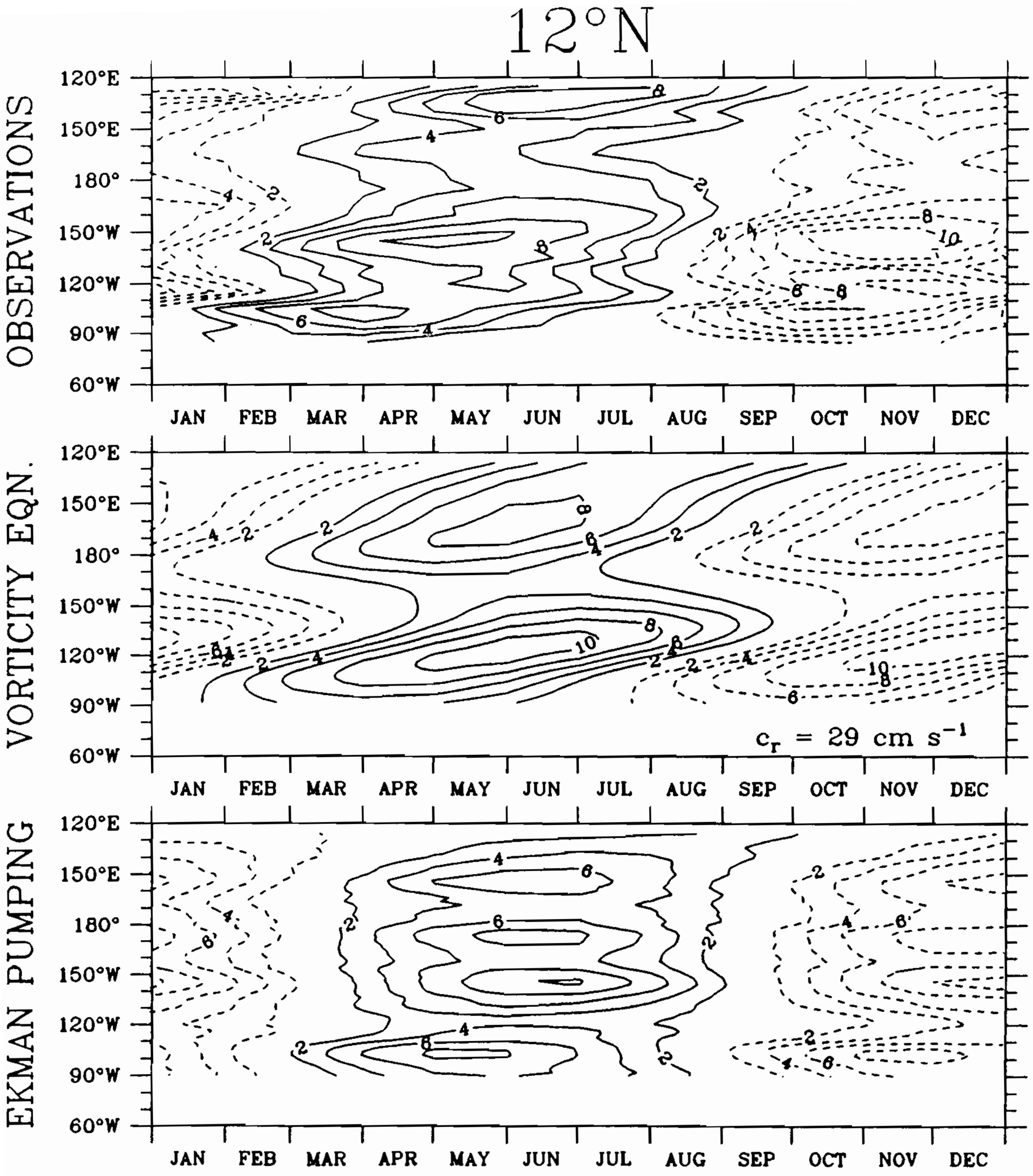

Figure 3.13e. As Figure 3.13a but at 12°N.

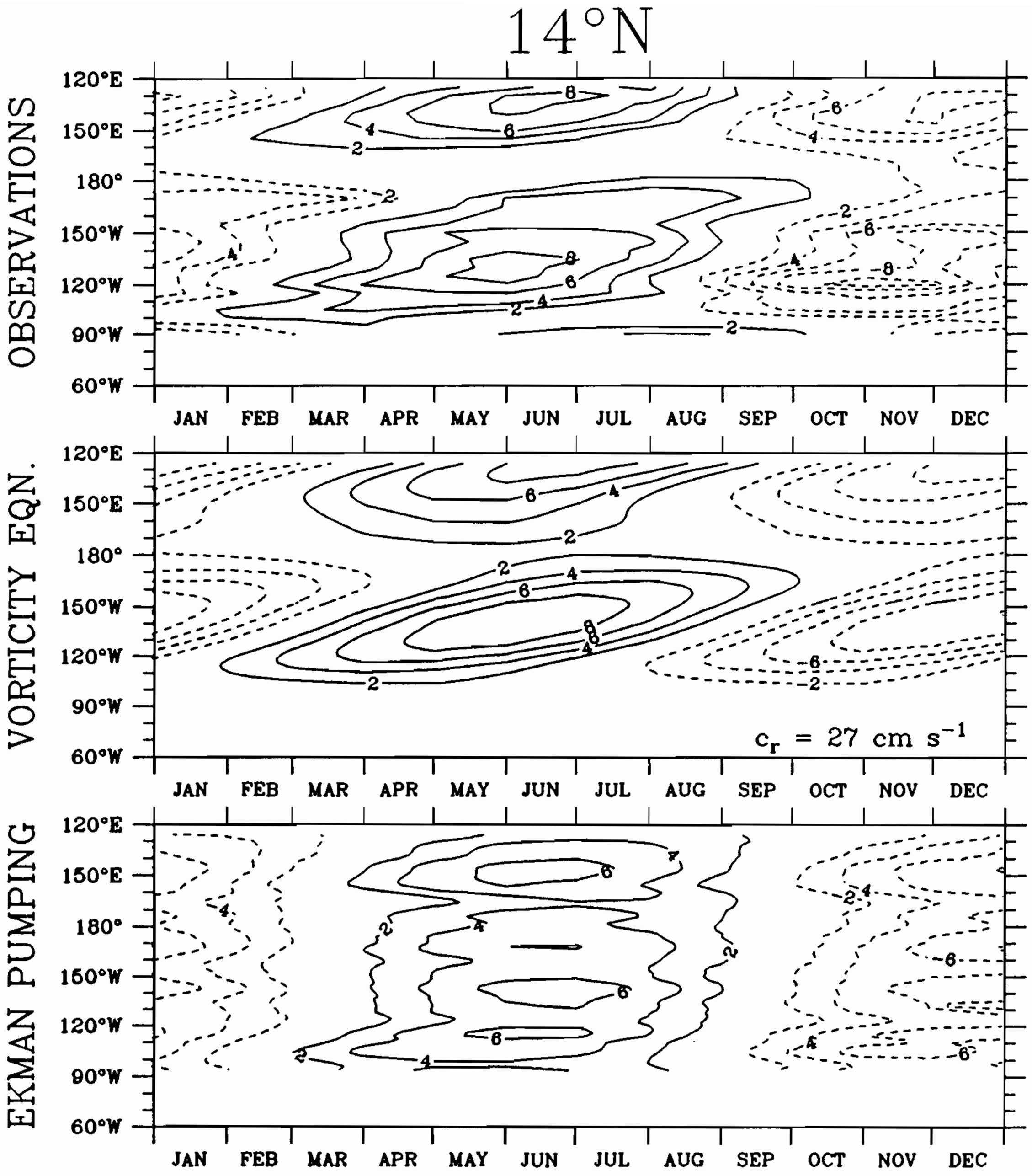

Figure 3.13f. As Figure 3.13a but at 14°N.

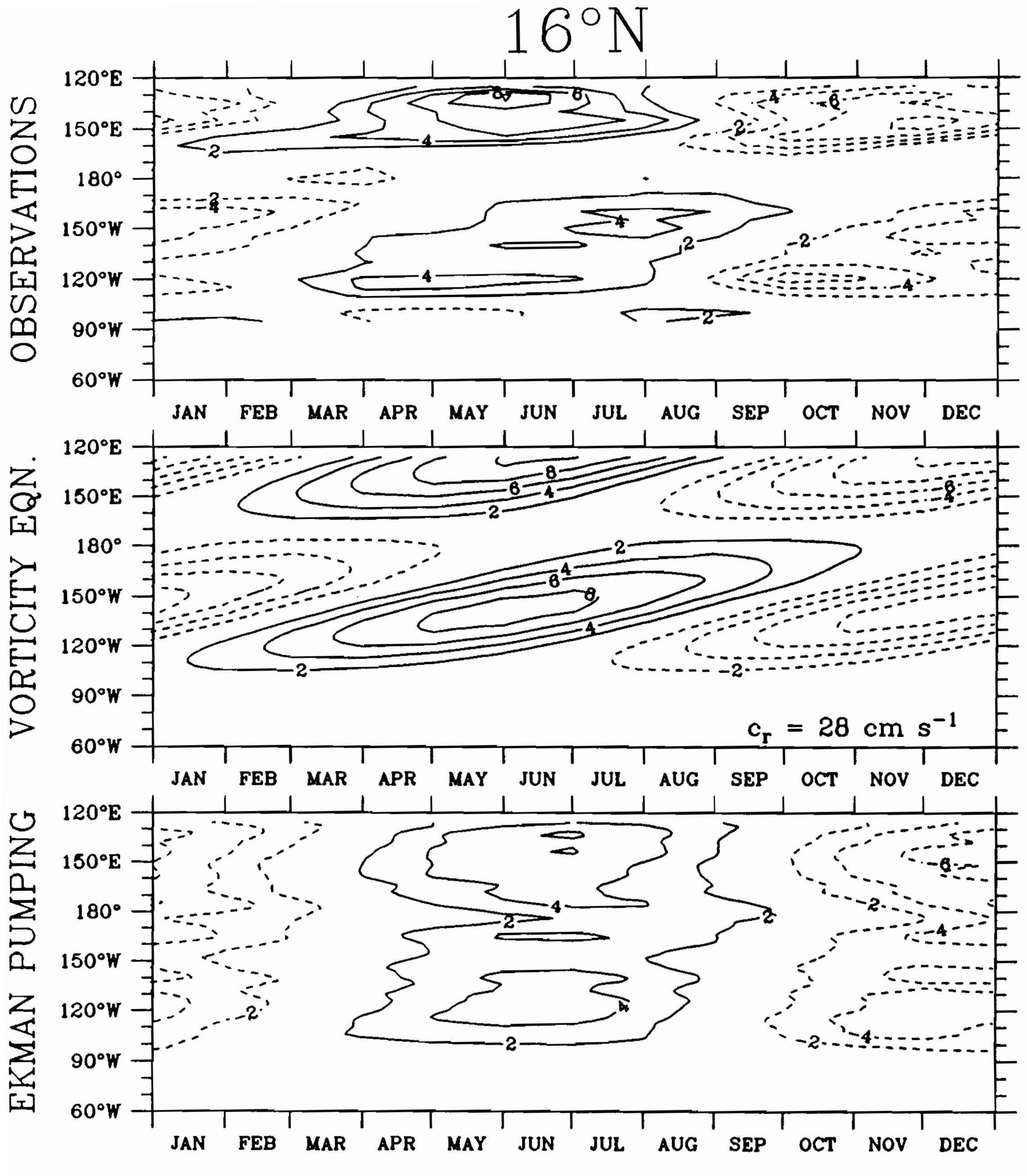

Figure 3.13g. As Figure 3.13a but at 16°N.

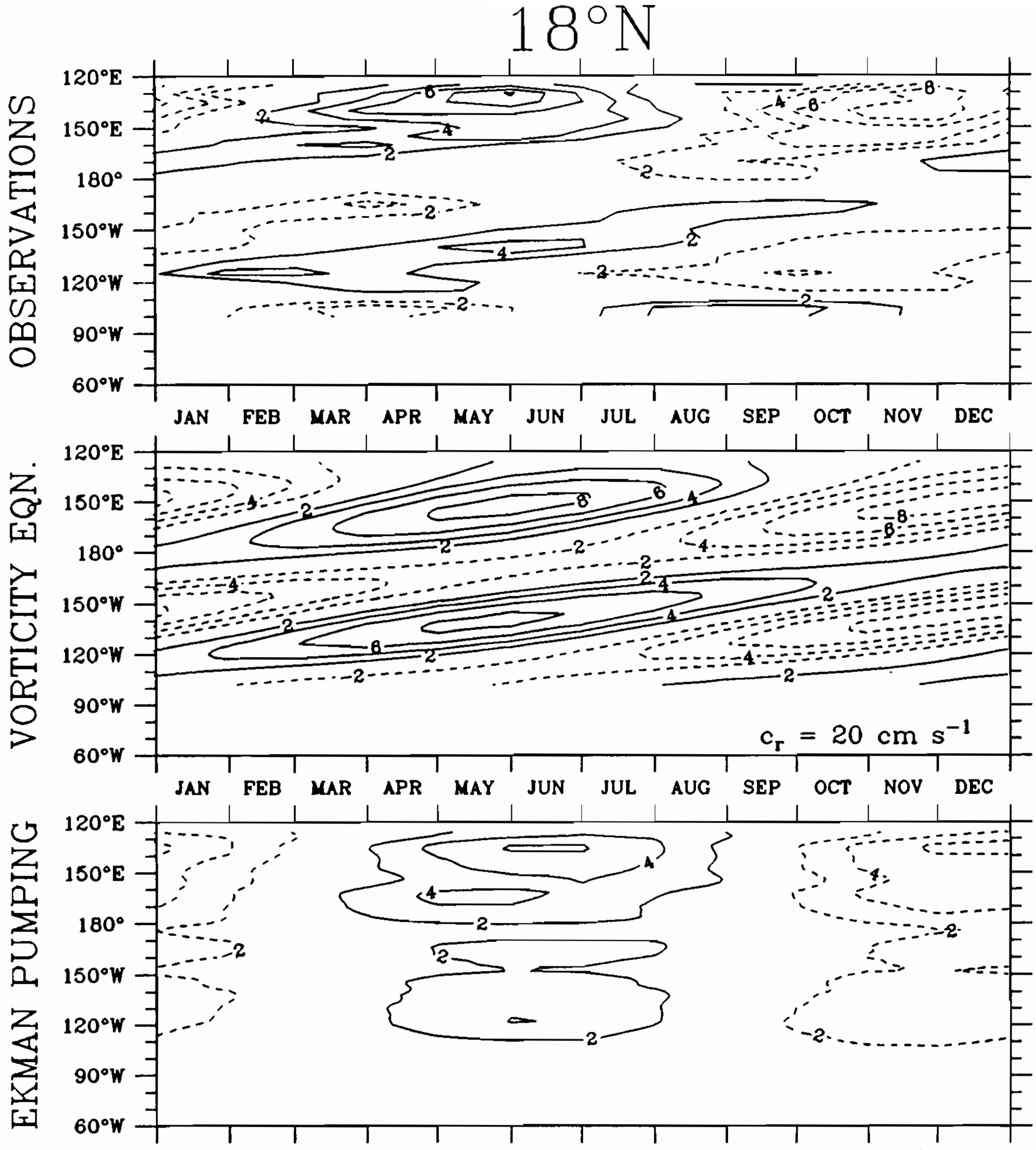

Figure 3.13h. As Figure 3.13a but at 18°N.

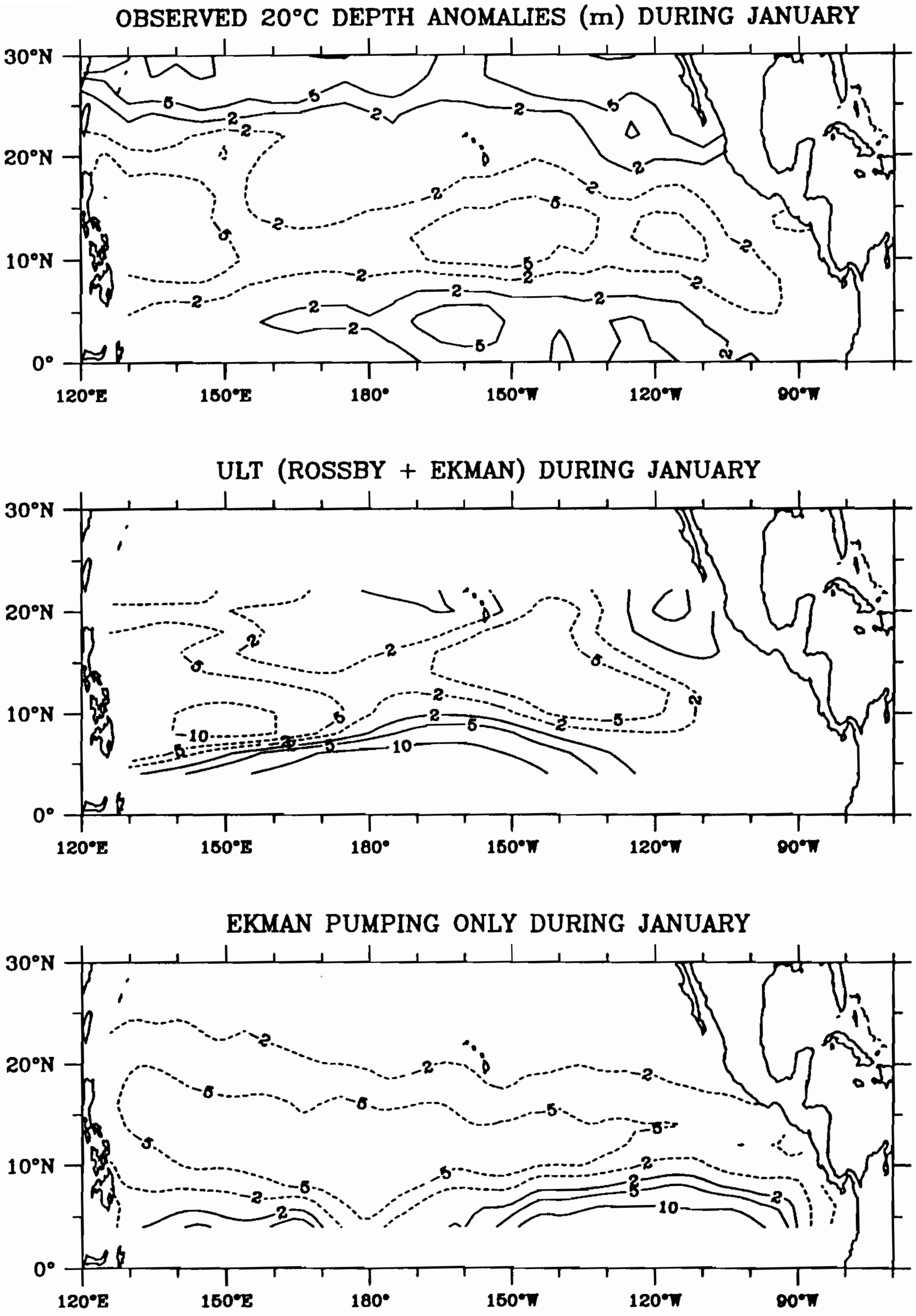

Figure 3.14a. Top: observed 20°C depth anomalies (m) during the average January (1970 through 1987). Solid contours indicate deep anomalies, dashed contours indicate shallow anomalies. Contours are given at ±2, 5 and 10 meters. Middle: hindcast of upper layer thickness (ULT) anomalies (m) for the average January made using the vorticity equation (2.4). Bottom: Hindcast of anomalies (m) during the average January made assuming Ekman pumping acting alone.

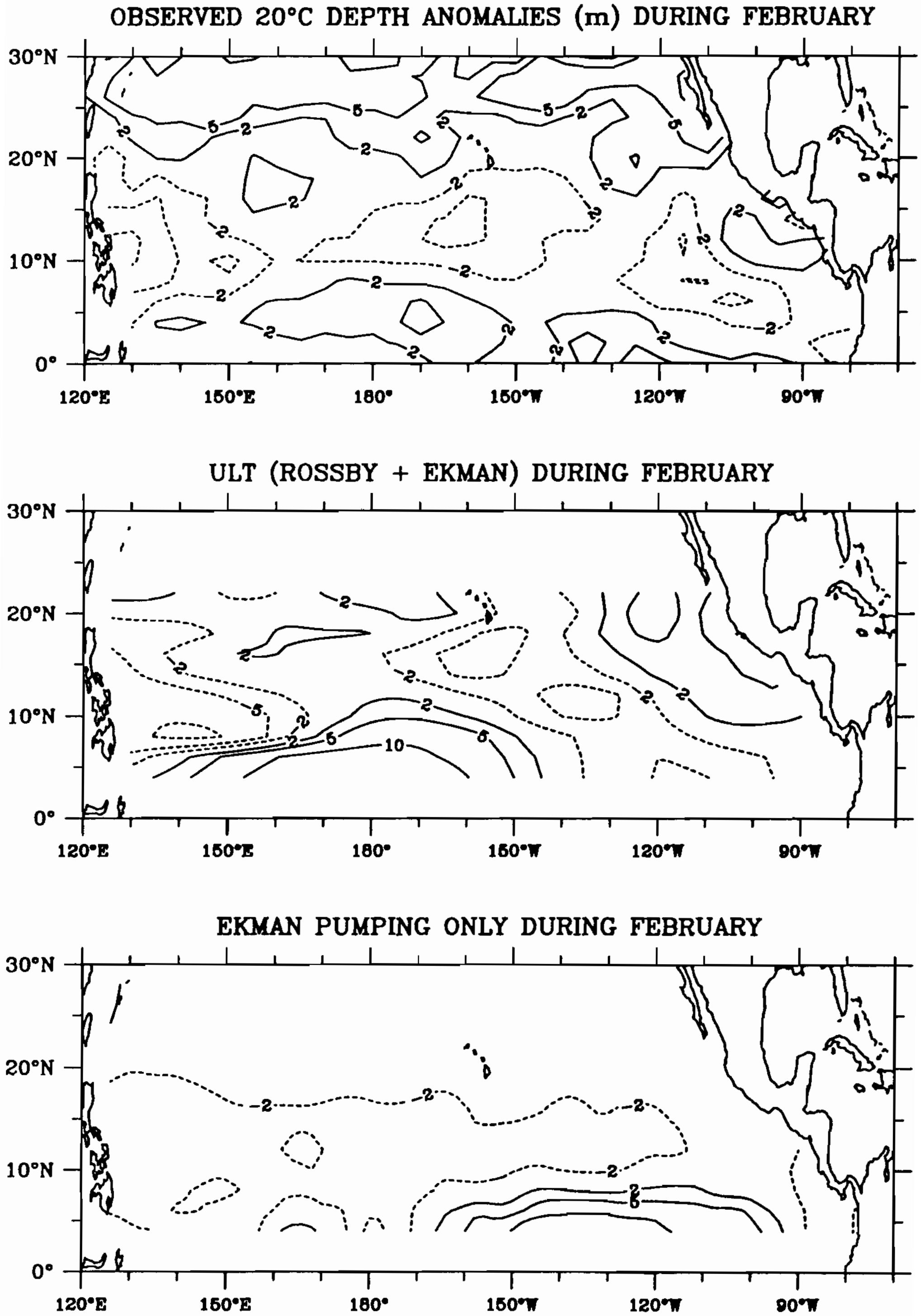

Figure 3.14b. As Figure 3.14a but for February.

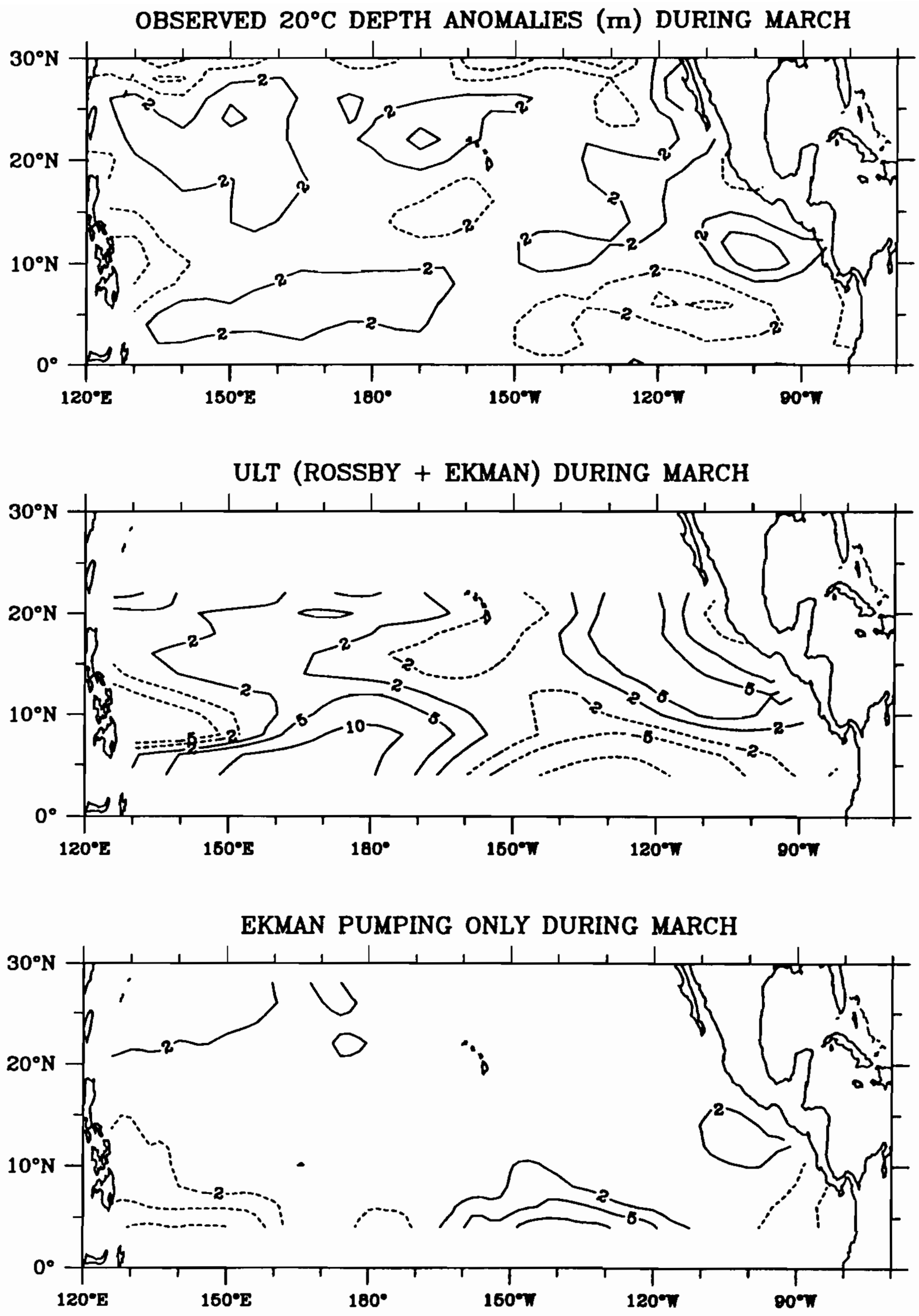

Figure 3.14c. As Figure 3.14a but for March.

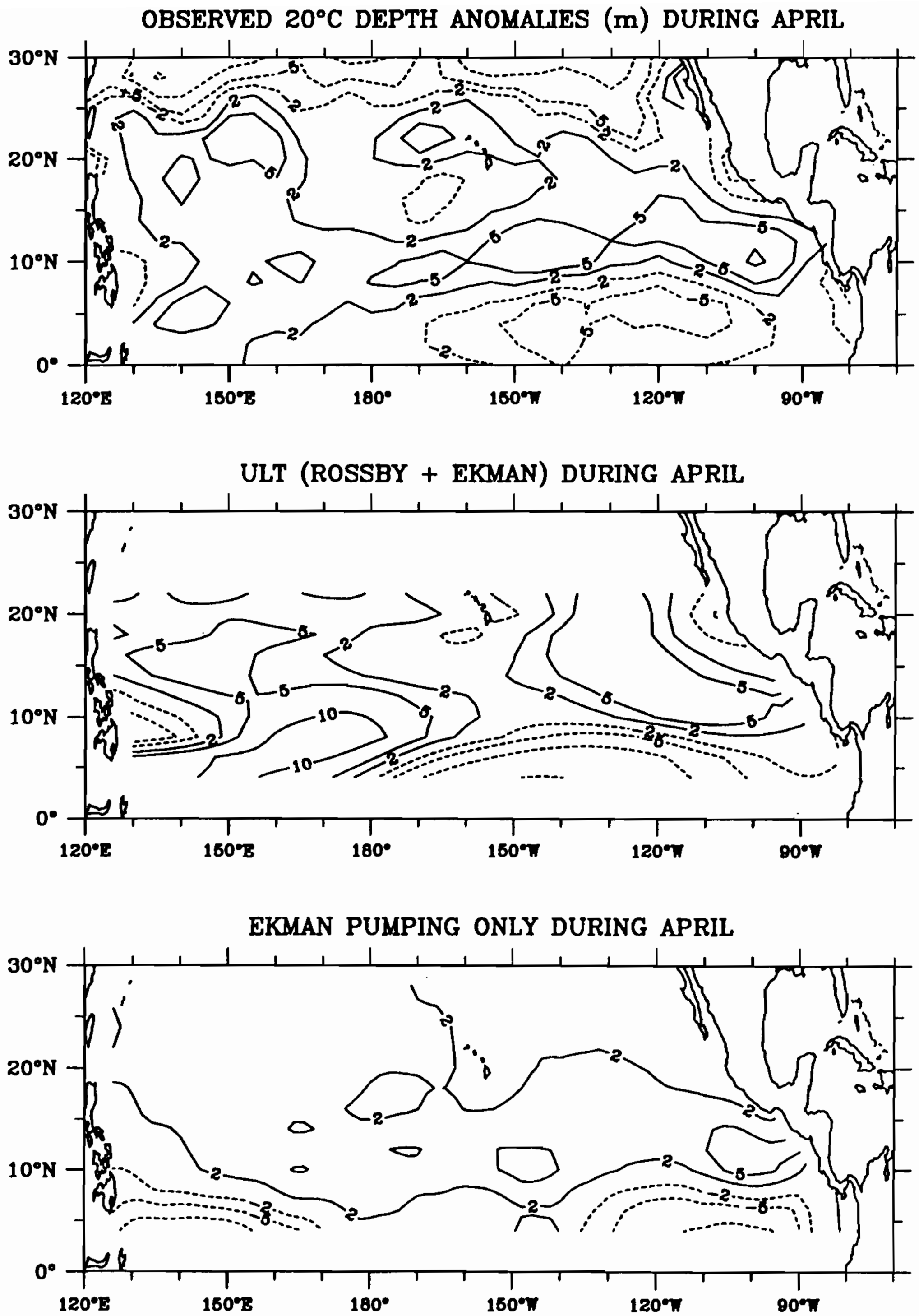

OBSERVED 20°C DEPTH ANOMALIES (m) DURING APRIL

ULT (ROSSBY + EKMAN) DURING APRIL

EKMAN PUMPING ONLY DURING APRIL

Figure 3.14d. As Figure 3.14a but for April.

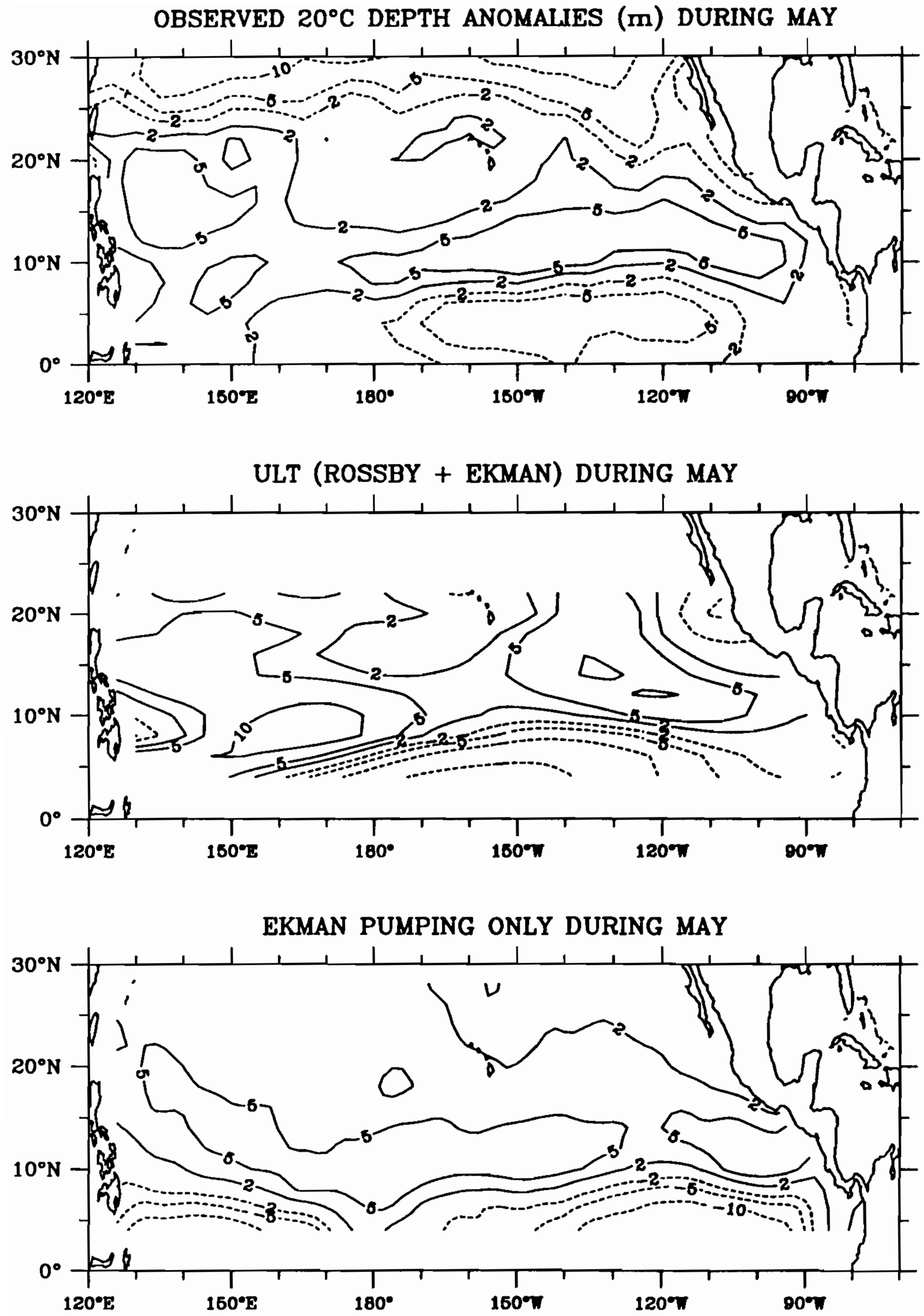

OBSERVED 20°C DEPTH ANOMALIES (m) DURING MAY

ULT (ROSSBY + EKMAN) DURING MAY

EKMAN PUMPING ONLY DURING MAY

Figure 3.14e. As Figure 3.14a but for May.

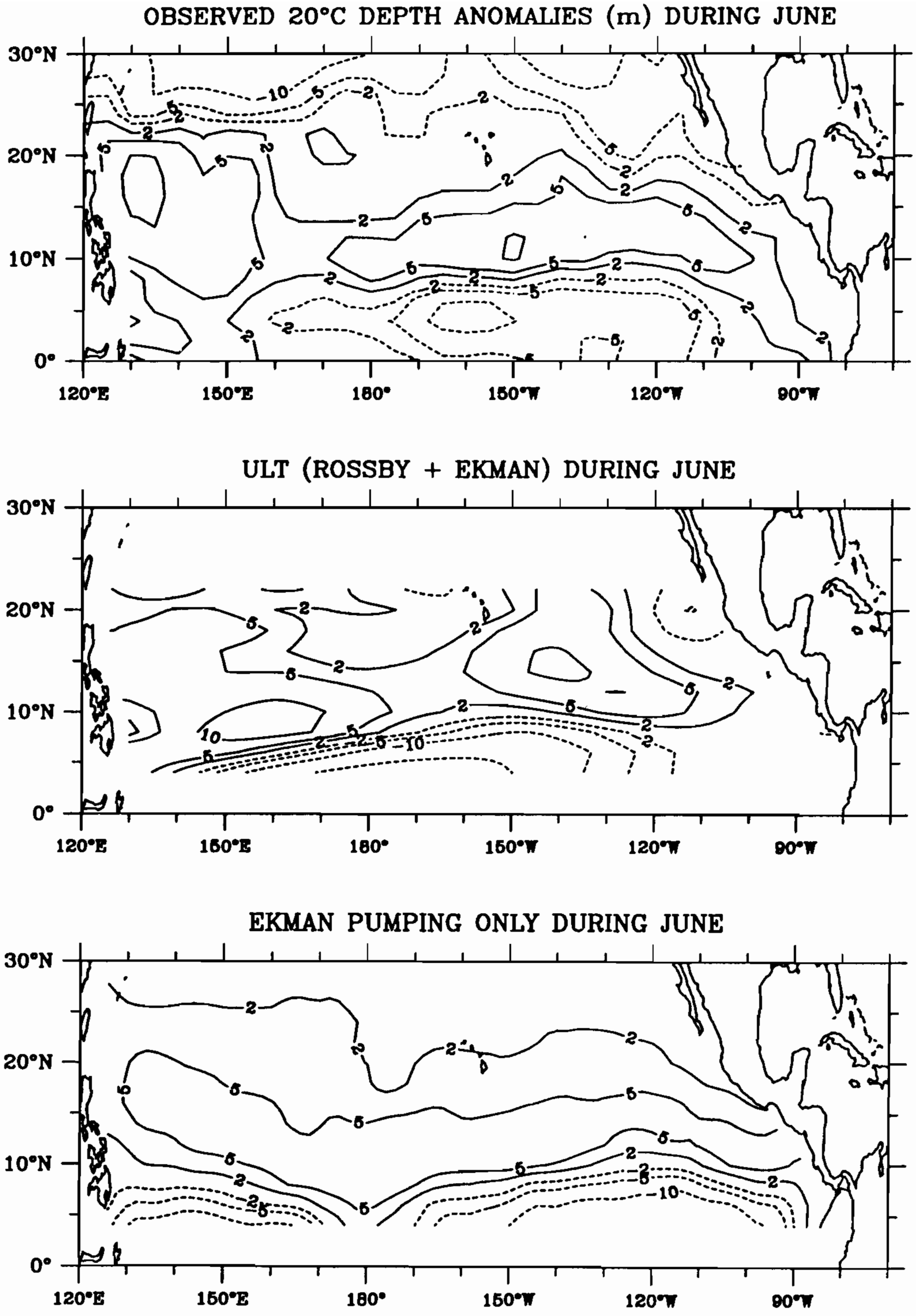

OBSERVED 20°C DEPTH ANOMALIES (m) DURING JUNE

ULT (ROSSBY + EKMAN) DURING JUNE

EKMAN PUMPING ONLY DURING JUNE

Figure 3.14f. As Figure 3.14a but for June.

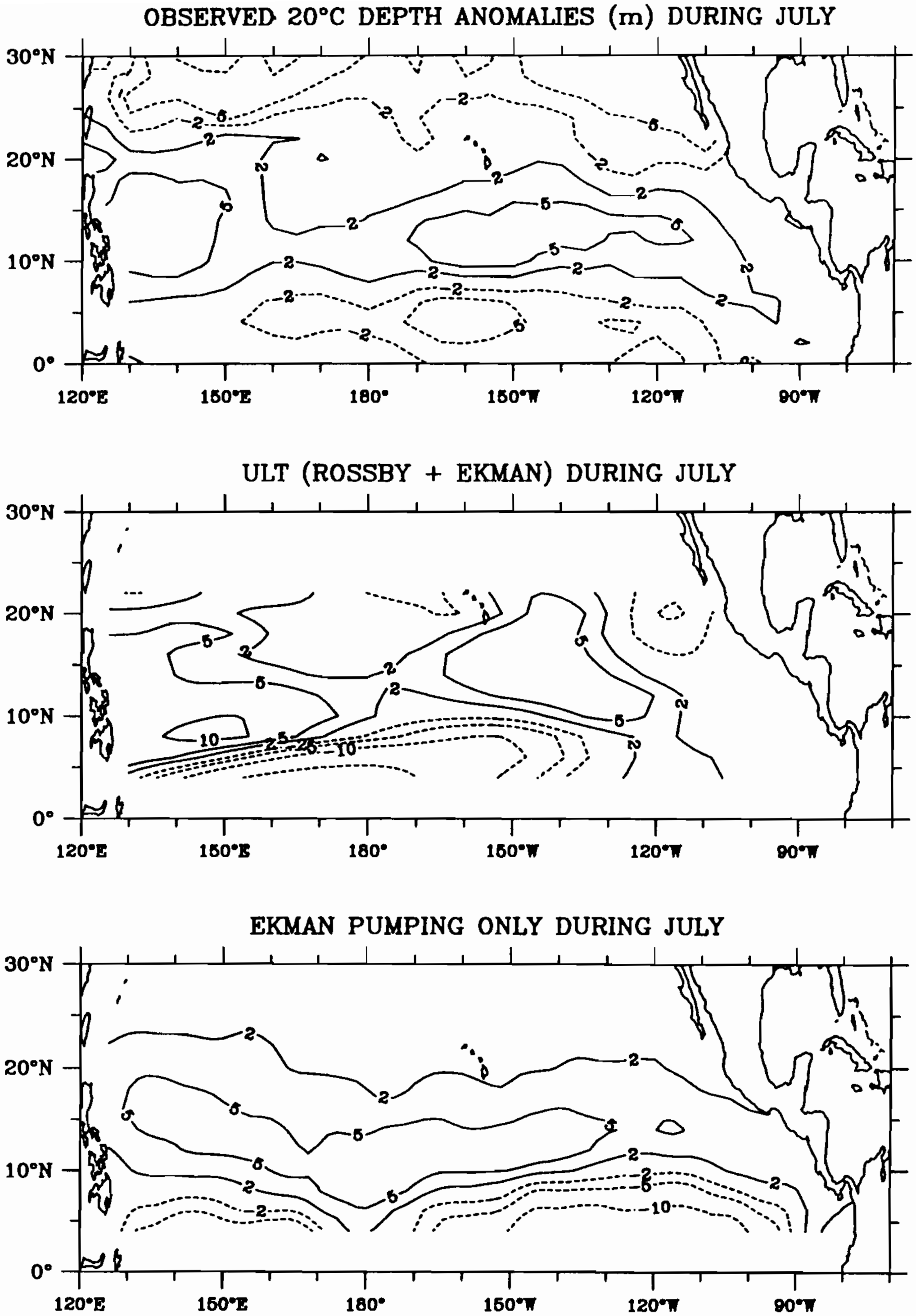 
OBSERVED 20°C DEPTH ANOMALIES (m) DURING JULY

ULT (ROSSBY + EKMAN) DURING JULY

EKMAN PUMPING ONLY DURING JULY

Figure 3.14g. As Figure 3.14a but for July.

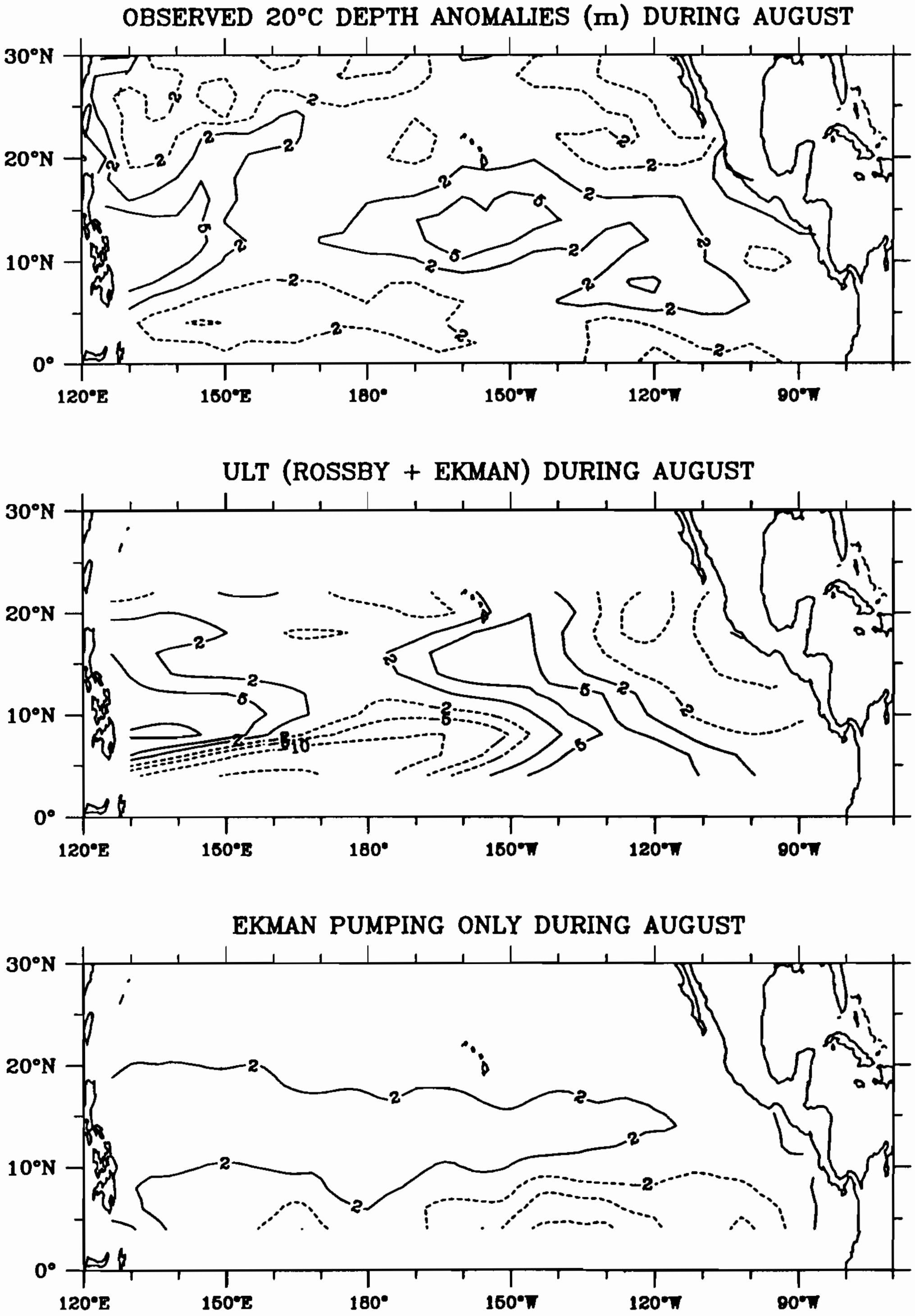

Figure 3.14h. As Figure 3.14a but for August.

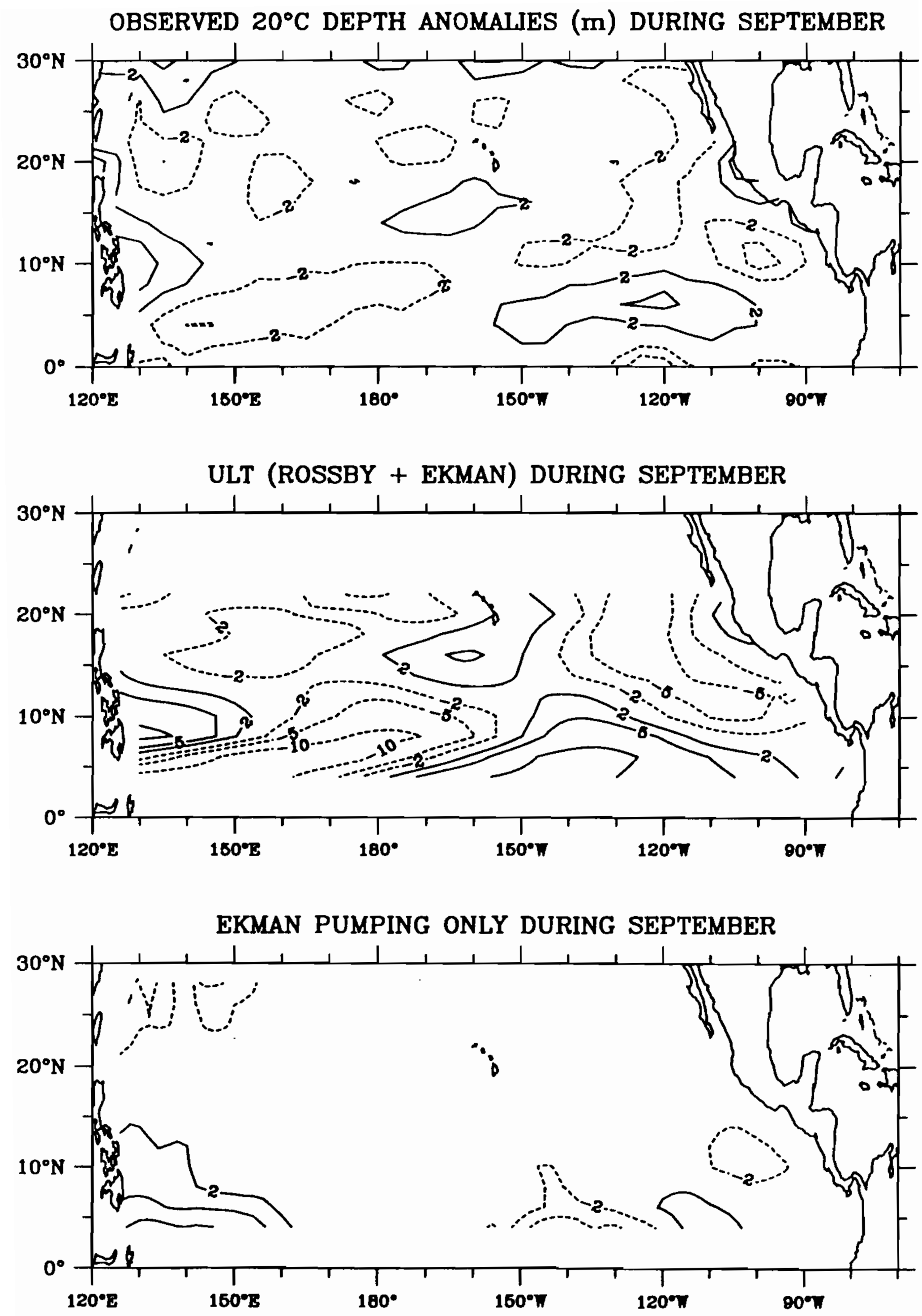
OBSERVED 20°C DEPTH ANOMALIES (m) DURING SEPTEMBER

ULT (ROSSBY + EKMAN) DURING SEPTEMBER

EKMAN PUMPING ONLY DURING SEPTEMBER

Figure 3.14i. As Figure 3.14a but for September.

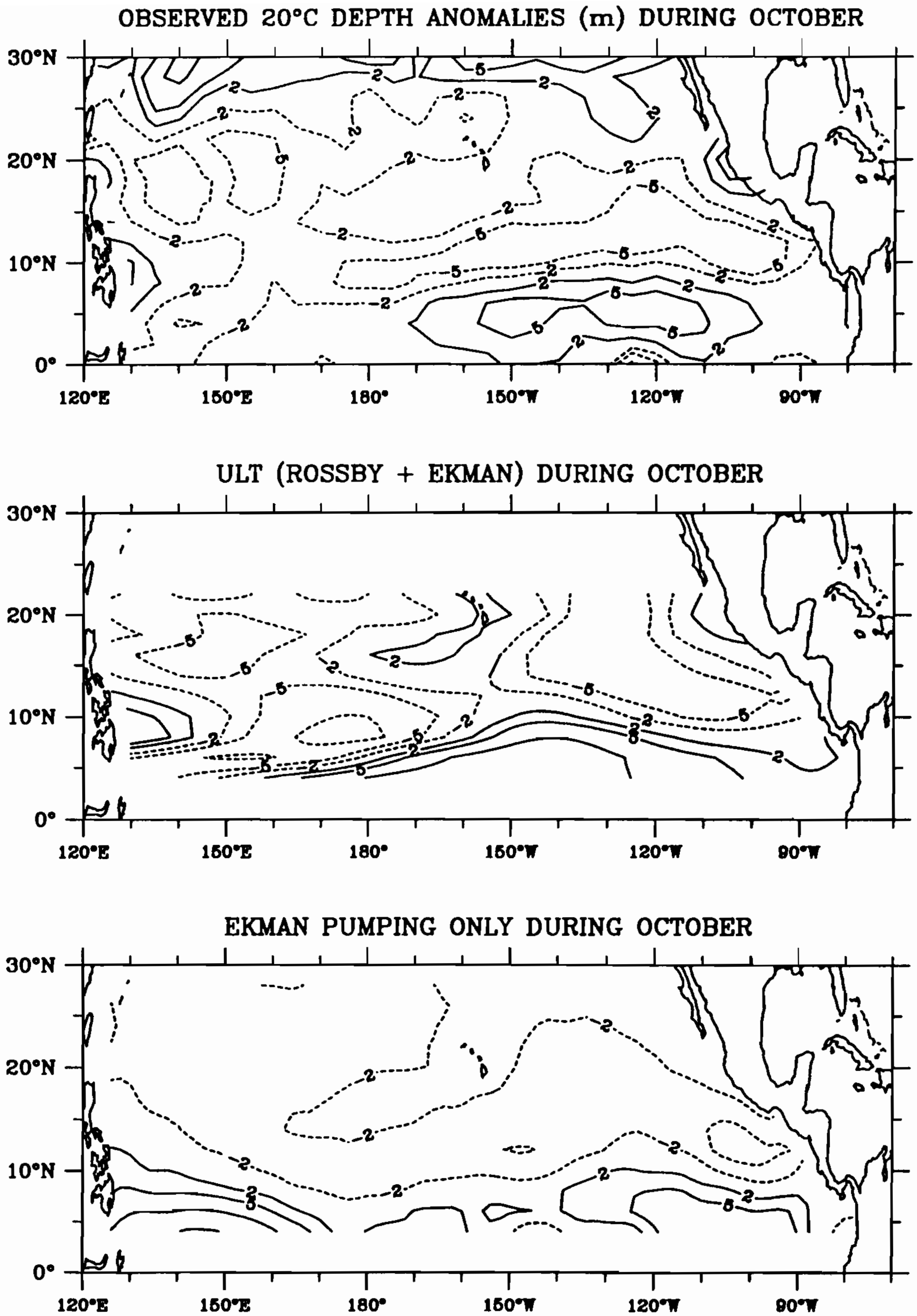

Figure 3.14j. As Figure 3.14a but for October.

OBSERVED 20°C DEPTH ANOMALIES (m) DURING NOVEMBER

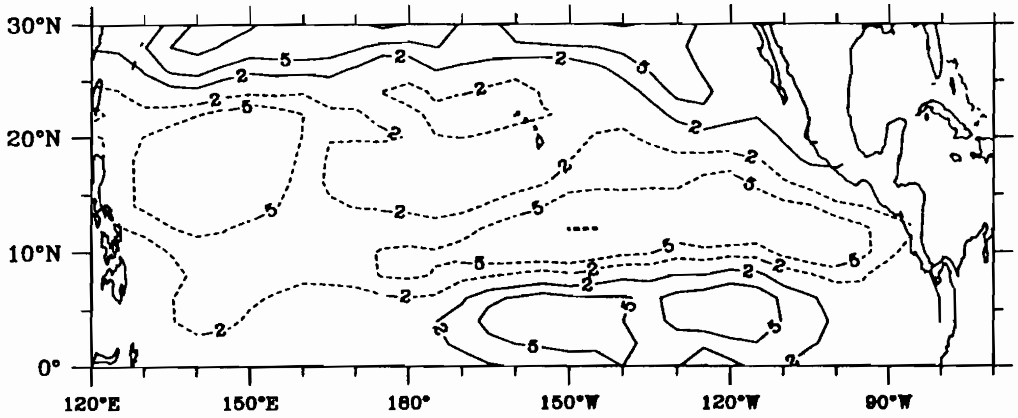

ULT (ROSSBY + EKMAN) DURING NOVEMBER

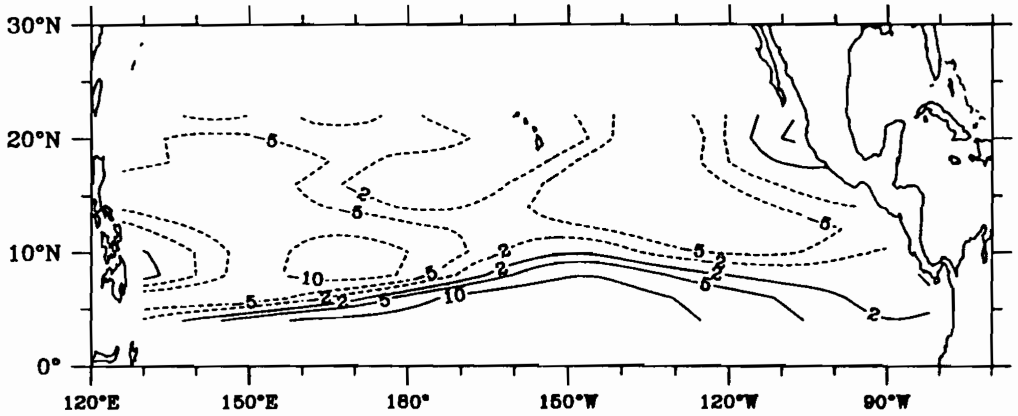

EKMAN PUMPING ONLY DURING NOVEMBER

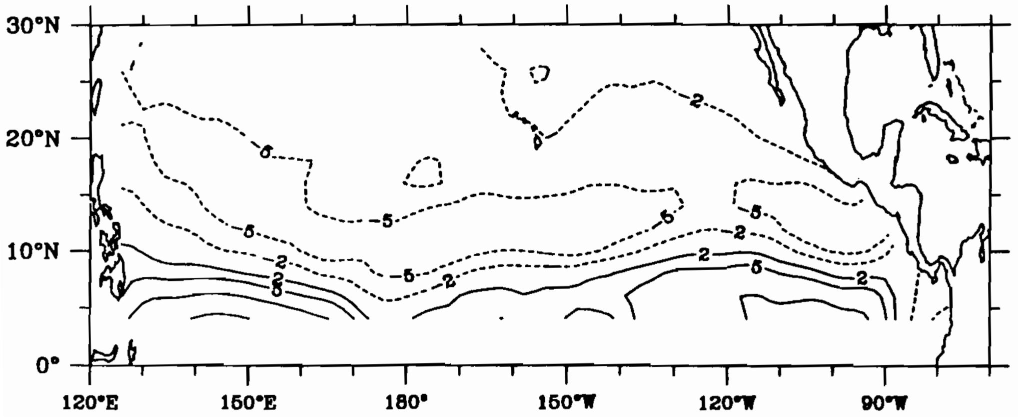

Figure 3.14k. As Figure 3.14a but for November.

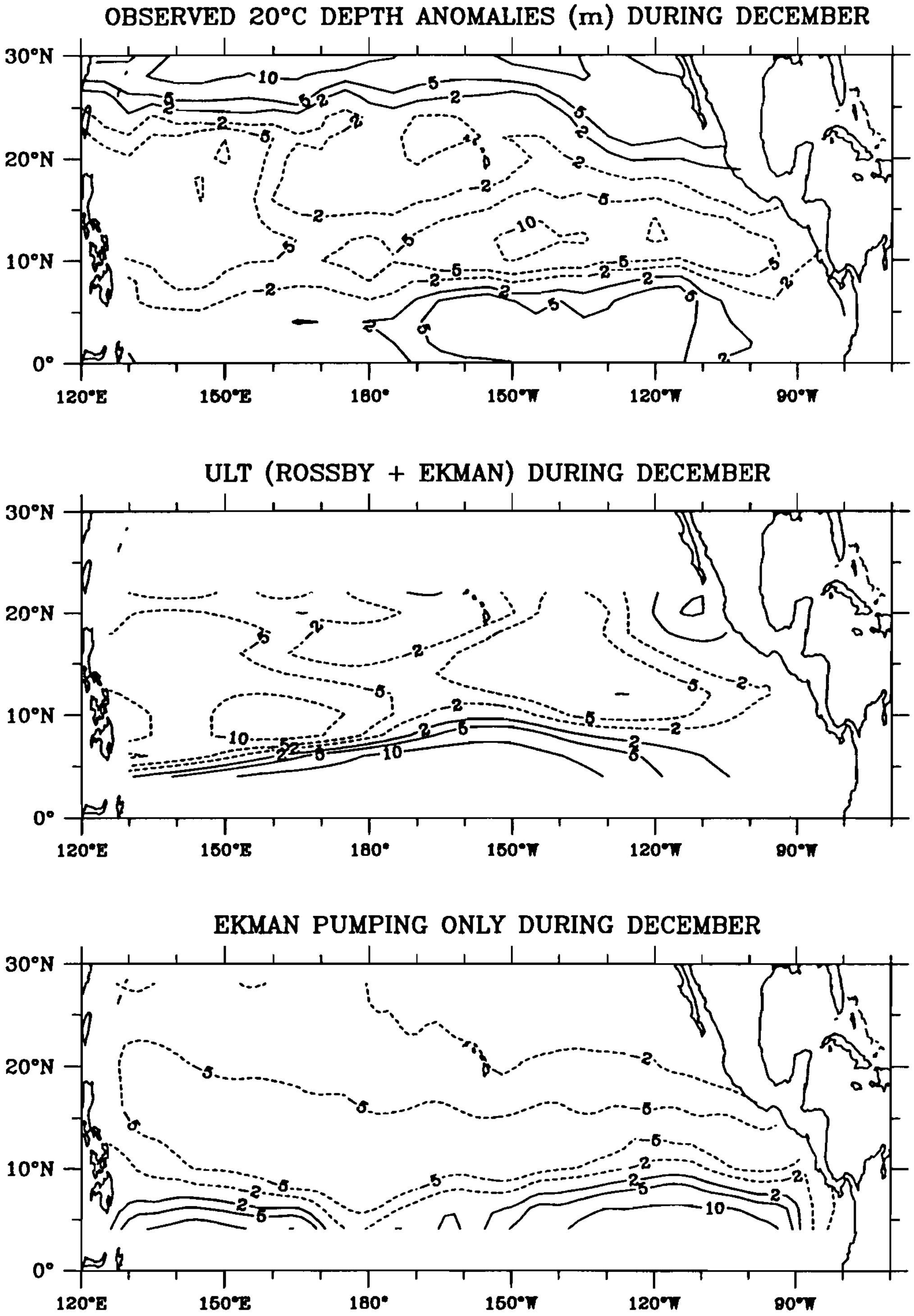

Figure 3.141. As Figure 3.14a but for December.

# 4. INTERANNUAL VARIABILITY OF 20°C DEPTH

## A. Introduction

Interannual variability was studied according to the same simple model as was annual variability, using the same vorticity equation (2.4). The reader is referred to Section 2.b for discussion of the model and its limitations. The primary issue addressed in this section is the role of long extra-equatorial Rossby waves in the evolution of the El Niño/Southern Oscillation. In general, two types of long Rossby waves are thought likely to be produced in the tropics during El Niños. First, upwelling long Rossby waves may be generated in mid-basin by the large-scale wind stress curl pattern associated with equatorial westerly wind anomalies. Secondly, downwelling waves may occur following an El Niño, initiated by reflection off the eastern boundary of deep equatorial pycnocline anomalies. Although both waves occur in the tropical, extra-equatorial region, both originate from events in the equatorial waveguide. Such wave-induced variability has been noted in many model experiments. McCreary (1983) and McCreary and Anderson (1984) developed a simple model of ocean-atmosphere interaction in which long Rossby waves were generated in the central tropical Pacific by idealized wind stress curl anomalies associated with changes of SST in the eastern equatorial Pacific. In this model, the travel time of these extra-equatorial waves set the oscillation period of El Niño events, and they played a crucial role in both triggering and turning off El Niños through reflection off the western boundary. Busalacchi *et al.* (1983) used a linear reduced-gravity model forced by observed winds and showed that in this model shoaling of the western Pacific pycnocline observed in the latter stages of El Niño was due to the arrival of long Rossby waves. These waves were generated by the off-equatorial wind stress curl pattern associated with strong westerly wind anomalies near the equator at the height of the event. The physics of the Busalacchi *et al.* (1983) model are similar to those expressed in the vorticity equation (2.4) for extra-equatorial regions, and one of the principal results of this section is that wave-induced fluctuations in the western Pacific similar to those seen in the model of Busalacchi *et al.* (1983) can be observed in 20°C depth. More recently, Graham and White (1988) suggested that a mechanism similar in some important respects to that proposed by McCreary (1983) could be verified as triggering several observed El Niños. Results presented in this section suggest problems with the Graham and White (1988) scenario.

## B. Interannual variability on the eastern boundary

As mentioned in Section 1, the NODC archives contain MBT data taken before 1970 which in a few regions of the Pacific is sufficient to construct long time series. One of these regions is along the shipping route between the U.S. West Coast and the Panama Canal, which hugs the coast of Mexico and Central America. A long time series of anomalous 20°C depth on the eastern boundary from 1954 through 1987 can be made by combining the early NODC MBT data with the later XBT data set. This time series shows El Niño events clearly as deep thermocline anomalies, which occurred in 1957, 1963, 1965, 1969, 1972, 1976, weakly in 1979, and in 1983 (Fig. 4.1). The large El Niños (in 1957, 1965, 1972, 1976 and 1983) had amplitudes of 10-15 m at the equator on the eastern boundary, and the anomalies generally extend north to about 22°-25°N (which, possibly coincidentally, is where the relatively smooth coast is broken by the Gulf of California). Thermocline deepening in these events typically lasted for 12-18 months (Fig. 4.1). Appendix 1 discusses in detail how an idealized ocean would respond to such pulse-like forcing along the eastern boundary by radiating Rossby waves offshore; however, as will be discussed later in this section, the signal of such offshore radiation is relatively weakly observed in 20°C depth and does not appear to be a major contributor to the subsequent evolution of El Niños.

On the compressed timescale of Fig. 4.1, it is not possible to estimate a phase lag which would indicate propagation along the coast. The lag correlation on the eastern boundary between all coastal latitudes and the equator is given in Fig. 4.2, which shows a clear poleward lag of about six months between the equator and 30°N; this translates to a phase speed of about 32 cm/s when the slope of the coast is taken into account. Chelton and Davis (1982), who studied monthly mean sea level between Acapulco (17°N) and Alaska during 1946 through 1974, estimated a phase speed for sea level anomalies of 40 cm/s. Enfield and Allen (1980), also studying monthly averaged sea level, but between Chile and Alaska, estimated that anomalies propagated poleward at a speed of about 87 cm/s. They showed that the a coastal sea level signal of El Niños in 1957, 1969 and 1972 was observed both north and south of the equator. No explanation is proposed for the slower apparent speed of thermocline anomaly propagation found here, although it is noted that the other two estimates are averages over very large latitudinal ranges.

Since the eastern boundary anomalies are probably initiated by events occurring west of the boundary on the equator, it would be desirable to use the BT data set to investigate this hypothesis. Unfortunately, unlike the northern tropical Pacific, along the equator 20°C depth was sampled principally along the three major ship tracks, leaving large gaps near 170°E and 130°W which make it difficult to convincingly draw direct evidence of zonal propagation (Fig. 1.5). In addition, it is impossible to bin the equatorial observations by time periods smaller than 2 months without heavy interpolation, and since a first baroclinic mode equatorial Kelvin wave would cross the entire basin in two to three months, the BT data set is in general a poor antenna for such variability (although specific examples may be found). Lag correlation of all points on the equator with the eastern boundary shows a well-correlated ($r > 0.6$) apparent eastward propagation of 20°C depth anomalies at a speed of 40 cm/s, with the eastern boundary lagging the west by about 15 months (Fig. 4.3). This is very likely a response to moving forcing, as is suggested by the time history of zonal wind stress on the equator (Fig. 4.4), which shows that the westerly anomalies associated with El Niños occur roughly a year or so earlier in the west than in the east. This occurred most clearly in 198283, but is also visible in 1965, 1972 and 1987.

## C. El Niño-related variability of the wind field

Although this paper does not focus on the wind field, it is appropriate to briefly discuss the type of wind fluctuations associated with El Niño which are important in generating extra-equatorial Rossby waves. The most prominent of these wind events is the occurrence of westerly anomalies in the equatorial waveguide at the height of El Niños, which leads to upwelling wind stress curl in the tropical regions. During several strong El Niños (in 1965, 1972, 1982 and 1986), major westerly wind anomalies (amplitude typically $3 \times 10^{-2}$ N $m^{-2}$, or roughly 4-5 m/s) occurred near the Dateline (Fig. 4.4). During the following year, easterly wind anomalies occurred in the same region with similar amplitude. The meridional pattern of these anomalies is shown by the third Empirical Orthogonal Function (EOF) of the zonal wind stress $\tau^x$ in the northern hemisphere, representing 12% of the total interannual variance in this region (Fig. 4.5). That this EOF is characteristic of El Niño variability is shown by the high correlation ($r = 0.75$) of the time amplitude function (bottom frame) with the time history of 20°C depth anomalies at the equator on the eastern boundary, which is a good index of El Niño events (Fig. 4.1, discussed in section 4.b above). The other EOF time amplitude functions have much lower correlations with this El Niño index ($r < 0.4$) and are not shown. The third EOF (Fig. 4.5) shows that the El Niño time history is associated with the westerly anomalies on the equator near the Dateline seen in Fig. 4.4, and that these anomalies are confined south of about 5°-6°N, with easterly anomalies centered near 15°N. This pattern of wind stress anomalies implies that strong upwelling curl characteristically occurs in the tropical region between 5° and 15°N near the Dateline at the height of El Niños, and is often followed by a return of equatorial easterlies and hence by downwelling curl in the same region one to two years later.

This sequence of events is seen in a detail of the wind stress curl field at 12°N and eastern equatorial thermocline depth during the El Niño of 1972 (Fig. 4.6). (12°N is approximately typical of latitudes between 5° and 15°N during this period.) 20°C depth at the South American coast peaked downward in May-June 1972, marking the height of the event. The wind stress curl field at 12°N indicates strong upwelling between about 170°W and 150°E slightly earlier than this, in March through July 1972. The following year, both fields had reversed sign, and the anomalies are smaller. The effect of the curl fluctuations is to force an upwelling Rossby wave in the tropics near the Dateline during the height of El Niño, then a downwelling wave a year or so later.

## D. Observed interannual 20°C depths and hindcasts from the simple model

Westward propagation of thermocline anomalies in the tropics is suggested by zonal lag correlations of anomalies at most extra-equatorial latitudes; Fig. 4.7 shows examples of such lag correlations at 10°N and 20°N. The apparent propagation speeds in these plots are about 25 cm/s at 10°N and about 12 cm/s at 20°N. However, although suggestive, this calculation makes no distinction between wave propagation and possible moving local forcing; to examine the dynamical processes a model is needed.

As was done in Section 3.e, the long Rossby speed $c_r = \beta c^2/f^2$ was treated as an unknown in the simple vorticity equation (2.4), and studied by solving (2.4) at each latitude using the interannual FSU winds, trying all values of $c_r$ from 1 cm/s to 1 m/s, then correlating each solution h(x,t) with the observed interannual variations of 20°C depth. Significant peaks of correlation were found at latitudes from 8°N through 22°N, and are shown in Fig. 4.8, with a summary of the results in Fig. 3.12. This meridional profile of best-fit long Rossby speeds falls roughly on the line $c_r = \beta c^2/f^2$, if the long gravity wave speed c is chosen to be 2.6 m/s, which is the overall northern tropical Pacific average c (Section 3.e; Fig. 3.12). An ad hoc estimate of the uncertainty of the fits of $c_r$ was made by finding the range of $c_r$ at each latitude such that the correlation of the solution h(x,t) with observed 20°C depth was within 10% of the best correlation (see Fig. 4.8 for an example); these uncertainties are shown as the "error bars" about the best-fit meridional profile in Fig. 3.12. The uncertainties ranged from about ±3 cm/s at 22°N to about ±20-30 cm/s at 8°N, and were typically about ±10 cm/s in the region 10° to 18°N (Fig. 3.12). The interannual best-fit long Rossby speeds were generally smaller than the annual speeds in the NEC region, but within the estimated uncertainty, except at 22°N. Despite the fact that clear evidence of an annual Rossby wave was found at 4° and 6°N, no interannual propagation could be detected at these latitudes.

Correlation of the long Rossby wave model with observed interannual 20°C depths was high in the west, with values above 0.7 west of the Dateline between 8° and 16°N, and also high east of the Dateline at 16° to 22°N (Fig. 4.9, top). If we take the interannual autodecorrelation timescale to be roughly four years (as suggested by the lag correlations in Fig. 4.7), then with bimonthly data there are about 24 degrees of freedom, and a correlation of 0.4 is significant at the 95% level. Since the simple model takes the observed 20°C depths at the American coast as a boundary condition, the correlations are exactly 1 at the coast; the fact that correlations fall off rapidly offshore south of about 14°N suggests that offshore radiation of boundary anomalies (which dominates the model variability in the region east of about 150°W) is probably not a major contributor to the variability in mid-basin in the deep tropics. Near 140°-150°W equatorward of about 12°N is a region of near-zero correlations. There is no obvious explanation for the poor model results in this area, which could be due to errors in the wind, aliasing or errors in the BT data (this is a relatively data-sparse area), or more complicated physical mechanisms at work than are expressed in the simple model (2.4). In most other areas of the northern tropical Pacific, however, the simple model hindcasts are considerably more closely correlated with observed conditions than hindcasts made assumed Ekman pumping alone (Fig. 4.9, bottom). Over much of the central basin, the Ekman pumping hindcast is essentially uncorrelated with the data; only in small regions in the far west and near Hawaii does the Ekman pumping hindcast appear significantly correlated with the observations, and even in these regions the correlation is less than the simple model including long Rossby waves. In the region near 140°-150°W where the simple model hindcast is poorly correlated with the observations, the Ekman pumping hindcast is also uncorrelated. The poor interannual correlation with Ekman pumping contrasts with the results found in Section 3.e for the annual cycle, in which at 10°-12°N Ekman pumping was found to be the dominant process at the annual period.

As was done in Section 3.e, solutions of the vorticity equation (2.4) (referred to again as the upper layer thickness anomaly, or ULT), using the best-fit speeds $c_r$ shown in Fig. 3.12, are compared with observations and with pycnocline anomalies hindcast by Ekman pumping alone (the solution to (3.2)) in time-longitude plots, Figs. 4.10a-h, for the period 1970 through 1975 (chosen because the sampling was denser during that time, and because it spans the strong El Niño of 1972). As described in Section 1, section d, the observations shown in the top panels of Fig. 4.10 are gridded by 5° longitude, 2° latitude and bimonthly, thus each plot (1970-75) represents 34 gridpoints in longitude and 36 in time. Laplacian interpolation was used to fill holes one gridbox in longitude or time from existing data; blank areas in the plots show the unsampled regions. The six-year period from 1970 through 1975 contains roughly half the total number of observations of the full eighteen years 1970-87; on average an observation was made every 23 days in each 5° longitude by 2° latitude gridbox during this period (versus 35 days for 1970-87).

Gross inspection of Figs. 4.10 shows that for interannual frequencies, Ekman pumping alone (bottom panels) hindcasts unrealistically large amplitudes of variability within about 15° of the equator. This contrasts with the results reported in Section 3.e for the average annual cycle where the amplitude of the Ekman pumping solution was found to be the same as that for the total ULT solution to (2.4) including Rossby waves (Figs. 3.13). The difference is due to the fact that at the annual period there are at most six continuous months of one sign of pumping, while interannual wind stress curl variations frequently persist for several years, so the (integrated in time) interannual Ekman pumping solution can get very large. If the dynamics includes Rossby waves, however, these anomalies radiate away before building up large amplitudes, thus the ULT (middle panels) has only slightly larger amplitude than the observations. To reduce the number of figures, the wind stress curl is not shown; connoisseurs may note that $\mathrm{Curl}(\tau/\rho f)$ is both the derivative in time of Ekman pumping and the derivative along the characteristics (wave rays) of the solution to (2.4). These rays have the slope obvious in Figs. 4.10 (middle), so the wind stress curl field can be visualized by noting the regions where the fluctuations change magnitude along the rays.

Many overall aspects of the forcing were similar over much of the northern tropical Pacific during the 1972 El Niño. Upwelling wind stress curl was generated to at least 16°N in mid-basin by equatorial westerly wind stress anomalies during the peak of the event. Along the eastern boundary, 5 to 15 m shallow thermocline anomalies were observed in 1970 and 1971 leading up to the event (Fig. 4.1); these also occurred preceding several other El Niños and may be a characteristic feature. This boundary signal radiates across the basin in the ULT, with the wind stress curl adding to the amplitude of the shoaling in mid-basin. However, as shown below in discussing the variability at specific latitudes, this boundary-induced shoaling is usually secondary in its effects on the mid-basin thermocline to that associated with the wind. In the next phase of the event, the deep equatorial pycnocline anomaly which is the primary signal of El Niño spread up the American coast in late 1972 (Fig. 4.1), with an amplitude of about 10 m; the ULT solution shows this radiating offshore. However, similarly to the shallow anomalies preceding the event, the boundary signal is in most cases a relatively small part of the thermocline deepening in the west observed in late 1973, most of which was due to downwelling wind stress curl as the equatorial easterlies returned in force. In general, the simple model brings out the fact that although the observations frequently appear as if a boundary reflection is propagating freely across the entire basin, this can be due to a coincidental occurrence of mid-basin curl-generated anomalies. It may be that the coincidence of timing has a deeper significance associated with the quasi-periodic nature of El Niño (which cannot now be determined), however the fact remains that at most locations in the western Pacific most of the amplitude of long Rossby waves generated by El Niños is produced in mid-basin by the wind stress curl. An exception is the region north of 15°N, where particular boundary forcing events can be traced for several years across much of the basin and account a for significant fraction of the variability.

At 8°N (Fig. 4.10a), the observations (top) show that in the two years leading up to the El Niño the thermocline was deep west of 150°W and shallow in the east. The ULT (middle) has a roughly similar pattern; the deep anomalies in the west were forced in the model by wind stress curl in the final stage of the 1969 El Niño, while the shallow pycnocline in the east has emanated from the boundary. Note that the Ekman pumping solution (bottom) hindcasts anomalies of the opposite sign from those observed near 120°W during this period, indicating that boundary radiation probably accounted for the observed shoaling. During the height of El Niño in 1972, the observed thermocline was anomalously shallow everywhere west of 90°W, while deep anomalies appeared in the east as the equatorial deepening arrived at the American coast. The simple model (middle) portrays the wide shoaling as due to upwelling curl between 120°W and 160°E during mid-1972, arriving at the western boundary at the end of the year. In 1973, the observed thermocline was anomalously deep across the basin; the ULT shows a similar pattern (though of much stronger amplitude), which is partly due to radiation of deep anomalies from the boundary, but most of the amplitude is generated in mid-basin. This is consistent with the observations. In general, the Ekman pumping solution at 8°N (bottom) has very high amplitudes as noted above; it is almost uncorrelated with the observations ($r < 0.4$ everywhere).

At 10°N, 12° and 14°N (Figs. 4.10b, c and d), the observed 20°C depth fluctuations (top) during the El Niño are similar to those seen at 8°N, except that both the shoaling in the west at the height of the event and the subsequent deepening following the event occurred several months later than at 8°N, which is consistent with the hypothesis that both were forced in mid-basin in mid-1972 and propagated west as long Rossby waves, with speeds about half as great as those near 8°N. At 10°, 12° and 14°N, the ULT (middle) appears to show the shoaling event of 1972 as a continuous upwelling emanating from the eastern boundary and propagating across the basin. However, this boundary signal was reduced by about half east of 150°W before amplifying in mid-basin due to the wind (to a much larger size than the original boundary fluctuation), so the western Pacific anomalies cannot be attributed primarily to the boundary reflection. Following the peak of El Niño, as at 8°N, deep anomalies on the eastern boundary were observed in late 1972 and then appeared to propagate westward and are observed at the end of 1973 in the west. The ULT makes clear that these are separate events, since the speed of free propagation means that waves emanating from the American coast in late 1972 do not arrive in the west until late 1974; in fact the deep anomalies in the west were forced near the Dateline in mid-1973. This is particularly clearly seen at 12°N (Fig. 4.10c, middle), which is quite similar to the observed thermocline fluctuations, and not consistent with a pure boundary reflection and free wave propagation. As at 8°N, there is little correlation between the Ekman pumping solution (bottom) and the observations (top); also, Ekman pumping again hindcasts amplitudes about twice as large as those observed.

The subtropical region from 16° through 22°N (Figs. 4.10e through h) has a somewhat different character in that the boundary reflection of the deep pycnocline anomalies along the American continent appears to be a major component of the observed variability in the period after the 1972 El Niño, while wind stress curl-forced variations played a lesser role. At all of these latitudes, the thermocline was observed to be anomalously shallow during most of 1970 through 1975 compared to the 1970 through 1987 longterm mean (note the preponderance of dashed contours in Figs. 4.10e-h), and the shoaling during the height of El Niño in 1972 does not stand out as clearly as it does at the lower tropical latitudes discussed above. However, the twin boundary signal of a shallow anomaly during 1971-early 1972 followed by a deepening at the end of 1972 can be observed propagating as a long Rossby wave across the entire basin in subsequent years. This is particularly clearly seen at 20°N (Fig. 4.10g), in which both the observations (top) and ULT (middle) display the twin anomalies, with amplitudes of 5-10 m, maintained their original structure for at least three years, arriving at the western boundary in

1975 and 1976 respectively. These fluctuations are completely unlike those hindcast by Ekman pumping (bottom).

The planetary wave character of this boundary reflection is shown by the meridional gradient of propagation speed, so that the anomaly arrived in the west much earlier at low latitudes. Figure 4.11 shows maps of observed 20°C depth anomalies at six-month intervals from January 1973 (which was a few months after the peak of the deep El Niño signal on the eastern boundary) to July 1976. A heavy line overlaid on these maps shows the position the anomaly would have if it left the boundary at the exact time of the coastal maximum (i.e. slightly earlier at low latitudes (see Fig. 4.1)) and propagated at a speed $c_r = \beta c^2/f^2$, with the long gravity wave speed c chosen to be 3 m/s. In January 1973 (first panel), deep anomalies were concentrated along the coast. In July 1973 and January 1974, description in the eastern Pacific is hampered by data gaps (note blank regions on the maps), but note that at low latitudes (south of about 14°N) a deep anomaly formed near the Dateline and moved west to the Philippines coast, well ahead of the hindcast boundary reflection. This deep anomaly was due to downwelling wind stress curl as equatorial easterlies returned strongly after the El Niño, and is seen as separate from the boundary reflection in the time-longitude plot at 12°N (Fig. 4.10c). In July 1974 (Fig. 4.11, fourth panel), the deep anomaly radiating off the coast is seen just arriving at Hawaii. In subsequent six-month intervals, the deep thermocline passed Hawaii and was moving faster nearer the equator, so the center at 16°N arrived at the western boundary by the end of 1976, while at 22°N it was near the Dateline. In front of the deep anomaly, the downwelling thermocline emanating from the shallow boundary event of 1971 is visible north of about 18°N. This sequence of events indicates that while south of about 15°N thermocline fluctuations were dominated by strong wind stress curl changes associated with El Niño, in the subtropical region where the curl forcing was weaker the large boundary event spawned a wave which stood out above locally forced variations.

The above discussion, showing that long extra-equatorial Rossby waves of significant amplitude arrive at the western boundary, raises the question of whether reflection of these waves from the boundary as equatorial Kelvin waves could be a contributor to the subsequent evolution of El Niño. As noted in the introduction to this section, such reflection has been suggested as a mechanism for triggering or turning off El Niño. In a recent paper, Graham and White (1988) proposed that downwelling long Rossby waves generated by wind stress curl anomalies near 12°N in mid-basin are reflected from the western boundary as downwelling equatorial Kelvin waves and act as triggers for El Niño. Aside from the question of how efficient such a reflection could be given the highly irregular nature of the Philippines and Indonesian coastline, which is beyond the scope of this work, the data available here can be used to examine the lag relationship between off-equatorial Rossby pulses arriving at the western boundary and the subsequent occurrence of El Niños. To make this comparison long time series are desirable. In section 4.b a long time series of 20°C depth anomalies along the eastern boundary is shown to be a good index of El Niños (Fig. 4.1); this time series will be summarized by the history at the equator along the eastern boundary. Along the western boundary it is not possible to construct a similarly long time series at most locations, however one location where data exist back to the 1950's is at 13°N, 125°E, which is where shipping headed for Manila from the east enters the Philippines Archipelago (San Bernardino Strait) (see Fig. 1.1). This location is almost exactly where Graham and White (1988) have proposed that the long Rossby waves in their scenario would arrive at the western boundary, and since the Rossby events large enough to trigger El Niño should have a relatively broad meridional extent, this time series is thought to be representative of extra-equatorial large-scale western boundary variability. The two time series (now referred to as the eastern boundary, equator and the western boundary, 13°N) are overlaid in Fig. 4.12, during 1956 through 1986, which includes eight El Niños (an El Niño is indicated by a deepening of the eastern boundary thermocline). Inspection of these time series shows that each El Niño is in fact preceded by a deep event in the west. However, there is not a consistent lag relation between the western and eastern deepening as would be expected if the connection between the two was an (nearly linear) oceanic wave process; the observed lag ranges from about three months to about fifteen months. Secondly, there were many more western boundary events than subsequent El Niños; during the thirty-one years shown in Fig. 4.12 there were thirteen major western boundary downwellings but only eight El Niños. Given the inconsistency of the lags observed, it would be possible to find western boundary downwelling to precede almost any sequence of events. Thirdly, there is no relation between the magnitude of the western deepening and that of the subsequent eastern event; for example a relatively large event in the west in 1978 was followed by a very weak El Niño in 1979, while a much weaker western downwelling in 1971 was followed by the strong El Niño of 1972. Lag correlation between the two time series (Fig. 4.13) shows only a very weak anticipation of eastern events by those in the west, with correlations just above 0.2 for the west leading by one to one and one-half years, and about 0.3 for the west leading by two and one-half years (which seems much too long for a triggering mechanism). The only significant peak of correlation ($r = -0.5$) between the two time series occurs with the east leading the west by six months, with opposite sign (Fig. 4.13). This represents the mechanism discussed in the main part of this section, in which upwelling long Rossby waves are generated in mid-basin near the height of El Niños (just slightly later than when the eastern boundary thermocline peaks downward), so that their arrival at the western boundary lags the eastern downward peak by about half a year. Such fluctuations can be seen in the two time series (Fig. 4.12), for example in the 1972 El Niño, where the eastern boundary downward peak occurs in late 1972, while the western boundary shoaling peak at 13°N arrives in early 1973. In sum, while the observations presented here are inadequate to examine the reflection process in detail, the long time series suggest that the Graham and White (1988) scenario is unconvincing in its assertion that extra-equatorial long Rossby waves are the trigger for El Niños. A more justifiable conclusion from the long time series is the more modest one that it is unlikely that an El Niño would occur at a time when the western tropical thermocline is anomalously shallow.

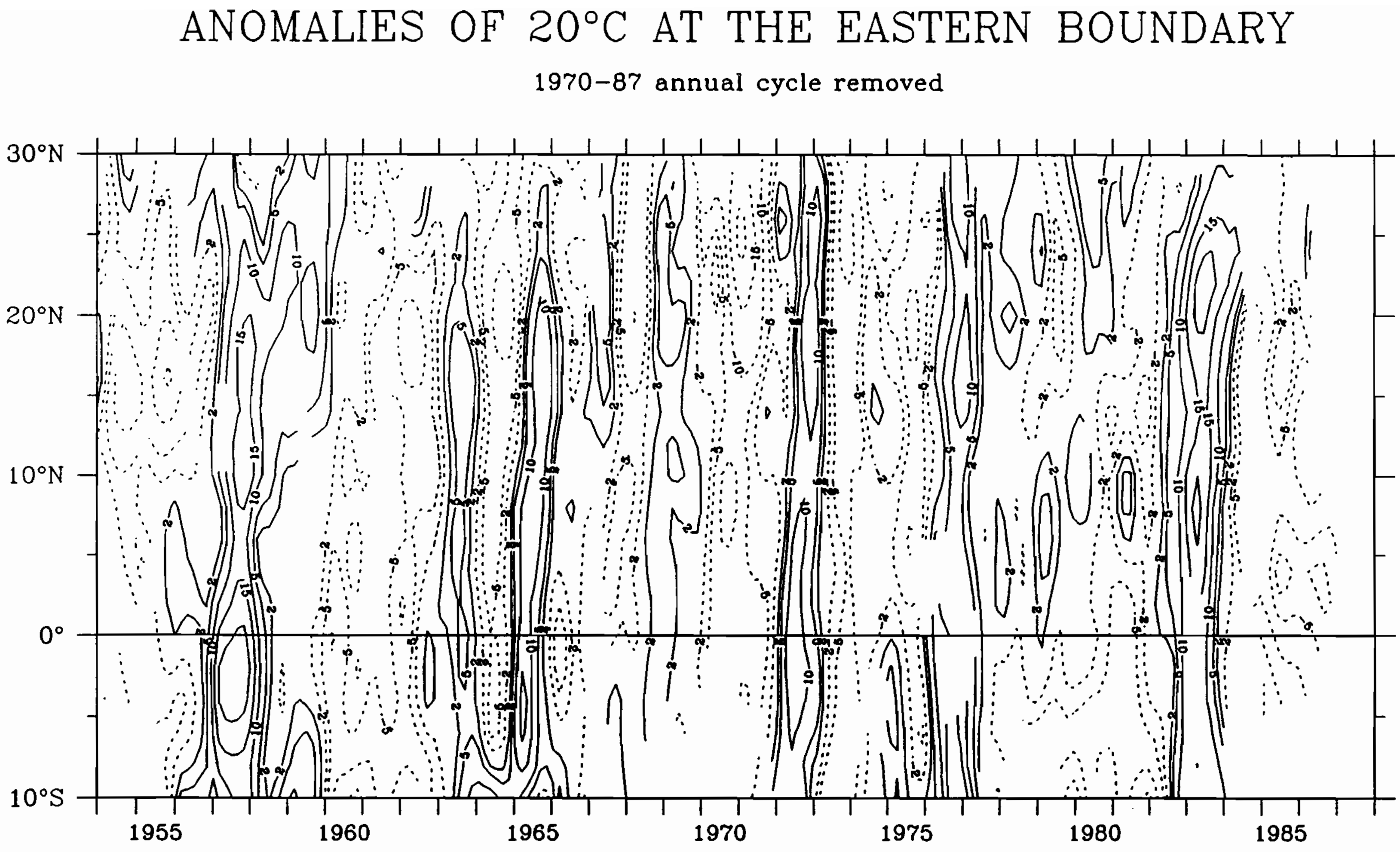

Figure 4.1. Interannual anomalies of 20°C depth (m) along the American coast. Contours are given at ±2, 5, 10, 15 and 20 m, with positive (deep) anomalies solid, negative (shallow) anomalies dashed.

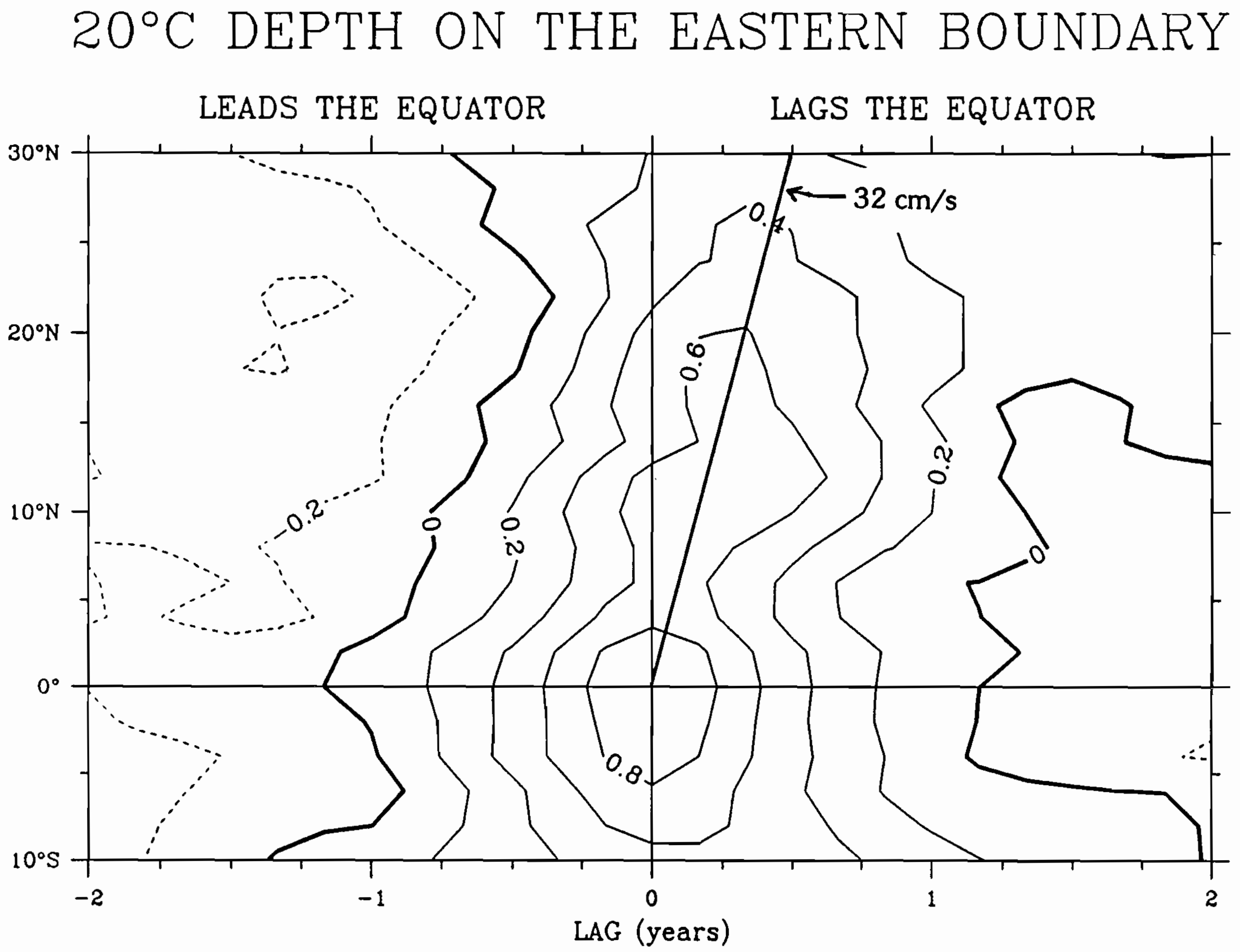

Figure 4.2. Lag correlation along the American coast between the depth of 20°C at the equator and at all points north and south along the boundary. The heavy line along the axis of high positive correlation represents a speed of 32 cm/s.

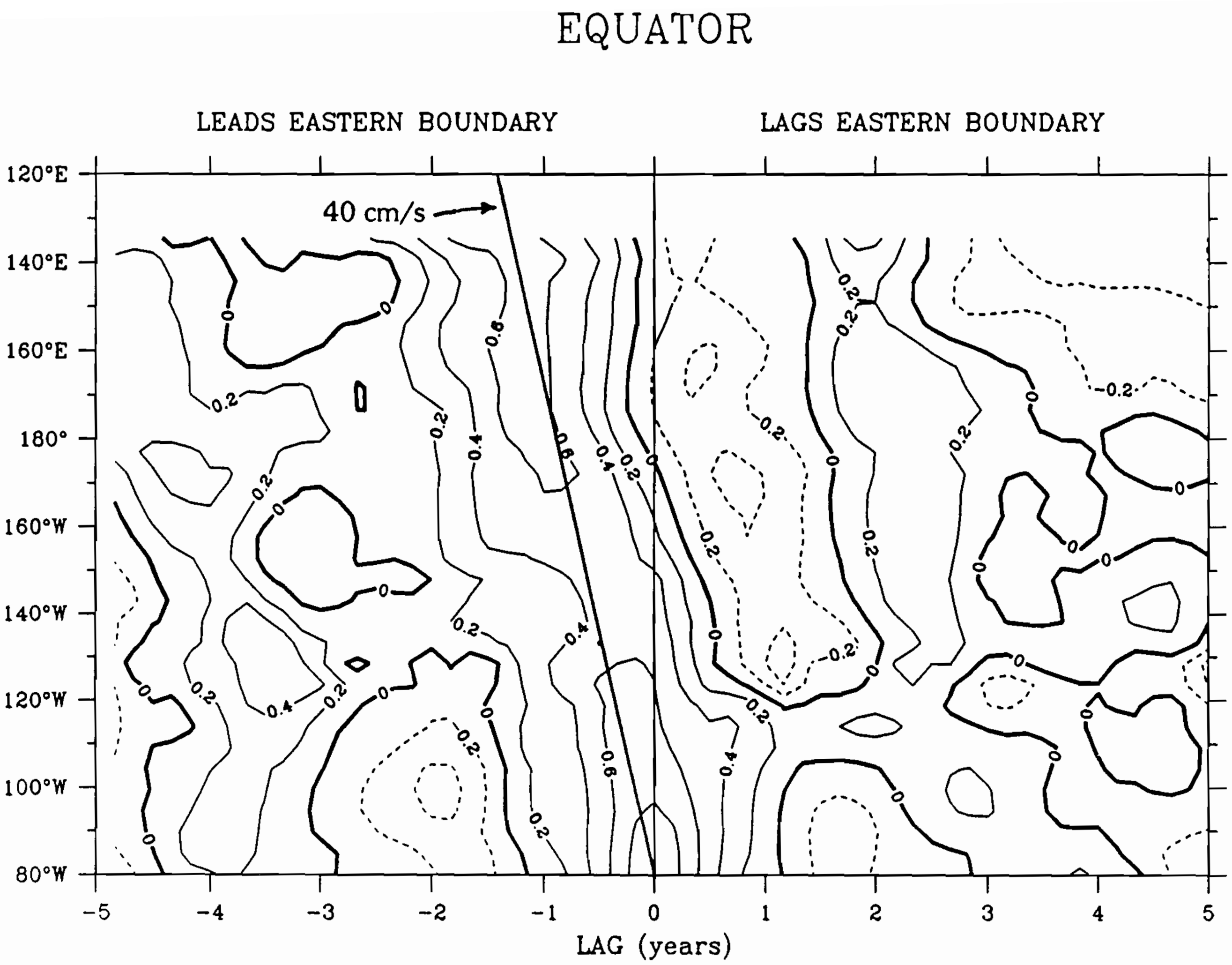

Figure 4.3. Lag correlation along the equator between the depth of 20°C at the eastern boundary and at all points west. The heavy line along the axis of high positive correlation represents a phase speed of 40 cm/s.

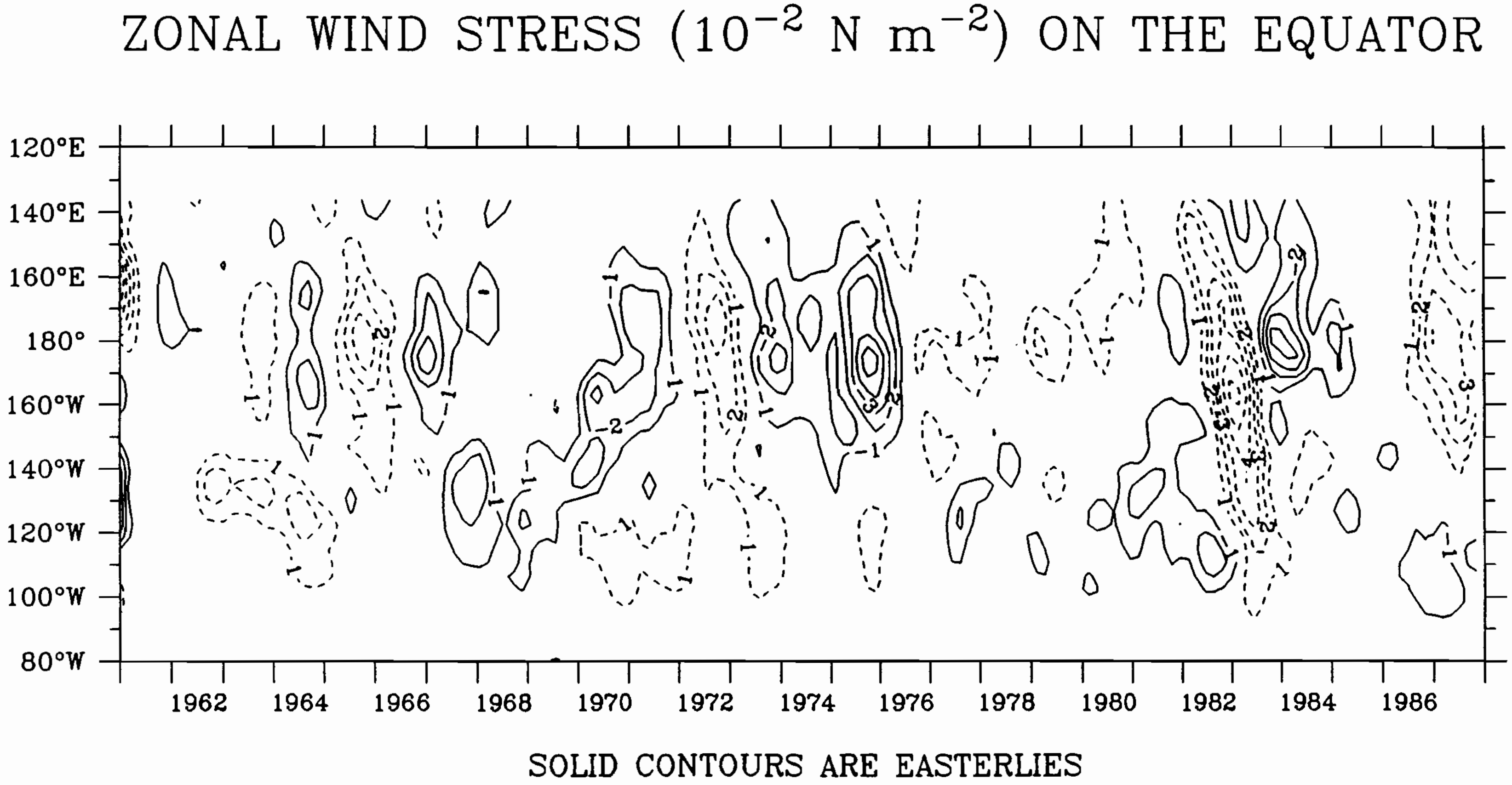

Figure 4.4. Anomalies from the average annual cycle of zonal wind stress ($10^{-2}$ N $m^{-2}$) on the equator. Contours are given every $10^{-2}$ N $m^{-2}$, with positive (eastward) anomalies dashed and negative (westward) anomalies solid lines.

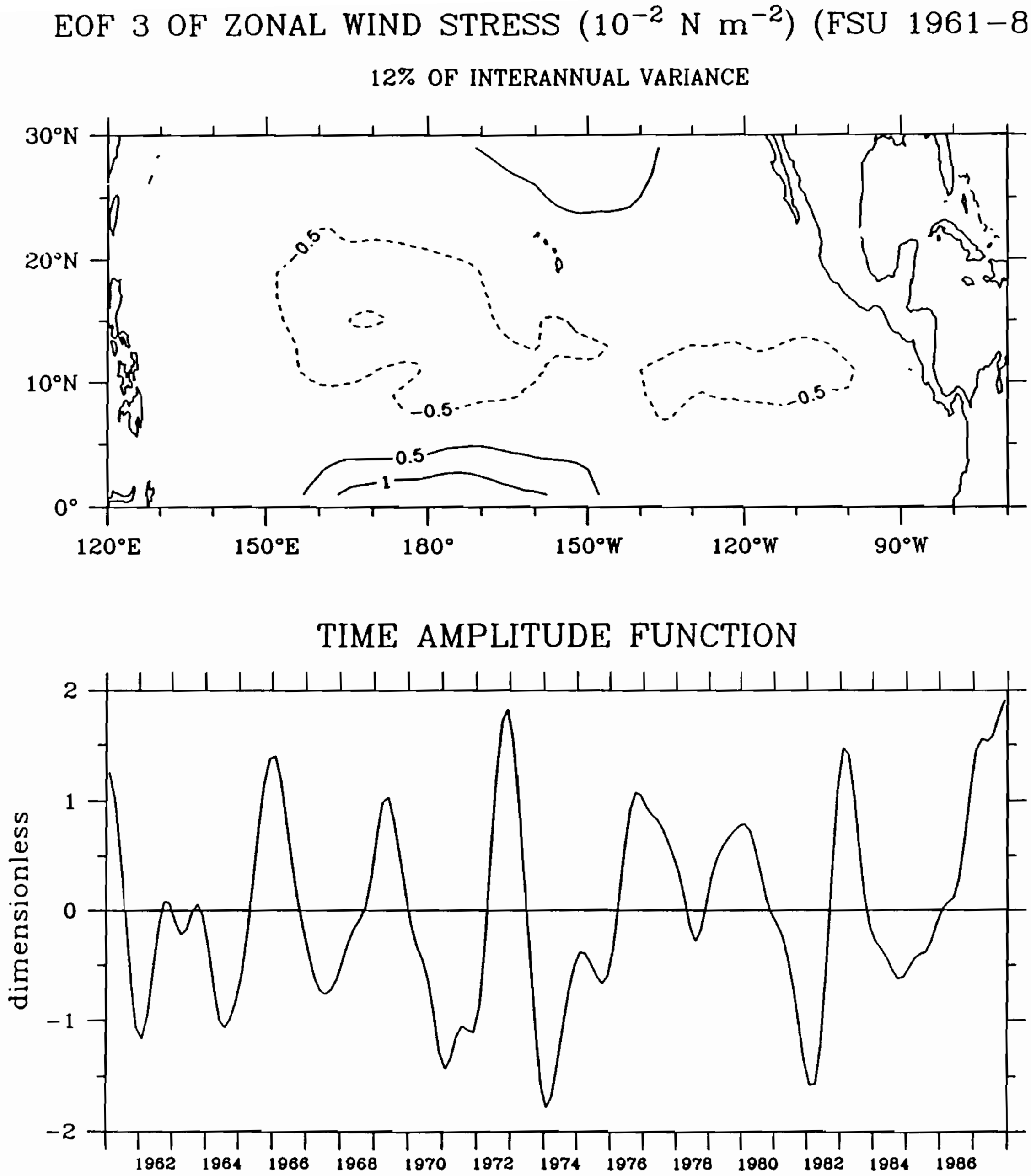

Figure 4.5. Third empirical orthogonal function of zonal wind stress (1961-87), representing 12% of the total interannual variance in the northern tropical Pacific. The top panel is the eigenvector, in units of $10^{-2}$ N $m^{-2}$, while the bottom panel is the (dimensionless) time amplitude function. A positive product between the eigenvector and time amplitude function represents an eastward stress anomaly.

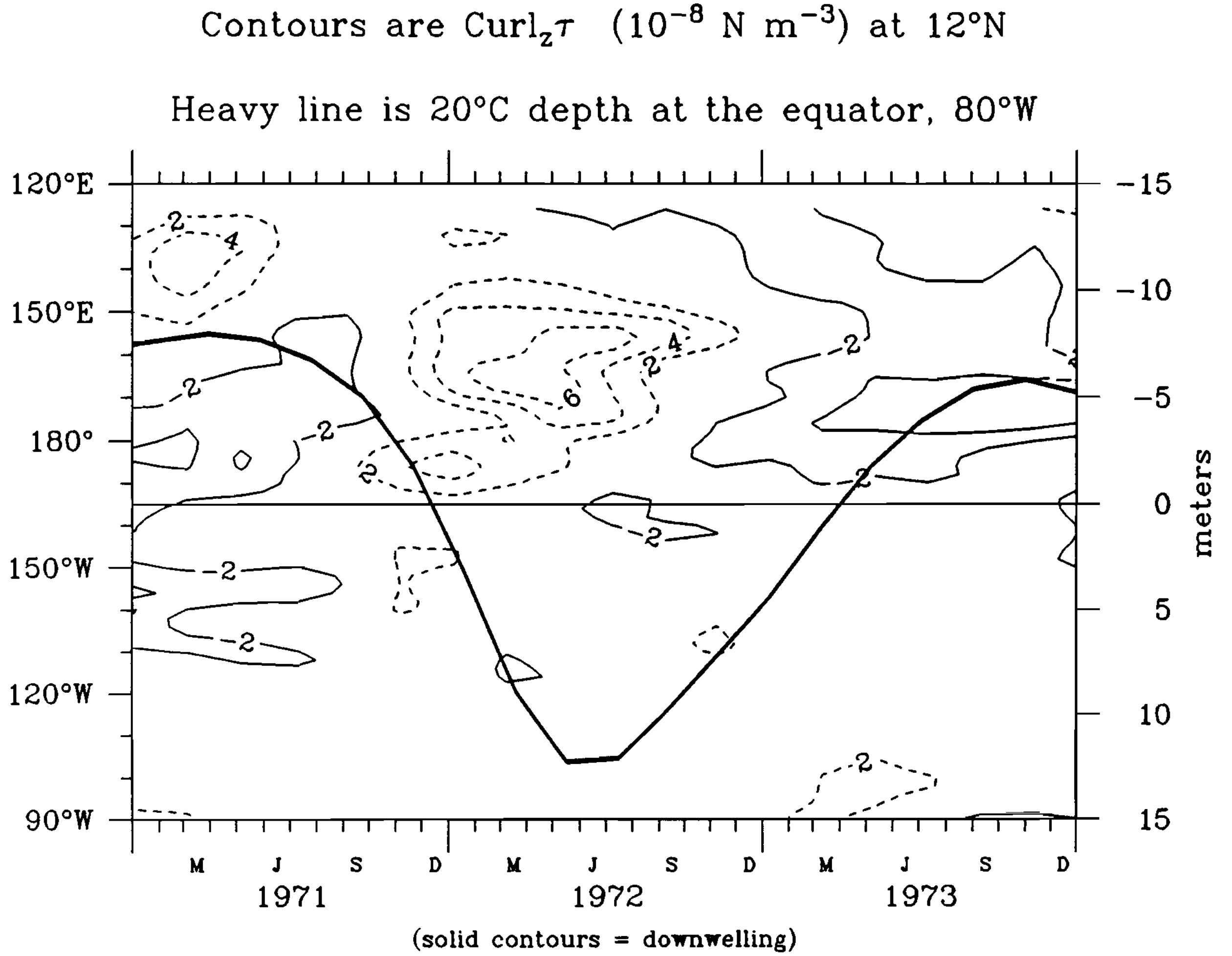

Figure 4.6. Contours of the curl of the wind stress $(10^{-8}$ N m$^{-3})$ along 12°N (longitude scale on left axis) during 1971 through 1973. Dashed contours are positive curl (Ekman upwelling); solid contours are negative curl (Ekman downwelling). The heavy overlaid line is the time history of 20°C depth (m) on the equator at the eastern boundary, which is used as an index of the peak of El Niño of 1972. The scale for 20°C depths is on the right axis, with negative (shallow) 20°C depths shown upwards and positive (deep) anomalies shown downward.

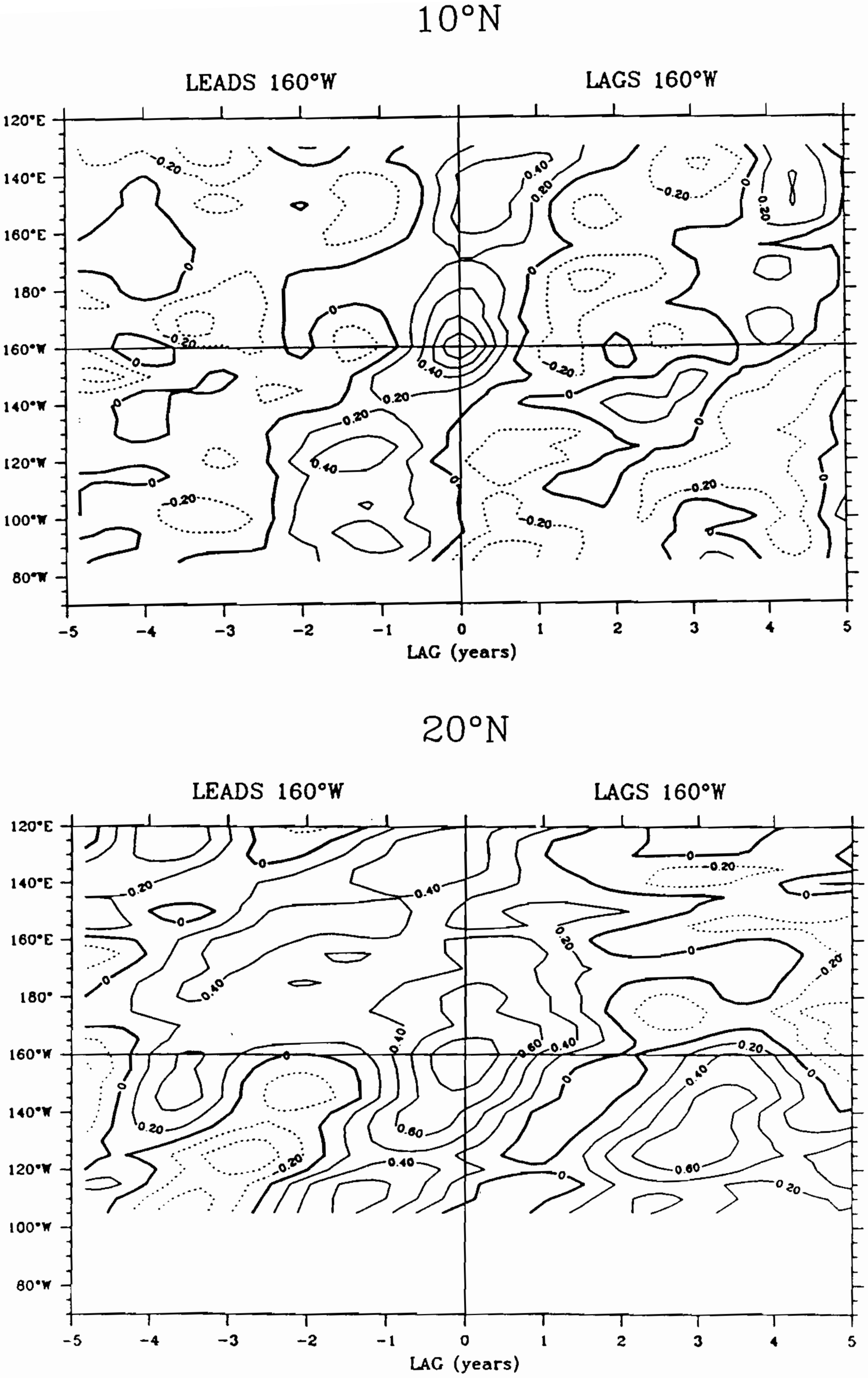

Figure 4.7. Lag correlation of 20°C depth at all longitudes with that at 160°W during 1970 through 1987. Top panel: 10°N. Bottom panel: 20°N.

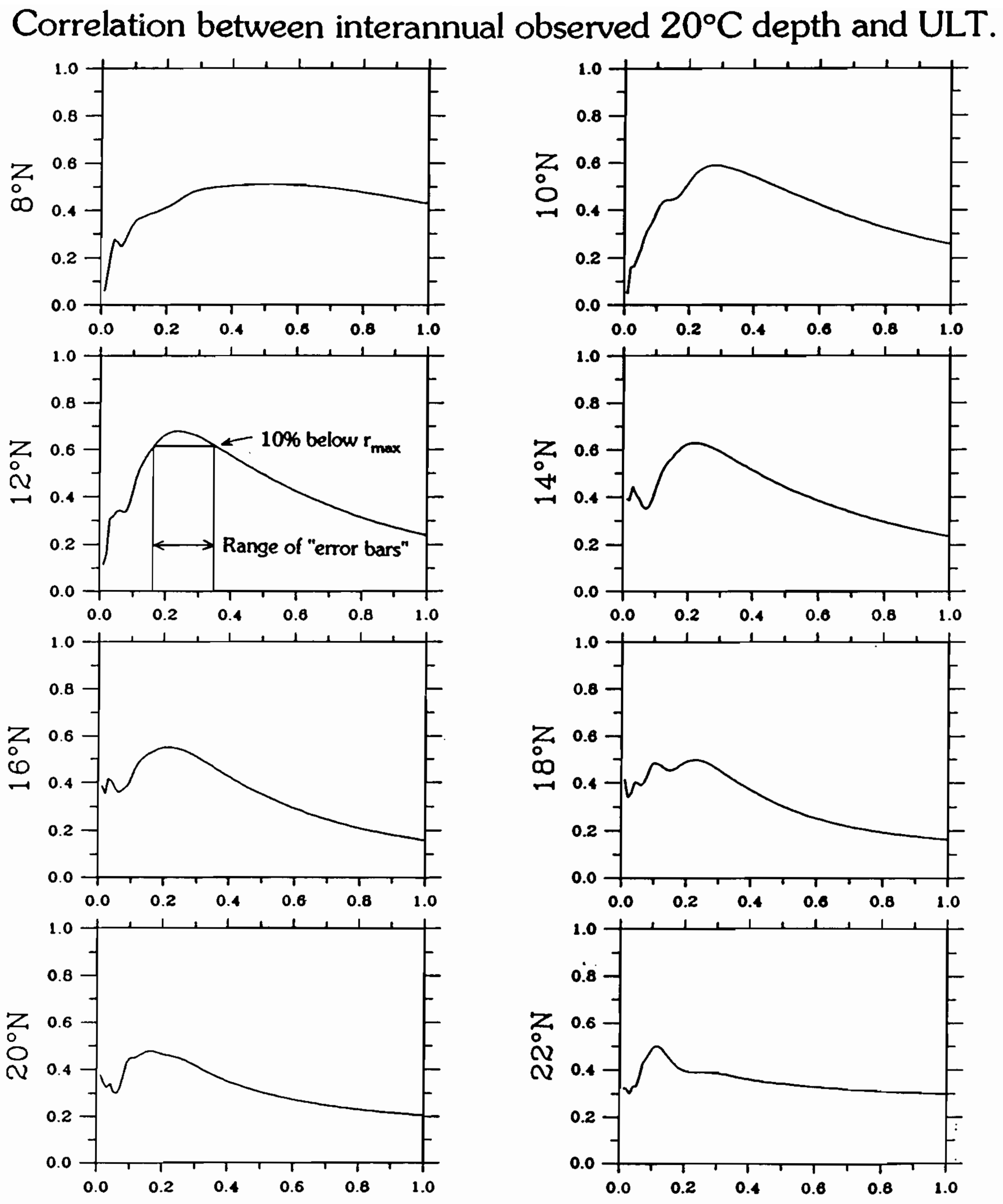
Correlation between interannual observed 20°C depth and ULT.

Figure 4.8. Correlation between observed interannual 20°C depths and upper layer thickness (ULT) hindcasts made using the vorticity equation (2.4), as a function of phase speed $c_r$ (on the bottom axes in m/s). The best-fit phase speed was chosen as the highest correlation at each latitude. At 12°N, an example is given of the estimation of the uncertainty of the fitting (these are shown as the "error bars" in Figure 3.12), which was computed by finding the range of speeds such that the correlation was within 10% of the highest correlation.

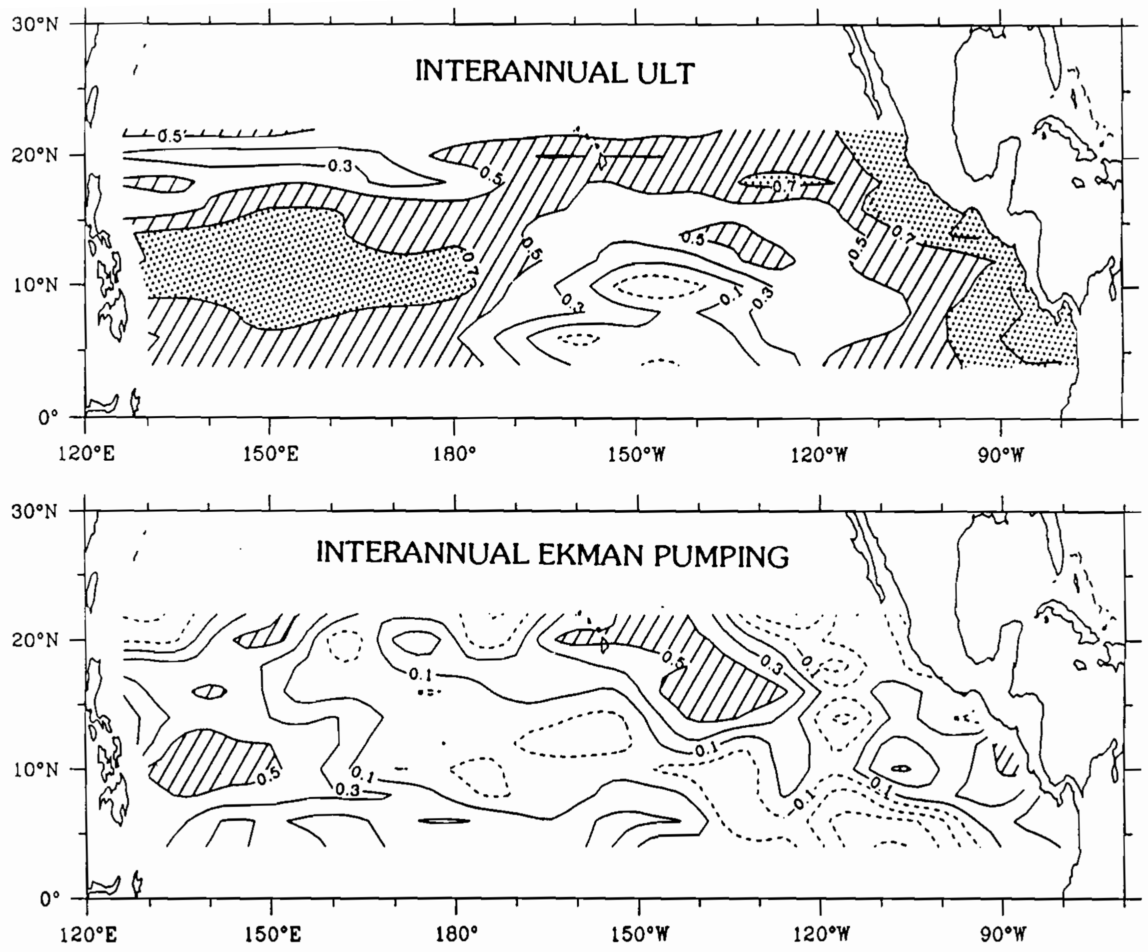

Figure 4.9. Top: correlation of observed interannual 20°C depth anomalies with the ULT hindcast made using the vorticity equation (2.4). Bottom: correlation of observed interannual 20°C depth anomalies with the hindcast made assuming Ekman pumping acting alone. In both, positive correlations are shown as solid contours, negative correlations as dashed contours. Dot shading is used to indicate correlations greater than 0.7, and hatching is used to indicate correlations greater than 0.5.

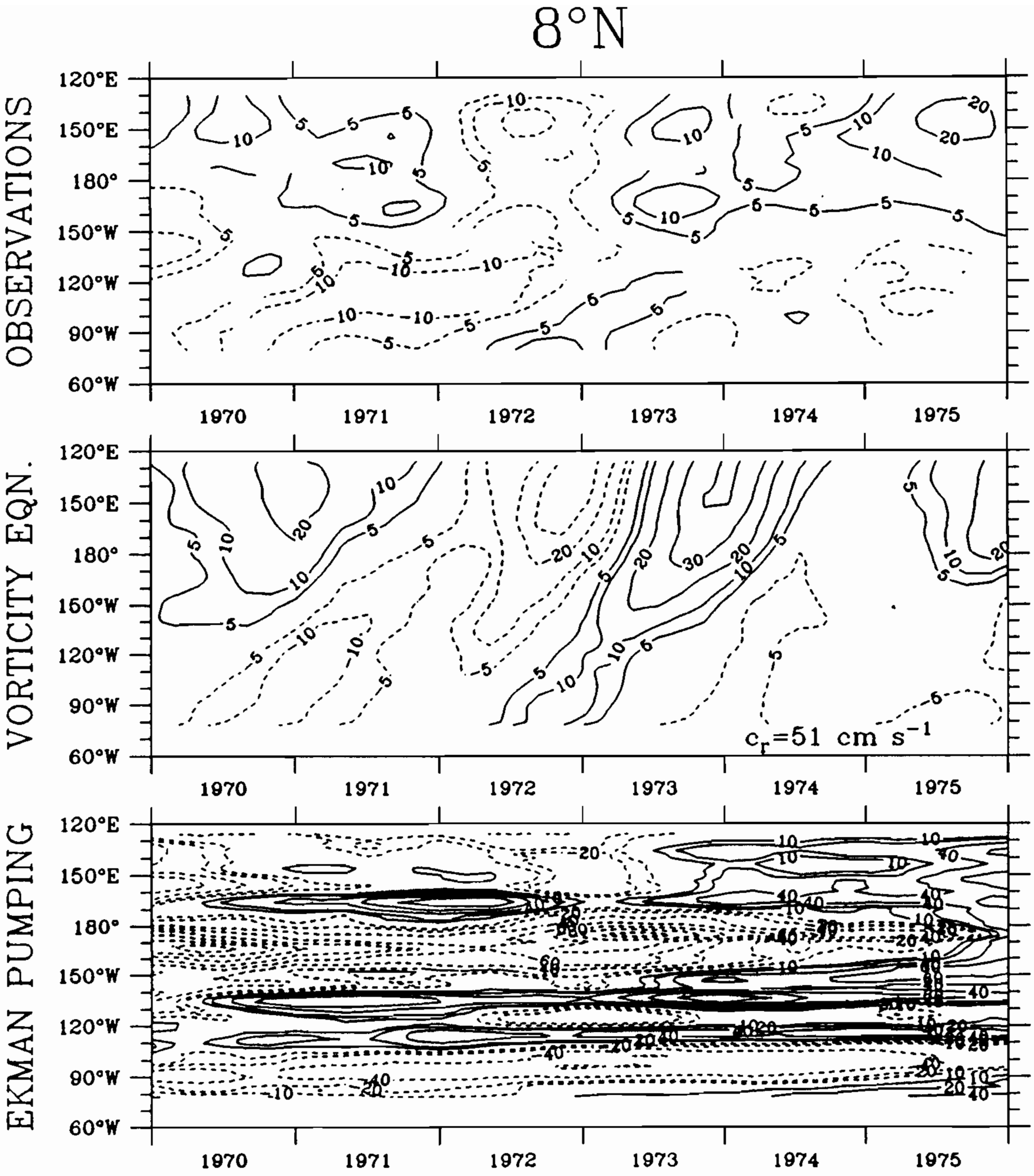

Figure 4.10a. Top: interannual anomalies of 20°C depth (m) at 8°N. Solid contours indicate deep anomalies, dashed contours shallow anomalies. Middle: hindcast of interannual upper layer thickness (ULT) anomalies (m) made using the vorticity equation (2.4) with best-fit speeds $c_r$ shown in lower right. Bottom: Hindcast of interannual pycnocline depth anomalies (m) made assuming Ekman pumping alone.

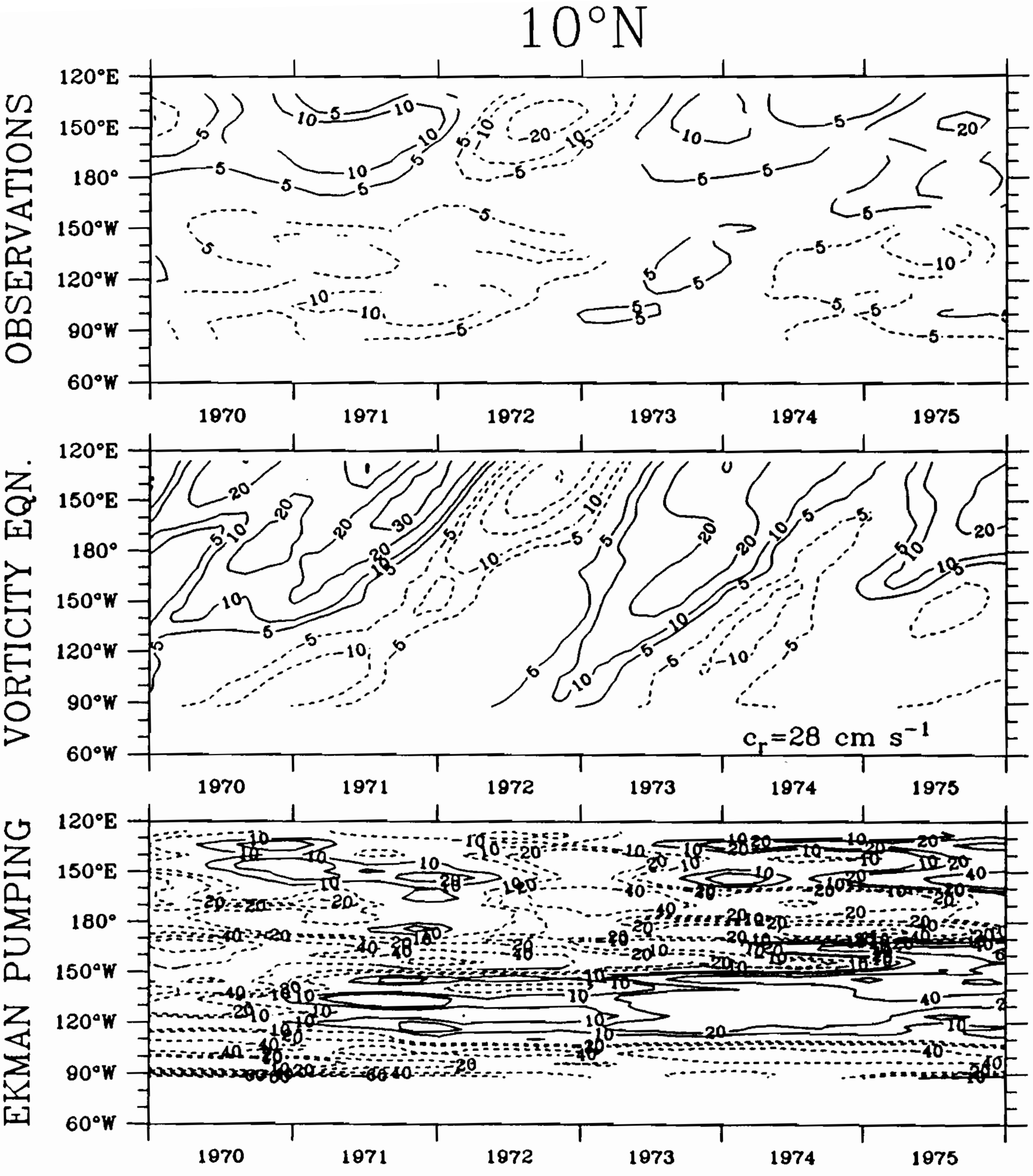

Figure 4.10b. As Figure 4.10a but for 10°N.

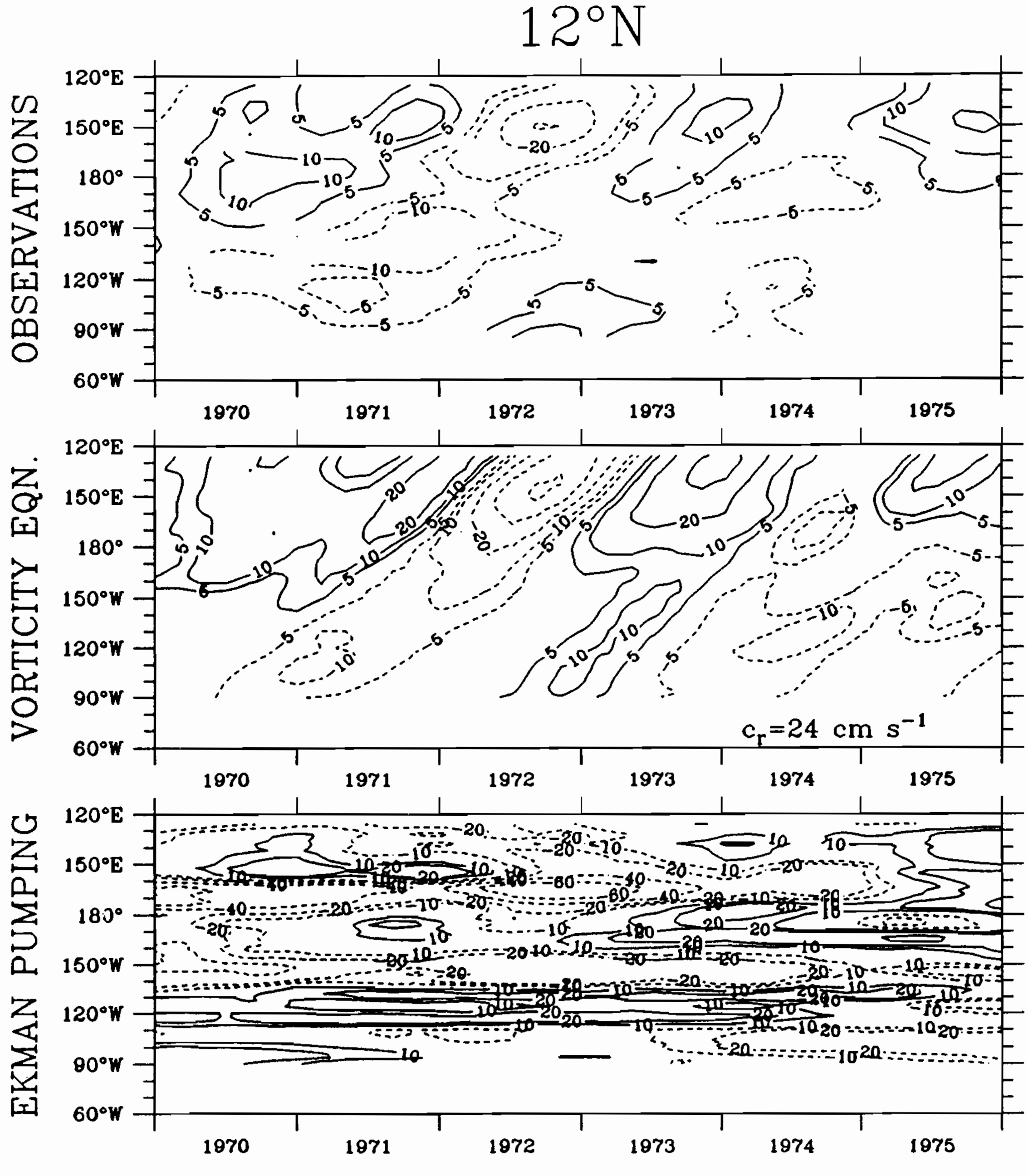

Figure 4.10c. As Figure 4.10a but for 12°N.

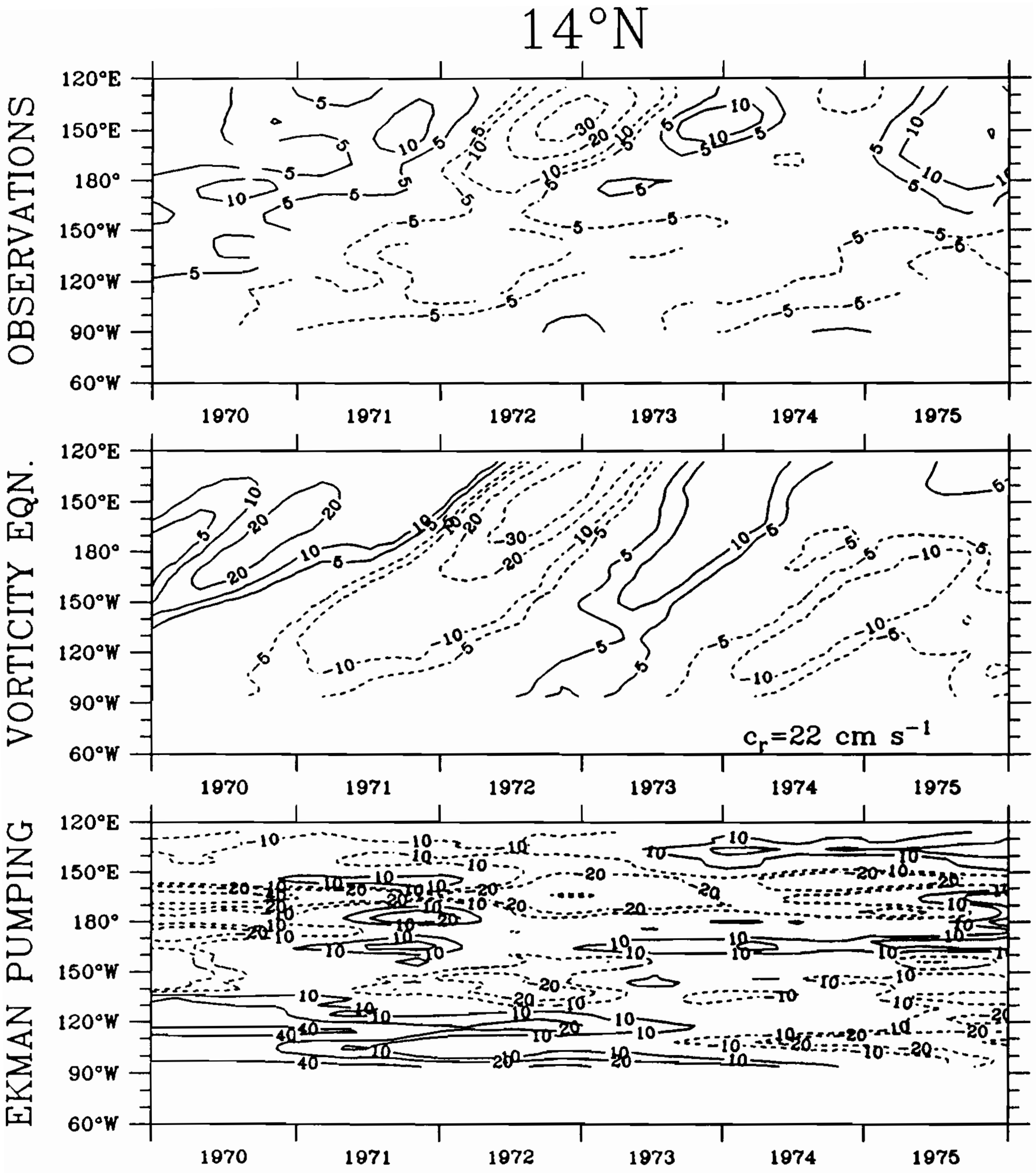

Figure 4.10d. As Figure 4.10a but for 14°N.

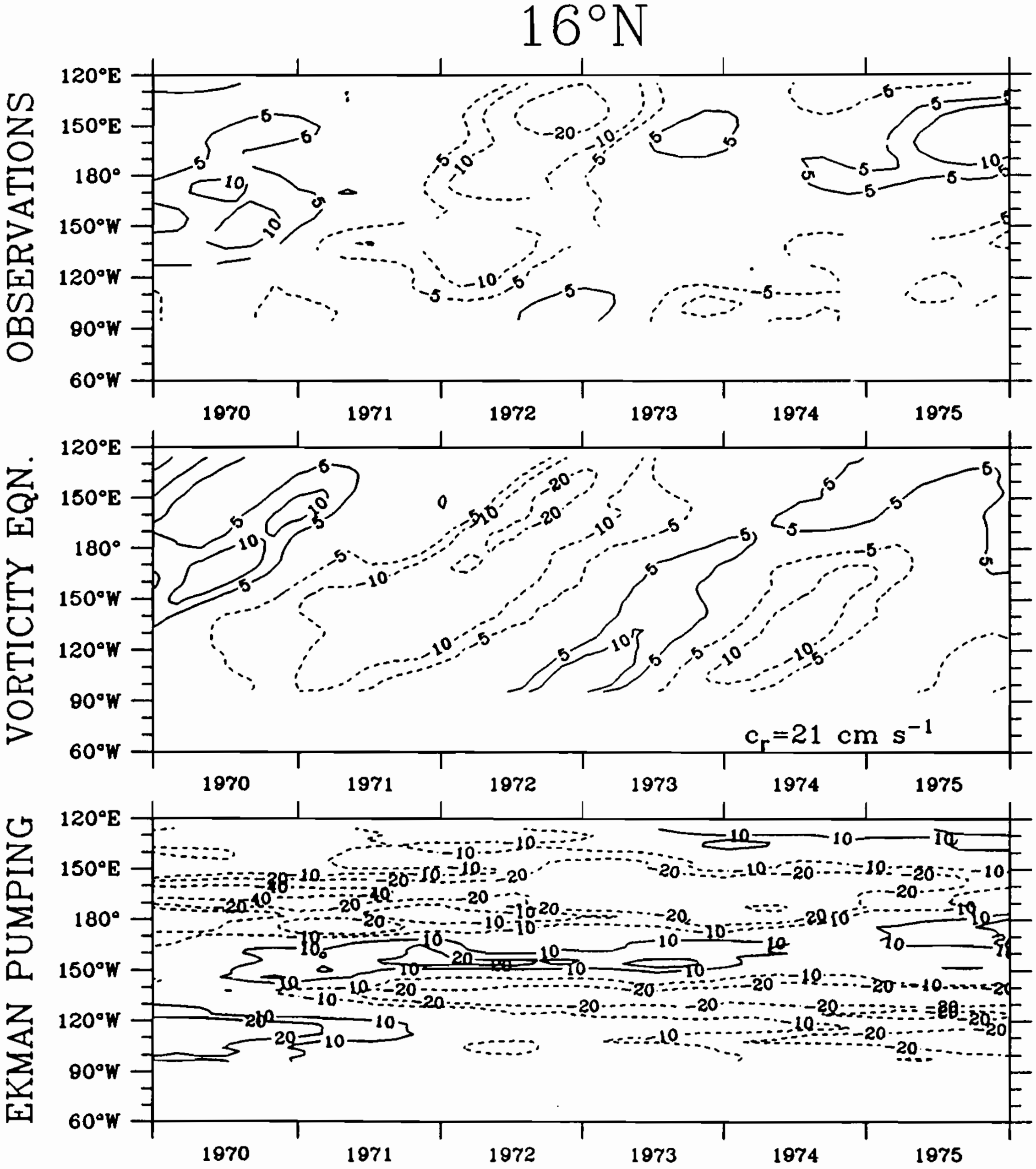

Figure 4.10e. As Figure 4.10a but for 16°N.

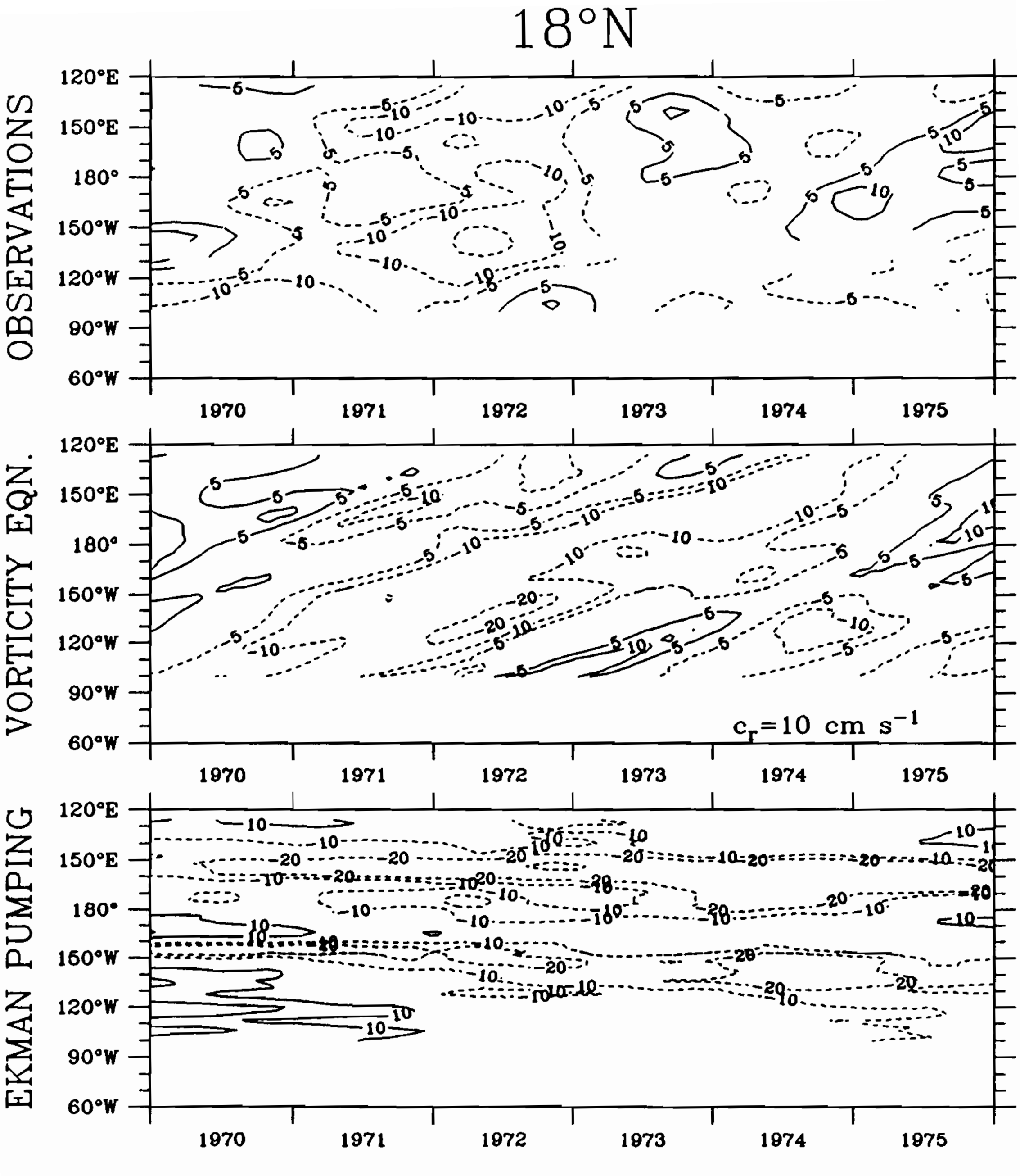

Figure 4.10f. As Figure 4.10a but for 18°N.

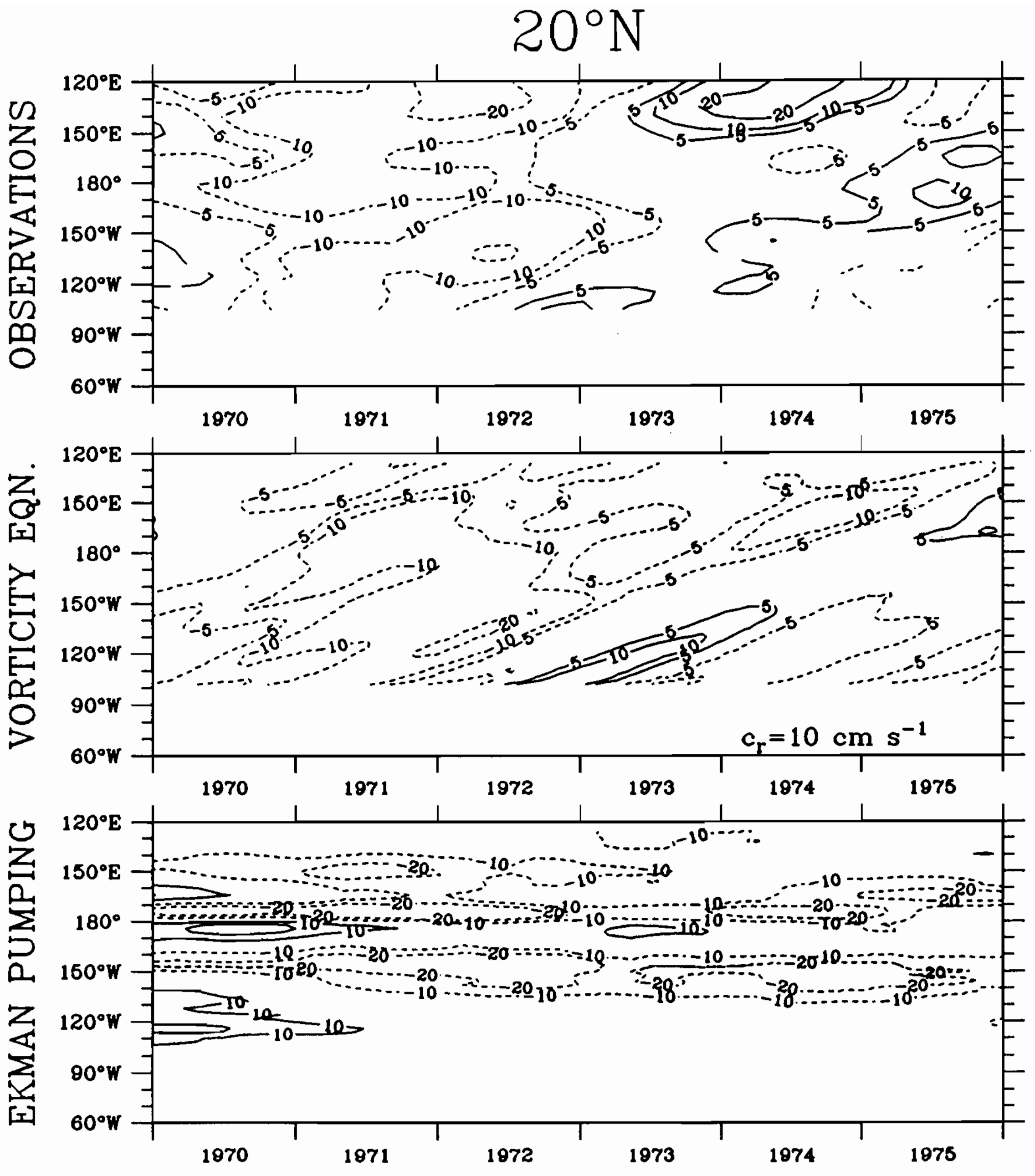

Figure 4.10g. As Figure 4.10a but for 20°N.

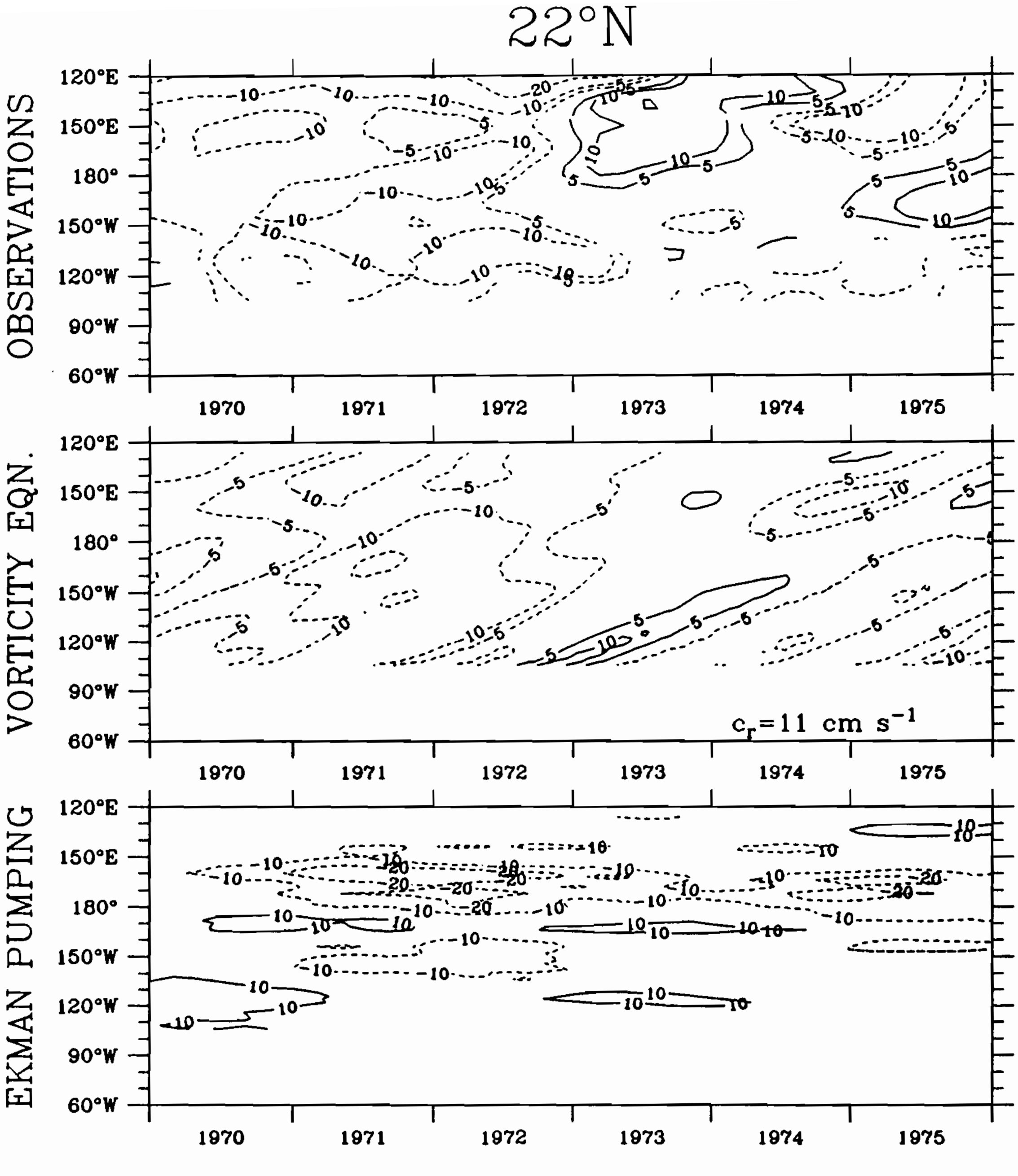

Figure 4.10h. As Figure 4.10a but for 22°N.

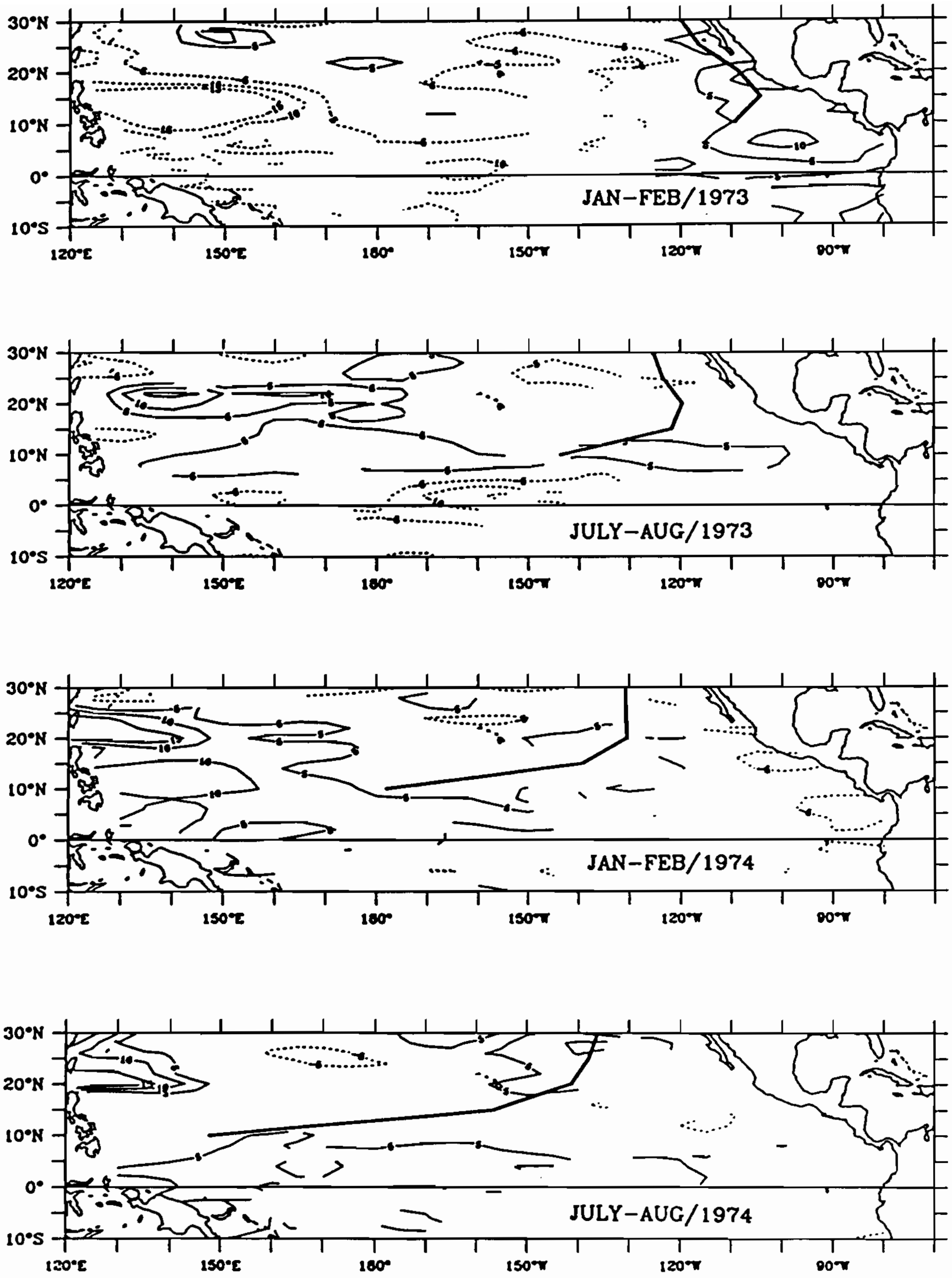

Figure 4.11. Anomalies of 20°C depth (m) during bimonths one-half year apart. Shallow anomalies are indicated by dashed contours, deep anomalies by solid contours; contours are given at ±5, 10, 15 m. The heavy line gives the (deep) crest position of a hypothetical long Rossby pulse which left the eastern boundary at the date of maximum observed boundary anomaly following the 1972 El Niño (Figure 4.1) and traveled at a speed $c_r = -\beta c^2/f^2$, with the long gravity wave speed c chosen to be 3 m/s.

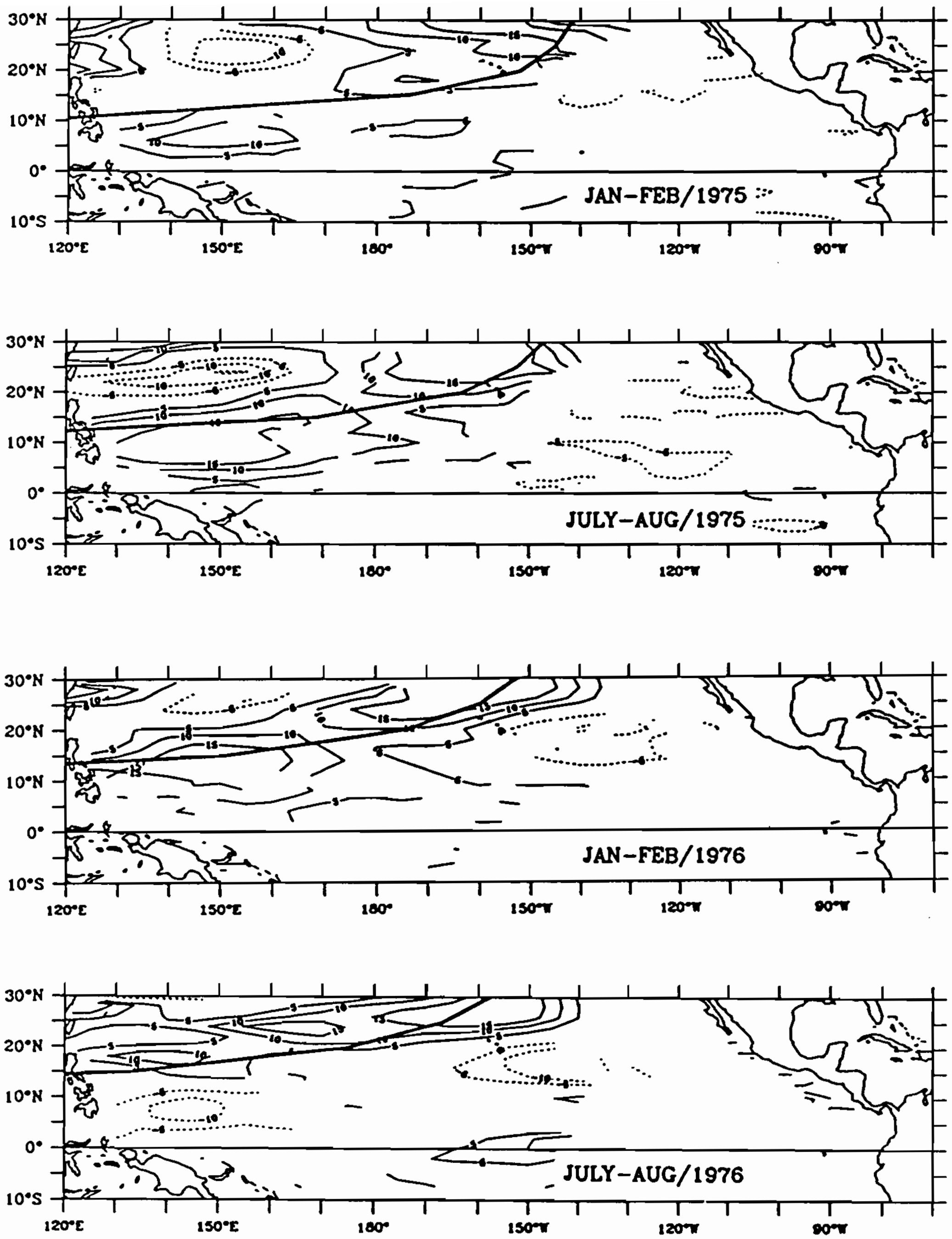

Figure 4.11. Continued.

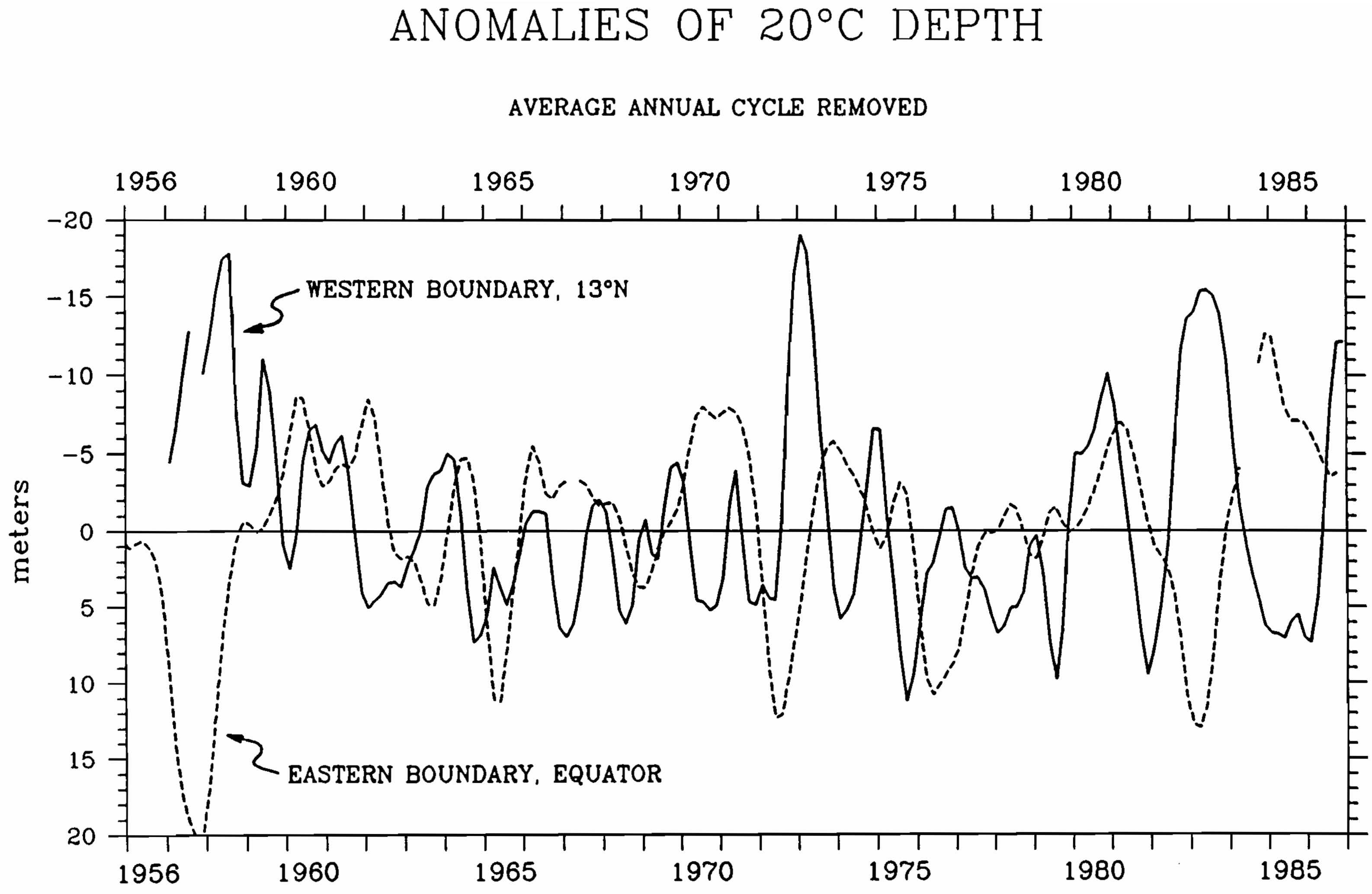

Figure 4.12. Time series of anomalous 20°C depth (m) at 13°N on the western boundary (solid line) and at the equator on the eastern boundary (dashed line) during 1956 through 1986. Deep anomalies are shown downwards and shallow anomalies upward.

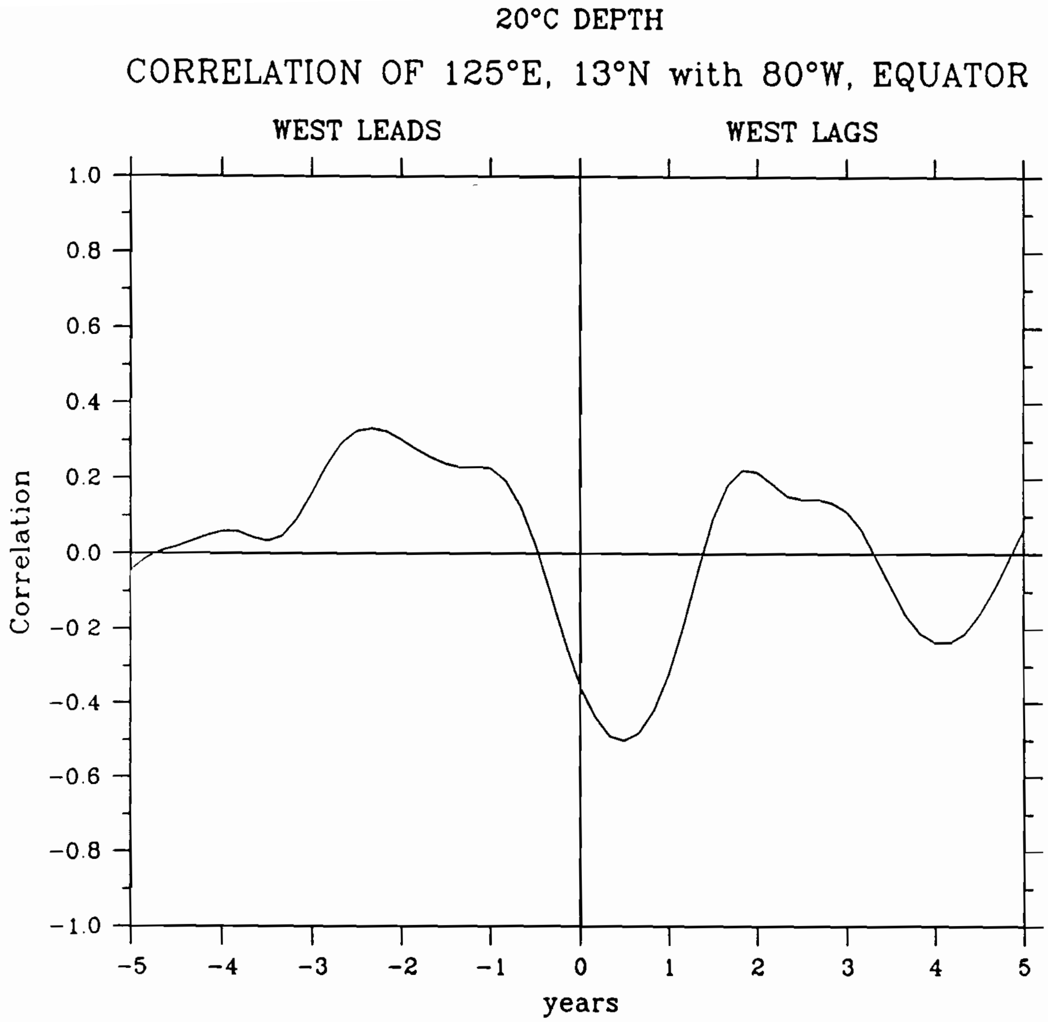

Figure 4.13. Lag correlation between anomalous 20°C depths at 13°N on the western boundary and at the equator on the eastern boundary (the two time series in Figure 4.12).

## 5. SUMMARY AND CONCLUSIONS

A new set of BT data makes it possible to examine zonal propagation of thermocline fluctuations without extensive interpolation. The archives of the NODC contain several hundred thousand BT observations in the Pacific which have formed the basis for several previous studies; however these data are primarily distributed along particular shipping routes and leave large gaps, particularly in an important region of the western tropical Pacific. This has resulted in the necessity of relatively elaborate interpolation schemes in order to interpret thermocline variability in terms of zonal long-wave propagation, and has made such interpretation controversial. The new data set consists of mechanical BT observations taken by Japanese fishing vessels during the 1970's; the sampling distribution complements the XBT data set in the western Pacific and allows the gridding of observations on a relatively fine 2° latitude by 5° longitude grid with a minimum of zonal interpolation. On this gridscale, the combined BT observations average one profile every 35 days in each gridbox during 1970 through 1987, with a higher density during the early 1970's. The sampling is concentrated in the northern hemisphere and in the southwest Pacific; the southeast Pacific is very poorly sampled. After extensive quality control, more than 185K profiles were available for analysis in the Pacific between 30°N and 30°S.

The field of 20°C isotherm depth was chosen as the clearest, simplest representation of the observed variability. The principal advantage of this choice is that it simplifies the three-dimensional thermal field into a two-dimensional variable which can be mapped and viewed conveniently. The assumption is made that the tropical Pacific may be approximated as a two-layer system divided by a sharp pycnocline, for which the depth of the 20°C isotherm is a proxy. This simplification has commonly been used in observational studies of the tropical Pacific, and in the same spirit many modeling experiments have used a reduced gravity, single-active-layer approximation.

At the annual period, east of the Dateline and at latitudes less than 25°, to a rough approximation most of the tropical Pacific thermocline fluctuates nearly in phase with the local Ekman pumping. The most prominent signal is an out-of-phase annual oscillation across the North Equatorial Countercurrent (NECC), in which the thermocline gradient associated geostrophically with this eastward flow is strongest in December and weakest in June, as has been previously shown by several investigators. This oscillation is due to the annual migration of the Inter-tropical Convergence Zone during the year. A similar out-of-phase variability is observed across the South Equatorial Countercurrent, which is associated with the South Pacific Convergence Zone which extends eastward from New Guinea during the southern summer. However, particularly in the western North Pacific, important discrepancies from this simple picture are observed. Near 4° and 6°N (at the southern edge of the NECC) and at 14° to 20°N (in the center of the North Equatorial Current (NEC)), the observed variations, which in the east are largely in phase with the local Ekman pumping, appear to propagate westward as long Rossby waves. Near the thermocline ridge at 10°N which separates these two currents there is little evidence of propagation, and the annual variations appear to be in phase with the local Ekman pumping across the entire basin.

The annual propagation of long Rossby waves was studied using a simple reduced-gravity vorticity equation (2.4) which allows the physical processes of Ekman pumping, the radiation of long (non-dispersive) Rossby waves due to such pumping in mid-basin, and the radiation of long Rossby waves from observed eastern boundary thermocline depth variations. The solution to this equation (forced with observed (FSU) winds) was best-fit to the observations of the annual cycle of 20°C depth; a high correlation of the solution with observations was considered evidence of long Rossby waves, and this hindcast was compared with a hindcast due to Ekman pumping alone. Clearly distinguishable peaks of correlation were found at 4° and 6°N, and at 14° through 18°N (Figs. 3.13), with values of correlation above 0.8. Assuming Ekman pumping alone produced generally much lower correlations with the observations, particularly in the west, indicating that long Rossby waves are an essential element of the dynamics of the annual cycle in these regions. In addition, the overall character of the solutions was very different: Ekman pumping alone hindcast an unrealistic simple annual oscillation of anomalies pivoting about 10°N, implying that at intermediate seasons the anomalies should all be near zero (Fig. 3.14c). The simple vorticity equation, on the other hand, hindcast a simple oscillation in the east but a more complicated pattern due to a combination of local pumping and incoming long waves in the west which is both qualitatively and quantitatively more like the observed annual variability. A major result of the long Rossby wave solution was to show that the difference between the annual cycle of the NECC in the east, where there is a strong annual transport fluctuation, and the west, where the annual transport signal is weak, is due to the arrival in the west near 4°N-6°N of long waves carrying the history of eastern Ekman pumping with about a six-month lag (Figs. 3.13a and b). Thus although the annual cycle of local Ekman pumping has little zonal change across the basin, the annual cycle of thermocline depths near the trough at 4°N in the west is nearly out-of-phase with the local pumping, reducing the oscillation of thermocline gradient across the NECC and hence the annual variation of geostrophic transport.

The same simple model (2.4) was used to study interannual pycnocline variability, with particular concentration on the El Niño of 1972 when the sampling was most dense (an observation on average every 23 days in each 2° latitude by 5° longitude gridbox). Ekman pumping alone hindcast unrealistically large amplitudes of interannual variability within about 15° latitude of the equator. This was due to the relative persistence of interannual wind stress curl anomalies, which commonly remain of the same sign for several years, so the (integrated in time) Ekman pumping solution can get very large. If the dynamics include Rossby waves, however, the anomalies radiate away before building up large amplitudes, so the simple model solution had approximately the same amplitude as the observations. The interannual hindcast assuming

Ekman pumping alone was poorly correlated with the observations almost everywhere, while the Rossby wave solution had high correlations in the western Pacific; neither was significantly correlated in the east central Pacific (Fig. 4.9), a region of poor data coverage (both wind and BT data). As in the case of the annual variability, the simple model (2.4) was best-fit to the observations of interannual 20°C depth variability to find the phase speed which gave the highest correlations. The planetary wave character of the variability is shown by the meridional profile of these best-fit speeds (Fig. 3.12), which falls roughly on the line $c_r = \beta c^2/f^2$, with the long gravity wave speed c chosen to be the zonal average of the first baroclinic mode long gravity speed found by Emery *et al.* (1984).

A characteristic zonal wind stress anomaly pattern associated with El Niño is equatorial westerlies during the height of the event in the central Pacific, followed by a return of stronger than average equatorial easterlies the following year (Fig. 4.5). Although the strongest wind *stress* anomalies are confined to the equatorial zone, the large scale wind stress *curl* pattern resulting from these anomalies is upwelling curl extending to about 15°N during the equatorial westerlies. In this tropical, extra-equatorial region, upwelling waves were generated during the height of the event which carried the upwelling signal to the western boundary, arriving about six months later (Fig. 4.10c). Thus although the anomalous wind stress curl forcing in the western extra-equatorial Pacific was relatively weak during El Niños, large shallow thermocline depth anomalies were observed there; these were forced in the central Pacific and radiated west. During the year following several El Niños, strong easterlies returned to the equatorial region, generating downwelling wind stress curl in the tropical central Pacific. The deep anomalies forced in this way in the central basin were also observed to propagate to the western boundary equatorward of about 14°N.

In addition to the mid-basin forcing, El Niños also generate boundary reflections of the deep equatorial thermocline anomalies which are the primary oceanic signal of the event. Along the American coast, deep anomalies of 20°C depth were observed to occur northward to at least 22°N, with typical amplitudes of 10-15 m (Fig. 4.1). The speed of propagation along the coast was observed to be about 32 cm/s, which is slower than estimates of coastal Kelvin wave propagation found from long time series of sea level. The simple model radiates these anomalies offshore and predicts that they should form an dominant part of the variability in the eastern and central Pacific. However, equatorward of 15°N, the observations do not appear to be consistent with this hypothesis, which is largely why the simple model was found to be poorly correlated with the observations in this region (Fig. 4.9). North of 15°N, however, the reflection following the 1972 El Niño can be observed propagating across the entire basin, arriving in the west more than four years after the event (Fig. 4.11). Thus while south of 15°N thermocline fluctuations were dominated by the strong wind stress curl forcing associated with the El Niño of 1972, in the subtropical region where the wind stress curl forcing was weaker the large boundary event spawned a wave which stood out above locally forced variability.

It is clear from the observations reported here that long Rossby waves propagate across the tropical, extra-equatorial north Pacific, and that these waves can arrive at the western boundary with significant amplitude. It has been proposed that these waves reflect from the western boundary as equatorial Kelvin waves and contribute to the triggering of subsequent El Niños (Graham and White, 1988). This mechanism has also been suggested in theoretical and modeling studies which hypothesize that the approximate three- to four-year periodicity of these events is due to the relatively slow travel time of the long tropical Rossby waves. In a few locations in the Pacific, it is possible to construct long time series of 20°C depths going back to the 1950's, and these time series, which span seven major El Niños, indicate problems with this idea. Figure 4.12 shows such long time series at 13°N on the Philippines coast (which gives a good index of waves arriving from the northern tropical Pacific, and is almost exactly where Graham and White have suggested that the triggering waves arrive at the boundary) and at the equator at the South American coast (which is a good index of El Niños). If a (nearly linear) oceanic wave mechanism connects these two locations, then there should be a significantly positively correlated lag relation between them, with the west leading the east. Figure 4.13 shows that the only significant correlation has the east leading the west by about six months, with opposite sign. This represents the process discussed above whereby upwelling Rossby waves are generated in mid-basin by wind stress curl associated with equatorial westerly wind anomalies (occurring only slightly before the deep equatorial thermocline anomalies arriving in the east), which then take about six months to reach the western boundary. The proposed correlation with the west leading the east is a weak, broad peak with correlations about 0.2, which is probably not significantly different from zero. There is a suggestion in the time series (Fig. 4.12) that many El Niños are preceded by a deep thermocline in the west, however there are almost twice as many deep events in the west as El Niños, and no apparent relation between the size of the western event and the subsequent eastern deepening, nor is the time lag at all regular, as would be expected if a nearly linear oceanic wave process were the primary mechanism. A more justifiable conclusion from these data is that it is apparently unlikely to have an El Niño occur following a period when the western Pacific thermocline is anomalously shallow. The data do not support the idea that there is a triggering of eastward propagation along the equator by long Rossby waves arriving at the tropical western boundary.

## 6. ACKNOWLEDGMENTS

The author wishes to acknowledge the teaching and inspiration of the physical oceanographers on my supervisory committee: Drs. Ed Harrison, Mike McPhaden, Lew Rothstein and Bruce Taft. My education was conducted principally by these four men; each of them contributed importantly to my development as a scientist. Many other members of the tropical oceanographic community: scientists, programmers and sea-going personnel have also generously shared ideas and welcomed me to the profession. It is a pleasure to acknowledge in particular the unstinting support and encouragement of Dr. Bruce Taft, who for six years has made sure that opportunities were provided and obstacles removed. My wife Christine Kessler endured many late nights alone while this work was in progress; her loving partnership has been a great source of strength.

# 7. REFERENCES

Anderson, D.L.T. and A.E. Gill, 1975: Spin-up of a stratified ocean, with applications to upwelling. *Deep-Sea Res., 22*, 583-596.

Baker, D.J., 1981: Ocean instruments and experiment design. In *Evolution of Physical Oceanography*, B.A. Warren and C. Wunsch, eds., MIT Press, Cambridge, MA.

Barnett, T.P. and W.C. Patzert, 1980: Scales of thermal variability in the tropical Pacific. *J. Phys. Oceanogr., 10*, 529-540.

Bjerknes, J., 1966: A possible response of the atmospheric Hadley circulation to equatorial anomalies of ocean temperature. *Tellus, XVIII*, 820-828.

Bracewell, R.N., 1978: The Fourier Transform and its applications. 2nd ed. McGraw-Hill, New York. 444 pp.

Bretherton, F.P. and C.J.R. Garrett, 1968: Wave trains in inhomogeneous moving media. *Proc. Roy. Soc. London, A, 302*, 529-554.

Buchanan, J.Y., 1886: On similarities in the physical geography of the great oceans. *Proc. Roy. Geogr. Soc., 8*, 753-770.

Busalacchi, A.J. and J.J. O'Brien, 1980: The seasonal variability in a model of the tropical Pacific. *J. Phys. Oceanogr., 10*, 1929-1951.

Busalacchi, A.J., K. Takeuchi and J.J. O'Brien, 1983: Interannual variability of the tropical Pacific – revisited. *J. Geophys. Res., 88*, 7551-7562.

Busalacchi, A.J. and M.A. Cane, 1985: Hindcasts of sea level variations during the 1982-83 El Niño. *J. Phys. Oceanogr., 15*, 213-219.

Cane, M.A. and E.S. Sarachik, 1981: The response of a linear baroclinic ocean to periodic forcing. *J. Mar. Res., 39*, 651-693.

Chang, P. and S.G.H. Philander, 1989: Rossby wave packets in baroclinic mean currents. *J. Mar. Res.*, in press.

Chelton, D.B. and R.E. Davis, 1982: Monthly mean sea-level variability along the west coast of North America. *J. Phys. Oceanogr., 12*, 757-784.

Chereskin, T.K., J.N. Moum, P.J. Stabeno, D.R. Caldwell, C.A. Paulson, L.A. Regier and D. Halpern, 1986: Fine-scale variability at 140°W in the equatorial Pacific. *J. Geophys. Res., 91*, 12,887-12,898.

Donguy, J-R. and A. Dessier, 1983: El Niño-like events observed in the tropical Pacific. *Mon. Wea. Rev., 111*, 2136-2139.

Emery, W.J., W.G. Lee and L. Magaard, 1984: Geographic and seasonal distributions of Brunt-Väisälä frequency and Rossby radii in the North Pacific and North Atlantic. *J. Phys. Oceanogr., 14*, 294-317.

Enfield, D.B. and J.S. Allen, 1980: On the structure and dynamics of monthly sea level anomalies along the Pacific coast of North and South America. *J. Phys. Oceanogr., 10*, 557-578.

Ericksen, C.C., 1982: Equatorial wave vertical modes observed in a western Pacific island array. *J. Phys. Oceanogr., 12*, 1206-1227.

Garzoli, S.L. and E.J. Katz, 1983: The forced annual reversal of the Atlantic North Equatorial Countercurrent. *J. Phys. Oceanogr., 13*, 2082-2090.

Gill, A.E. and A.J. Clarke, 1974: Wind-induced upwelling, coastal currents and sea-level changes. *Deep-Sea Res., 21*, 325-345.

Goldenberg, S.B. and J.J. O'Brien, 1981: Time and space variability of tropical Pacific wind stress. *Mon. Wea. Rev., 109*, 1190-1207.

Graham, N.E. and W.B. White, 1988: The El Niño cycle: A natural oscillator of the Pacific Ocean-atmosphere system. *Science, 240*, 1293-1302.

Harrison, D.E., Kessler, W.S. and B.S. Giese, 1989: Ocean circulation model hindcasts of the 198283 El Niño: Thermal variability along the ship of opportunity tracks. *J. Phys. Oceanogr.*, in press.

Heinmiller, R.H., C.C. Ebbesmeyer, B.A. Taft, D.B. Olson and O.P. Nikitin, 1983: Systematic errors in expendable bathythermograph (XBT) profiles. *Deep-Sea Res., 30*, 1185-1195.

Held, I.M., 1983: Stationary and quasi-stationary eddies in the extra-tropical troposphere: theory. In *Large-scale dynamical processes in the atmosphere.* B.J. Hoskins and R.P. Pierce, eds. Acad. Press, New York.

Hovmoller, E., 1949: The trough and ridge diagram. *Tellus, 1*, 62-66.

Inoue, M., O'Brien, J.J., White, W.B. and S.E. Pazan, 1987: Interannual variability in the tropical Pacific for the period 1979-1982. *J. Geophys. Res., 92*, 11,671-11,679.

Iselin, C.O'D. and F.C. Fuglister, 1948: Some recent developments in the study of the Gulf Stream. *J. Mar. Res., 7*, 317-329.

Kessler, W.S., B.A. Taft and M. McPhaden, 1985: An assessment of the XBT sampling network in the central Pacific. Univ. Corp. for Atmos. Res., US TOGA 4, 62 pp.

Kessler, W.S. and B.A. Taft, 1987: Dynamic heights and zonal geostrophic transports in the central tropical Pacific during 1979-84. *J. Phys. Oceanogr., 17*, 97-122.

Landsteiner M.C., M.J. McPhaden and J. Picaut, 1988: On the sensitivity of Sverdrup transport estimates to the specification of wind stress forcing in the tropical Pacific. Submitted to *J. Geophys. Res.*.

LeBlond, P. and L. Mysak, 1978: *Waves in the Ocean.* Elsevier Scientific Publishing Company, Amsterdam, 602 pp.

Levitus, S., 1982: Climatological atlas of the world ocean. NOAA professional paper 13, 173 pp.

Lighthill, M.J., 1969: Dynamic response of the Indian Ocean to the onset of the southwest monsoon. *Philos. Trans. Roy. Soc. London Ser. A, 265*, 45-92.

Lighthill, M.J., 1978: *Waves in Fluids.* Cambridge Univ. Press, Cambridge, 504 pp.

Lindstrom, E., R. Lukas, R. Fine, E. Firing, S. Godfrey, G. Meyers and M. Tsuchiya, 1987: The western equatorial Pacific Ocean circulation study. *Nature, 330*, 533-537.

Longuet-Higgins, M.S., 1964: Planetary waves on a rotating sphere. *Proc. Roy. Soc. of London A, 279*, 446-473.

Lukas, R., S.P. Hayes and K. Wyrtki, 1984: Equatorial sea level response during the 1982-1983 El Niño. *J. Geophys. Res., 89*, 10,425-10,430.

Lukas, R., 1988: Interannual fluctuations of the Mindanao Current inferred from sea level. *J. Geophys. Res., 93*, 6744-6788.

McCreary, J.P., 1976: Eastern tropical ocean response to changing wind systems: with application to El Niño. *J. Phys. Oceanogr., 6*, 632-645.

McCreary, J.P., 1981: A linear stratified ocean model of the equatorial undercurrent. *Phil. Trans. Roy. Soc. London, A302*, 335-415.

McCreary, J.P., 1983: A model of tropical ocean-atmosphere interaction. *Mon. Wea. Rev., 111*, 370-387.

McCreary, J.P. and D.L.T. Anderson, 1984: A simple model of El Niño and the southern oscillation. *Mon. Wea. Rev., 112*, 934-946.

McCreary, J.P., 1985: Modeling equatorial ocean circulation. *Ann. Rev. Fluid Mech., 17*, 359-409.

McPhaden, M.J., 1984: On the dynamics of equatorial subsurface countercurrents. *J. Phys. Oceanogr., 14*, 1216-1225.

McPhaden, M.J., A.J. Busalacchi, J. Picaut and G. Raymond, 1988: A model study of potential sampling errors due to data scatter around expendable bathythermograph transects in the tropical Pacific. *J. Geophys. Res., 93*, 8119-8130.

McPhaden, M.J., A.J. Busalacchi and J. Picaut, 1988: Observations and wind-forced model simulations of the mean seasonal cycle in tropical Pacific sea surface topography. *J. Geophys. Res., 93*, 8131-8146.

Meyers, G., 1979a: On the annual Rossby wave in the tropical North Pacific Ocean. *J. Phys. Oceanogr., 9*, 663-674.

Meyers, G., 1979b: Annual variation in the slope of the 14°C isotherm along the equator in the Pacific Ocean. *J. Phys. Oceanogr., 9*, 885-891.

Meyers, G. and J.-R. Donguy, 1980: An XBT network with merchant ships. *Trop. Ocean-Atmos. Newslett., 2*, 6-7.

Meyers, G. and J.-R. Donguy, 1984: The North Equatorial Countercurrent and heat storage in the western Pacific Ocean during 1982-83. *Nature, 312*, 258-260.

Moore, D.W., 1968: Planetary-gravity waves in an equatorial ocean. Ph.D. thesis. Harvard Univ., Cambridge, Mass.

Moore, D.W. and S.G.H. Philander, 1978: Modeling of the tropical ocean circulation. In *The Sea, 6*, 319-361.

Munk, W.H., 1950: On the wind-driven ocean circulation. *Journal of Meteorology, 7*, 79-93.

Pazan, S.E., W.B. White, M. Inoue and J.J. O'Brien, 1986: Off-equatorial influence on Pacific equatorial dynamic height variability during the 198283 ENSO. *J. Geophys. Res., 91*, 8437-8449.

Pazan, S.E. and W.B. White, 1987: Short-term climatic variability in the volume budget of the western tropical North Pacific Ocean during 1979-82. *J. Phys. Oceanogr., 17*, 440-454.

Pedlosky, J., 1965: A note on the western intensification of oceanic circulation. *J. Mar. Res., 23*, 207-209.

Peregrine, D.H. and R. Smith, 1979: Nonlinear effects upon waves near caustics. *Phil. Trans. Roy. Soc. London A, 265*, 45-92.

Philander, S.G.H., 1978: Forced oceanic waves. *Rev. Geophys. and Space Phys., 16*, 15-46.

Rattray, M., 1964: Time-dependent motion in an ocean; a unified two-layer, beta-plane approximation. In *Studies in Oceanography*, K. Yoshida, ed., Univ. of Tokyo Press, Tokyo, 19-29.

Rebert, J.P., J.-R. Donguy, G. Eldin and K. Wyrtki, 1985: Relations between sea level, thermocline depth, heat content and dynamic height in the tropical Pacific Ocean. *J. Geophys. Res., 90*, 11,719-11,725.

Reid, J.L., 1965: Intermediate waters of the Pacific Ocean. *The Johns Hopkins Oceanographic Studies, 2*, 85 pp.

Reid, J.L. and R.S. Arthur, 1975: Interpretation of maps of geopotential anomaly for the deep Pacific Ocean. *J. Mar. Res., 33*, 37-52.

Ripa, P., 1983: General stability conditions for zonal flows in a one-layer model on the β-plane or the sphere. *J. Fluid Mech., 126*, 463-489.

Ripa, P., 1989: Rays in the equatorial oceans. *Trop. Ocean-Atmos. Newslett., 48*, 1-5.

Schopf, P.S., D.L.T. Anderson and R. Smith, 1981: Beta-dispersion of low-frequency Rossby waves. *Dyn. Atmos. and Oceans, 5*, 187-214.

Seckel, G.R., 1975: Seasonal variability and parameterization of the Pacific North Equatorial Current. *Deep-Sea Res., 22*, 379-401.

Snodgrass, J.M., 1968: Instrumentation and Communications. In *Ocean Engineering: Goals, Environment, Technology*, J.F. Brahtz, ed., John Wiley and Sons, New York, 393-477.

Stommel, H., 1948: The westward intensification of wind-driven ocean circulation. *Trans. Amer. Geophys. Union, 29*, 202-206.

Stommel, H., 1965: *The Gulf Stream: A physical and dynamical description*, 2nd ed. University of California Press, Berkeley, 248 pp.

Sverdrup, H.U. 1947: Wind-driven currents in a baroclinic ocean, with application to the equatorial currents of the eastern Pacific. *Proc. Nat. Acad. Sci., 33*, 318-326.

Sverdrup, H.U., M.W. Johnson and R.H. Fleming, 1942: *The Oceans: Their Physics, Chemistry and General Biology*. Prentice-Hall, Englewood Cliffs, New Jersey, 1087 pp.

Taft, B.A. and W.S. Kessler, 1989: On the use of sea-level and XBT transects to measure geostrophic flow in the tropical Pacific Ocean. In preparation.

Tsuchiya, M., 1972: A subsurface north equatorial countercurrent in the eastern Pacific Ocean. *J. Geophys. Res., 77*, 5981-5986.

Tsuchiya, M., 1975: Subsurface countercurrents in the eastern equatorial Pacific Ocean. *J. Mar. Res., 33* (Supplement), 145-175.

Walker, J., 1988: Shadows cast on the bottom of a pool are not like other shadows. *Scientific American, 259*, 116-119.

White, W.B., 1977: Annual forcing of baroclinic long waves in the tropical North Pacific Ocean. *J. Phys. Oceanogr., 7*, 50-61.

White, W.B., G. Meyers and K. Hasunuma, 1982: Space/time statistics of short-term climatic variability in the western North Pacific. *J. Geophys. Res., 87*, 1979-1989.

White, W.B., 1983: Westward propagation of short-term climatic anomalies in the western North Pacific from 1964-74. *J. Mar. Res., 41*, 113-125.

White, W.B., G. Meyers, J.-R. Donguy and S.E. Pazan, 1985: Short-term climatic variability in the thermal structure of the Pacific Ocean during 1979-82. *J. Phys. Oceanogr., 15*, 917-935.

Wyrtki, K., 1974a: Sea level and the seasonal fluctuations of the equatorial currents in the western Pacific Ocean. *J. Phys. Oceanogr., 4*, 91-103.

Wyrtki, K. 1974b: Equatorial currents in the Pacific 1950 to 1970 and their relations to the Trade Winds. *J. Phys. Oceanogr., 4*, 372-380.

Wyrtki, K., 1975: Fluctuations of the dynamic topography in the Pacific Ocean. *J. Phys. Oceanogr., 5*, 450-459.

Wyrtki, K. and G. Meyers, 1975a: The trade wind field over the Pacific Ocean. Part I. The mean field and the mean annual variation. Rep. HIG751, Hawaii Inst. Geophys., Univ. of Hawaii, 26 pp.

Wyrtki, K. and G. Meyers, 1975b: The trade wind field over the Pacific Ocean. Part II. Bimonthly field of wind stress: 1950 to 1972. Rep. HIG752, Hawaii Inst. Geophys., Univ. of Hawaii, 16 pp.

Wyrtki, K. and G. Meyers, 1976: The trade wind field over the Pacific Ocean. *J. Appl. Meteorol., 15*, 698-704.

Wyrtki, K. and B. Kilonsky, 1984: Mean water and current structure during the Hawaii-to-Tahiti Shuttle Experiment. *J. Phys. Oceanogr., 14*, 242-254.

# APPENDIX 1: A Ray Theory Model of the Response to Pulse-like Eastern Boundary Forcing

## A. Introduction

The purpose of this Appendix is to examine the role of Rossby waves shorter than the long wave limit by considering in detail the dispersion of a Gaussian pulse (which contains waves of all frequencies) originating at the eastern boundary. Since the long wave limit is assumed rather freely in the main body of the report, this Appendix seeks to justify that simplification. Dispersion of shorter than long wave limit waves occurs not only through the gradient of the zonal component of group velocity, which modifies the westward speeds of the various frequencies of the pulse, but also through the meridional component, which affects the direction of energy propagation and can lead to shadow zones, focusing, and order one changes in the region of wave influence. One of the consequences of dispersion which is considered in this Appendix is the possibility of Rossby waves generated by large-scale forcing crossing the equator and affecting the dynamics in the opposite hemisphere. In addition, the existence of caustics, where the WKB solution breaks down and predicts that wave amplitudes can become large, is discussed. The mathematical technique used is ray theory, and begins with the basic ray description of Rossby dispersion as given in Schopf, Anderson and Smith (1981) (hereafter SAS), who showed that the equations describing Rossby wave ray paths on an equatorial β-plane can be written in a useful form; many of the most important equations in the first part of this section are exactly the same as in SAS. However, a further purpose of this Appendix is to show that it is possible to use the properties of the ray solution and go further than SAS; avoiding the traditional (and computationally tedious) time-stepping along a ray as in their paper. This further step has the advantage that the wave amplitude along ray paths can be found straightforwardly, unlike time-stepping where the amplitude is very difficult to compute. The basic idea for this improvement was suggested by Pedro Ripa. Finally, the difference between the use of an equatorial versus mid-latitude β-plane for examining Rossby waves in tropical latitudes is considered.

Although the observed thermocline depth fluctuations are in general quite disorganized and noisy, the pulse-like nature of the thermocline anomalies on the eastern boundary in 1972 (Fig. 4.1) might be expected to be one of the clearest opportunities to observe a distinct Rossby wave packet radiating freely from an eastern boundary forcing event. The process by which such an initial disturbance along the coast would evolve is investigated by means of ray theory. Baroclinic Rossby wave rays are traced on an equatorial β-plane, which allows periodic solutions to the linear equatorial vorticity equation to be studied. The model ocean is highly idealized, consisting of a rigid lid over a single active layer which is separated by a sharp pycnocline from a very deep resting layer. Both layers are homogeneous, and there are no mean pycnocline slopes (hence no mean geostrophic currents), so the only variation of the properties of the medium in the undisturbed state is due to the variation of the Coriolis parameter. In mid-basin the only physical process occurring is the free propagation of baroclinic Rossby waves which have radiated from prescribed forcing on the eastern boundary. The eastern boundary is taken to be a straight coast (but of arbitrary slope); examples of coast shapes made up of various straight line segments are also given. Although the ray solutions are perfectly valid across the equator, for several reasons discussed below no attempt is made to interpret the observed variability in terms of wave energy which has crossed the equator. Since the linear inviscid physics used here is inadequate to describe the situation at a western boundary, the model ocean is open in the west; some qualitative discussion concerning the western boundary response is offered.

The ray tracing method is appropriate for purely sinusoidal waves, but in the observations the initiating disturbance on the eastern boundary is event-like. A simple approximation to the observed time-dependent boundary condition is a downward pycnocline displacement which has a Gaussian time history and occurs simultaneously along the length of the coast. (It will be shown below that the fact that the observed disturbance is not truly simultaneous but occurs slightly later in the north makes little difference in the mid-basin solution.) The maximum amplitude of the pycnocline displacement is taken to be 10 m and the halfwidth of the Gaussian to be six months. The Gaussian time history can be decomposed as an infinite linear sum of sinusoidal fluctuations, the components of which can each be allowed to radiate separately, then summed to show the total response to the event-like forcing at any specified time. Figure A1.1 shows the frequency content of the boundary condition; note that the amplitude has fallen below one-tenth of its maximum value when the period is less than one year.

## B. Ray theory

Before discussing the results of the summation over many frequencies, it is appropriate to review the ray tracing method used for each frequency individually. The vorticity equation for the meridional velocity on an equatorial β-plane (the "v-equation"), first obtained by Rattray (1964) and used extensively by Moore and Philander (1977) and successors, is:

$$(1/c^2)\partial^3 v/\partial t^3 + [(\beta y/c)^2 - \nabla^2]\partial v/\partial t - \beta \partial v/\partial x = 0 \tag{A1.1}$$

where $c^2 = g'H$ is the squared gravity wave speed ($g'$ is the reduced gravity and H is the undisturbed upper layer depth), which is taken to be constant. The operator $\nabla^2 = \partial^2/\partial x^2 + \partial^2/\partial y^2$. Following SAS the $\partial^3 v/\partial t^3$ term is dropped, which removes the long gravity waves from the dynamics. WKB solutions to (A1.1) may be sought which are sinusoidal in time and in both spatial directions:

$$v = A(x,y,t) \exp \{i\phi(x,y,t)\} \tag{A1.2}$$

as long as the amplitude A varies only slightly over a single wavelength, and the scale of variation of the phase $\phi$ is small compared with the variations in the properties of the medium, which in this case is the global scale of the Coriolis parameter. Then the wavenumber components and frequency are defined:

$$k \equiv \partial\phi/\partial x, \quad l \equiv \partial\phi/\partial y, \quad \omega \equiv -\partial\phi/\partial t, \tag{A1.3}$$

and the vorticity equation (A1.1) reduces to the familiar Rossby dispersion relation:

$$\omega = -\beta k/(k^2 + l^2 + (\beta y/c)^2), \tag{A1.4}$$

which is the fundamental relation for the following ray tracing experiments (SAS). In this section it is assumed that a single frequency $\omega$ is known; in later sections a summation over many frequencies is undertaken.

The idea of ray tracing is that a partial differential equation such as (A1.1) can be reduced to a set of ordinary differential equations (whose independent variable is travel time along the ray) which hold along the ray paths, or characteristics, of (A1.1). In general the properties of the solution can then be found by time-stepping (integrating in time) along the ray paths. In the present case, because Rossby wave rays can be shown to have a simple sinusoidal shape about the equator it is not necessary to time-step; the solution will be seen to be determined at any (x,y,t) in the ray region knowing only the initial latitude and eastern boundary condition for a ray passing through (x,y).

The fundamental equations of ray theory (LeBlond and Mysak, 1978, section 6) give the group velocity components, which describe the ray paths as well as the speed of energy propagation along them, in terms of the gradient of the frequency in wavenumber space:

$$C_g^x = dx/dt = \partial\omega/\partial k, \quad C_g^y = dy/dt = \partial\omega/\partial l \tag{A1.5a,b}$$

while the variation of wavenumber and frequency along the ray paths is found from:

$$dk/dt = -\partial\omega/\partial x, \quad dld/dt = -\partial\omega/\partial y, \quad d\omega/dt = \partial\omega/\partial t, \tag{A1.6a,b,c}$$

where d/dt is the derivative observed moving along the ray at the group velocity:

$$d/dt = \partial/\partial t + \mathbf{C_g}\bullet\nabla, \tag{A1.7}$$

where boldface indicates the vector group velocity.

Using (A1.5) and (A1.6), the ordinary differential equations which describe the ray paths and the variation of wavenumber along them can be written by differentiating the dispersion relation (A1.4):

$$dx/dt = \omega/k + 2\omega^2/\beta, \qquad dy/dt = 2\omega^2 l/\beta k, \tag{A1.8a,b}$$

$$dk/dt = 0, \qquad dl/dt = -2\omega^2\beta y/kc^2, \qquad d\omega/dt = 0. \tag{A1.9a,b,c}$$

Since there is no variation of the properties of the medium in the zonal direction or in time k and ω are constant along a ray. Each frequency is treated individually so ω is taken as given at the outset, while the zonal wavenumber k (upon which all the other variables depend) is set by the boundary condition at the eastern coast, as will be shown below.

We observe that the dispersion relation (A1.4) can be rewritten as:

$$-\beta k/\omega - k^2 = l^2 + (\beta y/c)^2,$$

where the left hand side is constant along a ray since k and ω are constant. Thus the maximum latitude reached by a given ray (denoted by the turning latitude $y_T$) occurs when $l = 0$, and is given by:

$$y_T{}^2 = (c/\beta)^2\,(-\beta k/\omega - k^2) = y_0{}^2 + (l_0 c/\beta)^2, \tag{A1.10}$$

where the subscript zero refers to the value of a quantity at the coast where the ray started. Rays are trapped about the equator.

The zonal component of the group velocity, dx/dt, is constant along a ray, so the x-position varies linearly with time. The parallel structure of the equations (A1.8b and A1.9b) for the meridional position and wavenumber suggests that a solution to these two can be found by differentiating either one and substituting the other to form a second order homogeneous ODE with constant coefficients which straightforwardly gives sinusoidal variations of both y and l. Following SAS, a scaled time coordinate is:

$$\theta = (-2\omega^2/kc)t, \tag{A1.11}$$

which increases by 2π while a ray crosses the equator twice and returns to its original latitude. θ is thus equivalently a distance coordinate. Since k is negative, θ is positive for t positive. Solutions to (A1.8) and (A1.9) can now be written:

$$x = x_0 - (c/2\omega)\,(1 - (2\omega y_T/c)^2)^{1/2}\theta \qquad \text{(A1.12a)}$$

$$y = y_T \cos(\theta + \theta_0) \qquad \text{(A1.12b)}$$

$$k = k_0 \qquad \text{(A1.12c)}$$

$$l = (\beta/c)y_T \sin(\theta + \theta_0) \qquad \text{(A1.12d)}$$

where $k_0$ is still to be determined and $\theta_0$ is chosen so that the argument of the trigonometric functions is zero at the first turning latitude of the rays. This will be true if:

$$\theta_0 = \pm \cos^{-1}(y_0/|y_T|), \qquad \text{(A1.12e)}$$

with the sign of the right hand side corresponding to the sign of $l_0$. The solution describes sinusoidal ray paths about the equator. Note that expressions (A1.12) give the ray variables x, y, k and l as functions of $k_0$, $y_0$ and $\theta$ only. It will shortly be shown that the initial wavenumber of each ray $(k_0,l_0)$ is also a function only of $y_0$ and the boundary condition at $(x_0,y_0)$. Thus only the two parameters $y_0$ and $\theta$ and the boundary condition are required to define all the ray variables (SAS).

The two remaining quantities of interest are the phase $\phi$ and amplitude A which complete WKB solutions to (A1.2). Using the definitions (A1.7) of the derivative along a ray and (A1.3) of the wavenumber components and frequency, we can write the rate of change of phase as measured by an observer moving along the ray at the group velocity:

$$d\phi/dt \;=\; k\,dx/dt + l\,dy/dt - \omega \;=\; \mathbf{k}\bullet\mathbf{C_g} - \omega, \qquad \text{(A1.13a)}$$

where $\mathbf{k}\bullet\mathbf{C_g}$ is the rate of change due to the motion of the observer and $-\omega$ the local rate of change (which is the same everywhere, always). The right hand side may be rewritten using expressions (A1.8) for the group velocity components and the ray solutions (A1.12b and c) to find:

$$d\phi/dt = -2\omega - 2\omega^2\beta y^2/kc^2, \qquad \text{(A1.13b)}$$

in which all quantities are constant except $y^2$, which is given by (A1.12b). Equation (A1.13b) may be (somewhat tediously) integrated in time to get a simple expression for the phase as a function of time along a ray:

$$\phi(t) = \phi_0 + \{k(x - x_0) + (ly - l_0y_0) - \omega t\}/\,2 - \omega t \;+\; n\pi/2, \qquad \text{(A1.14)}$$

where $\phi_0$ is the phase at the boundary at $t = 0$ (which will be required by the boundary condition to be zero all along the boundary, and is now set to zero). The factor $n\pi/2$ reflects the fact that the phase increases by $\pi/2$ as the ray passes a caustic (discussed further below). This expression takes into account both the changing location of the observer moving along the ray and the changing phase at any fixed location, so it is useful for time-stepping. It has the disadvantage common to time-stepping along a ray that the phase relation between two locations can be expressed only if they are both on the same ray. However, since the local rate of change at any location (x,y) is just $-\omega$, we may therefore project back in time (by adding $\omega t$ to (A1.14)) to find the phase distribution at $t = 0$ for all (x,y). Equivalently this pattern is the phase difference between locations (x,y) and the boundary at any time; it is denoted $\phi_d(x,y)$. $\phi_d$ is what the crest/trough pattern would look like from overhead at time zero (an example is in Fig. A1.6, fourth panel). The phase difference map is stationary since the medium does not vary in time; crests move across the pattern always parallel to isolines of $\phi_d$, at a rate proportional to the distance between isolines. Note that adding $\omega t$ to (A1.14) does not remove the term $-\omega t/2$ which appears within the curly brackets; this remains in the expression for the phase at (x,y,0). This is because the t in the curly brackets refers to the travel time to (x,y) with the group velocity; here it serves the function of a distance coordinate along the ray, and is now denoted t*, a function of (x,y), so that:

$$\phi_d \;=\; \{k(x - x_0) + (ly - l_0y_0) - \omega t^*\}/\,2 \;+\; n\pi/2. \qquad \text{(A1.15)}$$

The phase at any (x,y,t), where t is any local time can now be written:

$$\phi(x,y,t) = \;\phi_d(x,y) - \omega t. \qquad \text{(A1.16)}$$

As in the case of the ray variables, $\phi_d(x,y)$ may be written as a function of $y_0$, $\theta$ and the boundary condition only (knowing $y_0$, t* is a linear function of x since the zonal group speed is constant).

The variation of wave amplitude A along a ray is found from the principle of conservation of wave-action density for small amplitude waves with no damping. This is expressed:

$$\partial([E]/\omega)/\partial t + \nabla\bullet(C_g[E]/\omega) = 0, \qquad \text{(A1.17)}$$

where the square brackets indicate an an average over one wavelength; the quantity $[E]/\omega$ is the wave-action density (LeBlond and Mysak, 1978, section 6; Bretherton and Garrett, 1968). It must be kept in mind that the energy in (A1.17) is not just the amplitude of the meridional velocity, but includes contributions of both the kinetic and potential energy, which in general exchange along a ray as the wavelength varies. The wave-action density is proportional to the total wave amplitude squared and the frequency is constant along a ray so the rate of change of the amplitude along a ray may be written:

$$dA/dt = -(A/2)\, \nabla \bullet \mathbf{C_g}, \tag{A1.18}$$

which shows that the amplitude increases (decreases) as adjacent ray paths converge (diverge). This expression might be used for time-stepping, however in general there is no way while time-stepping to find out information about a second ray, in particular whether or not rays are converging or diverging. Therefore, it is necessary to have an expression for the amplitude as a function of $y_0$ and $\theta$, as we do for all the other variables of interest. Ripa (1989) showed that the Jacobian of the transformation from (x,y) to $(y_0,\theta)$ (between cartesian coordinates and sinusoidal rays), which is:

$$J = \frac{\partial(x,y)}{\partial(y_0,\theta)} = \frac{\partial x}{\partial y_0}\frac{\partial y}{\partial \theta} - \frac{\partial x}{\partial \theta}\frac{\partial y}{\partial y_0}$$

satisfies:

$$dJ/dt = J\, \nabla \bullet \mathbf{C_g},$$

which, coupled with (A1.18), shows that the amplitude is proportional to $1/|J|^{1/2}$, and can now be evaluated at any (x,y) knowing only $y_0$, $\theta$ and the boundary condition (Ripa, 1988):

$$A(x,y) = A_0(\omega)\, |J_0/J(x,y)|^{1/2}, \tag{A1.19}$$

where $A_0(\omega)$ is set by the decomposition into periodic frequencies of the Gaussian time history at the boundary (Fig. A1.1). The Jacobian can be evaluated by taking rewriting (A1.12a and b) in terms of $y_0$, $\theta$ and constants, and taking derivatives. The Jacobian decreases to zero at caustics where adjacent rays cross (see next section), indicating that the WKB solution is no longer valid since the amplitude found using the WKB assumption varies very rapidly (blows up) within one wavelength. However, as will be shown, the present experiments produce a caustic only in a very few peripheral locations (because of the shape of the eastern boundary), so this complication does not cause a major problem.

The form of the initial disturbance, which occurs nearly simultaneously along the entire eastern boundary (Fig. 4.1), implies that the appropriate condition at the boundary is that the longshore wavenumber be zero. The propagation of Rossby waves away from a boundary is conveniently found using the dispersion diagram (Longuet-Higgins, 1964). The diagram is found by manipulating the dispersion relation (A1.4) to the form:

$$(k + \beta/2\omega)^2 + l^2 = (\beta/2\omega)^2 - (\beta y/c)^2 = r^2,$$

which, on the (k,l) plane, is a circle centered at $(-\beta/2\omega,0)$ with radius r (Fig. A1.2). The circle represents the locus of all possible wavenumber vectors at the given frequency and latitude. For a fixed frequency the center is fixed but the radius increases at low latitude (the circle touches the origin at the equator); while at a fixed latitude the center moves left and the radius increases as the frequency decreases. The group velocity, which is the gradient of the frequency in wavenumber space, always points towards the center of the circle. The zonal wavenumber component k is fixed along a ray (k will be set by the boundary condition), but l and the radius of the circle vary with the latitude, so we may picture the circle with fixed center expanding and contracting with time along a ray, while the wavenumber vector is given by the intersection of the circle and the line k = constant. The turning latitude occurs where the group velocity is directly westward, which is when l is zero and the circle is smallest. Conversely, as the ray approaches the equator, the circle expands to touch the origin, so the fixed k implies that l is at its maximum/minimum ($l_{eq} = \pm\beta y_T/c$) and the group velocity is at its largest angle from the zonal. The diagram is extremely useful in visualizing the behavior of solutions satisfying the dispersion relation (A1.4).

The condition that the longshore wavenumber is zero means that the wavenumber vector at the boundary is perpendicular to the boundary, as shown in Fig. A1.2. Since wave-induced motion is to first and second order perpendicular to the wavenumber, the condition of no flow through the coast is satisfied. The perpendicular to the boundary may intersect the circle at two, one or no locations; if there is an intersection, then there is a possible Rossby wave which satisfies both the dispersion relation and the boundary condition, otherwise the disturbance is trapped to the coast. If there are two intersections, as in Fig. A1.2, then there is one possible wave which has group velocity towards and another away from the boundary; these waves form an incident/reflected pair. (Note that the group velocity reflects by Snell's law since the angle between the center of the circle and the two wavenumber intersections is halved by a line parallel to the coast.) The shorter of the two possible wavenumbers is the offshore propagating ray. If the coast is meridional, the initial group velocity of this ray is due west. On a sloped coast, the initial propagation is not due west, and since the circle shrinks away from the equator the group velocity at the coast becomes more angled from the zonal direction in higher latitudes (Fig. A1.2). The limiting case where the wavenumber perpendicular to the boundary just touches the edge of the circle is the poleward limit of possible Rossby waves leaving the boundary at the given frequency; this ray propagates parallel to the coast. If the coast is steeply sloped, an intersection becomes possible only when the circle is large, in other words when the frequency or latitude is small. Thus a sloped coast tends to emphasize the low frequency, low latitude waves.

The boundary wavenumber is found geometrically as the intersection of the circle at latitude $y_0$ and the perpendicular to the boundary through the origin. If $\gamma$ is the angle of this perpendicular from the zonal direction (see Fig. A1.2), $(k_0,l_0)$ can be written:

$$k_0 = (-\beta \cos^2\gamma / 2\omega)\,[1 - \{1 - (2\omega y_0/c \cos\gamma)^2\}^{1/2}] \qquad \text{(A1.20a)}$$

$$l_0 = k_0 \tan\gamma, \qquad \text{(A1.20b)}$$

showing that the initial wavenumber can be written as a function only of the boundary slope and the initial latitude. If the quantity in the curly brackets in (A1.20a) is positive, then the perpendicular intersects the circle and a Rossby wave satisfying both the boundary condition and dispersion relation exists.

The principal results of the preceding section are: 1) ray paths are sinusoidal about the equator; 2) for given frequency, the ray path through any point (x,y) is determined once the initial latitude and wavenumber of that ray is known (in fact, it is only required that the latitude and wavenumber at any other point on the ray be known), so it is not necessary to time-step along each ray. The computational problem is only in finding the latitude where the ray through a particular (x,y) left the coast; 3) the wavenumber, group velocity, phase difference from the boundary and amplitude are constant at any point (x,y), and these quantities are determined everywhere in the ray region once the ray paths are known.

## C. Ray results for individual frequencies

There are several issues which an examination of ray behavior for individual frequencies can resolve before consideration is given to the problem of the observed single pulse-like disturbance. Of particular interest is the possibility of rays crossing the equator; also the possible occurrence of caustics where the WKB theory breaks down. The shape of the eastern boundary will be found to be crucial for these questions.

Rays with period 0.5 years are shown in Fig. A1.3 for three coast shapes: purely meridional, sloped 50° from the meridional, and sloped in the northern hemisphere but meridional in the southern, which is an extremely crude representation of the west coast of the American continent. The boundary condition in each case is that of zero longshore wavenumber (equations A1.20); ray paths were calculated using equations (A1.10), (A1.11) and (A1.12). The 0.5 year period was chosen because the entire behavior can be seen in a reasonable distance; lower frequency waves make similar, but stretched, patterns (to a good approximation the pattern expands in both x and y in direct proportion to the period). Rays are shown in Fig. A1.3 leaving the boundary at 2° latitude intervals (excluding the equator) over the full latitude range at this frequency; each ray is traced while the scaled time parameter $\theta$ (defined by equation A1.11) increases by $2\pi$, so each ray crosses the equator twice and returns to its original latitude. The relative zonal extent of these rays are proportional to the zonal group speed.

In the case of the meridional coast (Fig. A1.3a), rays are symmetric about the equator and span the largest meridional range possible at the given frequency. Moving poleward, each ray has a slower group velocity than the previous one, so the cosine shapes in Fig. A1.3a become much shorter in x; equation (A1.20a) with $\gamma = 0$ shows that the polewardmost ray leaves the coast at 33.85° latitude and has zero zonal group speed by equation (A1.8a). (Thus this ray is not shown.) A prominent feature of the rays from a meridional coast is the caustic lines where adjacent rays cross; a caustic separates a region with two groups of intersecting waves from a region with no waves (more specifically from a region with *two fewer* wave groups, since in this pattern rays from north and south of the equator form overlapping but independent wave systems) (Lighthill, 1978, section 4.11). The energy-like quantity wave action density is concentrated at caustics because the ray paths converge (equation A1.17); an everyday example is the bright spots seen on the bottom of swimming pools in the sun which are caused by wavelets on the surface focusing rays of sunlight (Walker, 1988). The ray theory solution is valid as a ray approaches and after it leaves a caustic, but exactly at the caustic the WKB method predicts that the amplitude grows without bound. If the dynamics near the caustic are important, Airy matching can be used to get a solution valid across the caustic region (Peregrine and Smith, 1979). The Airy solution shows that the phase increases by $\pi/2$ each time a ray passes a caustic (Lighthill, 1978, section 4.11) as noted in equations (A1.14) and (A1.15). Two caustics are visible in each hemisphere; they meet at cusps on the equator near $x = -5900$ km and $-18{,}200$ km. SAS show that the position of the first cusp (where one might expect a focusing of wave energy) is approximately at $x = -\pi c/4\omega$; the caustic meets the coast at a 45° angle. The first (easternmost) caustics are composed only of rays originating in the same hemisphere as the caustic, while the second caustics include only rays from the opposite hemisphere. (A third set of caustics would be seen if the pattern was continued past $\theta = 2\pi$.) The primary wave regions (east of the first caustic) are seen to be "illuminated" by many individual rays, which at any location can be ordered by their simultaneously increasing turning latitude, decreasing zonal group speed and decreasing wavelength: first, the ray coming directly off the boundary; second, the ray past the caustic from the same hemisphere, third, the ray from the opposite hemisphere which has just crossed the equator; fourth the ray from the opposite hemisphere which has already past the turning latitude and is moving equatorward again. This list continues infinitely for a meridional coast; each successive ray is slower and represents a shorter wave from a higher latitude than the previous one.

A uniformly sloping boundary (Fig. A1.3b) distorts the pattern, which appears to be pushed over like the coastline. The wavenumber perpendicular to the coast points southwest as pictured schematically in Fig. A1.2, so the group velocity (towards the center of the circle) is northwestward everywhere along the coast, with the largest difference from zonal propagation at the poleward limits. (The ray exactly at the poleward limit initially propagates parallel to the coast; this is the limit where the wavenumber just grazes the dispersion circle.) Thus the southern hemisphere rays leaving the coast are propagating equatorward after passing their turning latitudes (and are converging), while in the north rays are approaching turning latitudes (and diverging). Since higher latitude rays are most affected by a coast slope, the pattern is bent over more than the coast since the turning latitude of each ray occurs further west of the coast than that of the ray just south of it; the line connecting the crest of each sinusoidal ray path is tilted more than the coast. The intersection of the wavenumber vector and the dispersion circle for a particular latitude is at a more negative value of k than would be the case if the wavenumber was directly westward (Fig. A1.2); thus the wave leaving each latitude is shorter than in the case of the meridional coast. The slope of the coast also means that the rays span a smaller latitude range, since there is a minimum radius of the circle which intersects the perpendicular to the coast.

The first caustic for most rays (originating both north and south of the equator) from the sloped coast is in the southern hemisphere, on a long curve near the equator which makes a smooth transition from southern to northern hemisphere rays at the same location ($x = x_0 - \pi c/4\omega$, $y = 0$) where the cusp was located in the case of the meridional coast (Fig. A1.3b). (This is because rays very near the equator are least distorted by the coast slope. Thus the location where the ray just south of the equator crosses the equator, which is very nearly the position of the previous cusp, is moved slightly east by the coast slope, while the first northern ray crosses slightly west of this.) West of the previous focus, rays from the north meet at a *south-facing* caustic. The cusp, where most of the northern rays meet for the first time, is south of the equator; a narrow caustic composed of the very highest latitude northern rays extends a short distance northeastward from the cusp. This important change in the pattern of the caustic means that most of the northern hemisphere region illuminated directly off the sloping boundary is not bounded in the north by a caustic. (This is seen more clearly in Fig. A1.3c, which has the same northern rays.) Rays from the north are diverging off the boundary. The region past the northern edge of these rays is comparable to the dark area outside a flashlight beam; there is no increase of wave action density at the edge, and no special computational treatment is necessary, as it would be if a caustic existed. There is only one less wave group outside the directly-illuminated region than inside, not two less as in a caustic-bounded system. (The caustic which spans the width of the northern hemisphere in Figs. A1.3b and c is composed of rays originating in the south, which overlie but are completely independent of the north-originating rays).

The uniformly sloping coast does not resemble the eastern boundary of the Pacific, however a very crude model of the American coast is a combination of a 50° slope in the north and a meridional coast in the south (Fig. A1.3c), which is a just a superposition of the northern-originating rays from Fig. A1.3b and the southern-originating rays from A1.3a. Like the uniformly sloping coast, most of the northern hemisphere region illuminated directly off the sloping boundary is not bounded by a caustic. The only caustic in the northern hemisphere is due to rays which have crossed the equator.

To examine whether the rays originating from a southern hemisphere meridional coast can be an important contribution to the physics in the north, it is necessary to look at the wavenumber, frequency and amplitude in the regions before and after the caustic. It is convenient to do this using one-year period waves, as shown in Fig. A1.4 for the wave variables directly off the boundary (primary rays), and Fig. A1.5 after the first caustic (secondary). These two figures contain exactly the same set of rays, which are shown overlapping in Fig. A1.3a, but now are separated before and after the caustic to allow the wavenumber, phase and amplitude to be contoured and studied. Note that at the caustic edge all the variables shown in one plot approach the values at the other side of the caustic in the other plot, and the ray paths (top plot) meet across the caustic. Only the southern hemisphere is shown; the northern hemisphere is of course just the mirror image. Rays cross the equator only after the caustic; the higher latitude rays cross the equator east of the low latitude rays (Fig. A1.5).

There is a large difference at any location in the wave properties of the two rays before and after the caustic, which is not due to anything occurring at the caustic (in linear ray theory variables except the amplitude vary smoothly along a ray through a caustic) but reflects the fact that the secondary ray through a given location originated at a much higher latitude then the primary ray (top plot). The wavenumbers after the caustic are typically nearly an order of magnitude larger than before the caustic (second and third plots). The phase pattern at time zero (fourth plot), which is the quantity $\phi_d$ defined in equation (A1.15), varies much more rapidly after the caustic than before (note that the contour interval is $2\pi$ before the caustic and $10\pi$ after); this is consistent with the ray theory definition of the wavenumber vector: $\nabla\phi = \mathbf{k}$. SAS note that these very short waves after the caustic would be especially damped by frictional dissipation in the real ocean. The amplitude (bottom plot, found from equation (A1.19)), which increases (decreases) as adjacent ray paths converge (diverge) shows the pathological nature of WKB solutions in the neighborhood of the caustic, where the amplitude is predicted to grow without bound. In the main body of the ray region, before the caustic, the amplitude shows a small increase until quite near the caustic, while after the caustic the amplitude is smaller by about a factor of two since the rays diverge widely (top plot).

In summary, rays originating at the nearly meridional coast of South America enter the equatorial zone with reduced amplitude and short wavelength, compared with the values of these quantities near the turning latitudes of each ray. Presumably, any damping in the real ocean would tend to dissipate these waves more strongly than the waves in the same location coming directly off the boundary. In addition, the probability of distortion of the slower, high-latitude ray paths by zonal advection and meridional shear in the rapid currents of the equatorial zone suggests that a hypothesis which depended on these rays crossing the equator as predicted by the linear equations would be highly speculative. It is not until quite far west that tropical latitude rays (which have reasonably large wavelength and group speeds) cross the equator. For annual period waves, rays originating equatorward of 30° latitude do not cross the equator and emerge from the waveguide in the opposite hemisphere until more than 12,000 km west of the boundary. The pulse-like signal which is being modeled here consists very largely of waves with periods much longer than one year (Fig. A1.1), so it is not expected that rays originating at the nearly meridional coast of South America and crossing the equator will significantly affect the physics in the northern hemisphere, except possibly far to the west. Therefore in the remainder of this work the assumption is made that rays entering the waveguide disappear from the ocean, and no wave energy enters the northern hemisphere except from the eastern boundary. This assumption makes for simplicity of calculation in the region of interest and eliminates only a very small contribution of the high frequency, low amplitude waves which are the only ones crossing the equator in the main region of interest.

There remains to examine the wavenumber, frequency and amplitude of waves from the tilted coast of North America, which are now assumed to be the only rays which illuminate the northern hemisphere ocean. Nine-month period waves are shown in Fig. A1.6. The ray paths (top plot) are seen to leave the coast heading poleward towards their turning latitudes, in contrast to rays from a meridional coast (e.g. Fig. A1.4. The location of the turning latitudes is neatly shown by the zero line of the meridional wavenumber l (middle plot); east of this line where l is negative all rays are propagating poleward and vice versa (see for example the dispersion diagram Fig. A1.2). The zero line is tilted more than the coast. The phase pattern relative to the boundary is similar to the case of the meridional coast, however the amplitude (bottom plot) is smaller over most of the mid-basin than at the coast because ray paths are diverging and wave action density is being conserved (equation A1.17). The slight packing of contours of amplitude in the southwest corner of the ray region is an indication of the caustic there. As discussed above (e.g. Fig. A1.3b), most of the northern hemisphere rays do not reach their first caustic until they cross the equator (the lowest latitude nine-month period ray at which meets a caustic north of 5°N is the ray from 30°N). The short northern hemisphere caustic occurs only at the higher frequencies which have very small amplitude to begin with in the present experiment, and then only where the highest latitude rays approach the equator, so it poses only a minor problem. More typical of the frequencies which make up the bulk of the pulse-like signal to be studied is the two-year period wave shown in Fig. A1.7. Although the qualitative features are the same as the nine-month period wave, rays are nearly due westward (top plot) and the amplitude is close to the boundary amplitude everywhere (bottom plot). If the plot was continued westward a caustic would not be found until more than 35,000 km west of the boundary near the equator, so it does not affect the solution even in a basin as wide as the Pacific. It is concluded that the WKB solution is uniformly valid for the low frequencies which are most important for the present experiment. For the high frequencies the slope of the coast moves most of the caustic into the equatorial zone. In practice, since the region of high WKB amplitude is very narrow (much less than one wavelength) (Fig. A1.6), high amplitudes occur only occasionally on even a relatively dense cartesian grid. WKB amplitudes more than twice the amplitude at the boundary were never found in more than 3 grid boxes out of 2622 at any frequency for the sloped coast, in contrast to the meridional coast where typically 30-50 boxes had high amplitudes. It is hypothesized that the amplitude increase near the caustic is not an important part of the dynamics of the response to the pulse-like disturbance on a sloping coast. Therefore, in the following experiment, any gridpoint for which the amplitude is found to be more than twice the amplitude at the boundary at a given frequency is dropped from the solution at that frequency.

## D. The total response to the observed event-like forcing: a summation over many frequencies

The ray tracing technique described above is based on the vorticity equation (A1.1) for the meridional velocity on the equatorial $\beta$-plane. The use of this equation displays the fact that the ray theory method is valid both in mid-latitudes and at the equator, and allows consideration of the question of whether or not wave energy from the southern hemisphere would be likely to cross the equator and affect the physics in the north. However, the disturbance under study is observed not in meridional velocity but in thermocline depth, which obeys a somewhat more complex (and much more rarely used) dynamical equation in the equatorial zone than does the meridional velocity (Philander (1979); LeBlond and Mysak (1978), section 15). Having determined (in part (c) above) that the signal of interest consists primarily of long low-frequency waves which emanate from the eastern boundary in the tropical, extra-equatorial region (and remain there), it is appropriate to make a quasi-geostrophic mid-latitude approximation by assuming that fluctuations of the meridional velocity diagnosed by ray theory are to first order balanced geostrophically by the pycnocline slopes. Alternatively, mid-latitude quasi-geostrophic theory could have been used from the beginning, in which case the governing vorticity equation would be written for the pycnocline depth anomalies h:

$$[(f/c)^2 - \nabla^2]\,\partial h/\partial t - \beta\,\partial h/\partial x = 0, \qquad \text{(A1.21)}$$

which is similar to (A1.1) (after dropping the $\partial^3 v/\partial t^3$ term) with v replaced by $v_g = (g'/f_0)\partial h/\partial x$

and $\beta y$ by $f = f_0 + \beta(y - y_0)$. For solutions of the form $h = A(x,y) \exp\{i\phi(x,y,t)\}$, the dispersion relation becomes:

$$\omega = -\beta k / (k^2 + l^2 + (f/c)^2),$$

which differs from the equatorial β-plane relation (A1.4) only in that $\beta y$ is replaced by f. It is useful to examine briefly how the mid-latitude ray equations differ from those on the equatorial β-plane. The mid-latitude approximation is valid only within a meridional range (much smaller than the radius of the earth) about the initial latitude where $f = f_0$. Defining $Y_0 \equiv y_0 - f_0/\beta$, where $Y_0$ is constant along a ray as long as the ray remains in the region of the approximation, allows the Coriolis parameter to be written $f = \beta(y - Y_0)$. Now mid-latitude analogies to every equation in part (b) above can be derived from (A1.21) in exactly the same form as the equatorial β-plane expressions based on (A1.1), with the only change being that the previous meridional position coordinate y (measuring actual distance from the equator) is replaced by $(y - Y_0)$ every time it appears. Similarly the starting position $y_0$ of each ray is replaced by $(y_0 - Y_0)$ and the turning latitude $y_T$ by $(y_T - Y_0)$. The ray paths, wavenumber and phase variation are found to be very closely as in the previous section for the equatorial β-plane case; the difference being due entirely to the small stretching of the meridional coordinate since the factor $Y_0$ is slightly different for each ray which starts at a different latitude. In the present case, where the region of interest is between about 5°N and 30°N, it makes little difference (less than 10%) which set of equations is used. For consistency with the discussion of ray theory in part (b) above, the use of the equatorial β-plane equations is continued.

In either case, whether a mid-latitude approximation is made explicitly by beginning with (A1.21), or the equatorial β-plane is used with the additional assumption that the meridional velocity is geostrophic, the analysis is now valid only away from the equator. The experiment is henceforth limited to the region north of 5°N latitude. As a consequence of the assumption of quasi-geostrophic long waves, to first order the wave amplitude is composed of potential energy only, which, for a single active layer with a rigid lid, is directly proportional to pycnocline depth fluctuations. This allows the observed thermocline disturbance to serve exactly as a boundary condition.

As mentioned in the introduction, the time-dependent boundary condition is that along the eastern boundary north of 5°N the pycnocline is displaced downward in a pulse-like fashion with a Gaussian time history (the halfwidth of the Gaussian is six months) and a total amplitude of 10 meters. The origin of the disturbance is unstated and immaterial to the subsequent evolution; presumably the source is a coastal Kelvin wave initiated by the deep equatorial pycnocline anomaly associated with the El Niño (Moore, 1968), however, as discussed in Section 3, the observations do not clearly confirm this hypothesis. The Gaussian time history centered at $t = 0$

may be decomposed as a sum of cosines all of which have zero phase at $t = 0$. In theory an infinite sum is required to exactly reproduce the Gaussian form; in practice a low frequency cutoff merely means that the Gaussian signal is periodic; the lowest frequency is chosen so that the repetitions are very far apart (in this case the Gaussian hump repeats (with reversed sign) every 240 years). The high frequency cutoff is chosen so that the "wiggles" about the Gaussian shape are sufficiently small; note that as the period gets smaller the latitude range does also, so including very high frequencies affects only a limited region near the equator. Figure A1.1 shows the amplitude at each frequency: these have fallen to 1/10th the maximum value at periods shorter than about one year and to 1/1000th the maximum value by periods shorter than about seven months. Experiments showed that continuing the summation to periods shorter than eight months produced essentially no further changes. The experiment described below has been carried out for a variety of coast slopes; a slope of 50° from the meridional was chosen to best represent the coast of Central America and Mexico between 5°N and 30°N.

The boundary condition sets the amplitude at the boundary at $t = 0$ for each frequency; then the rays and all the wave variables can be diagnosed for each frequency separately. As shown in part (b) above, the wave at a given position is fully specified knowing the boundary slope, frequency and the initial latitude of the ray passing through that point. The computational problem is only in finding the initial latitude of the ray passing through the given position. All variables are found on a cartesian grid with spacing of 200 km in the zonal direction and 1° latitude in the meridional direction. (A sensitivity test in which this grid spacing was reduced by a factor of ten in both directions gave indistinguishable results.) These gridpoints were looped over in the following manner: first the initial latitude of the southwesternmost gridpoint was found by searching up the coast from the equator until a ray was found which passed through that point. Each initial latitude was found to the nearest 1/100th of a degree latitude. The second gridpoint studied was at the same value of x and one gridbox north in y, for which the initial latitude is slightly north of the first, so the search was resumed from the first initial latitude at the coast. This method continued north until either the 50°N gridbox or the poleward limit of rays leaving the coast at the given frequency was reached. Then the next column of gridpoints to the east was worked with in the same manner, always moving north then east which minimized the computation since subsequent initial latitudes were always just slightly further north than the one before. Thus all variables were found over the entire grid for each frequency.

An alternative (the classical) method as used by SAS would have been to time-step along rays. In this case the computation would work up the coast, initiating rays at set latitude intervals and diagnosing the ray quantities at set time intervals along each ray, then gridding the results. There are two difficulties with time-stepping: first, since rays may diverge, it is necessary to start with a great number of rays in order to avoid holes in the final grid; while on the other hand since rays may converge, it becomes necessary to average over the several rays with different properties which may share a single grid box. Second, in order to find the amplitude at a given point the divergence of the ray paths must be known (equation A1.18); it is not possible while time-stepping to know the path of adjacent rays, so it becomes necessary to "remember" all the rays at once, and at each time step find $\nabla \bullet C_g$ directly, which is computationally very tedious. The present method finds the single ray which passes exactly through the center of each gridbox (if such exists), and finds the amplitude at that point through evaluation of the Jacobian (equation A1.19). After gridding of all ray variables for a given frequency, the pycnocline displacement at each point due to that frequency was found bimonthly over the time range from 5 years before the center of the eastern boundary event to 15 years after by an expression of the form:

$$h_\omega(x,y,t) = A(x,y) \cos(\phi_d(x,y) - \omega t),$$

where A(x,y) is found from (A1.19) and $\phi_d(x,y)$ from (A1.15). The total solution h(x,y,t) shown in the figures was then found by summing over the contributions $h_\omega$ of all frequencies at each location and time.

The total Rossby response to the pulse-like boundary disturbance on a sloping coast is mapped in Figs. A1.8 at selected times. Figure A1.9 shows the disturbance on the (x,t) plane at selected latitudes, which allows the estimation of propagation speed, and Fig. A1.10 gives a typical time history as would be observed in the western part of the ocean. Figure A1.11 shows time-latitude sections at the eastern boundary and at 15,000 km west of the origin. At t = 0, which is the time of maximum displacement (10 m) at the coast, the disturbance is much wider in the tropics (Fig. A1.8, top panel), reflecting the longer wavelengths required by the boundary condition near the equator. At successive times, the disturbance propagates away from the coast, much faster at low latitudes, so that after 15 years, the wave is gone from the study region, which is roughly the size of the north Pacific, everywhere south of 30°N (Fig. A1.8). One of the main motivations for the paper by SAS was to criticize earlier studies of Rossby waves which neglected dispersion and assumed that Rossby rays propagated due west at each latitude without turning (e.g. White, 1977). Results reported in part (c) above (Figs. A1.3 through A1.6) show clearly that medium to high frequency rays turn towards the equator, so the wave field differs substantially between the eastern and western regions, and thus dispersion and ray turning cannot be neglected. For sufficiently low frequencies, however, rays do in fact propagate nearly due west, even over the width of a basin as wide as the Pacific. Waves with periods of more than two years can be considered roughly non-dispersive (e.g. Fig. A1.7); for higher frequencies the turning of rays cannot be ignored (Fig. A1.6). (In a smaller ocean like the Atlantic, turning would be less important except at higher frequencies.) In addition, the slope of the Central American coast reduces the meridional propagation, as shown above in part (c). Since the decomposition of the Gaussian boundary time history puts most of the amplitude in low frequencies (Fig. A1.1), the total result of the pulse-like disturbance behaves very much, although not exactly, like a long wave limit non-dispersive wave. To a rough approximation, the disturbance simply moves west at the long wave speed ($c_{LWL} = \beta g'H/f^2$) for each latitude, retaining the Gaussian time history at any location (Fig. A1.8). There are three principal differences from the non-dispersive limit in the present experiment. First, the zonal propagation speed of the peak of the main front is about 80-90% as large as the long wave speed (with the larger discrepancies at low latitudes). Second, perhaps most important, in the long wave limit the amplitude of the wave remains the same while the waveform propagates westward, but in the presence of dispersion the amplitude of the main front decreases steadily, so that five years after the eastern boundary event the amplitude in the western part of the ocean is about 60% of the original (Fig. A1.8, sixth panel). This decrease is partly due to the fact that the higher frequency components turn towards the equator and do not reach the western ocean. Third, there is a wake behind the main front, consisting of alternating bands of positive and negative anomalies. These bands have crests which spread to roughly one to two years apart and propagate slower than the main front, so they fall steadily further behind the wave front (Fig. A1.9). Figure A1.10 shows the time history of the disturbance as it would be observed at 15°N, 13,000 km west of the boundary at that latitude. The wave front makes a smooth transition from the undisturbed fluid to the main peak which here has an amplitude of 6.9 m (compared with 10 m at the boundary), and peaks at 3.38 years after the event on the eastern boundary (compared with 2.91 years as would be predicted from the long wave speed). Behind the main front the wake consists of a decreasing train of oscillations; these continue to gain amplitude at the expense of the main front and increase in period and zonal wavelength the further west they propagate (Fig. A1.9). This kind of wave form (which is described by solutions to an Airy-type differential equation) occurs whenever an originally Gaussian wave-packet with components of varying group velocity evolves freely. (It is even possible to have the oscillatory part of the wave arrive at a given location before the main front if the group velocity decreases with increasing wavelength, as occurs with capillary waves.) Although a Gaussian halfwidth of six months was chosen to best represent the observed anomaly on the eastern boundary in 1972-73, experiments were also carried out with halfwidths of one year (which would be more like the 1982-83 disturbance) and three months. The speed of the main peak and the wavelength of the wake oscillations is the same in all cases, but dispersion is much enhanced by the shorter halfwidth, resulting in a reduced amplitude of the main peak and increased amplitude of the wake peaks.

At the eastern boundary, the total solution is, as expected, a Gaussian in time occurring simultaneously along the entire boundary. Figure A1.11 (top panel) shows the disturbance at the first gridpoint west of the boundary; the disturbance appears jerky because the distance from the boundary to the first gridpoint changes since the grid is rectangular but the coast is tilted. In addition, the disturbance occurs slightly later at the first gridpoint at high latitudes since the zonal propagation is so slow there that it takes an appreciable time to get from the boundary to the first gridpoint (Fig. A1.11, top panel). This phenomenon allows a qualitative resolution to the question of how different would the solution be if accurate account were taken of the fact that the observed disturbance actually occurs not simultaneously along the coast but somewhat later at high latitudes (Fig. 4.2), presumably because of the finite propagation speed of coastal Kelvin waves. The boundary condition in this case would look very much like Fig. A1.11 (top panel), with the disturbance appearing about six months later at 30°N than at the equator. Thus the simpler solution displayed in Figs. A1.8 through A1.11, derived from the assumption of simultaneous occurrence along the coast, passes through a state qualitatively like the more accurate boundary condition of delayed occurrence far from the equator. Thus this more accurate condition would produce a solution very much like the one shown, but shifted one or two gridpoints (2-400 km) east.

The linear inviscid dynamics used here are inadequate to describe the full effect of the Rossby front on the western boundary. Although the ray theory solution can consistently and straightforwardly be continued through a western boundary reflection similarly to how the eastern boundary was treated (e.g. the argument leading up to equations (A1.20)), the result of this calculation would be a set of extremely short (wavelength << Rossby radius), slow eastward propagating waves. Pedlosky (1965) showed that in the presence of dissipation (either bottom (Stommel, 1948) or lateral (Munk, 1950)) these small-scale motions will be trapped to the boundary, forming a thin boundary layer in the west (see also Lighthill, 1969; Anderson and Gill, 1975). Without friction (or non-linear advection of relative vorticity), this boundary layer will not occur; therefore the physics of the present model are insufficient to develop the correct western boundary solution. Nevertheless, since the incidence of Rossby waves at the western boundary has been suggested as a possible trigger mechanism for a subsequent El Niño (McCreary, 1983; McCreary and Anderson, 1984; Graham and White, 1988; Schopf and Suarez, 1988), it is worthwhile to show the pattern of the wave arriving at the western ocean (Fig. A1.11, bottom panel). The waveform, which left the eastern boundary at a single time, arrives much later and becomes weaker further from the equator. Compared with a similar experiment with a meridional coast, the principal difference is that the slope of the coast allows higher frequency rays to reach the west and add to the total (partly because of the shorter distance at high latitudes but also due to the poleward group velocity at the coast required by the boundary condition (e.g. Fig. A1.6)), so the amplitude of the main front in the far west is larger by about one-third when the coast is sloped.

It is important to note that a major simplification of the dynamics was made by assuming that the model ocean had a spatially uniform mean pycnocline depth, hence no mean geostrophic currents. Since in fact the zonal geostrophic currents in the tropical Pacific have typical speeds of the same order as long Rossby zonal propagation speeds in some regions it might be expected that the ray paths described in this section would be strongly modified by the observed mean currents. As shown in Section 2, section c, the modification is in part canceled between the potential vorticity gradient due to the pycnocline slope and the Doppler-shifting by the mean current; this surprising result has been called the "non-Doppler effect" by Held (1983) (see also Chang and Philander, 1988). The reader is referred to Section 2, section c for details; a few of the results of that analysis may be summarized as follows: 1) Zonal propagation speeds of long Rossby waves remain nearly the same in the presence of mean geostrophic currents as in a mean resting ocean due to the cancellation mentioned above (in the long wave limit the cancellation is exact), with the long gravity wave speed c chosen to reflect the mean pycnocline depth at that latitude. The major effect of mean currents is directly through the variation of c, so that in a westward mean current, where c decreases towards the equator due to the pycnocline slope, the long zonal speed will be smaller near the equator and larger near the poles than would be guessed from the overall mean pycnocline depth, while in an eastward current the opposite occurs. 2) In a westward mean current, meridional propagation speeds are reduced, while in an eastward current, they are enhanced. In both cases, the modification occurs most strongly for the shorter wavelengths. 3) Zonal propagation speeds of medium-length (long enough to be westward-propagating in a resting ocean) waves are increased by a westward mean current, so these speeds are closer to the long wave speed and dispersion is reduced. In an eastward mean current the opposite occurs. Figure 2.3 summarizes the dispersion characteristics of Rossby waves in mean zonal currents.

At the outset of this work the intention was to include the effects of the mean current structure in the ray tracing. If the only variability of the mean ocean is meridional (as it was taken to be in Chang and Philander, 1988), then the analysis in Section 2, section c shows that it is relatively straightforward to do this (although then the ray paths are no longer sinusoidal so the simple method of analysis used in part (b) above would not be possible and time-stepping would be necessary). However, the present work is crucially dependent on the existence of the eastern boundary, which requires zonal variability of the zonal mean currents and also meridional mean currents in order that there be no mean flow through the coast. The addition of zonal variability to the problem makes it highly intractable, since if $\partial/\partial x \neq 0$, then the zonal wavenumber k is no longer constant along a ray (equation A1.6a), and the fundamental differential equations (A1.8) and (A1.9), in which k appears repeatedly, become much more difficult to solve, even with simple mean fields. Therefore, after much study, the effort was abandoned for the present. Four qualitative conclusions can be offered: First, in the NEC region 10°N to 25°N, there is expected to be little modification to the ray paths since the bulk of the rays are long waves with small meridional propagation to begin with (e.g. Fig. A1.7). Reducing the meridional group speed will hardly alter these ray paths at all. The main change in ray paths due to the westward flowing NEC will be felt by the high frequency rays, which will tend to turn less towards the equator than if there were no mean current. Thus one qualitative difference from the ray results presented above is expected to be that more of the shorter (but still westward-propagating) waves will reach the western ocean in the NEC region, so the solution would look more like the long wave limit. This will reduce the amplitude loss noted as the front moved west (Fig. A1.8), and also the wake behind the main front which is due to dispersion. Second, in the NEC region the major modification to the ray results presented here will be due to the direct effect on the local long wave speed by the changing pycnocline depth, which is roughly 50% deeper near 20°N than near 10°N all across the basin (Fig. 3.1). According to equation (A1.26) the long wave speed will have a smaller meridional gradient than if there were no mean current so the main front will be more meridional in orientation than shown in Fig. A1.8. The value 3 m/s chosen for c in the calculations is more typical of conditions near 15°-25°N west of 150°W (Fig. 2.2), so the modification would appear as a slowing of the front by 30-50% near 10°N. A timestepping calculation with a realistic meridional pycnocline slope showed that the main wave front approximately retains its form in the NEC region but is slowed by the reduced depth near 10°N. Third, since in the southern hemisphere the thermocline slope is up towards the equator from about 20°S to the equator (in the South Equatorial Current), rays will tend to turn less towards the equator, thus reducing the possibility of southern hemisphere rays crossing the equator, further supporting the earlier conclusion (in part (c) above) that southern-originating rays will not affect the dynamics in the north. Fourth, the most likely location for strong modification of ray paths in the tropical Pacific is in the NECC region between 5° and 10°N. This eastward current increases the meridional component of the group velocity, thus rays tend to pass rapidly across the current into the equatorial waveguide. Only the very longest waves can propagate zonally for long distances in this region.

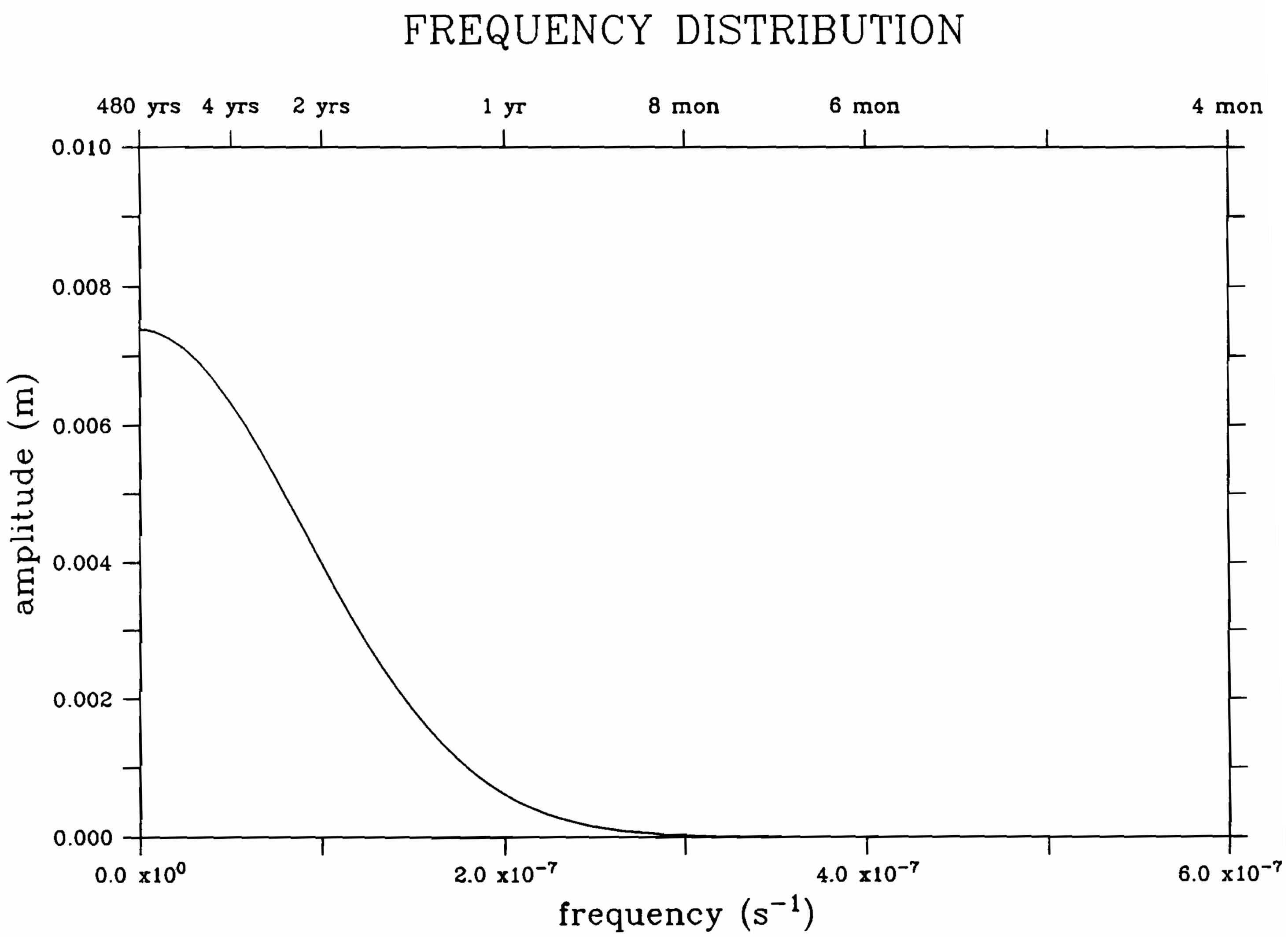

Figure A1.1. Frequency distribution of the gaussian pulse at the eastern boundary.

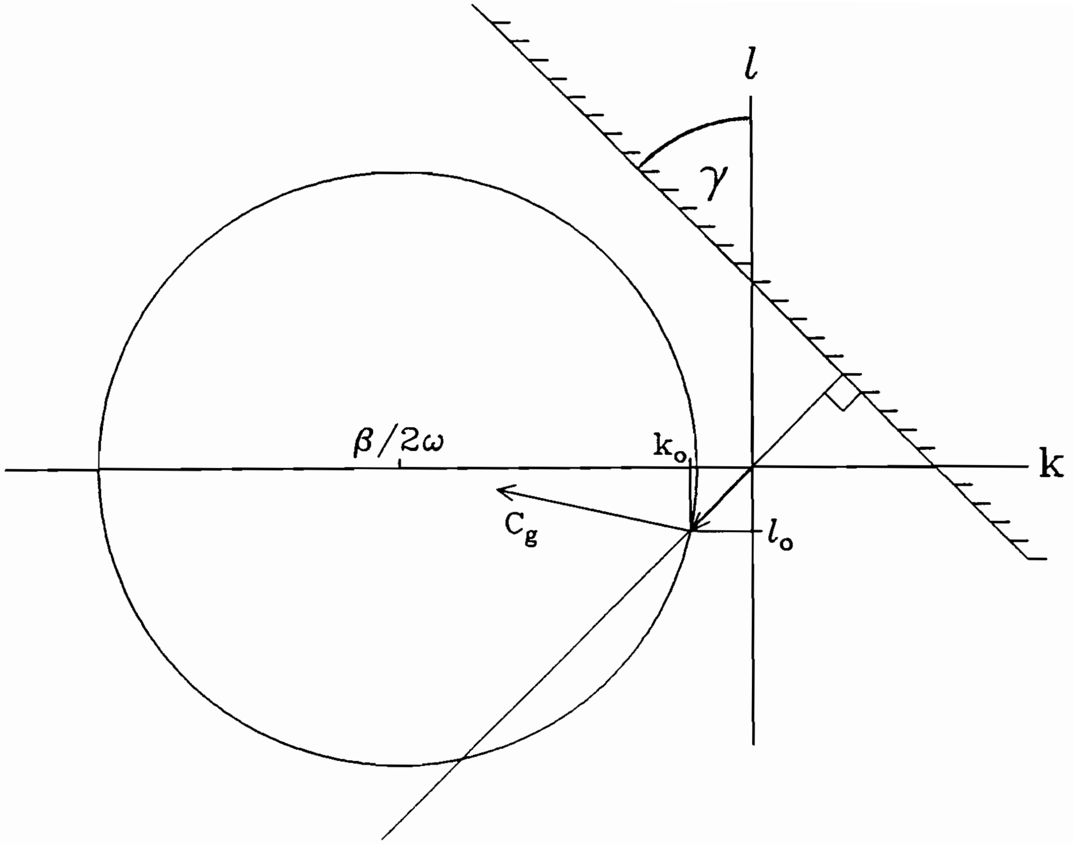

Figure A1.2. Schematic wavenumber diagram for Rossby waves reflecting from an eastern boundary, which is indicated by hatching and is at an angle $\gamma$ from the meridional. The locus of possible wavenumbers (all emanating from the origin) satisfying the dispersion relation (A1.4) is a circle with center at $k = -\beta/2\omega$, $l = 0$. The wavenumber vector with zero longshore component is perpendicular to the boundary, and here intersects the circle at two points, thus there are two wavenumbers which satisfy both the dispersion relation and the boundary condition. The group velocity vector (denoted $c_g$) points towards the center of the circle, so one of the possible waves is offshore propagating and the other onshore propagating.

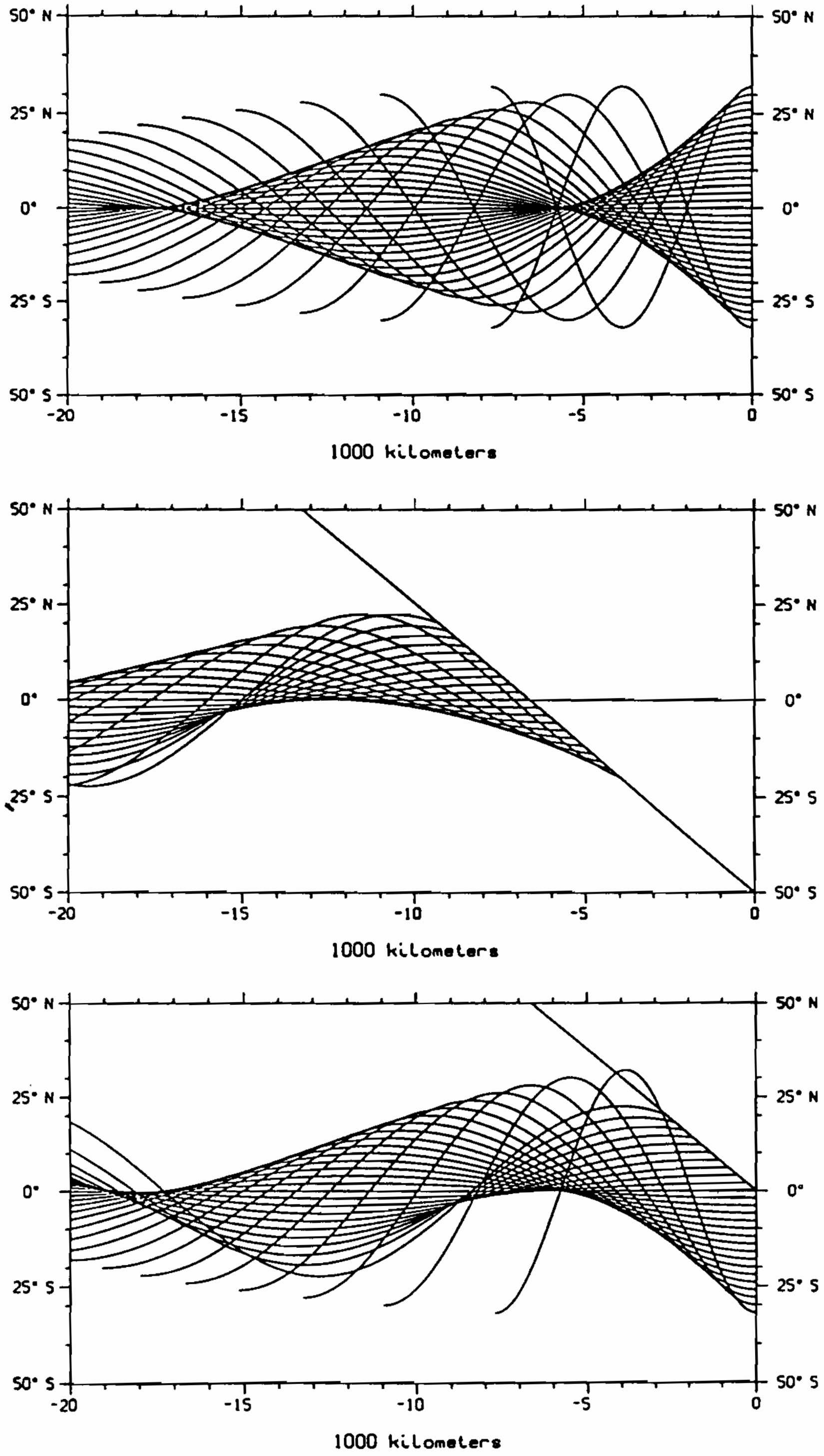

Figure A1.3. Ray paths for rays of one-half year period leaving a meridional coast (top), a sloped coast (middle), and a coast which is meridional in the southern hemisphere and sloped in the northern hemisphere (bottom).

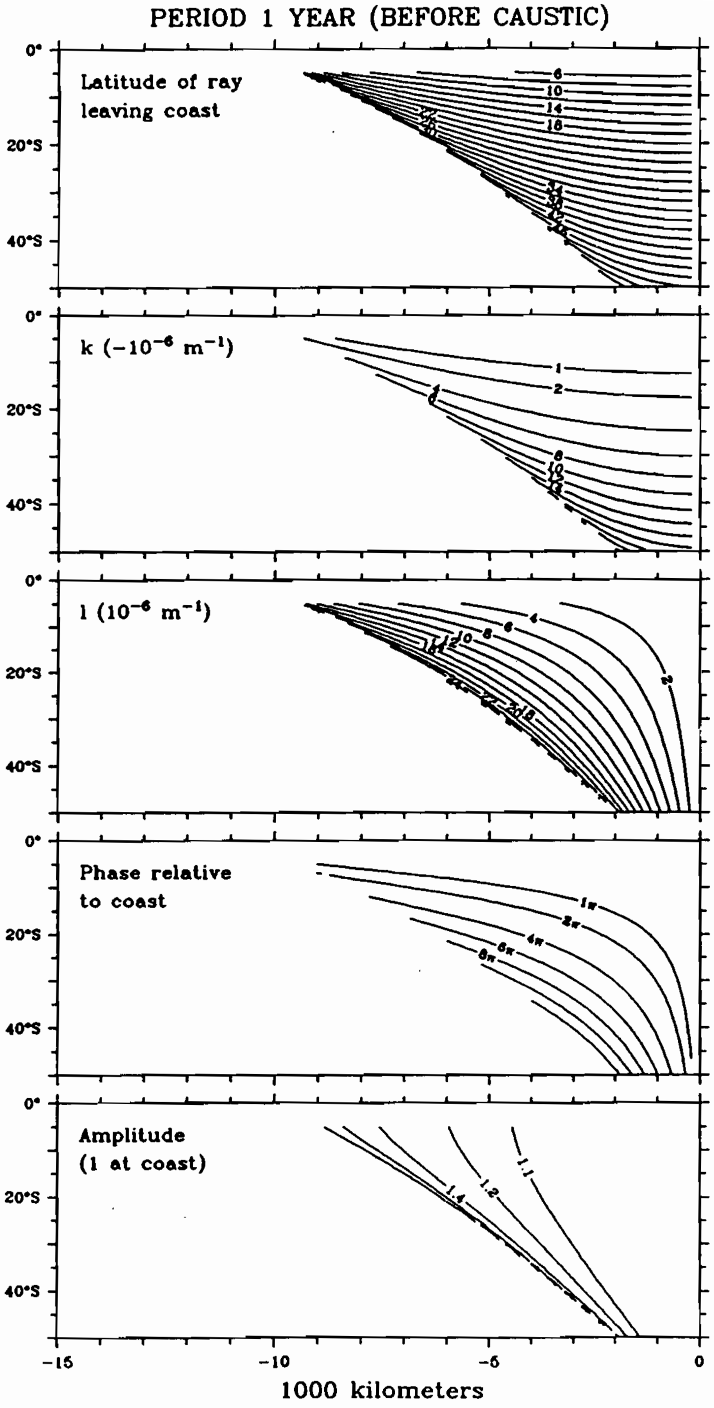

PERIOD 1 YEAR (BEFORE CAUSTIC)

Figure A1.4. Ray variables for rays of period one year leaving a meridional coast before the first caustic. Top: latitude of origin at the coast of rays. These contours show the ray paths leaving the boundary at 2° latitude intervals. Second: zonal component of the wavenumber vector. Since k is constant along a ray these contours also fall on ray paths. Third: meridional component of the wavenumber vector. Fourth: phase of the wave relative to the phase at the coast (the quantity $\phi_d$ given by equation (A1.15)). Bottom: amplitude of the wave found from equation (A1.19).

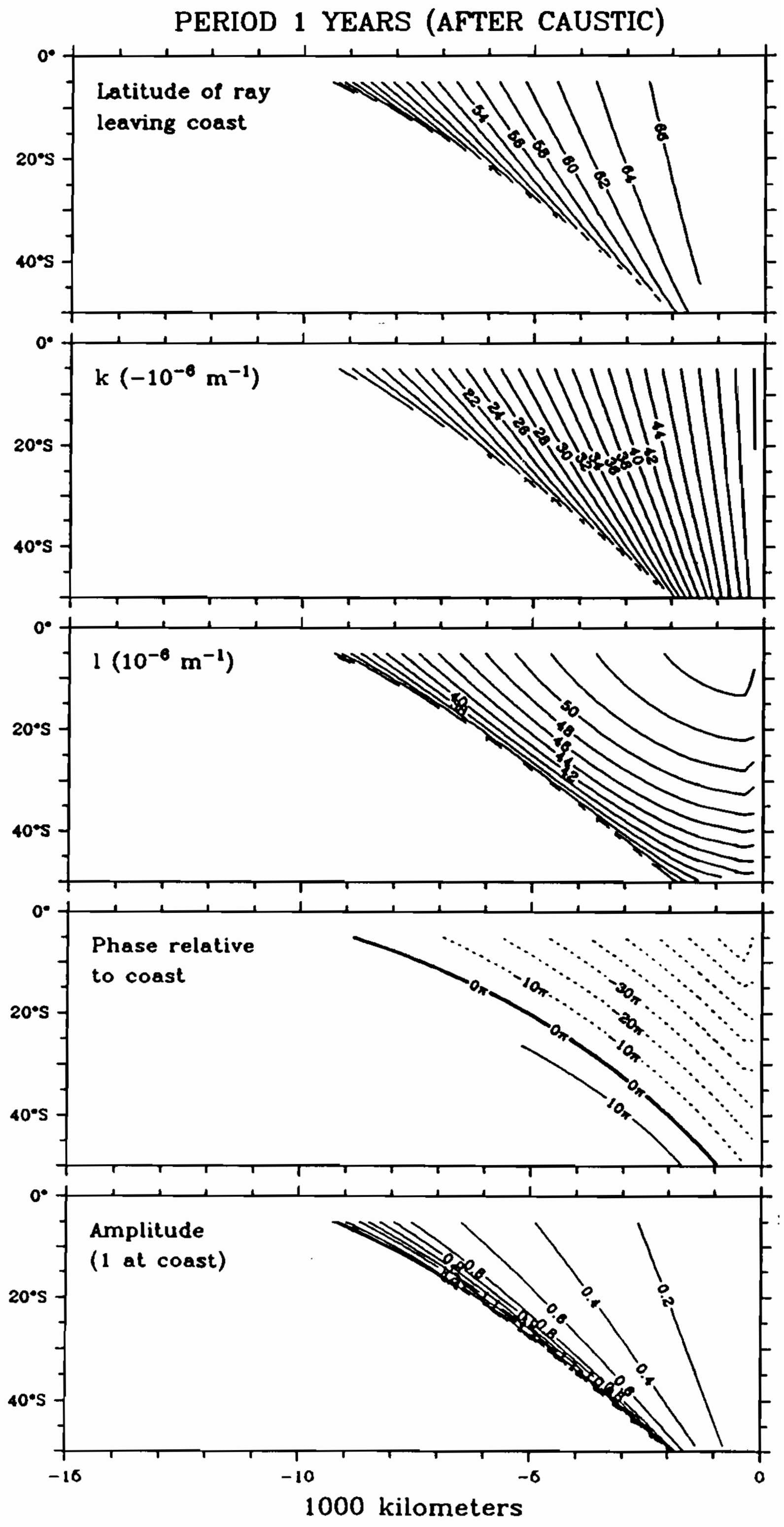

Figure A1.5. As Figure A1.4 but for rays *after* the caustic.

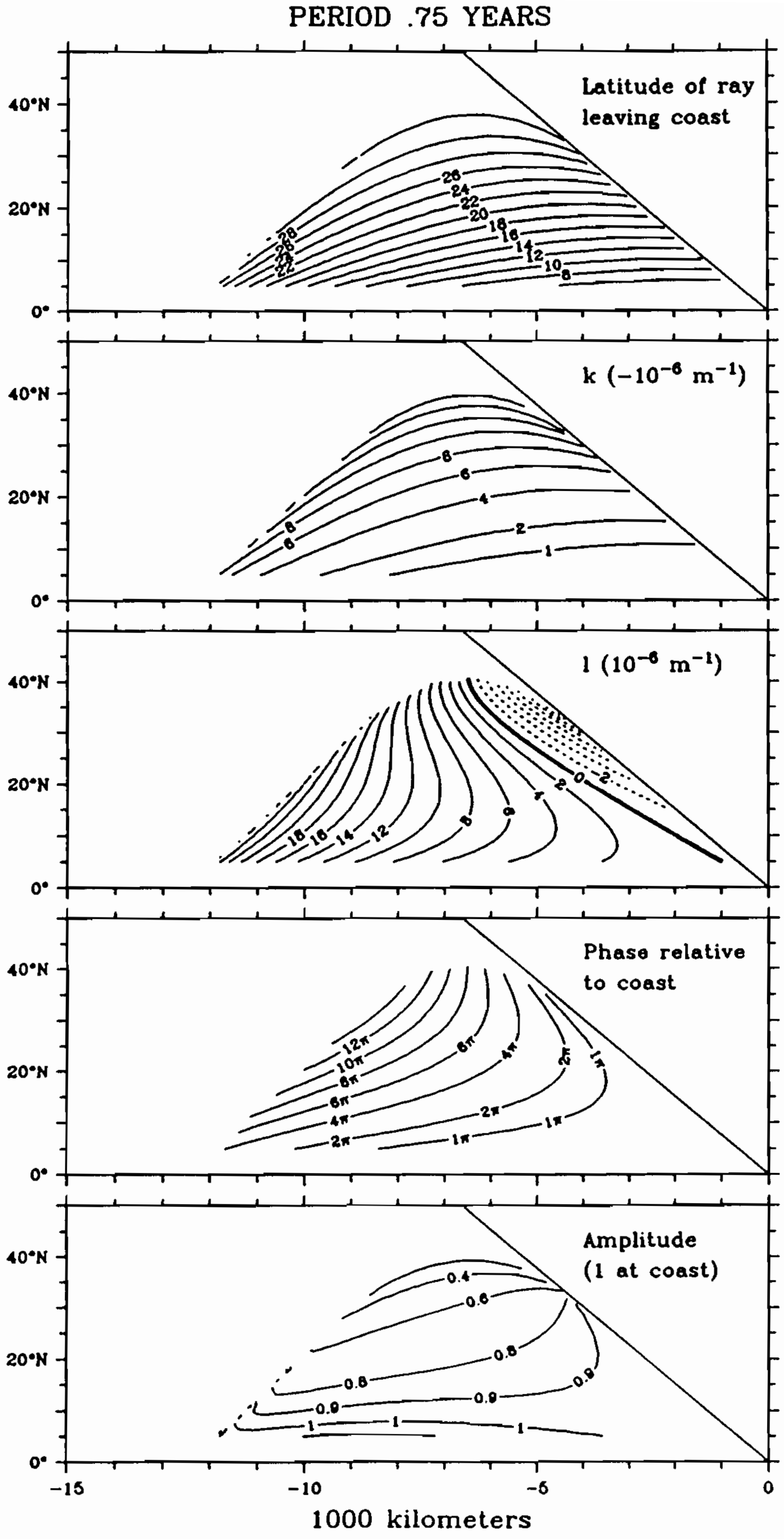

Figure A1.6. As Figure A1.4 but for rays of period 0.75 years leaving a coast sloped 50° from the meridional.

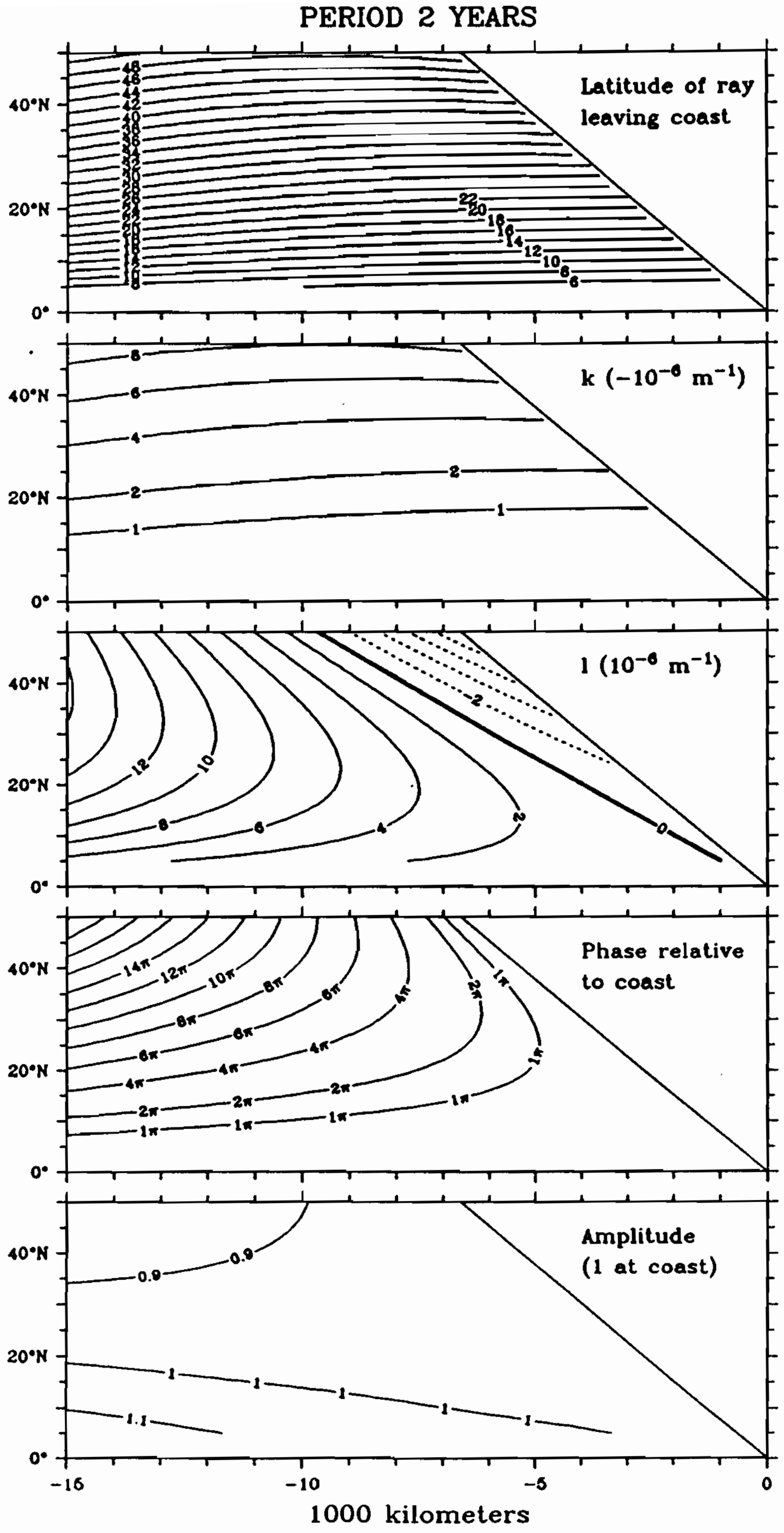

Figure A1.7. As Figure A1.4 but for rays of period two years leaving a coast sloped 50° from the meridional.

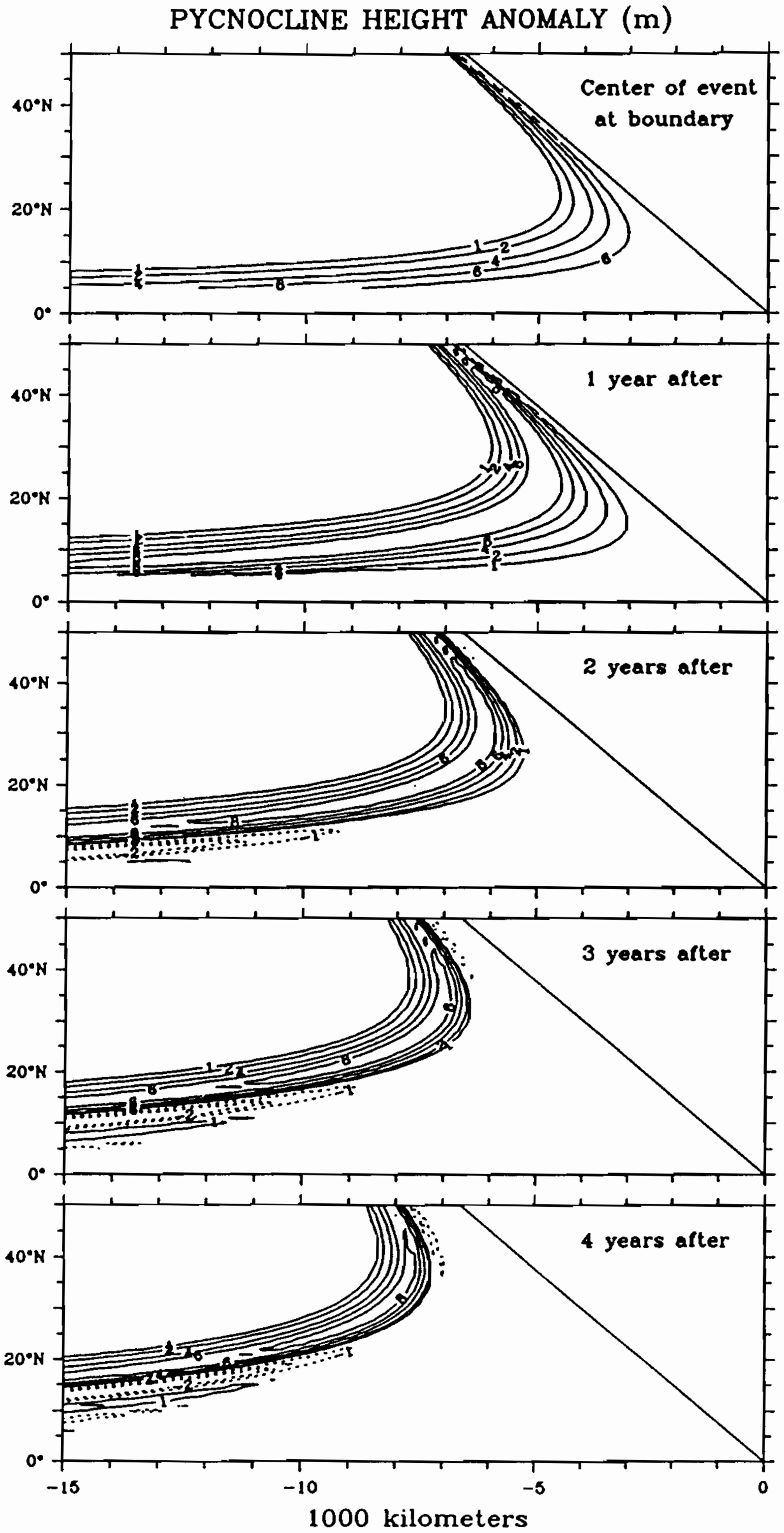

Figure A1.8. Pycnocline height anomaly (m) maps showing the time evolution of a pulse leaving the sloping boundary.

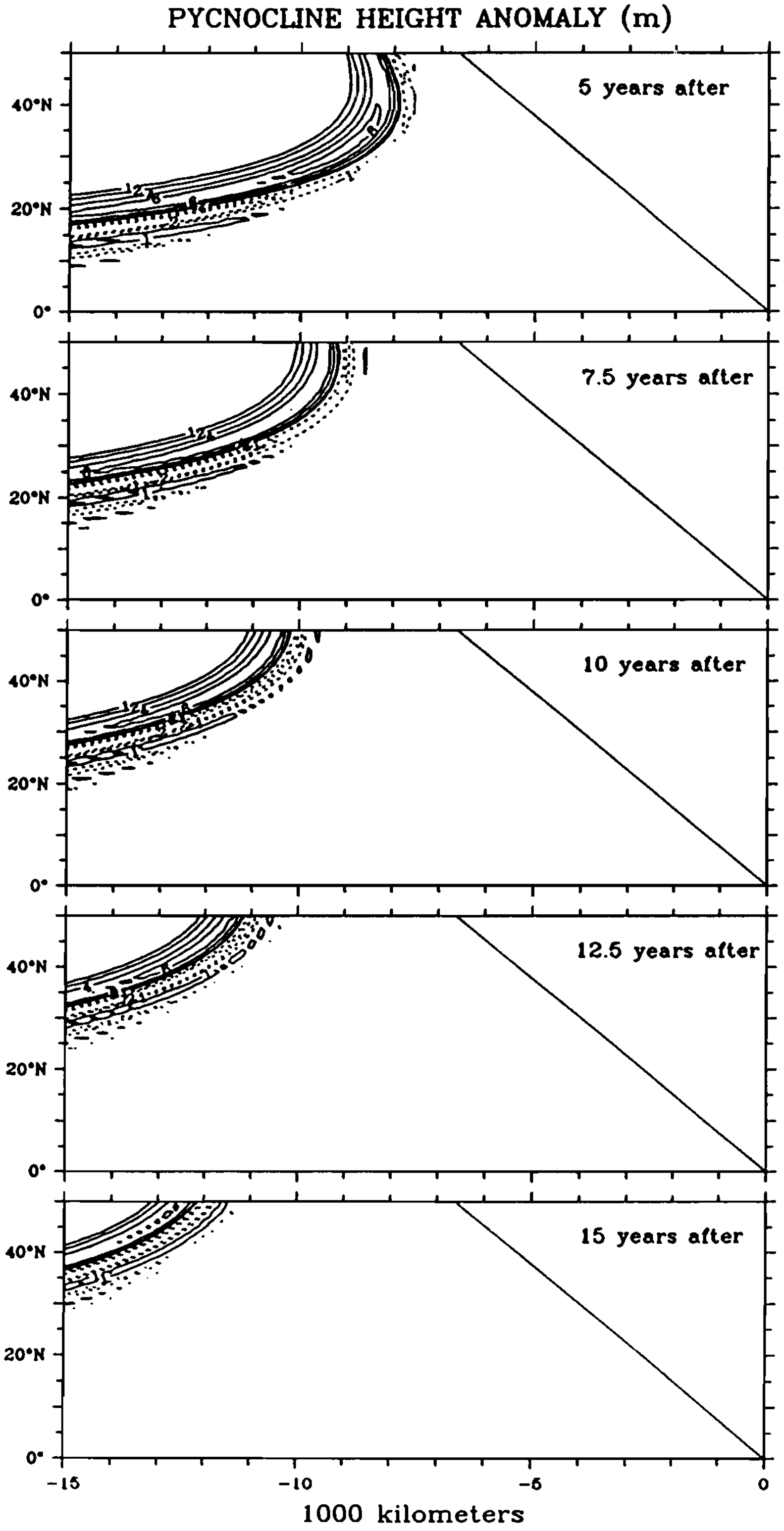

Figure A1.8 (continued).

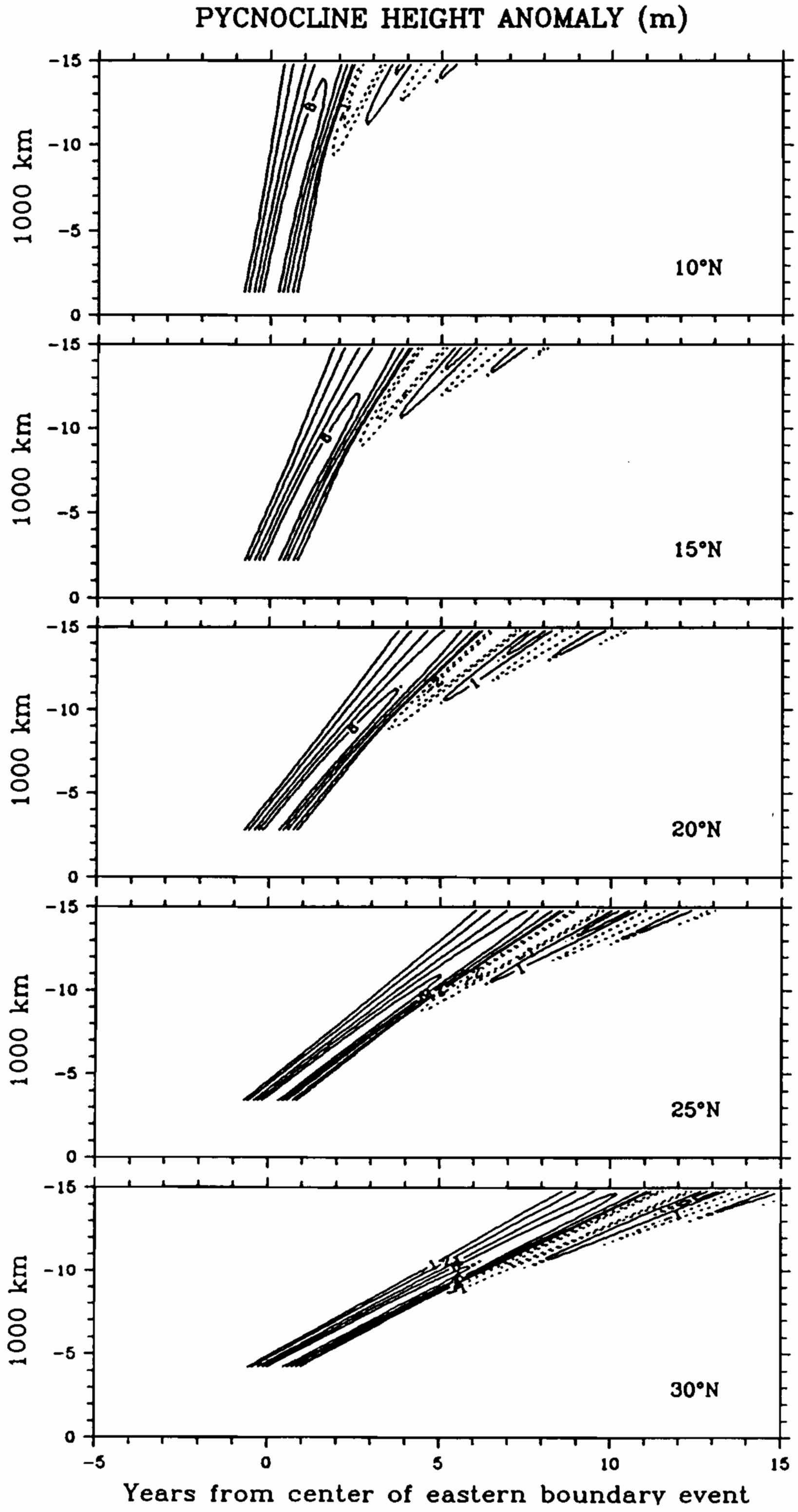

Figure A1.9. Time history of pycnocline height anomaly (m) at selected latitudes for a pulse leaving a sloping boundary as in Figure A1.8.

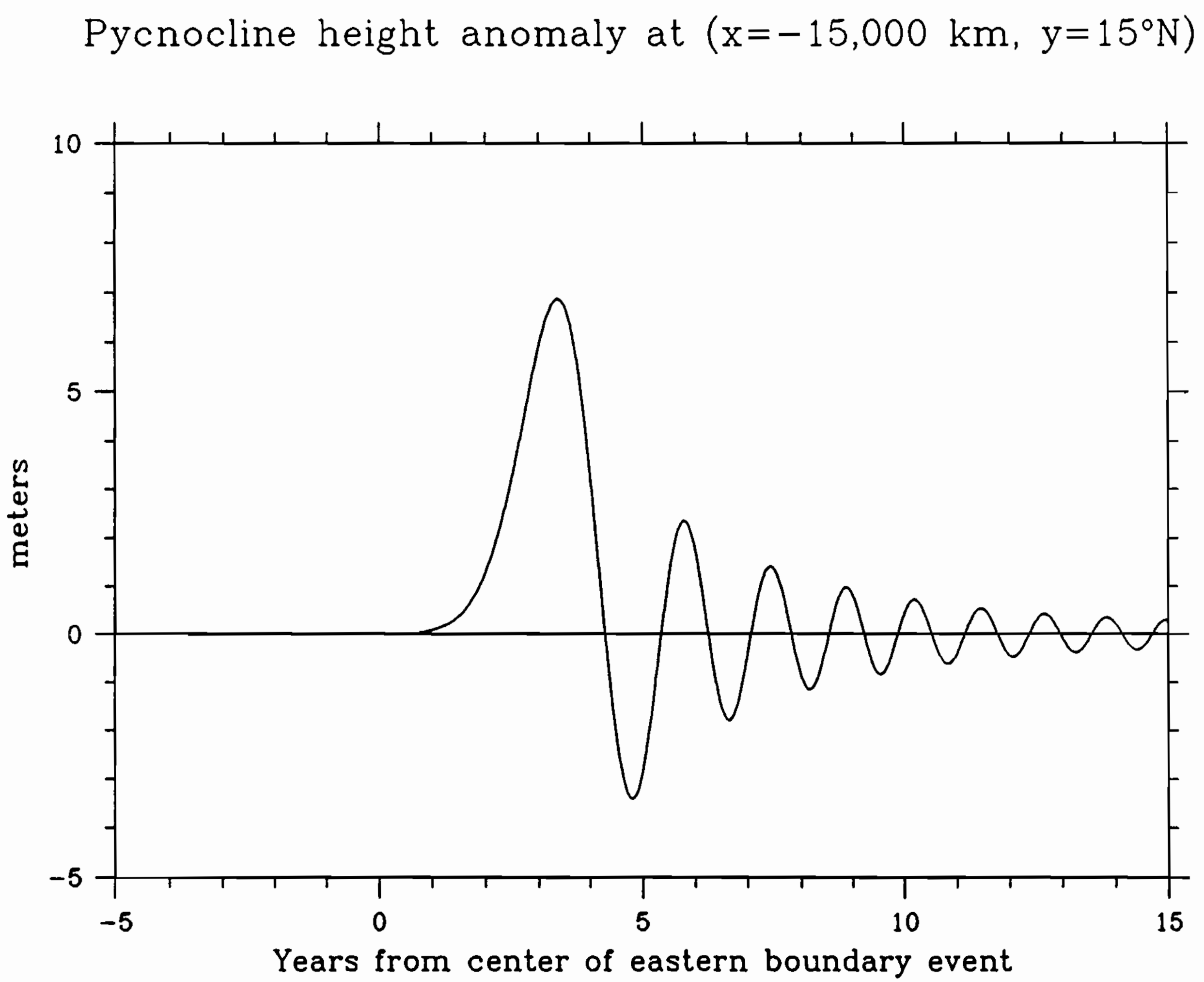

Figure A1.10. Time history of the pycnocline height anomaly (m) at x = -15,000 km, y = 15°N due to a pulse leaving a sloping eastern boundary as in Figures A1.8 and A1.9.

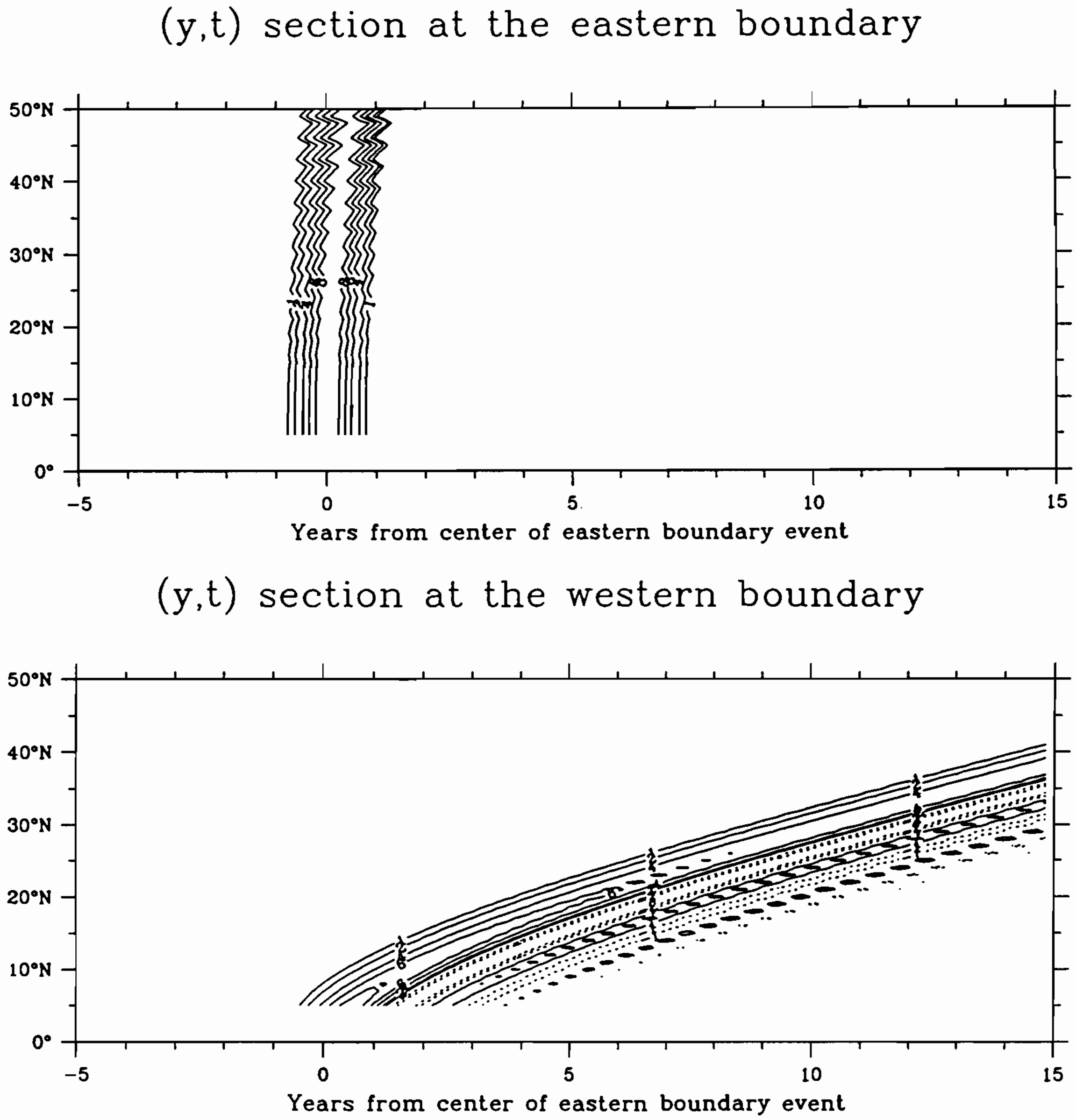

Figure A1.11. Time history of pycnocline height anomaly (m) along the eastern boundary (top) and at x = -15,000 km for a pulse leaving a sloping eastern boundary as in Figures A1.8 and A1.9.

# APPENDIX 2: Mean Vertical/Zonal and Vertical Meridional Temperature Sections

Although most of this work concerns the variability of 20°C isotherm depths, it is useful to have plots of the full mean thermal structure as a reference. These plots were made by combining all XBT and MBT data, after quality control (see Section 1), for a total of 144,297 profiles. For the purpose of constructing these mean vertical sections, the data were gridded into 2° latitude, 5° longitude and 10 meters depth gridboxes and averaged. Thus, for example, the mean zonal section at 10°N includes data within 9° to 11°N, and the mean meridional section at 170°W includes data within 172.5° to 167.5°W. Each section is smoothed three times with a Laplacian smoother in both depth and either latitude or longitude. Contours are given every degree centigrade, with every fifth contour bolded.

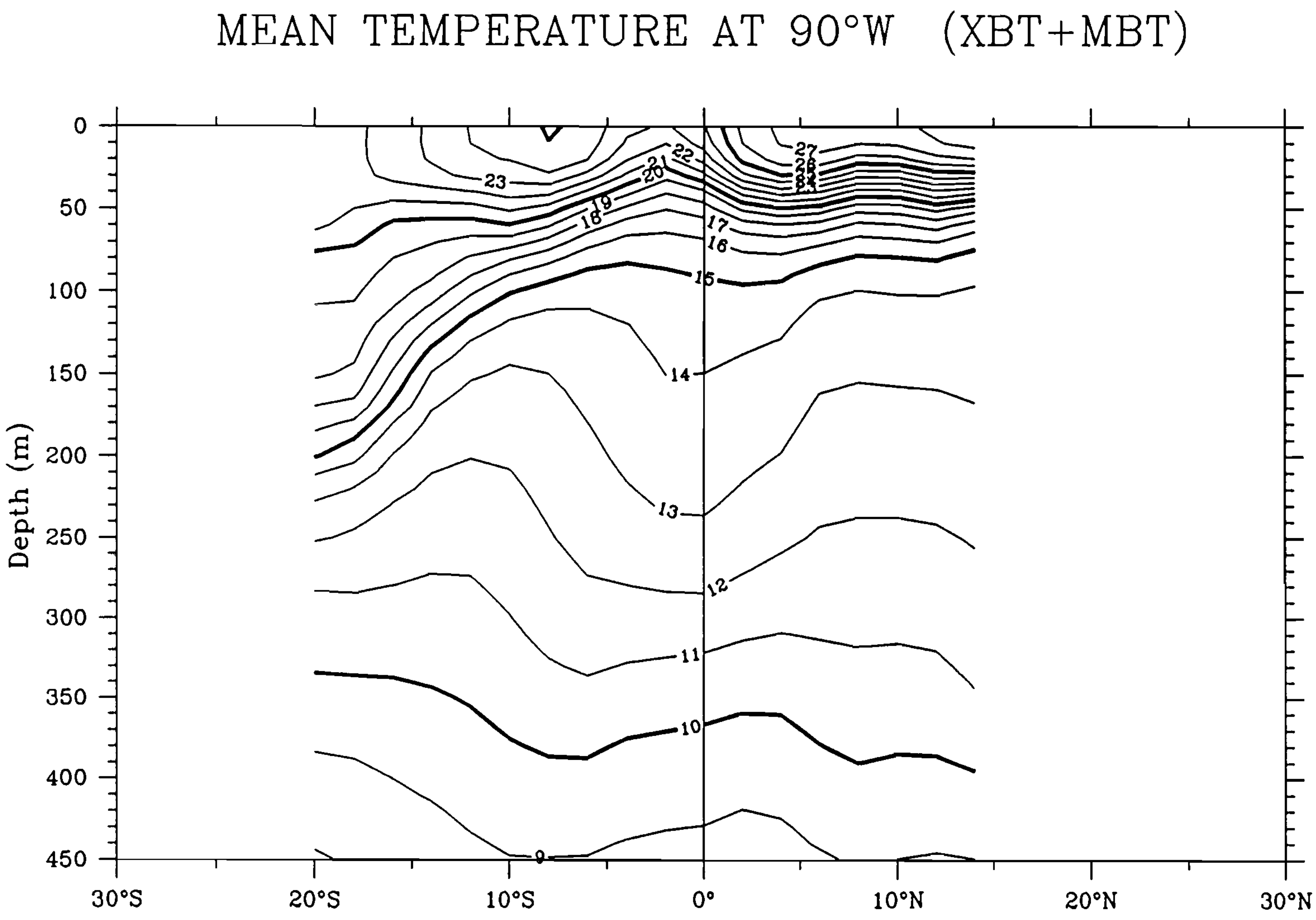

Figure A2.1a. Mean temperatures during 1970 through 1987 at 90°W.

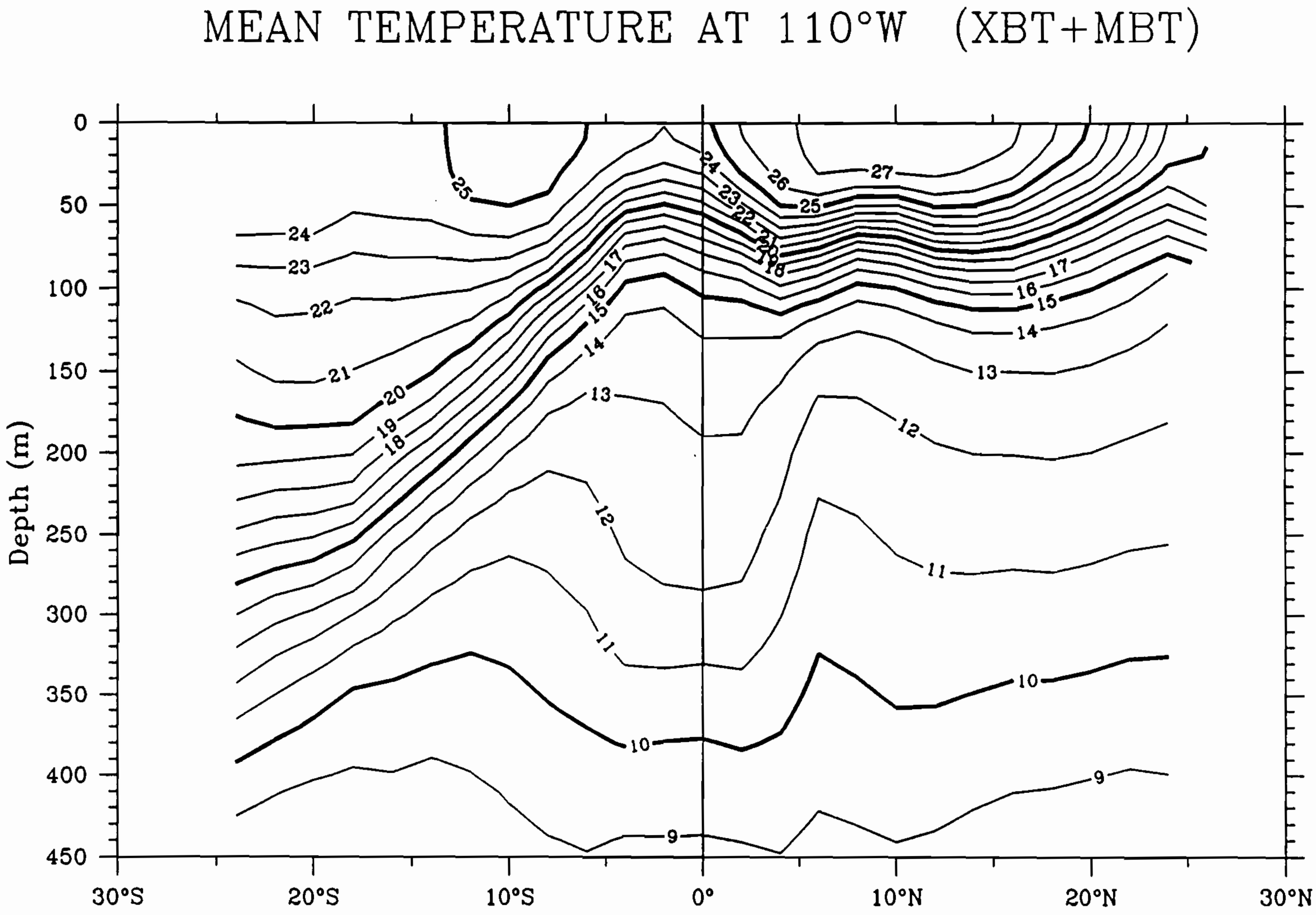

Figure A2.1b. Mean temperatures during 1970 through 1987 at 110°W.

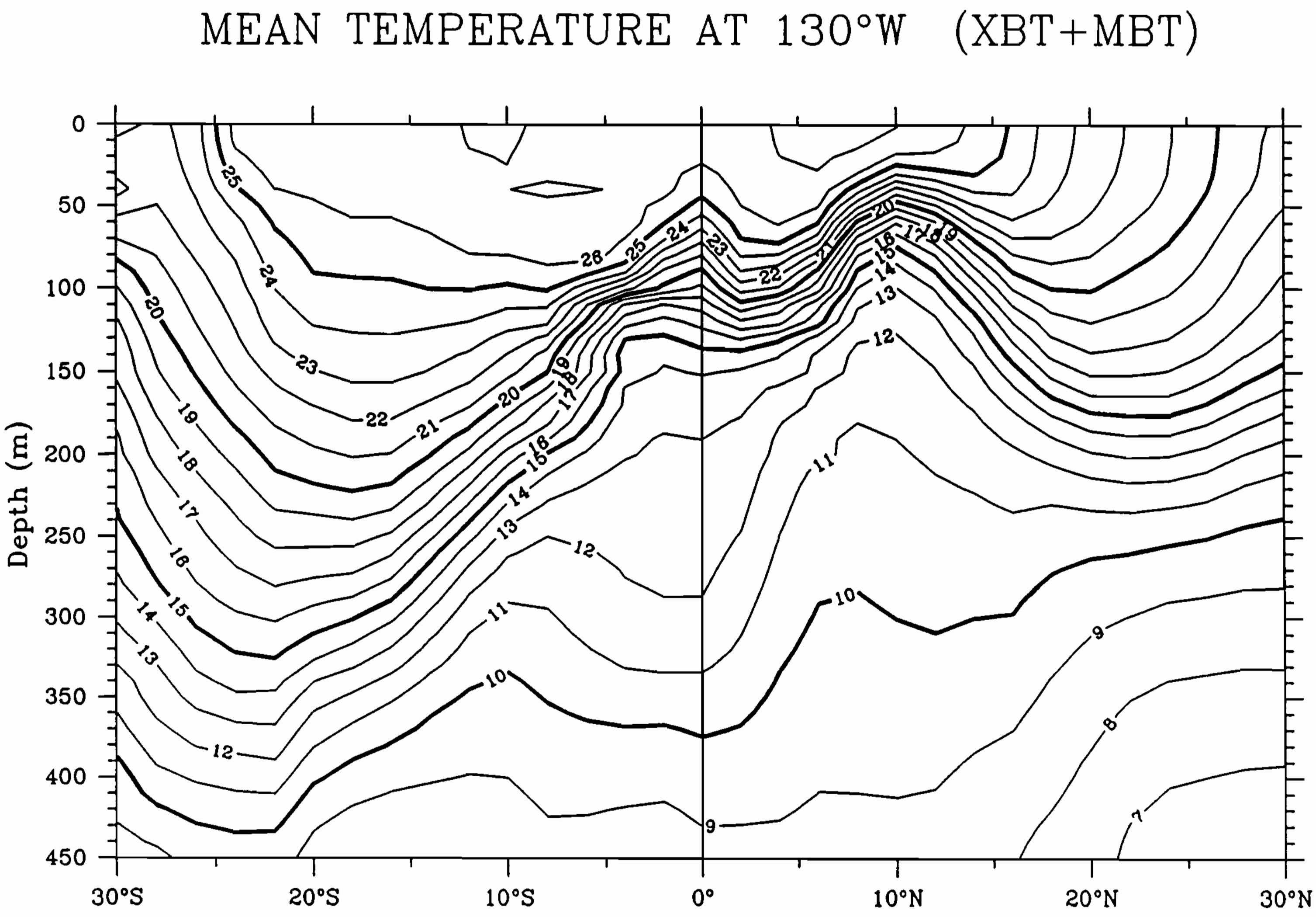

Figure A2.1c. Mean temperatures during 1970 through 1987 at 130°W.

MEAN TEMPERATURE AT 150°W (XBT+MBT)

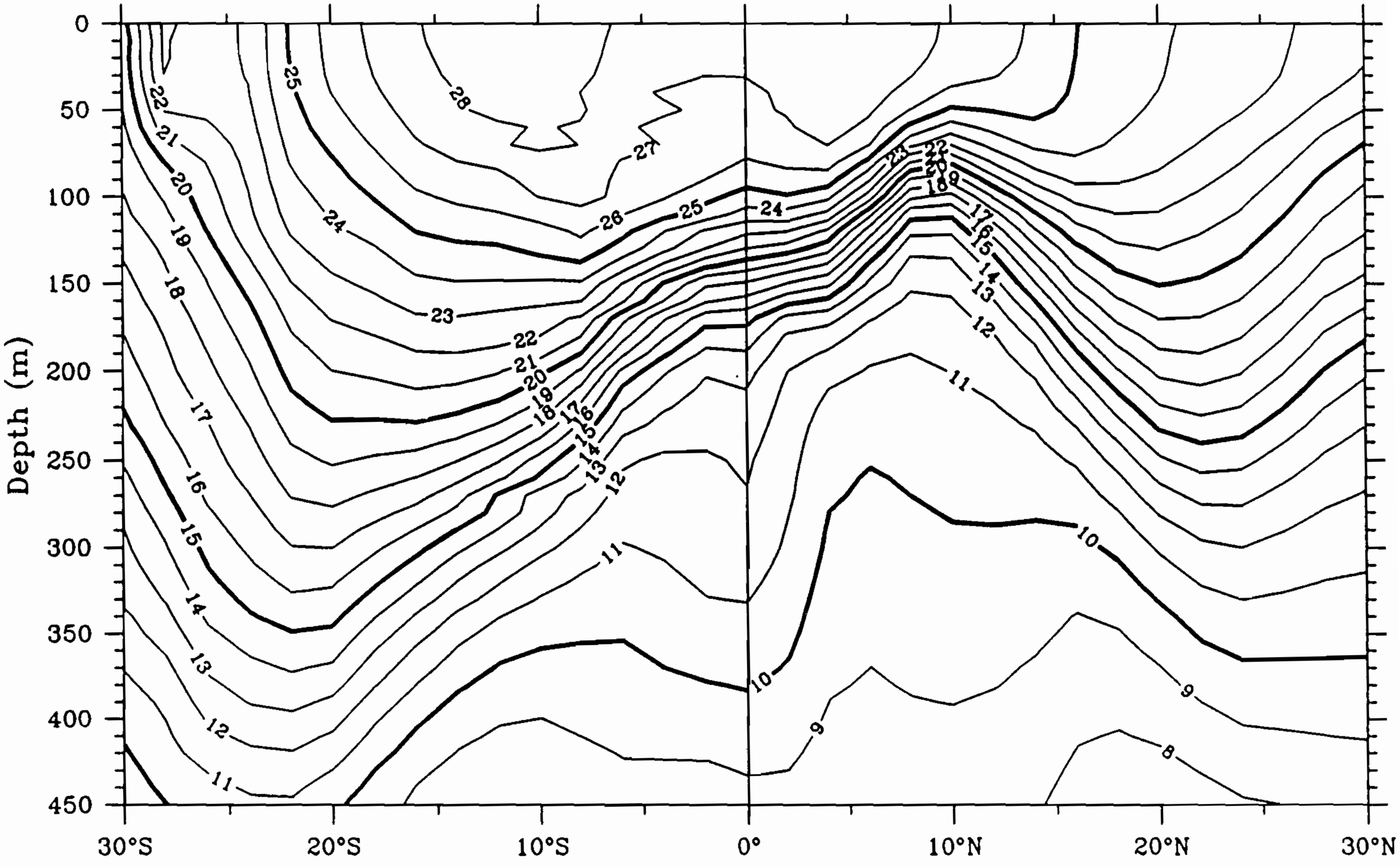

Figure A2.1d. Mean temperatures during 1970 through 1987 at 150°W.

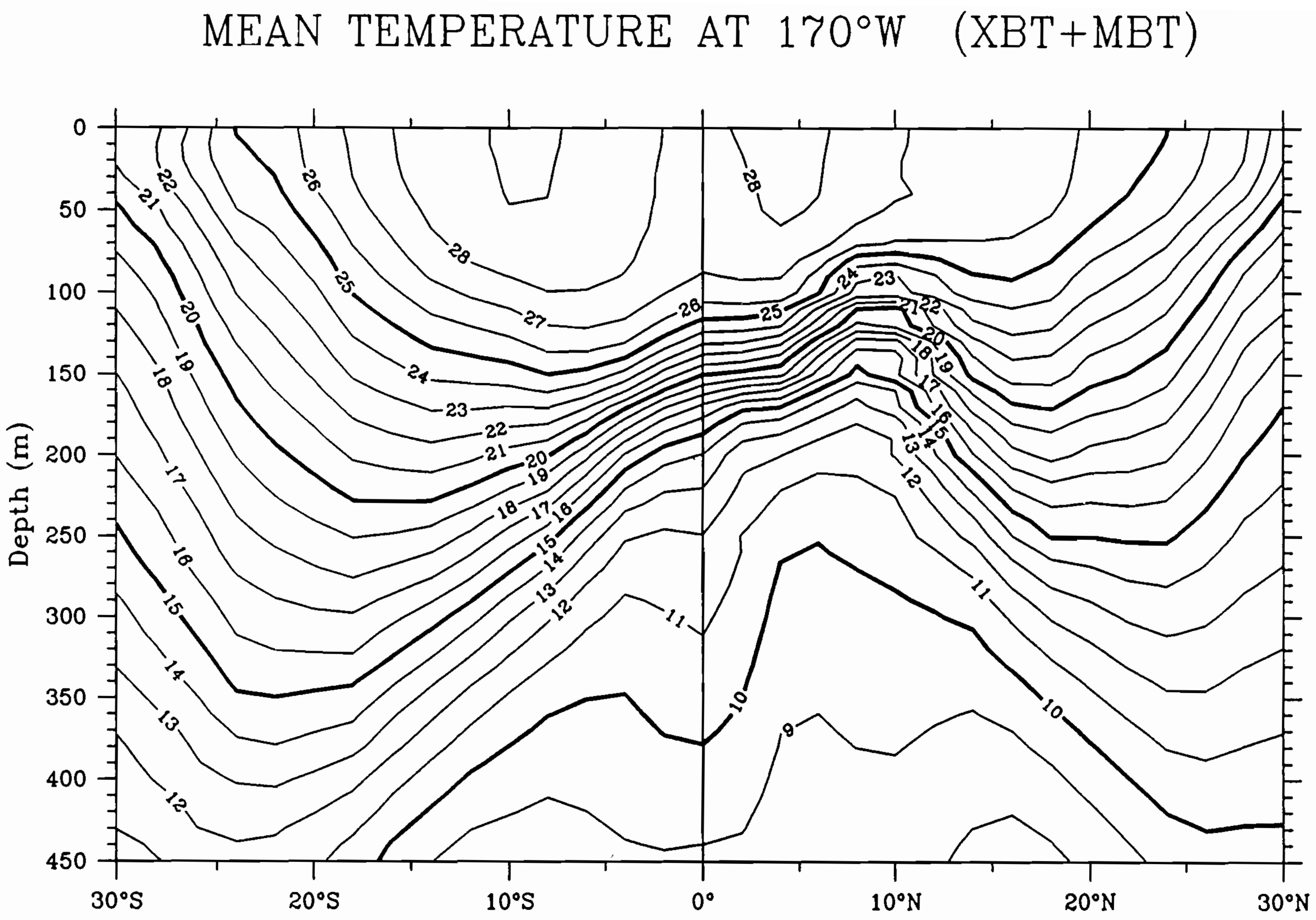
MEAN TEMPERATURE AT 170°W (XBT+MBT)

Figure A2.1e. Mean temperatures during 1970 through 1987 at 170°W.

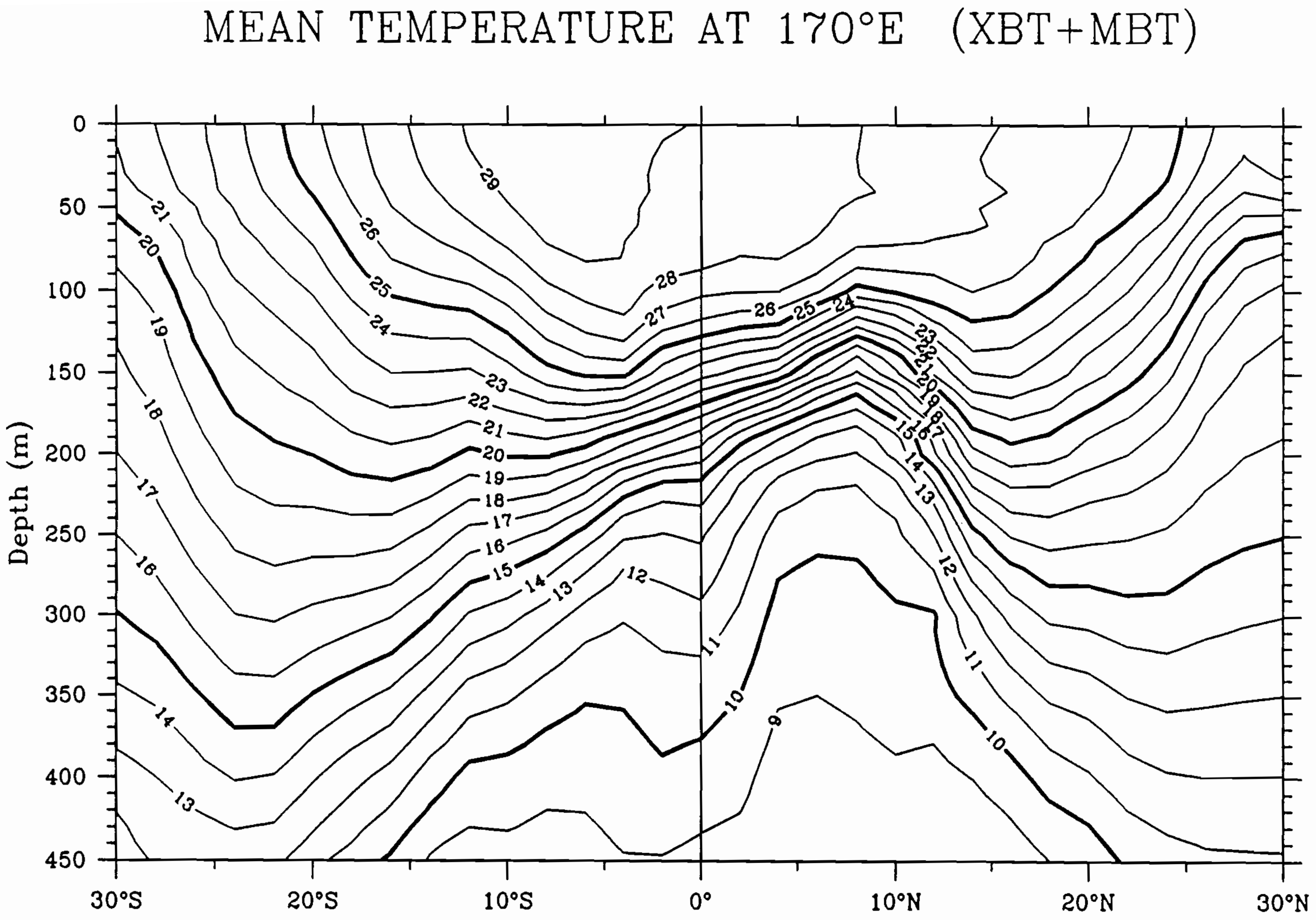

Figure A2.1f. Mean temperatures during 1970 through 1987 at 170°E.

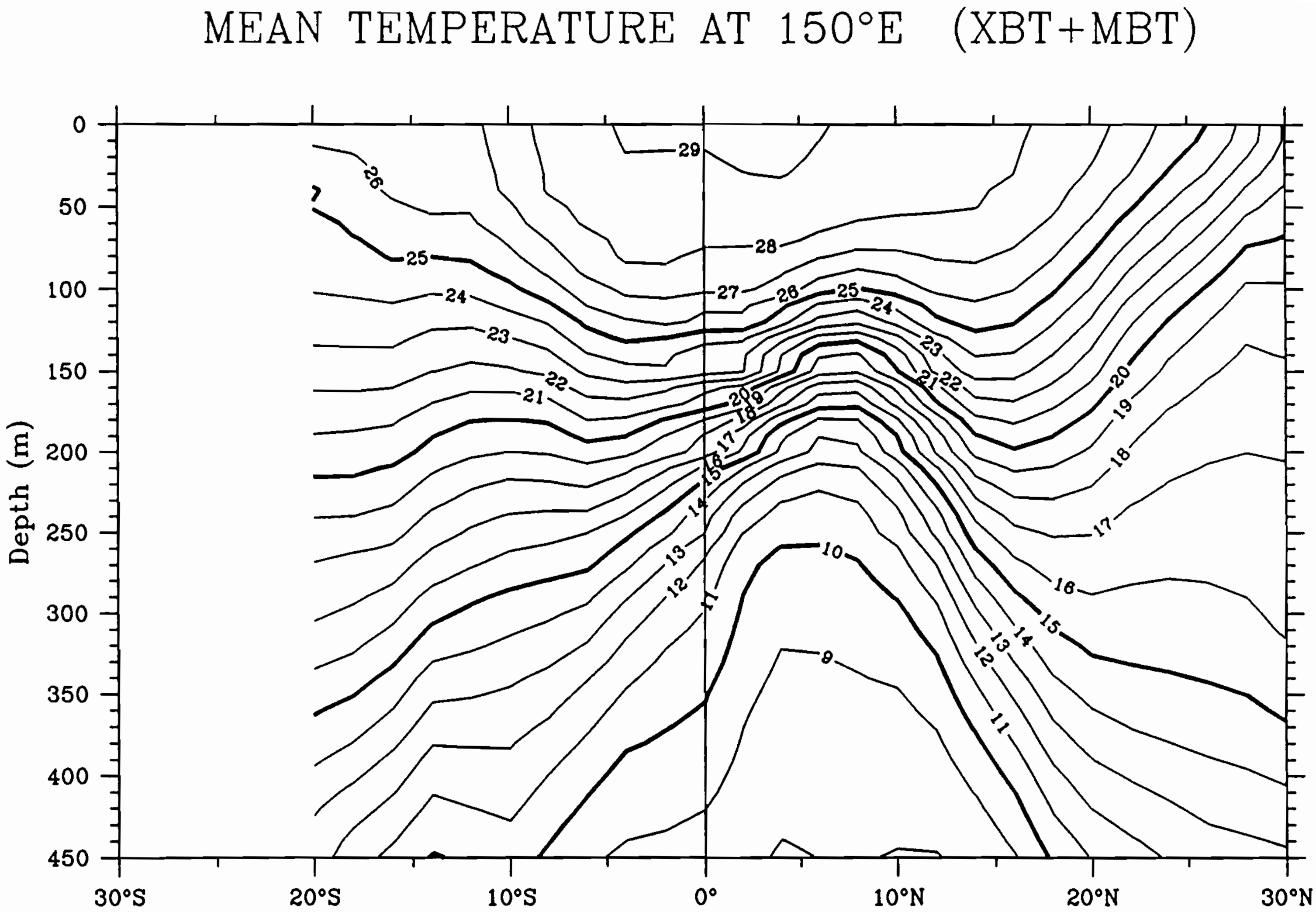

Figure A2.1g. Mean temperatures during 1970 through 1987 at 150°E.

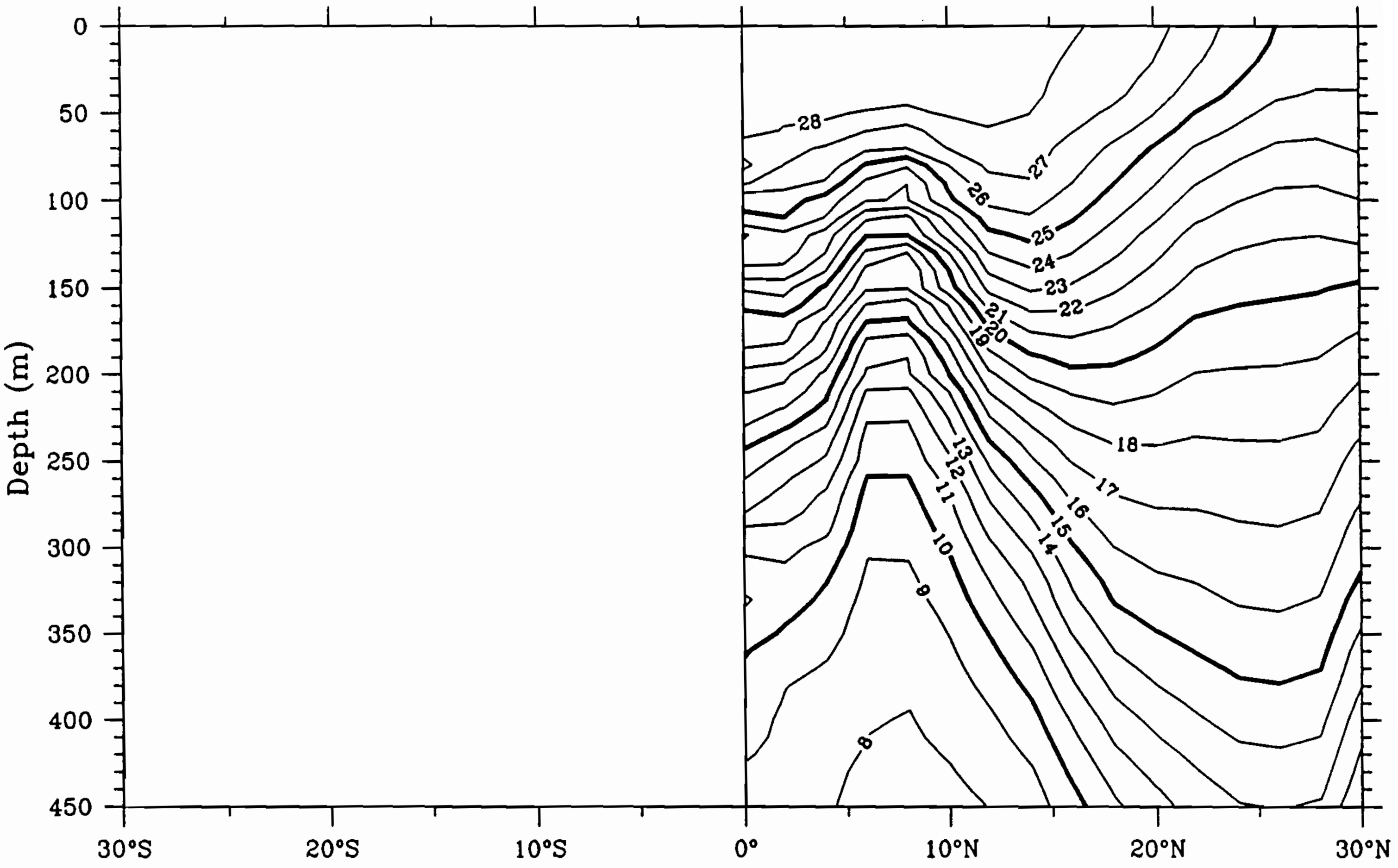
MEAN TEMPERATURE AT 130°E (XBT+MBT)

Figure A2.1h. Mean temperatures during 1970 through 1987 at 130°E.

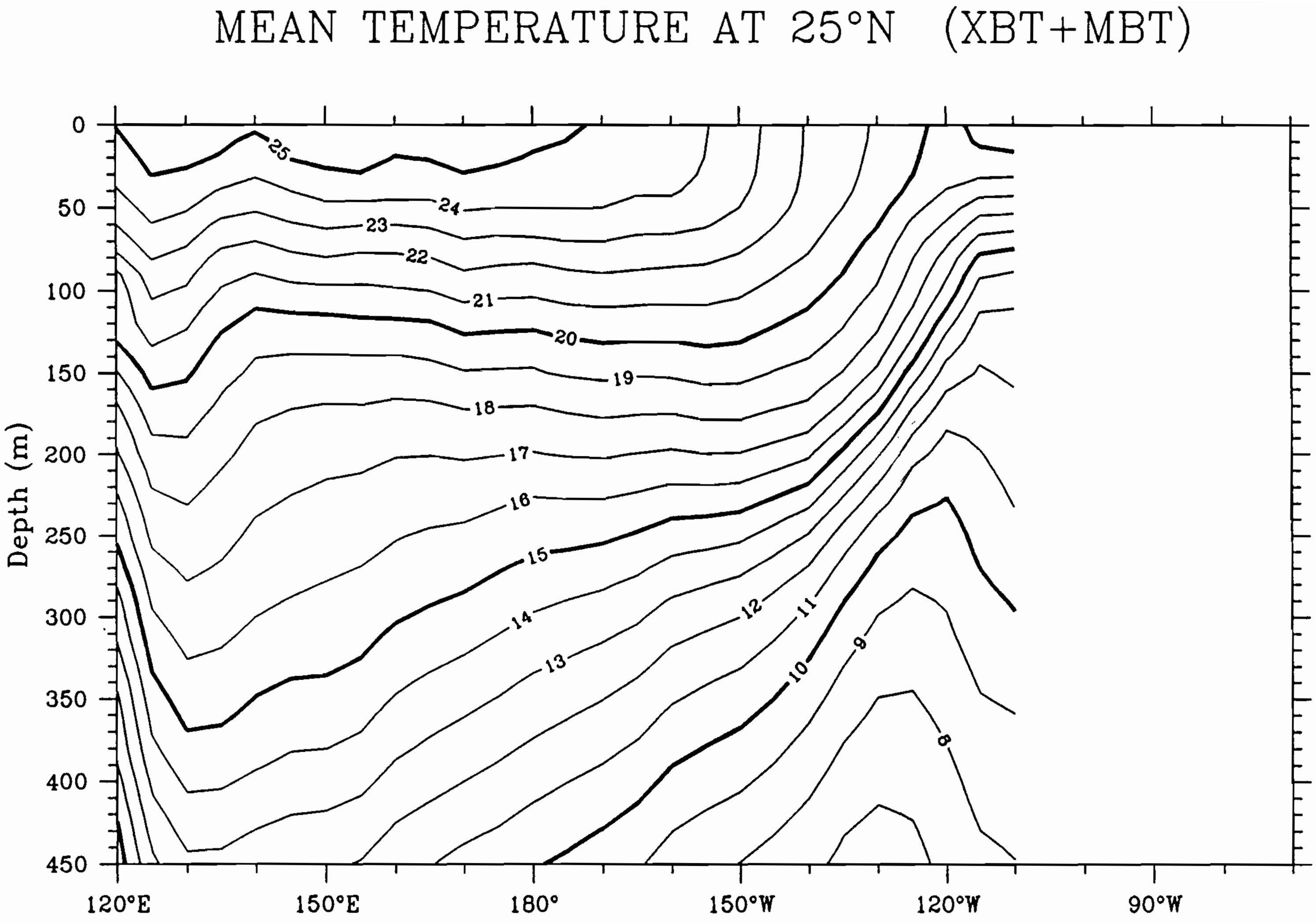

Figure A2.2a. Mean temperatures during 1970 through 1987 at 25°N.

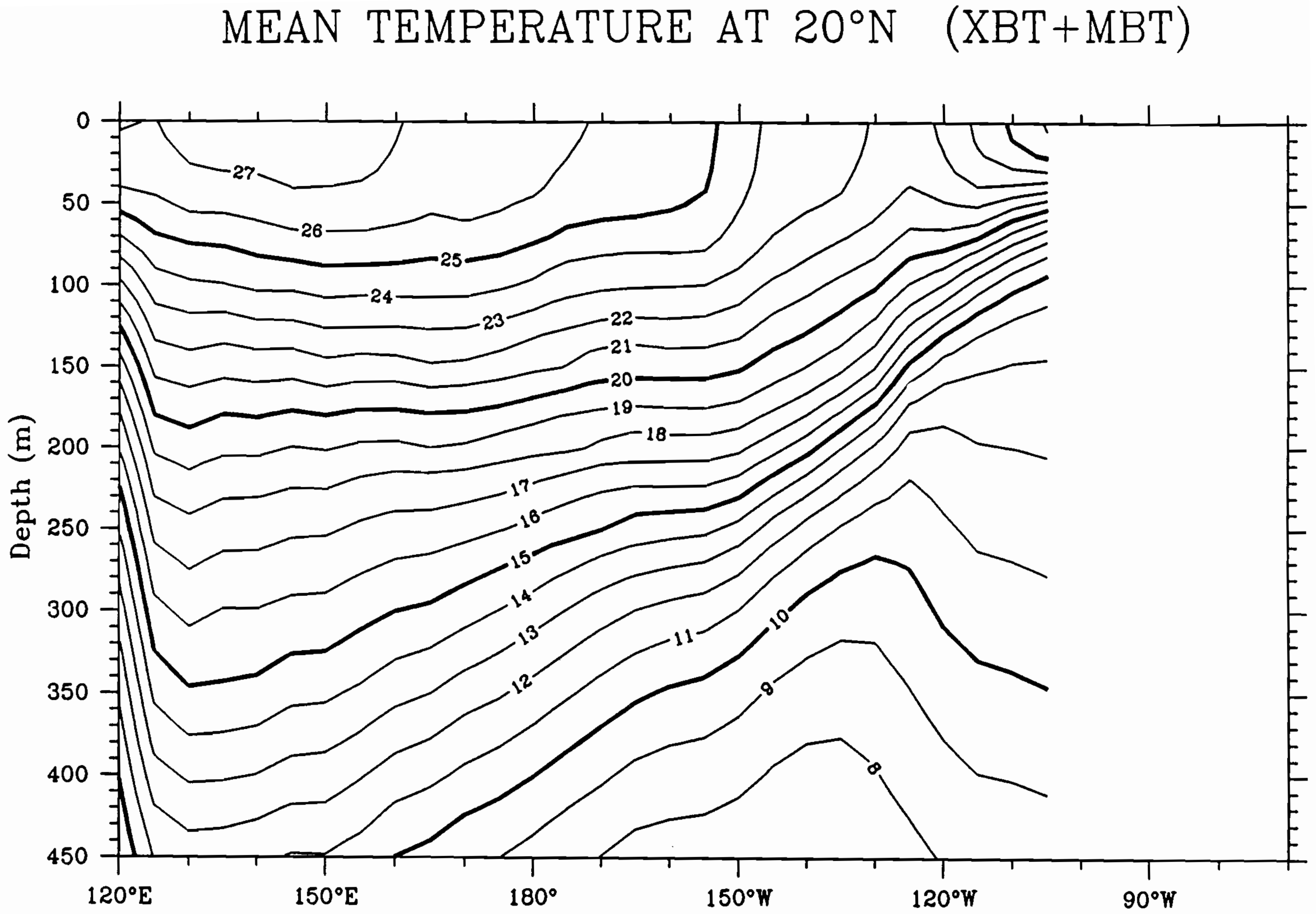
MEAN TEMPERATURE AT 20°N (XBT+MBT)

Figure A2.2b. Mean temperatures during 1970 through 1987 at 20°N.

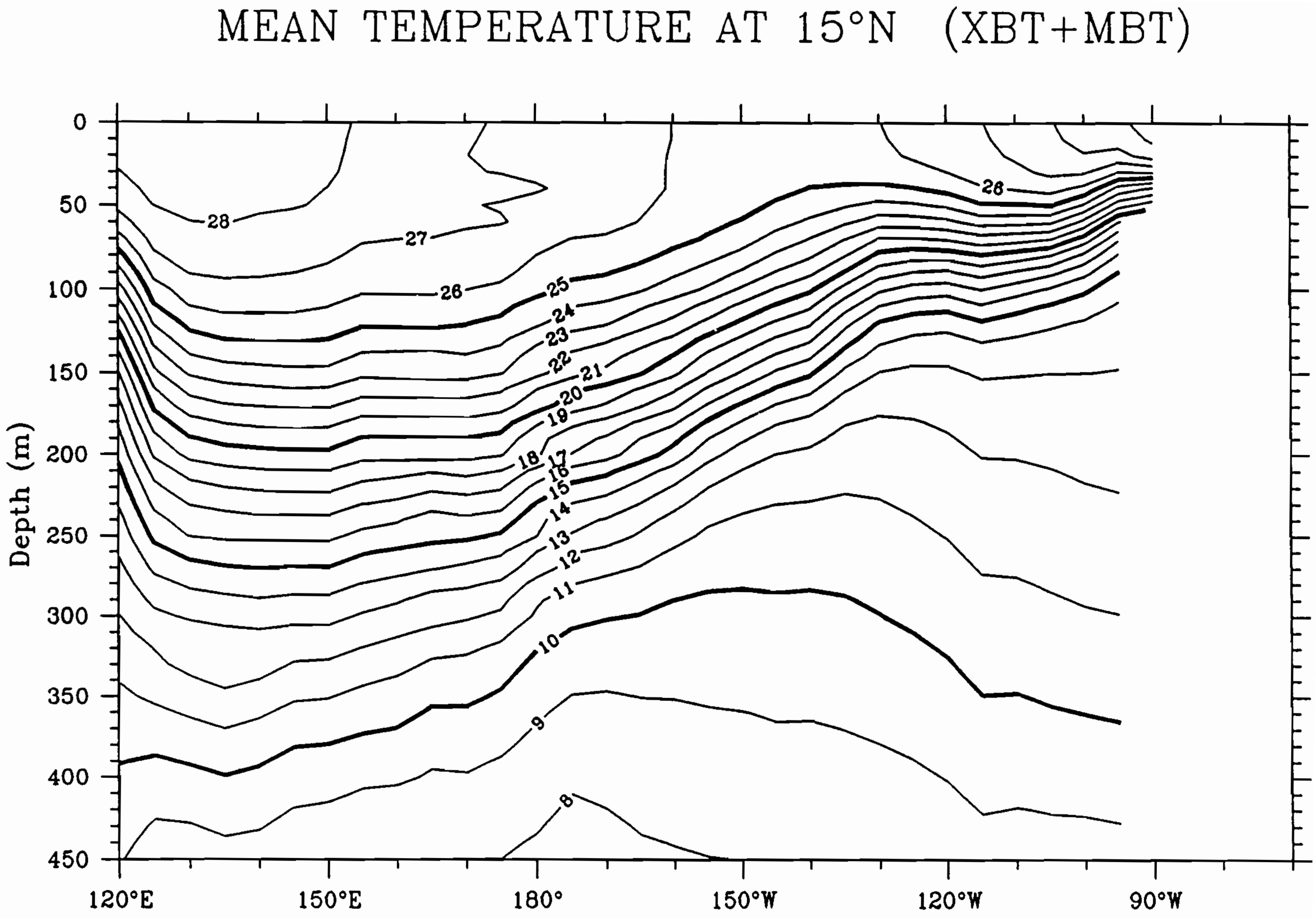

Figure A2.2c. Mean temperatures during 1970 through 1987 at 15°N.

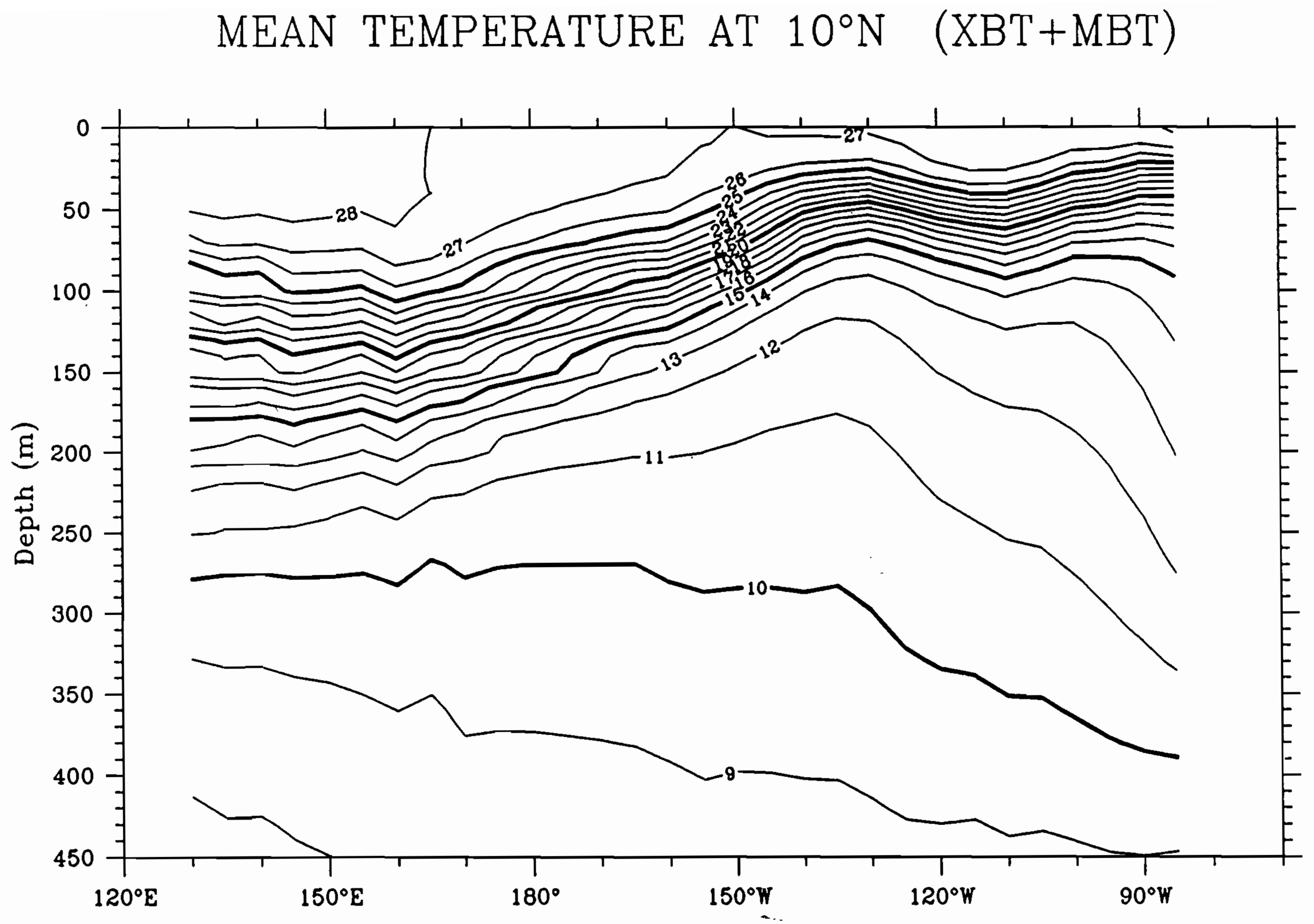

Figure A2.2d. Mean temperatures during 1970 through 1987 at 10°N.

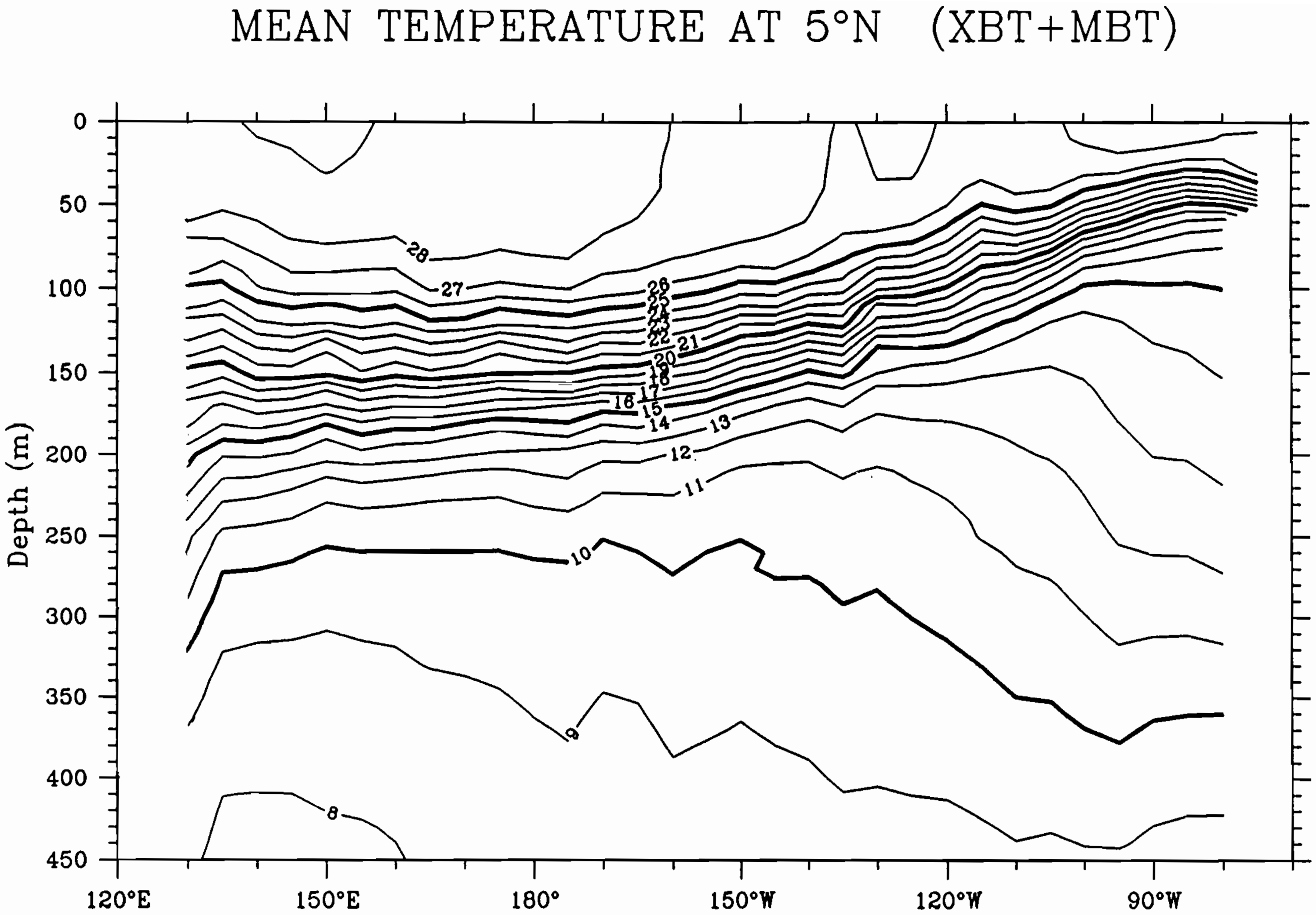

Figure A2.2e. Mean temperatures during 1970 through 1987 at 5°N.

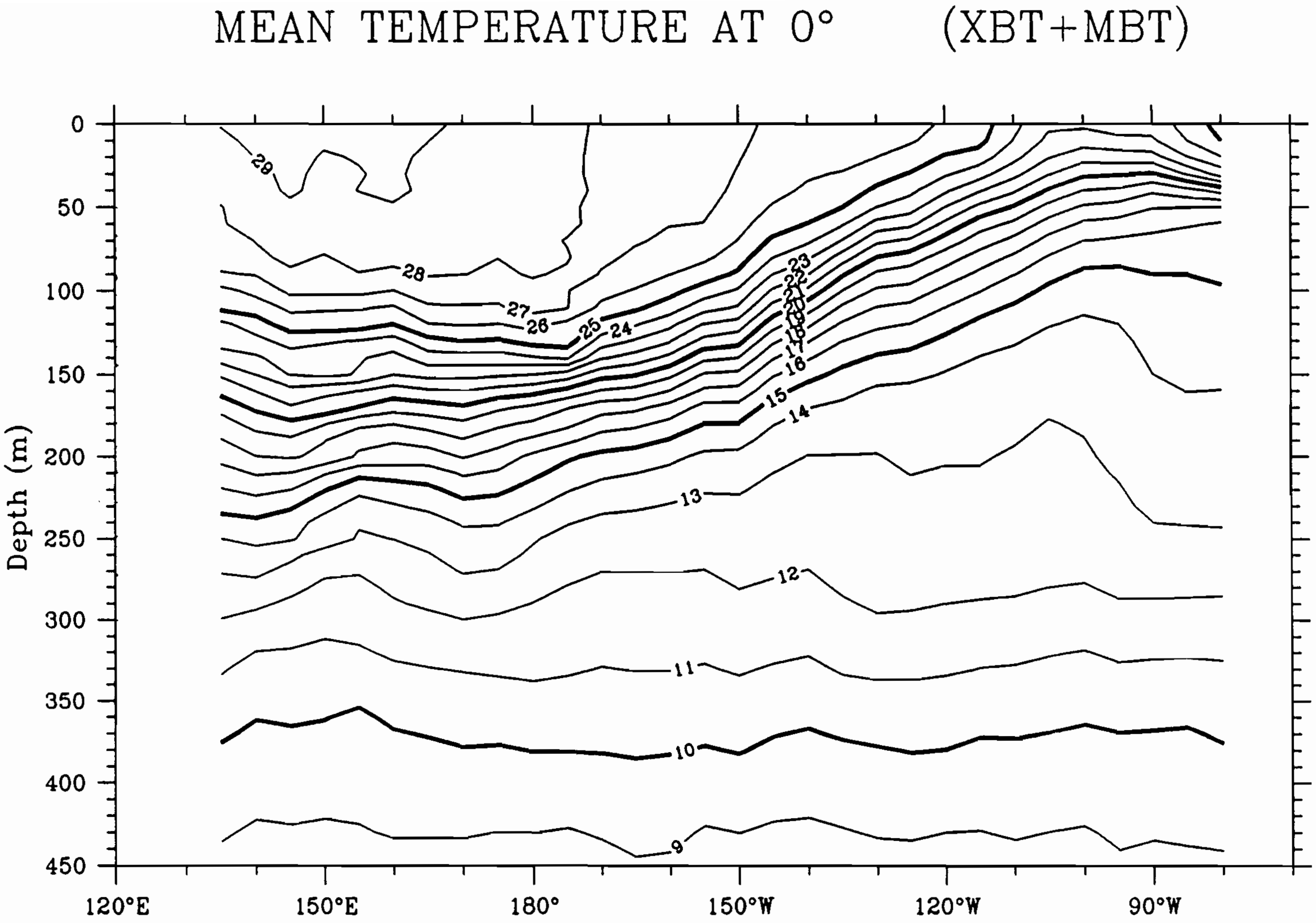

Figure A2.2f. Mean temperatures during 1970 through 1987 at the equator.

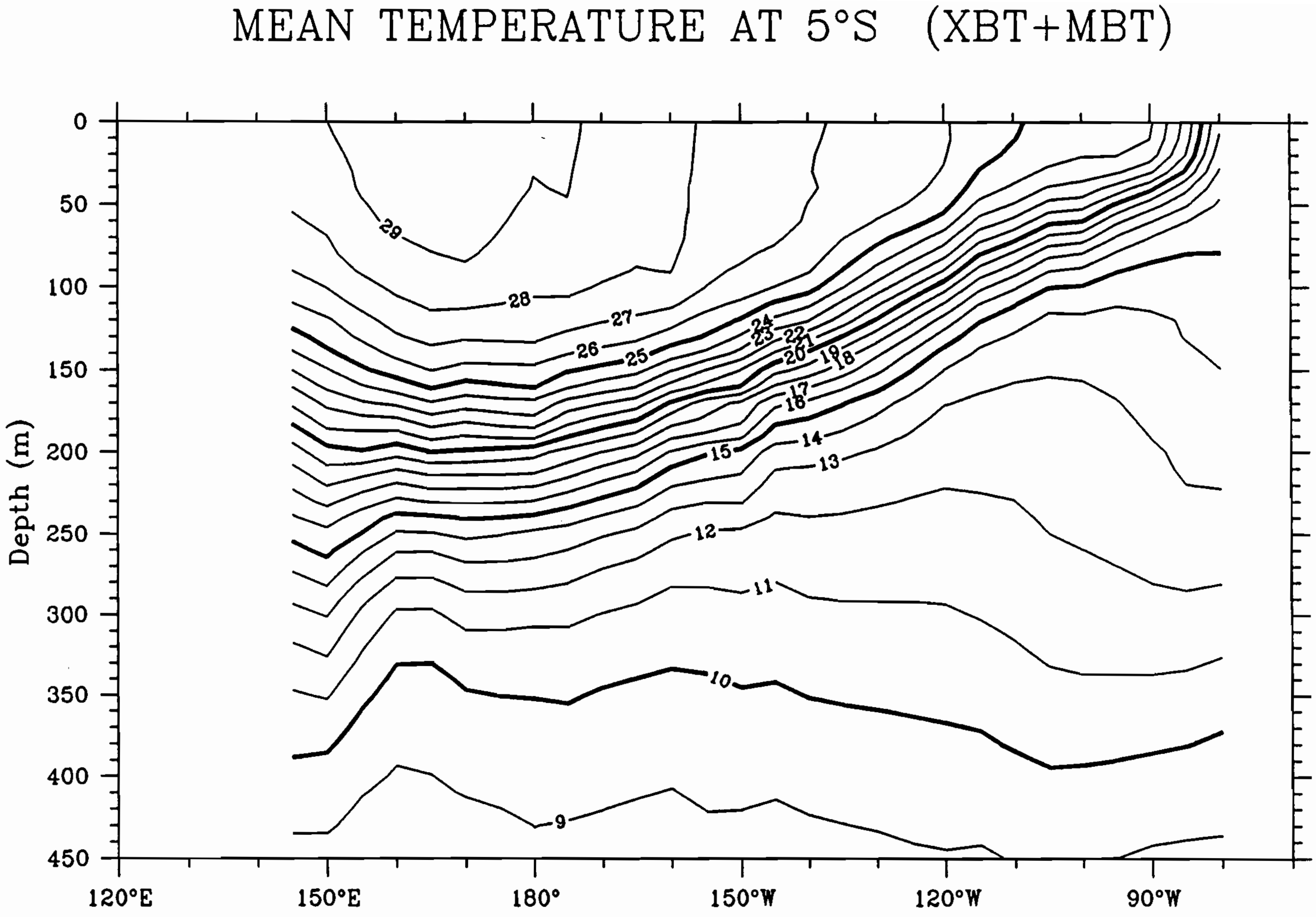
MEAN TEMPERATURE AT 5°S (XBT+MBT)

Figure A2.2g. Mean temperatures during 1970 through 1987 at 5°S.

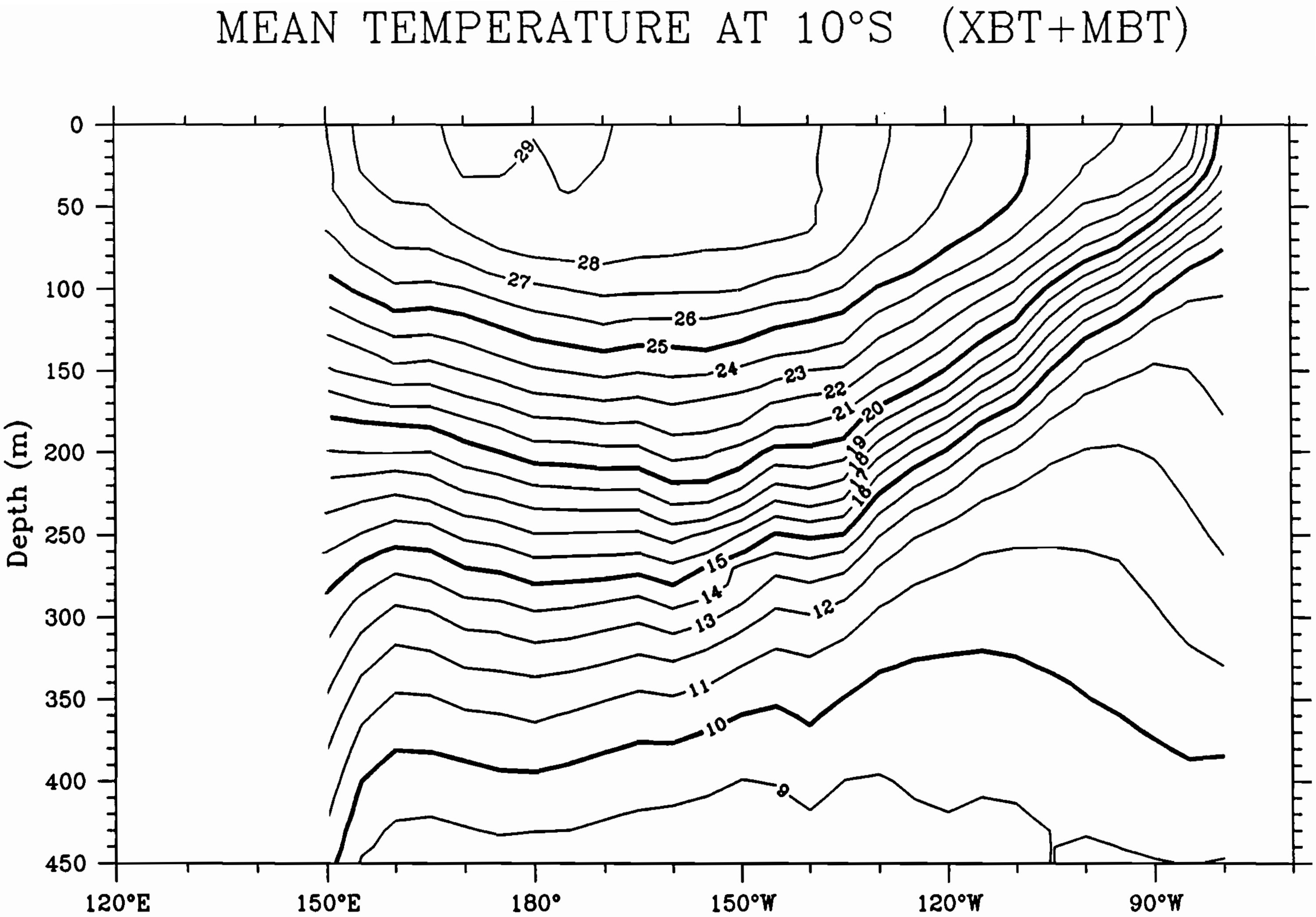

Figure A2.2h. Mean temperatures during 1970 through 1987 at 10°S.

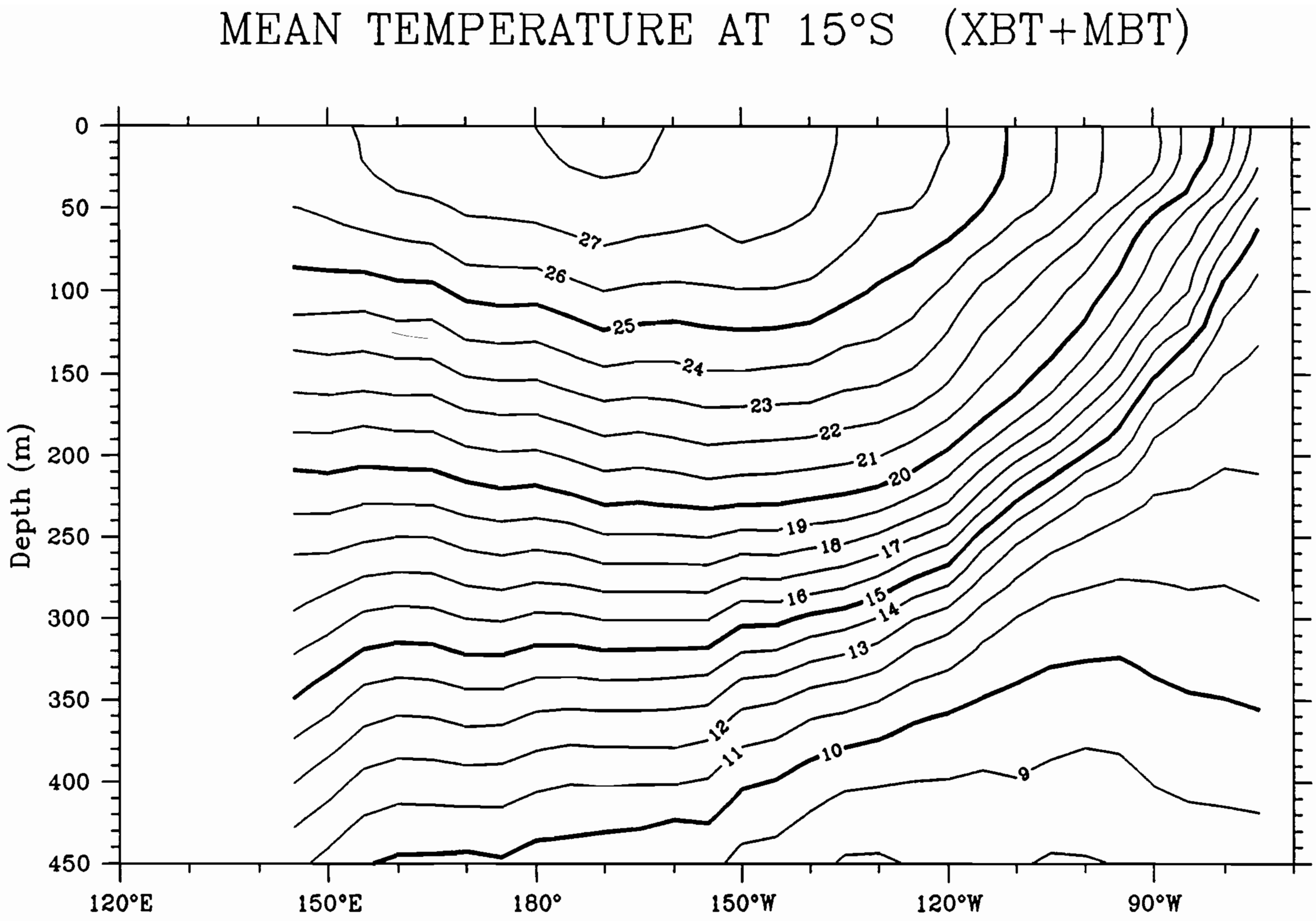
MEAN TEMPERATURE AT 15°S (XBT+MBT)

Figure A2.2i. Mean temperatures during 1970 through 1987 at 15°S.

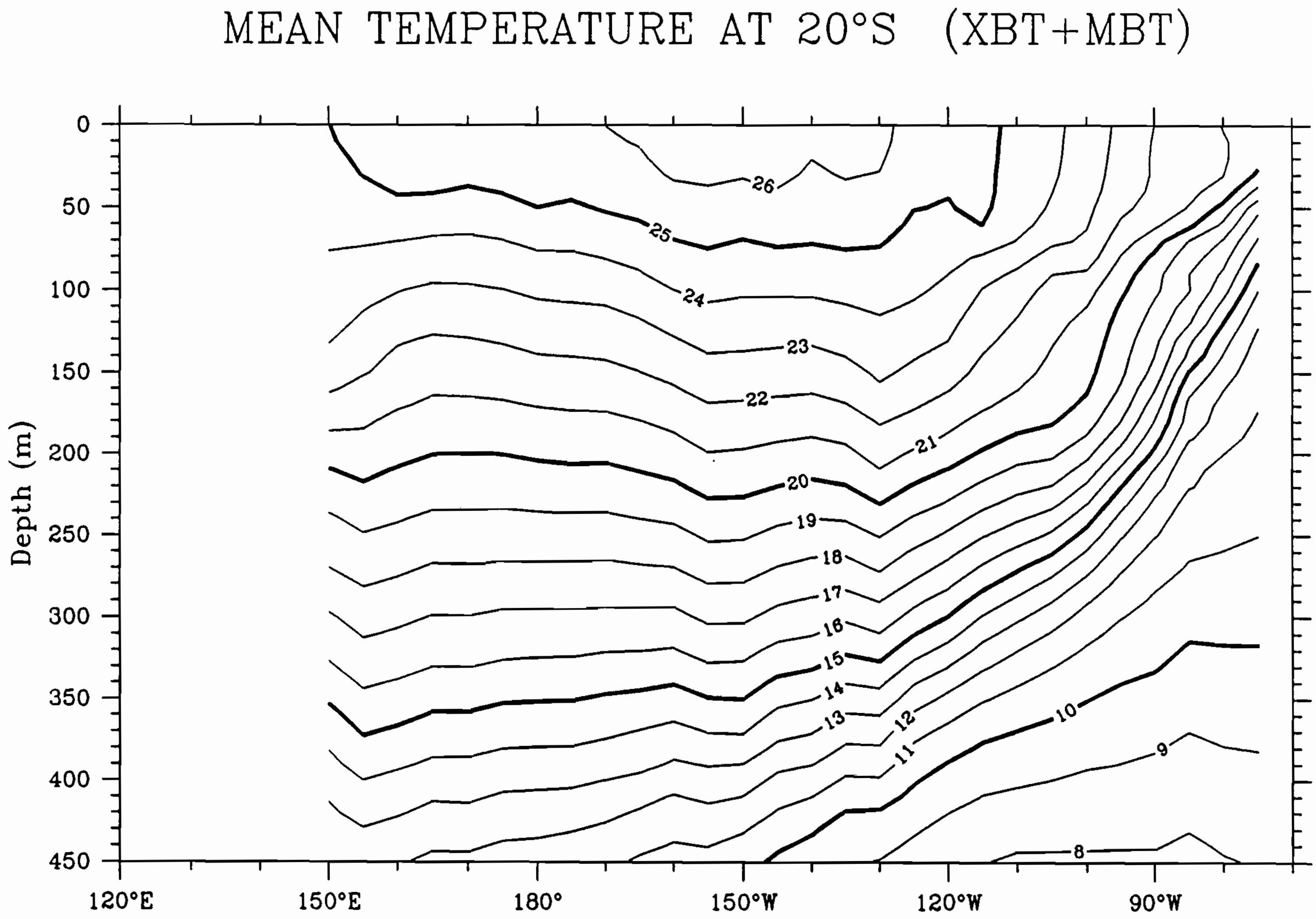

Figure A2.2j. Mean temperatures during 1970 through 1987 at 20°S.

* U. S. GOVERNMENT PRINTING OFFICE: 1989 -673-002/ 92034

# ERRATA

Page 18, line 15 should read: "$c^2 = g'H$ is the long baroclinic gravity wave speed squared".

Page 26, line 3: the equation in this line should be: "$c_r = \beta c^2/f^2$".

Page 30, line 2 should read: "quasi-geostrophic vorticity equation (2.6)".